This is to certify that the

dissertation entitled

Charm Muoproduction In Deep
Inelastic Scattering At 269 GeV/c

presented by

James Philip Kiley

has been accepted towards fulfillment
of the requirements for

Ph.D. degree in Physics

K.W. Chen
Major professor

Date 11-2-81

CHARM MUOPRODUCTION IN DEEP INELASTIC SCATTERING AT 269 GeV/c

BY

James Philip Kiley

A DISSERTATION

Submitted to
Michigan State University
in partial fulfillment of the requirment
for the degree of

DOCTOR OF PHILOSOPHY

Department of Physics

1981

ABSTRACT

CHARM MUOPRODUCTION IN DEEP
INELASTIC SCATTERING AT 269 GeV/c

BY

JAMES PHILIP KILEY

An experiment was performed at the Fermi National Accelerator Lab, located near Batavia, Illinois, using a positive 269 GeV muon beam incident on a 7.38 meter long iron-plastic scintillator target. With an incident flux of 1.0974×10^{10} muons (total luminosity of $2.80 \times 10^{37}/cm^2$), 449 events with two muons in the final state were observed. Applying the track reconstruction and scanning efficiency of $\sim$ 70% gave the expected number of dimuons (644) for this experiment (FNAL experiment 319). Subtracting the Monte Carlo calculated π/K internuclear cascade decay and prompt muon production backgrounds (a total of 56 events), and the QED trident dimuon background (a total of 10 events), yielded 578 dimuon events which were attributed to associated charmed D meson production and semileptonic decay. Using a $D\bar{D}$ Monte Carlo simulation based on the Nieh $D\bar{D}$ production model, the p_T (transverse momentum of the produced muon with respect to the virtual photon direction) acceptance was calculated and used to unfold the background subtracted renormalized data dimuon p_T spectra, yielding the total number of dimuon events expected for the experiment without apparatus acceptance. This number of events was used to calculate the cross section for associated charmed meson production, which was calculated to be (3.2 ± 0.8) nanobarns per nucleon. This cross section compares favorably with the cross section calculated

by Barger et al., based on the photon-gluon fusion model of quantum chromodynamics, of approximately 5 nanobarns per nucleon for our incident muon energy.

DEDICATION

To Anna, without whose friendship and inspiration I might never have finished what I had begun.

ACKNOWLEDGEMENTS

As with any endeavor of this magnitude, a large number of people were responsible for its ultimate success. The experiment was performed by the following people: Dr. K. Wendell Chen (thesis advisor), Dr. Adam Kotlewski, Dr. Larry Litt, Bob Ball, Dan Bauer, Sten Hansen, Phil Schewe, and myself. Without the 150% effort put forth by these dedicated individuals, there would have been no experiment. Our Fermilab collaborator, Dr. Andy Van Ginneken, proved invaluable in the analysis of both the single and multimuon data, since his Monte Carlo simulations were ultimately used for both.

Sten Hansen must be commended for his tireless dedication to the cause, especially since he was not a graduate student. The early work done on the construction and design of equipment by Bob Mills and Frank Early will never be forgotten. The endless encouragement and help given by Dr.'s Litt and Kotlewski has proved invaluable on many occasions. The tireless work and friendship of Dan Bauer and Bob Ball, and their contributions to the analysis effort, are without comparison. The help, friendship, and assistance of Dr. Mehdi Ghods is also deeply appreciated.

A very special thanks is due a very special person, Karen Stricker, whose friendship, love, concern, and help during graduate school can never be repaid.

I would like to take this opportunity to thank the Fermilab neutrino line crew, and the computing departments at Fermilab and Michigan State University; and especially the taxpayers of this

country, for their support of basic research.

Thanks are due Patricia Veverica for her work on the drawings in Chapter V, Ms. Donna Sorge for her magnificent job of typing this thesis, and Mr. Paul Owens and Raymond Kelso for help in editing and completing this thesis.

TABLE OF CONTENTS

LIST OF TABLES

LIST OF FIGURES

CHAPTER I

INTRODUCTION

1.1 Theoretical Overview

The current picture of the structure of matter is based on the belief that matter is composed of quarks[1] and leptons, both of which are spin ½ point-like fermions. Leptons (e.g. the electron, muon, and neutrino) feel the electromagnetic and weak forces, but not the strong force (i.e. leptons are not "colored"[2]). Quarks, which are predicted to have fractional electric charges, see Table 1.1, feel the strong, electromagnetic, and weak forces, and are thought to be the building blocks of which the strongly interacting particles (hadrons) are composed (e.g. the proton, neutron, pion, and kaon). There are two kinds of strongly interacting particles: a) the baryons, common examples of which are the proton and the neutron, which are fermions (i.e. they obey Fermi-Dirac statistics[3] and have intrinsic spins which are half-integral multiples of $h/2\pi$, h the Planck constant) and are composed of three quarks (antibaryons are composed of three anti-quarks) and, b) the mesons, common examples of which are the pion and the kaon, which are bosons (i.e. they have intrinsic spins which are integral multiples of $h/2\pi$, and obey Bose-Einstein statistics[3]) and are composed of a quark and an antiquark.

The forces between these elementary particles are viewed as due to the exchange of spin one bosons (spin two for gravity). For the strong force, the quarks are assumed to occur in three "colors"[2], a property of the quarks (analogous to the charge of a lepton, the strong force can be thought of as due to the "color charge" of the

Table 1.1 Quark Properties

	Baryon number	Isospin (I)	I_3	Strangeness (S)	Hypercharge (Y)	Charm (C)	Charge (Q)
u	1/3	1/2	+1/2	0	1/3	0	2/3
d	1/3	1/2	-1/2	0	1/3	0	-1/3
s	1/3	0	0	-1	-2/3	0	-1/3
c	1/3	0	0	0	0	1	2/3

$$Q = I_3 + Y/2 + 2/3\ C$$

Table 1.2 Pseudoscalar Meson ($J^P = 0^-$) Properties

Pseudoscalar Meson Octet

	Quark Content	Mass (MeV)	Mean Life Time (sec)
π^+	$u\bar{d}$	139.6	2.6×10^{-8}
π^-	$\bar{u}d$	139.6	2.6×10^{-8}
π^o	$1/\sqrt{2}\ (u\bar{u}-d\bar{d})$	135.0	0.83×10^{-16}
K^+	$u\bar{s}$	493.7	1.24×10^{-8}
K^-	$\bar{u}s$	493.7	1.24×10^{-8}
K^o	$d\bar{s}$	497.7	$>5.18 \times 10^{-8}$
$\bar{K}^o$	$\bar{d}s$	497.7	$>5.18 \times 10^{-8}$
η^o	$1/\sqrt{6}\ (u\bar{u}+d\bar{d}-2s\bar{s})$	548.8	

Pseudoscalar Meson Singlet

η'	$1/\sqrt{3}\ (u\bar{u}+d\bar{d}+s\bar{s})$	957.6	

quarks, just as the electromagnetic force is due to the charge of a particle) which distinguish them from the leptons, which are colorless. The strong force between the colored quarks is seen as being due to the exchange of the colored vector gluons, eight spin one massless particles (note that the gluons carry the color charge and can interact with themselves). The electromagnetic force between charged particles is seen as being due to the exchange of photons, which are spin one massless particles. The weak force between quarks or leptons (a common example of the weak force is nuclear beta decay, $n \rightarrow p^+ e^- \bar{\nu}_e$) is viewed as the exchange of the intermediate vector (spin one) mesons, the W^+, Z^o, and W^-, which are thought to have relatively large masses (> 80 GeV/c^2, compared to the proton masses of ~ 1 GeV/c^2), which helps account for the short range of the weak force.

In the 1950's[4], only two flavors of quarks, the u and the d quarks, were necessary to explain the observed hadronic structure. In the late 1950's, one more quark, the strange (or s) quark, was introduced[4], which helped to explain the large number of new strongly interacting particles observed. By the 1960's, there were four leptons: the electron, the electron neutrino, the muon, and the muon neutrino (as well as the four corresponding antileptons). In the mid 1960's[5], theorists suggested a fourth quark, the charmed (or c) quark, was needed. This quark had to be relatively massive ($m_c \sim 1.5$ GeV/c^2, compared with masses of ~ 300 MeV/c^2 for the u and d quarks, and a mass of ~ 510 MeV/c^2 for the s quark) and was needed to explain certain theoretical and experimental observations[6], which will be described in detail later. The discovery of the ψ (3095)[7,8] and its family of associated states[9] in 1974 was interpreted as the discovery

of a family of mesons composed of a charmed quark and a charmed antiquark. So with four leptons (and their corresponding antileptons) and the four flavors of quarks (and antiquarks), each of which occured in three colors, all of the "necessary" fundamental particles seemed to have been discovered. The discovery of the tau lepton[10] ($m_\tau \sim 1.8$ GeV/c^2) in 1975, and its assumed neutrino, added two more leptons to the lepton family, breaking the quark-lepton symmetry[5] (one of the compelling reasons for the c quark's existence). The quarks gained another new member, with the discovery in 1977[11] of the upsilon, which is now interpreted as a bound $b\bar{b}$ quark pair, b being a new quark flavor, similar to the strange quark but with a mass of ~ 5 GeV/c^2. Another quark is expected, one which is associated with the b quark and is called the t quark, which is expected to be much heavier than the b quark. Bound particle states containing t quarks have not yet been discovered. How many quarks and leptons will ultimately be discovered is one of the remaining interesting problems of elementary particle physics.

This thesis is concerned with the production, and semileptonic decay, of charmed mesons in deep inelastic muon-nucleon scattering, this being the most likely interpretation of multimuon final states observed in deep inelastic muon scattering experiments at Fermilab in the early[12] and late[13] 1970's.

1.2 Ultimate Structure of Matter

Man has always been curious about the smallest building blocks of which matter is composed. The ancient Greeks developed the concept of the atom as the smallest, indivisible building block of matter.

The discovery of radioactivity in 1896 by Henri Becquerel dispelled the idea of atoms as permanent entities, and the 1911 experiments of Ernest Rutherford showed that atoms consisted of a small, dense nucleus surrounded by a cloud of atomic electrons. The discovery that the atomic nucleus was composed of nucleons[4] (protons and neutrons) seemed, for a while, to make these particles, along with the electron, the only ones necessary to explain the structure of matter. Early low energy electron-nucleon scattering experiments,[14] where the structure of the atomic nucleus and nucleons was probed by virtual photons (photons for which the relationship $E^2 = p^2c^2 + m^2c^4$ gives a non-zero mass) emitted by the scattering electrons, revealed that the nucleon was not homogeneous, but rather had a complex structure. The discovery of the muon, pion, and neutrino added new particles to be accounted for, and in the 1950's and 1960's hundreds of new "fundamental" particles were discovered[4], including the strange particles (which possessed a new quantum number, strangeness, and had to be created in pairs when created via the strong interactions), the kaons and hyperons. High p_T jet structure (the final state particles coming out in well defined "jets" at large angles relative to the incident particles directions) in pp scattering looked remarkably like the jet structure observed in electron-positron scattering, suggesting that protons contained point like constituents.

In an attempt to explain the spectrum of observed strongly interacting particles, Gell-Mann and Ne'eman[1] in 1961 developed a theory based on symmetry groups[15] (called the eightfold way, based on SU(3) symmetry). All known strongly interacting particles at that time

fit into this scheme, and a new particle, the omega minus, was predicted to exist (it was discovered[16] in 1964). The theory predicted the existence of a fundamental triplet of particles from which all the other "known" hadrons could be constructed. These were the three flavors of quarks, called u, d, and s. The quarks are point-like fermions (spin ½ particles which obey the Fermi-Dirac statistics) and were predicted to have fractional electric charges. The charge of the u quark is 2/3 |e| , while the charges of the d and s quarks are - 1/3 |e|, with |e| being the magnitude of the electron's charge. Corresponding to these three quarks, there are three antiquarks (the $\bar{u}$, $\bar{d}$, and $\bar{s}$) with the same mass but with the opposite electric charge of the corresponding quark.

The particles which feel the strong force (the hadrons) are divided into two groups, the mesons and the baryons. The mesons are bosons (i.e. their intrinsic spin is an integral multiple of $\hbar$) and are composed of a quark and an antiquark. Common examples of mesons are the $\pi^+(u\bar{d})$, the $\pi^-(\bar{u}d)$, the $K^+(u\bar{s})$, the $K^-(\bar{u}s)$, the $K^\circ(d\bar{s})$, and the $\overline{K}^\circ(\bar{d}s)$. The properties of the lowest mass mesons are shown in Table 1.2. The baryons are fermions (i.e. their intrinsic spin is a half-integral multiple of $\hbar$) and are composed of three quarks (anti-baryons are composed of three antiquarks). Common examples of spin ½ baryons are the proton (uud), the neutron (udd), the Σ^-(dds), and the Σ^+(uus). The properties of the lowest mass baryons are shown in Table 1.3.

The pseudoscalar mesons, which are composed of a quark and an antiquark in a state of zero relative orbital angular momentum, have

Table 1.3 Lowest Mass Baryon Properties

	Quark Content	Mass (MeV)	Mean Lifetime (sec)
Baryon Octet ($J^P = 1/2^+$)			
p	uud	938.3	$>10^{31}$ years
n	udd	939.6	918
Σ^+	uus	1189.4	0.80×10^{-10}
Σ^o	$1/\sqrt{2}$ (ud+du)s	1192.5	5.8×10^{-20}
Σ^-	dds	1197.4	1.48×10^{-10}
Ξ^o	uss	1314.9	2.9×10^{-10}
Ξ^-	dss	1321.3	1.65×10^{-10}
Baryon Singlet ($J^P = 1/2^+$)			
Λ^o	$1/\sqrt{2}$ (ud-du)s	1115.6	2.6×10^{-10}
Baryon Decuplet ($J^P = 3/2^+$)			
Δ^{++}	uuu	1232	
Δ^+	uud	1232	
Δ^o	udd	1232	
Δ^-	ddd	1232	
Σ^{*+}	uus	1382.3	
Σ^{*o}	uds	1382.0	
Σ^{*-}	dds	1387.5	
Ξ^{*o}	uss	1531.8	
Ξ^{*-}	dss	1535.0	
Ω^-	sss	1672.2	

a total of nine possible physical states (in the language of group theory[15], 3 x 3* = 1 + 8), which can be divided into a singlet and an octet of particle states, as shown in Figure 1.1. Given two spin ½ constituent particles, there are two possible results for the total angular momentum of the particle state (for zero orbital angular momentum), spin zero (pseudoscalar mesons) and spin one (vector mesons). The corresponding vector meson states are the K^{*+}, K^{*o}, ρ^+, ρ^o, ρ^-, K^{*-}, $\bar{K}^{*o}$, ω, and $\phi(s\bar{s})$, shown in Figure 1.2.

For the baryons, there are 19 lowest lying physical states (3x3x3 = 1+8+8'+10, but because of symmetry, one of the 8's does not correspond to physically observed particles), which can be grouped as a singlet, a baryon octet (spin ½), and a baryon decuplet (spin 3/2), shown in Table 1.3; the only possible total spins being ½ and 3/2, as the result of adding three spins of ½. The weight diagrams for the spin ½ baryon octet and spin 3/2 baryon decuplet are shown in Figures 1.3 and 1.4.

In the weight diagrams for the particle states discussed above, the states are classified according to two quantum numbers, I (isospin) and Y (hypercharge). The isospin quantum number (I) is a measure of the number of charged particle states which have approximately the same mass, the total number of charged states being: 2I + 1. For the pions I = 1 (i.e. there are 2I + 1 = 3 charged states), and the states in the pion multiplet are distinguished by their values of I_3 (+1 for the π^+, 0 for the π^o, and -1 for the π^-). For the nucleons (proton and neutron) I = ½ (i.e. there are 2I + 1 = 2 charged states), with the proton having I_3 = +½ and the neutron having I_3 = -½. The other

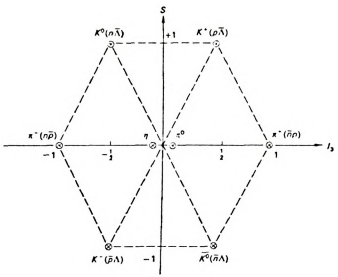

Figure 1.1 Pseudoscalar Meson Nonet

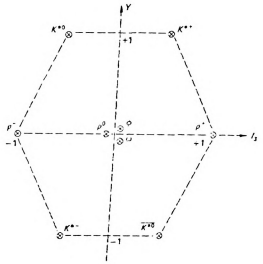

Figure 1.2 Vector Meson Nonet

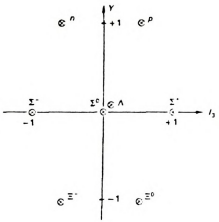

Figure 1.3 Baryon Octet

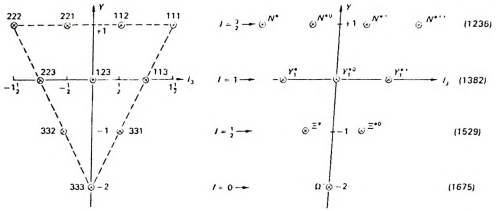

Figure 1.4 Baryon Decuplet

additive quantum number Y (hypercharge) is defined as: $Y = B + S$, where B is the baryon number and S is the strangeness quantum number. The baryon number of a quark is +1/3 (B for an antiquark is -1/3), so the baryon number of a baryon (composed of three quarks) is +1, the baryon number of an antibaryon (composed of three antiquarks) is -1, and the baryon number of a meson (composed of a quark and an antiquark) is 0. The strangeness quantum number for the u and d quarks is zero, and for the s quark is -1 (+1 for the $\bar{s}$ antiquark), so the strangeness quantum number is a measure of the number of strange quarks in a particle state. The isospin and strangeness quantum numbers are conserved in the strong interactions, while the strangeness quantum number is not conserved in the weak interactions. Baryon number seems to be conserved in all interactions, and is the reason the proton (the lightest baryon) is so stable[17].

The one remaining property of quarks to be discussed is color. Each flavor of quark (u,d,s,...) is assumed to occur in three different colors (called red, green, and blue, for simplicity), a property of the quark analogous to the charge of a charged particle. The quarks that make up hadrons are colored, but the physical hadrons themselves are colorless (i.e. net color equal to zero). For the baryons, the three quarks in a baryon each have a different color, giving the baryon itself a net color of zero. For the mesons, the color of the antiquark is the anticolor of the quark's color, giving a net color of zero for mesons. These three colors form an SU(3) color group, which is thought to be an exact symmetry (i.e. quarks of the same flavor but different colors have the same mass). The generators of this SU(3) color symmetry (i.e. the objects which rotate the quarks

from one color state to another) are the eight massless colored vector (spin 1) particles called gluons (these are thought to hold the quarks together in hadrons). These gluons are the carriers of the strong force, in much the same way that the photon is the carrier of the electromagnetic force between charged particles. Quarks interact with each other by exchanging gluons (gluon emission changes the quarks' color, but not its flavor).

The color property of quarks was hypothesized for the following reasons: 1) Color was needed to preserve the Fermi statistics for baryons. Baryons are fermions (they have half integral values of intrinsic spin and must be created and destroyed in pairs) and their total wave function must be antisymmetric. For the Δ^{++} (composed of three u quarks in a state of zero orbital angular momentum), which is a spin 3/2 baryon, all three quarks must have their spins aligned. So the total wave function in this case is symmetric with respect to the exchange of any two of the quarks (since the quarks all have the same orbital angular momentum and spin alignment). If each of the u quarks in the Δ^{++} is a different color, then the quarks are antisymmetric in color, and the total wavefunction is now antisymmetric with respect to the exchange of any two quarks. In this case, it is seen that there must be at least three colors. 2) Color helps explain why the only quark combinations seen so far for hadrons are qqq ($\bar{q}\bar{q}\bar{q}$) for baryons (antibaryons) and $q\bar{q}$ for mesons. There are no other simple colored quark and antiquark combinations which give colorless hadrons. 3) Color helps explain the difference between quarks and leptons. Quarks are colored and hence feel the

strong force, leptons are colorless and hence do not feel the strong force, only the electromagnetic and weak forces. 4) Color is necessary in order to get the correct answer for the calculation of the π^o lifetime. The calculated lifetime of the π^o is off by a factor of three from the measured value if quarks are not colored. 5) Color is needed to help explain the value of $R(=\sigma (e^+e^- \rightarrow \text{hadrons})/\sigma(e^+e^- \rightarrow \mu^+\mu^-))$ measured in electron-positron scattering[18]. The calculated value for this ratio (which will be described later) is low by a factor of approximately three when compared to the experimentally measured value if quarks are not colored, and the agreement between theory and experiment is very good if quarks are colored.

The family of leptons (literally "light ones") do not feel the strong force (i.e. leptons are not colored), but they do feel the electromagnetic (for charged leptons) and weak forces. Leptons are spin ½ fermions (they must be created or destroyed in pairs) and seem to be point-like particles. The electron (discovered in 1897 by J. J. Thomson; $m_e = 0.511$ MeV/c^2) was the only known lepton until the discovery, in cosmic ray cloud chamber experiments[19] in 1937 and 1938, of the muon (whose mass is 105.66 MeV/c^2, or approximately 207 times that of the electron; the mean life of the muon is 2.20×10^{-6} sec). Conservation of momentum, energy, and angular momentum in nuclear beta decay led Pauli[20] in 1933 to postulate the existence of light, uncharged spin ½ particles, called neutrinos (and their antiparticles, the antineutrinos). The existence of neutrinos was demonstrated by Reines and Cowan[21] in 1959, using the intense anti-neutrino fluxes from a nuclear reactor. Experiments at Brookhaven and

CERN[22] in 1962-1963 proved the existence of two types of neutrino; one was associated with the electron (and occured in nuclear beta decay), while the other neutrino was associated with the muon (and occured in pion decay). Muons and electrons each have separate additive leptonic quantum numbers associated with them, quantum numbers that are conserved in any allowed reaction. Negative leptons and neutrinos have lepton number eigenvalues of +1, while positive leptons and antineutrinos have values of this leptonic quantum number of -1. The decay $\mu^- \rightarrow e^- \gamma$ does not seem to occur (it does not conserve muon or electron number), whereas the decay $\mu^- \rightarrow e^- \bar{\nu}_e \nu_\mu$ does occur (this accounts for approximately 98.6% of muon decays, and does conserve both muon and electron number). The current upper limits on the masses of the neutrinos are: mass $(\nu_e) < 6 \times 10^{-5}$ MeV/c^2, and mass $(\nu_\mu) < 0.57$ MeV/c^2. Being point-like particles whose electromagnetic interactions are well understood (using quantum electrodynamics[23]), the charged leptons are used in many scattering experiments as probes of nuclear and nucleon structure[14].

If neutrinos are massless, then there are only two possible directions their intrinsic spin vectors can point relative to their direction of motion, either parallel or antiparallel. Nature has made the choice[23] that there are only left-handed neutrinos and right-handed antineutrinos (i.e. for neutrinos, the spin vector is antiparallel to the momentum vector).

After a short discussion of gauge theories[24] (the current set of theories that seem to explain the forces and interactions between the quarks and leptons), the role of the charmed quark can be discussed.

1.3 Gauge Theories

In this section, the forces which act between elementary particles will be discussed. There are four known forces: the gravitational force, the strong force (responsible for holding the nucleons inside the atomic nucleus together), the weak force (responsible for nuclear beta decay, pion and kaon decays, and neutrino interactions), and the electromagnetic force (which is felt by the atomic electrons in their orbits of the atomic nucleus). The relative strengths of these forces can be seen by comparing their respective coupling constants. The strong force has a coupling constant (α_s) equal to ~ 1, the electromagnetic force has a coupling constant (α) equal to 1/137, the weak force has a coupling constant (G) equal to $\sim 10^{-5}/m_p{}^2$, and the gravitational force between two elementary particles has a strength of $\sim 10^{-43}$ relative to the strong force.

The range of the electromagnetic (EM) and gravitational forces is infinite, since these forces are thought to be due to the exchange of massless particles (the spin two graviton for gravity and the spin one photon for the EM force), while the strong and weak forces have a finite range ($< 10^{-13}$ cm), due (for the weak interactions) to the exchange of massive particles (the spin one intermediate vector mesons, the W^+, Z^o, and W^-, whose masses are expected to be greater than 80 GeV/c^2). The lifetimes of particles which decay strongly are typically about 10^{-23} sec, compared to about 10^{-16} sec for EM decays, and about 10^{-8} sec for weak decays.

All of the particles necessary to explain the structure of matter (the quarks and leptons) are fermions, which obey Fermi-Dirac statistics and must be created or destroyed in pairs, while all of the particles responsible for interactions between these particles are bosons (i.e. the vector gluons of the strong interaction, the intermediate vector mesons of the weak interaction, and the photon of the EM interaction) which obey Bose-Einstein statistics, can be created or destroyed singly, and which have no restrictions as to how many particles can occupy the same quantum state (for fermions, no two identical fermions can occupy the same state, identical implying having all the same quantum numbers, such as spin, isospin, hypercharge, charge, and orbital angular momentum).

One of the first successful theories to be developed was the theory of electromagnetism[25], which is described by the Maxwell equations. Besides successfully describing the electric and magnetic properties of matter, it predicted the existence of electromagnetic radiation. The development of special relativity in 1905 (by A. Einstein) and quantum mechanics in the early 1920's led to a successful description of the then known atomic physics phenomena (such as the electron energy levels of atoms). The merger of special relativity and quantum mechanics into quantum electrodynamics (QED) in 1928 by Dirac[26] led to one of the most accurate theories to date. It accounted for the spin of particles (spin being the intrinsic angular momentum of elementary particles), was the first theory which allowed for the creation and destruction of particles, and predicted

the existence of antiparticles (the first of which, the positron, which is the antiparticle of the electron, was discovered in 1932[27]). The electromagnetic force between two charged leptons is due to the exchange of virtual photons, and using this concept the cross sections for $e^+e^- \rightarrow e^+e^-$ and $e^-e^- \rightarrow e^-e^-$ scattering can be successfully predicted using QED[23].

The current theory of the strong interactions, quantum chromodynamics (QCD), is based on the idea that the strong force is due to the exchange of colored gluons (gluons are thought of as the "glue" that holds the hadrons together). The eight vector gluons are spin one massless particles, and are the generators (i.e. the objects which change the quarks from one of the three possible color states to another color state) of the exact SU(3) color theory (exact in that the masses of quarks of the same flavor but different color are the same). Unlike QED, where the carrier of the force (the photon) does not carry the property of the particle which is responsible for the force (i.e. the charge of the particle emitting the photon), in QCD the gluons are themselves colored and can interact with each other. Quarks in a hadron continually emit and reabsorb gluons, some of which break up into low momentum quark-antiquark pairs (which compose the quark-antiquark "sea", i.e. the non-valence quarks of a hadron, the valence quarks being the quarks which determine the identity of the hadron under consideration). Gluon emission changes the color of a quark, but not the quark's flavor (i.e. a u quark emitting a gluon remains a u quark). Lepton-nucleon scattering experiments[28] have shown that only about ½ of the momentum of a nucleon is carried

by the charged quarks, the remainder is thought to be carried by the electrically neutral gluons.

In QED, the shorter the distance from a bare electron that is probed, the stronger the EM force is measured to be. The "bare" charge of a lepton is screened by a cloud of virtual electron-positron pairs which come from the electromagnetic vacuum[23]. The QCD force appears to act in just the opposite way, the closer one gets to a bare quark (or equivalently, the higher the energy of the probe used to look at nucleon structure), the weaker the strong force seems to get. This property is known as asymptotic freedom, and accounts for the fact that as higher and higher energy probes are used to look at nucleon structure, the probes seem to be looking at essentially free quarks. This is due to the "antiscreening" of quarks by gluons.

The strong force seems to become stronger at large distances (i.e. when low energy particles are used to probe the structure). This "infrared slavery" is thought to be responsible for the fact that free quarks have not been observed. As a quark is pulled further from the other quarks making up a hadron, a point is reached where enough energy has been added to the system that one of the gluons holding the quark in the hadron fractures, yielding a quark-antiquark pair. The antiquark of the pair combines with the quark to yield a meson (bound $q\bar{q}$ pair), while the quark of the pair remains in the hadron. As more and more energy is added to a hadron, instead of producing free quarks, quark-antiquark pairs are created which are seen as mesons in the final state of the interaction. The only observable particles seem to have a net color of zero, and this seems to account for the nonobservation of free quarks.

Finally, the form of the weak interaction will be discussed. The prototype theory of weak interactions is the Weinberg-Salam[29] model of weak and electromagnetic interactions. The Weinberg-Salam model is an SU(2) X U(1) model (SU(2) for the weak interactions, and U(1) for the electromagnetic interactions) which combines the weak and electromagnetic forces into one force, the electroweak force. The weak interactions are seen as being due to the exchange of the triplet of intermediate vector (spin one) mesons (the W^+, Z^o, and W^-, the generators of the SU(2) weak group), while the electromagnetic force is seen as being due to the exchange of spin one photons (the generator of the U(1) electromagnetic group). The charged weak interactions (the exchange of W^+ or W^- mesons) change the flavors of quarks and leptons, coupling the members of the quark and lepton weak isospin doublets to be described later. Nuclear beta decay ($n \rightarrow p^+ e^- \bar{\nu}_e$) is seen as being a process in which one of the d quarks of a neutron emits a W^- and becomes a u quark, while the W^- couples to an electron and an electron antineutrino, leaving a proton and two leptons in the final state. This interaction can be viewed as one current (i.e. the hadronic current) interacting with another current (i.e. the leptonic current), mediated by the exchange of an intermediate vector meson (i.e. a current-current interaction[4]), in much the same way that electron-electron scattering can be viewed as one leptonic current interacting with another leptonic current, mediated by the exchange of a virtual photon.

The leptons (which only interact weakly and electromagnetically) are grouped into left-handed weak isospin doublets:

$$\begin{pmatrix}\nu_e\\ e\end{pmatrix}_L \qquad \begin{pmatrix}\nu_\mu\\ \mu\end{pmatrix}_L \quad .$$

The electromagnetic current (mediated by photon exchange) takes the form[6]:

$$J_\mu^{em} = -\bar{e}\gamma_\mu e - \bar{\mu}\gamma_\mu \mu \ ,$$

while the charged currents are the sum over the two leptonic doublets:

$$J_\mu^{(\pm)} = \sum_i \bar{\psi}_i \ \tau_\pm \ \gamma_\mu \ (1 + \gamma_5)\psi_i$$

where: ψ_i is the Dirac wave function

$\tau_\pm$ is the isospin raising or lowering operator

$\gamma_\mu \ (1 + \gamma_5)$ means $(V\text{-}A)^{23}$ space-time structure for the current

which, for the charge raising current (mediated by the W^+) gives:

$$J_\mu^{(+)} = \bar{\nu}_e\gamma_\mu(1 + \gamma_5)e + \bar{\nu}_\mu\gamma_\mu(1 + \gamma_5)\mu$$

the first term of which is for the coupling between the W^+, an electron, and an electron neutrino, while the second term is for the coupling between the W^+, a muon, and a muon neutrino. From $J_\mu^{(+)}$, $J_\mu^{(-)}$, we get $J_\mu^{(o)}$:

$$J_\mu^{(o)} = \tfrac{1}{2} \sum_i \bar{\psi}_i \ \tau_3 \ \gamma_\mu \ (1 + \gamma_5) \ \psi_i$$

and a second term, which comes from the symmetry breaking of this model:

$$J_\mu^{(o,W)} = -2 \ \sin^2\theta_W \ J_\mu^{em}$$

where θ_W is the Weinberg angle and has been measured as $\sin^2\theta_W = 0.20 \pm 0.03$[30]. In its final form, the weak neutral current for leptons takes the form:

$$J_\mu^{(o)} = \tfrac{1}{2} \ \bar{\nu}_e\gamma_\mu(1 + \gamma_5)\nu_e - \tfrac{1}{2}\bar{e}\gamma_\mu(1 + \gamma_5)e + 2 \ \sin^2\theta_W\bar{e}\gamma_\mu e$$

$$+ \tfrac{1}{2} \ \bar{\nu}_\mu\gamma_\mu(1 + \gamma_5)\nu_\mu - \tfrac{1}{2}\bar{\mu}\gamma_\mu(1 + \gamma_5)\mu + 2 \ \sin^2\theta_W\bar{\mu}\gamma_\mu\mu.$$

In this form, the neutrino couples to itself left-handedly and the electron and the muon remain uncoupled by the neutral current (i.e. electron and muon quantum numbers are conserved separately).

For the weak hadronic current (with only the u, d, and s quarks), we get a weak isospin doublet (whose form was suggested by Cabibbo[31] in 1963):

$$\begin{pmatrix} u \\ d_\theta \end{pmatrix}_L$$

where $d_\theta = d \cos \theta_c + s \sin \theta_c$, and θ_c is the Cabibbo angle (given by $\tan \theta_c = 0.22 \pm 0.02$). The form of the charge raising current becomes:

$$J_\mu^{(+)} = \bar{u}\gamma_\mu(1 + \gamma_5)d \cos\theta_c + \bar{u}\gamma_\mu(1 + \gamma_5)s \sin \theta_c$$

and we see that the W^+ couples the u and d quarks with a strength proportional to $\cos\theta_c$, and that the W^+ couples the u and s quarks with a strength proportional to $\sin\theta_c$. The form of the neutral current is (with three quarks):

$$\begin{aligned} J_\mu^{(o)} = \tfrac{1}{2} \{&\bar{u}\gamma_\mu(1 + \gamma_5)u - \bar{d}\gamma_\mu(1 + \gamma_5)d \cos^2\theta_c - \bar{s}\gamma_\mu(1 + \gamma_5)s \sin^2\theta_c \\ &- \bar{s}\gamma_\mu(1 + \gamma_5)d \sin\theta_c \cos\theta_c - \bar{d}\gamma_\mu(1 + \gamma_5)s \sin\theta_c \cos\theta_c\} \\ &- 2 \sin^2\theta_W J_\mu^{em}. \end{aligned}$$

Two questions arise looking at this form of the hadronic weak currents. Why do we seem to have an unused quark ($s_\theta = s \cos\theta_c - d \sin\theta_c$), and why are the forms of the leptonic and hadronic currents not more symmetric? In 1964, Bjorken and Glashow[5] proposed adding a new left-handed hadronic doublet:

$$\begin{pmatrix} c \\ s_\theta \end{pmatrix}_L$$

where c is a new quark (the charmed quark) with Q = + 2/3 |e|, and which has isospin I = 0, strangeness S = 0, and is an SU(3) singlet. The hadronic neutral current ($J_\mu^{(o)}$ above) for three quarks contains pieces which couple the u quark to itself and the d quark to itself with different strengths (which would not be expected); it also contains pieces which couple the d and s quarks, but this is not observed experimentally, as there seems to be no strangeness-changing neutral hadronic currents (i.e. the decays $K^o \to \mu^+\mu^-$ and $K^- \to \pi^-\nu\bar{\nu}$ are not observed). Glashow, Iliopoulos, and Maiani[32] noted in 1970 that using this second doublet (containing the charmed quark and the Cabibbo rotated s quark) would solve these problems, giving a hadronic neutral current of the form:

$$J_\mu^{(o)} = \tfrac{1}{2}\{\bar{u}\gamma_\mu(1+\gamma_5)u + \bar{c}\gamma_\mu(1+\gamma_5)c - \bar{d}\gamma_\mu(1+\gamma_5)d - \bar{s}\gamma_\mu(1+\gamma_5)s\} - 2\sin^2\theta_W J_\mu^{em}$$

the same form as for the leptonic neutral current. Note that this form of the neutral current is "flavor conserving" or diagonal in the flavors (i.e. weak neutral currents do not change the flavors of quarks).

1.4 Charm

By the early 1970's, theorists[6] had many compelling reasons to want another flavor of quark (besides u, d, and s), which they called charm. One reason was to reestablish quark-lepton symmetry (i.e. there were two lepton weak isospin doublets, but only one quark weak isospin doublet and a singlet). Another reason was the absence of strangeness changing neutral currents (which the four quark theory doesn't give). This fourth quark would also make the u quark and d quark self-couplings (through the weak neutral current) have the same strength, as was to

be expected. A final piece of evidence was the fact that the value of R (ratio of $\sigma(e^+e^- \rightarrow \text{hadrons})/\sigma(e^+e^- \rightarrow \mu^+\mu^-)$) measured in electron-positron scattering experiments was lower than expected for electron-positron energies greater than three GeV (even after accounting for the factor of three in $\sigma(e^+e^- \rightarrow \text{hadrons})$ due to color). If hadrons are made of quarks, then both of the processes $e^+e^- \rightarrow$ hadrons and $e^+e^- \rightarrow \mu^+\mu^-$ are due to the couplings of the virtual photon (created by the e^+e^- annihilation) to two spin ½ structureless fermions, see Figure 1.5. The only difference is that quarks occur in three colors and have fractional charges. Neglecting kinematic terms, $\sigma(e^+e^- \rightarrow \mu^+\mu^-) \propto e_\mu{}^2 = 1$, while for hadrons, $\sigma(e^+e^- \rightarrow \text{hadrons}) \propto 3\ \Sigma e_q{}^2 = 3\ ((2/3)^2 + (1/3)^2 + (1/3)^2) = 2$ for three quarks, and $= 3\ ((2/3)^2 + (1/3)^2 + (1/3)^2 + (2/3)^2) = 3 \cdot 1/3$ for four quarks, the factor of three being due to the fact that quarks come in three colors. The measured value of R (see Figure 1.6) is much closer to $3 \cdot 1/3$ than to 2 for energies above 3 GeV (where $c\bar{c}$ pair production is expected to begin).

A fourth quark would yield a whole new set of particle states, mesons and baryons with one (or more) of the usual quarks replaced by a charmed quark. For the lowest mass mesons ($q\bar{q}$ bound states), there are 16 expected pseudoscalar states (i.e. $4 \times 4^* = 1 + 15$). There is the already discussed pseudoscalar meson nonet (for which charm = 0), a new singlet state (the η_c, which is a $c\bar{c}$ state and has a net charm of zero), and six new charmed mesons, the D and F mesons. The weight diagram for the pseudoscalar ($\text{spin}^{\text{parity}} = 0^-$) mesons is shown in Figure 1.7. The quark contents of these new charmed mesons

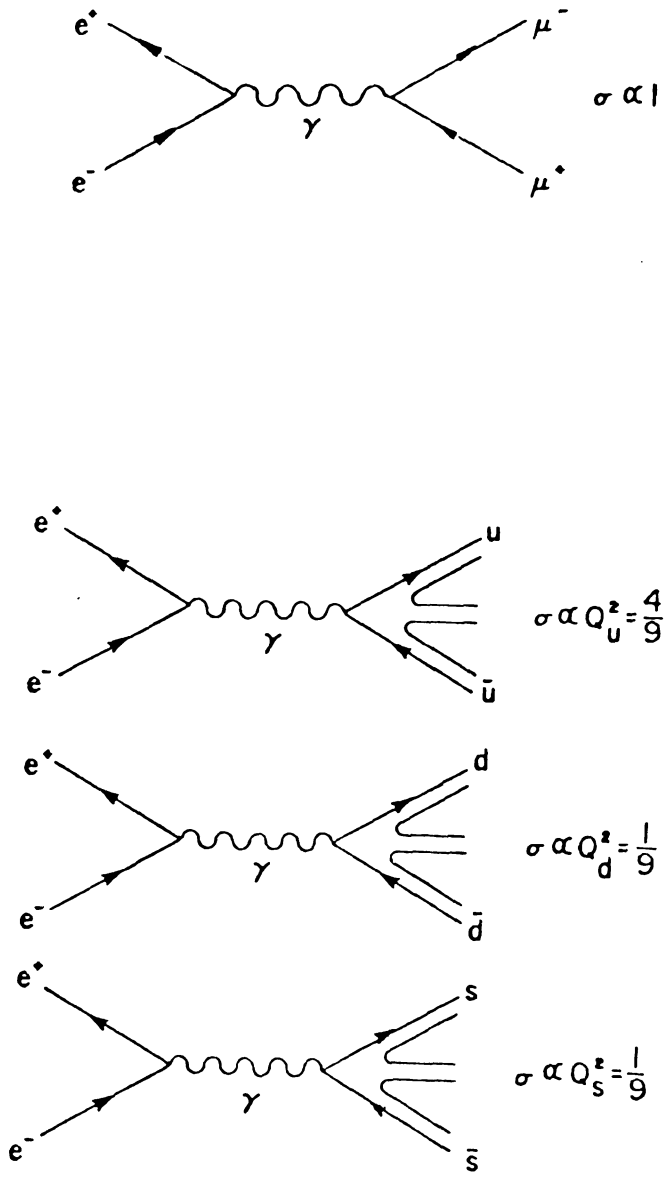

Figure 1.5 e^+e^- Annihilation into Quarks and Leptons

$$R = \frac{\sigma_{e^+e^- \rightarrow \text{hadrons}}}{\sigma_{e^+e^- \rightarrow \mu^+\mu^-}} = \left[\frac{\text{quarks}}{}\right]^2 = \sum_i q_i^2/e^2$$

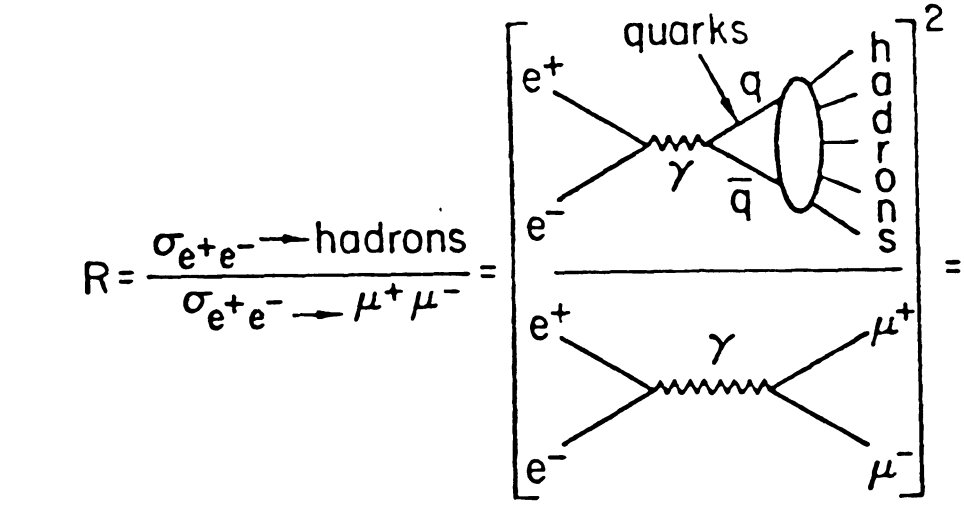

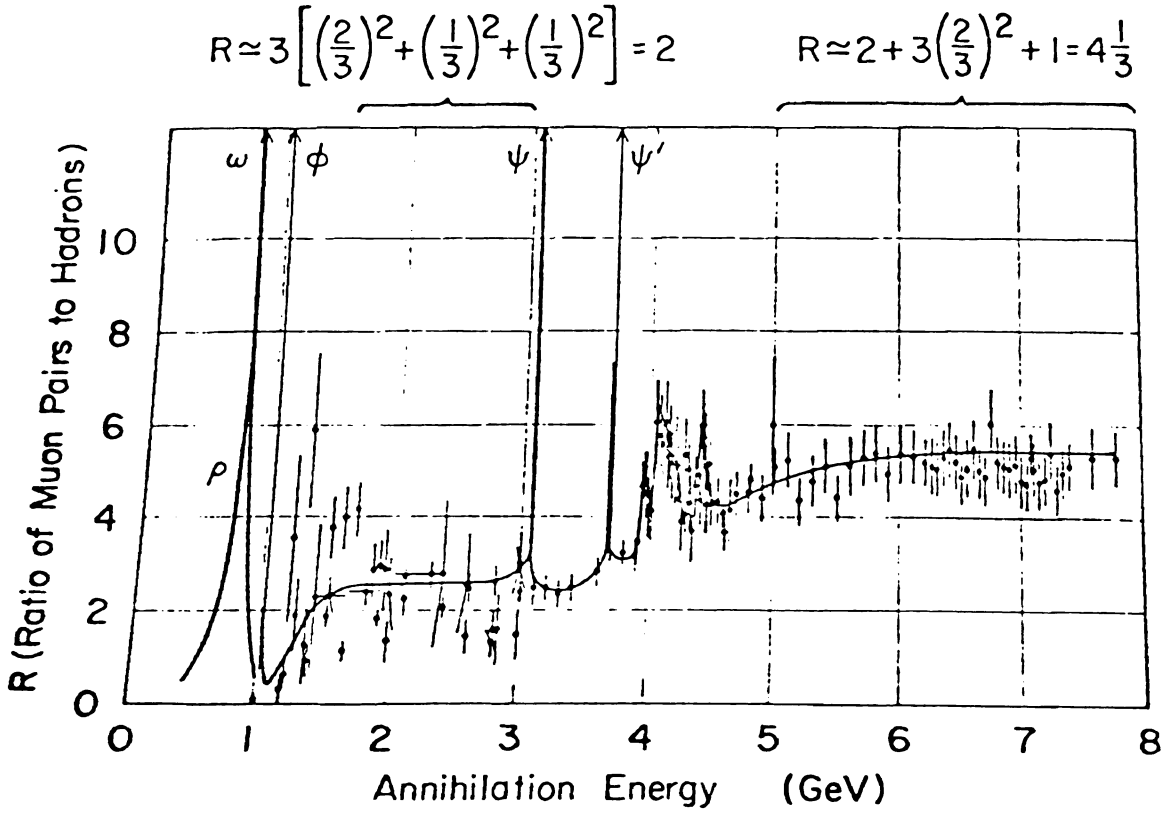

Figure 1.6 Experimentally Measured Value of R

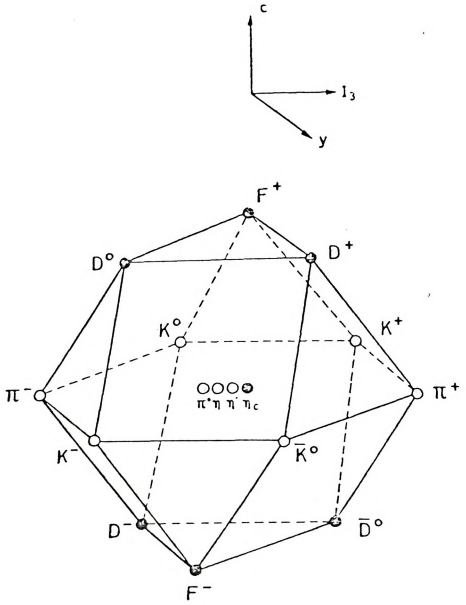

Figure 1.7 Pseudoscalar Meson 15-plet

are as follows: $D^+(c\bar{d})$, $D^0(c\bar{u})$, $F^+(c\bar{s})$, $D^-(d\bar{c})$, $\bar{D}^0(u\bar{c})$, and $F^-(s\bar{c})$; the first three of these have C (charm) = +1, while the last three have C = -1.

The first new particle discovered which contained charmed quarks was the $\psi(3095)$ meson, discovered at SLAC[7] in e^+e^- scattering and at Brookhaven[8] in p-Be scattering in 1974. The ψ is a vector meson ($spin^{parity} = 1^-$), and excited states of the ψ, the $\psi'(3684)$, the $\psi''(3772)$, and the $\psi'''(4414)$, were soon observed in e^+e^- scattering experiments[9]. The ψ has an extremely narrow width (width $\sim$ 67 keV, compared to a typical hadronic width of $\sim$ 200 MeV), implying a very long lifetime for such a massive state (i.e. some conservation law keeps the ψ from decaying strongly, giving it a relatively long lifetime compared to a typical hadron). The ψ is now believed to be the lowest mass vector bound state of a c and a $\bar{c}$ quark (since C = +1 for a charmed quark and C = -1 for a charmed antiquark, the ψ has a net charm of zero and is said to have hidden charm). The ψ decays about 7% of the time into e^+e^- pairs and 7% of the time into $\mu^+\mu^-$ pairs. Assuming the mass of the charmed quark to be about $\frac{1}{2}$ the mass of the ψ gives a charmed quark mass of approximately 1.5 GeV/c^2, compared to a u or d quark mass of $\sim$ 300 MeV/c^2.

The discovery of the first charmed meson was in 1976, when the D meson was discovered at SLAC[23] in e^+e^- scattering experiments. The D^0 (whose mass is 1863 MeV/c^2) was seen as a mass peak in $K^-\pi^+$ final states, while the D^+ (whose mass is 1868 MeV/c^2) was seen as a mass peak in $K^-\pi^+\pi^+$ final states. Shortly afterwards, the F meson (whose mass is 2030 MeV/c^2) was discovered[34]. These discoveries, along with the discovery of the $\eta_c(2830)$ at DESY[35] in e^+e^- scattering (a pseudo-

scalar $c\bar{c}$ bound state), completed the 15-plet of pseudoscalar mesons.

Because of the relative strength of the c quark-s quark coupling (which is $\propto \cos \theta_c$, compared to the c quark-d quark coupling which is $\propto \sin \theta_c$), the hadronic and semileptonic decays of D mesons are expected to have strange particles in the final state (usually K or K* mesons). The purely leptonic decay modes of the D and F mesons are shown in Figure 1.8, along with the analogous strange meson leptonic decay mode of the K_{ℓ_2}. The strength of this D decay mode is relatively small, as it is suppressed by a factor of $\sin \theta_c$. The main decay modes we will be interested in are the semileptonic decays of the D mesons, shown in Figure 1.9. These can be interpreted as a c quark in a D^+ or D^o meson emitting a W boson, becoming an s quark in the final state (coupling strength $\propto \cos \theta_c$), while the W couples to a lepton and a neutrino, giving a kaon (or K*), a lepton, and a neutrino in the final state. This is the suspected source of multimuon final states observed in νN[36] and μN[12] scattering experiments in the early 1970's.

1.5 Lepton Scattering

Charged leptons (i.e. muons or electrons) can be used to probe the electromagnetic structure of nucleons. At low energies, the electric and magnetic properties of the nucleon itself are probed (i.e. the electric and magnetic nuclear form factors are measured[14]), while at high energies the structure inside the nucleon itself is probed. A charged lepton, in the nuclear field, can emit a virtual photon, which can then interact with one of the quarks inside a nucleon. Since the leptonic vertex of this interaction is well understood

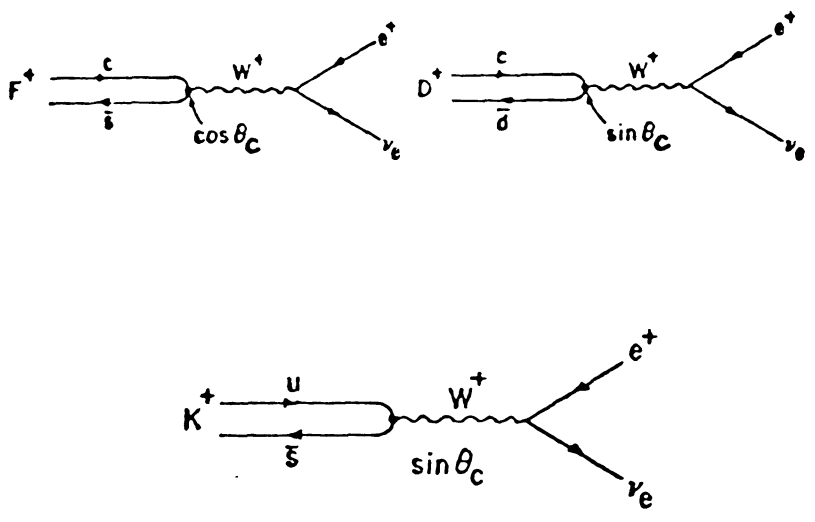

Figure 1.8 Leptonic Decays of the D and F Mesons

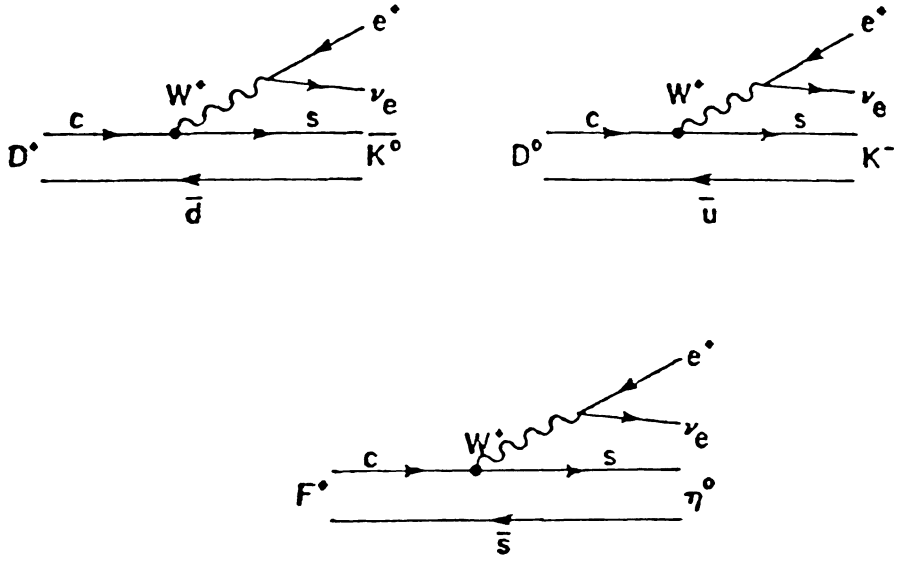

Figure 1.9 Semileptonic Decays of the D and F Mesons

(using QED), what is being measured is the structure of the nucleon with which the virtual photon interacts. The cross section for deep inelastic lepton-nucleon scattering is given by[37]:

$$\frac{d^2\sigma}{dE'd\Omega} = \frac{\alpha^2\cos^2(\theta/2)}{4E_o^2\sin^4(\theta/2)} \{W_2(q^2,\nu) + 2\tan^2(\theta/2)\, W_1(q^2,\nu)\}$$

where E_o is the incident lepton's energy, E' is the scattered lepton's energy, α is the electromagnetic fine structure constant ($\sim 1/137$), θ is the polar scattering angle of the lepton, and W_1 and W_2 are the structure functions of the nucleon. W_1 can be eliminated using the relationship[37]:

$$\frac{W_1}{W_2} = \frac{1 + \nu^2/q^2}{1 + R}$$

where ν is the energy transfer to the nucleon ($= E_o - E'$), q^2 is the four momentum transfer squared of the virtual photon ($=4E_oE'\sin^2(\theta/2)$, in the lab frame), and R is the ratio of the longitudinal photon absorption cross section to the transverse photon absorption cross section[37]. This gives the result:

$$\frac{d^2\sigma}{dE'd\Omega} = \frac{\alpha^2\cos^2(\theta/2)}{4E_o^2\sin^4(\theta/2)} \frac{\nu W_2}{\nu} \{1 + 2\tan^2(\theta/2)\frac{1 + \nu^2/q^2}{1 + R}\}$$

for the deep inelastic lepton-nucleon scattering cross section. The Feynman diagram for this process is shown in Figure 1.10, along with a definition of some of the kinematic variables. Taking the value of R (=0.25) from low energy electron-proton scattering experiments[38], a measurement of this cross section will give us νW_2 (also called F_2), the nucleon structure function.

The structure functions W_1 and W_2 depend on the two Lorentz

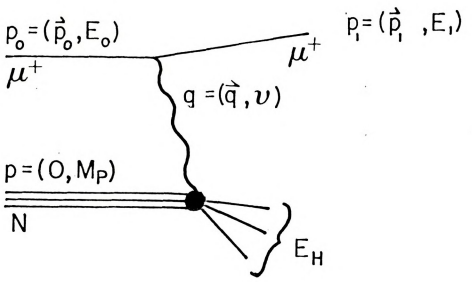

E_0 = incident muon energy

E_1 = scattered muon energy

$\theta = \cos^{-1}((\vec{p}_0 \cdot \vec{p}_1)/|\vec{p}_0||\vec{p}_1|)$ = scattered muon polar angle

$q^2 = 4E_0E_1\sin^2(\theta/2)$ = four momentum transfer squared

$\nu = E_0 - E_1$ = energy transfer to nucleon

$x = q^2/2M_p\nu$ = Bjorken scaling variable

$y = \nu/E_0$ = hadronic fractional energy

$\omega = 1/x$

$W = (M_p^2 + 2M_p\nu - q^2)^{\frac{1}{2}}$ = hadronic final state mass

elastic scattering: $\omega = 1$

inelastic scattering: $\omega > 1$

$W > (M_p + m_\pi)$

Figure 1.10 Deep Inelastic Muon Scattering Kinematics

invariants q^2 and ν. As the energy of the virtual photon becomes large, the scattering process is expected to look like elastic photon-quark scattering, with the effects caused by the other quarks in the nucleon becoming negligible[39]. In the limit of large q^2 and ν, the structure functions should depend only on the ratio of q^2 and ν (i.e. on $x = q^2/2m\nu$, m being the nucleon mass). This is the concept of Bjorken scaling[39], and was observed at low q^2 in early SLAC ep scattering experiments[40]. However, scaling violations (i.e. the nucleon structure functions depending on q^2 as well as x) were observed in μFe[41], μp[42], μd[43], and ep[44] scattering experiments in the early 1970's. Quantum chromodynamics calculations of the form of this scaling violation[45] (based on the corrections to the cross section due to the emission of gluons by the quarks inside a nucleon) have been reasonably successful[46]. Scaling violations will be discussed again in Chapter IV.

In the early 1970's, multimuon final states were observed in μFe[12] and νN[36] scattering experiments. For muon scattering, one of the final state muons was the scattered incident muon, while the second (for dimuon final states) and third (for trimuon final states) muons were due to some other physical process besides deep inelastic muon-nucleon scattering. For neutrino (antineutrino) scattering, one of the muons in the final state comes from the neutrino's (antineutrino's) coupling to a $W^+(W^-)$ and a $\mu^-(\mu^+)$, where the W boson then couples to one of the quarks in the nucleon, changing the quark's flavor (as shown in Figures 1.11 and 1.12). Conventional sources for the second and third muons in the final state, such as π/K internuclear cascade decays (the decay of pions or kaons produced in the hadronic showers

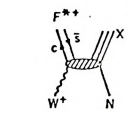

νN Charged Current

$\cos\theta_C$ diffractive

$\sin\theta_C$ valence quarks

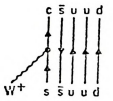

$\cos\theta_C$ sea quarks

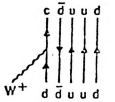

$\sin\theta_C$ sea quarks

Figure 1.11 Neutrino Nucleon Scattering Diagrams

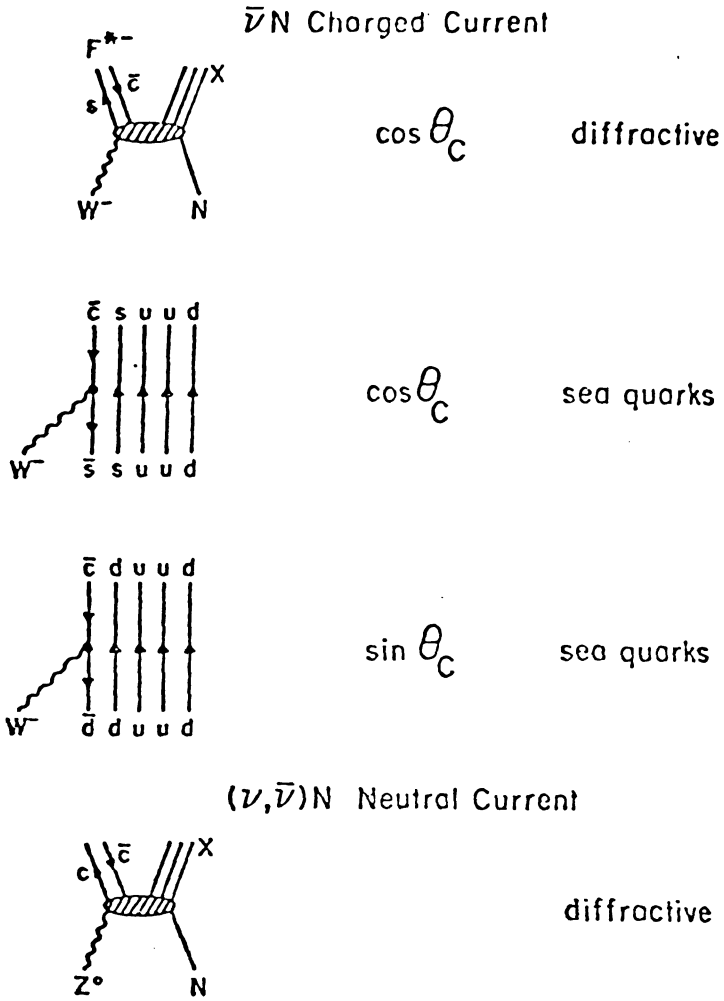

Figure 1.12 Antineutrino Nucleon Scattering Diagrams

accompanying a deep inelastic interaction), prompt muon[47] production at the interaction vertex, or QED trident[48] production are expected to yield produced muons with very low momentum (p_2 or p_3), and very low p_T's (momentum of the produced muon relative to the virtual photon or W meson direction), which was not observed. These processes are shown in Figure 1.13 and 1.14 for deep inelastic muon-nucleon scattering. Also, the calculated rates for these processes[12] did not account for the entire dimuon or trimuon sample observed.

The associated production (for μN scattering, single charmed meson production is possible for νN and $\bar{\nu} N$ scattering) and semileptonic decay of charmed D mesons is the most likely source of these high p_2 and high p_T produced final state muons. The observation of $K_S\ e^+\mu^-$ events in bubble chamber experiments[49] seemed to suggest that charmed mesons were being produced in the energy range available to the μN and νN scattering experiments (these events can be interpreted as $D\bar{D}$ production, with a D meson decaying semileptonically to yield a muon, while a $\bar{D}$ meson decays semileptonically to yield an electron of charge opposite that of the produced muon; the kaon in the final state suggests D meson production because of the Cabibbo favored c-s quark coupling). These events were not observed at lower energies because of the charm production threshold, i.e. enough energy has to be available in the production rest frame to produce a D and a $\bar{D}$ meson, at least 3.72 GeV (plus the energy of any other particles in the final state). Figure 1.15 shows the scattering diagram for muon induced dimuon events and gives definitions of some of the relevant kinematic variables.

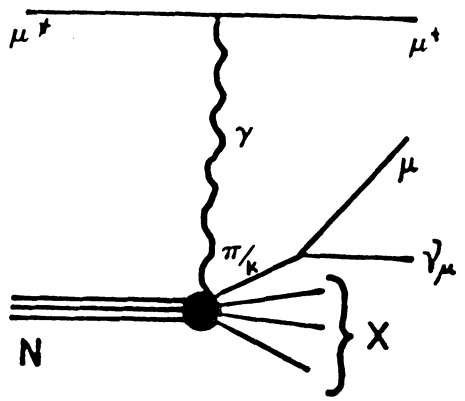

a). Decay

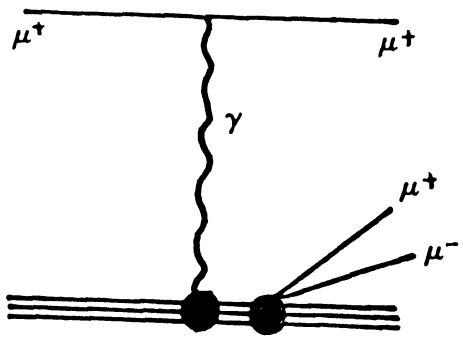

b). Quark Recombination

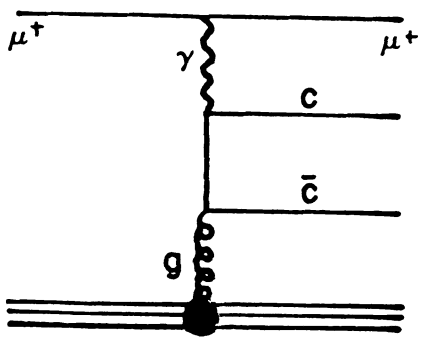

c). Associated Charm Prod.

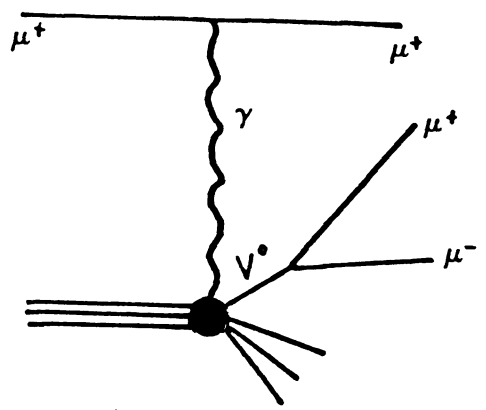

d). Vector Meson Prod.

Figure 1.13. Hadronic Multimuon Diagrams

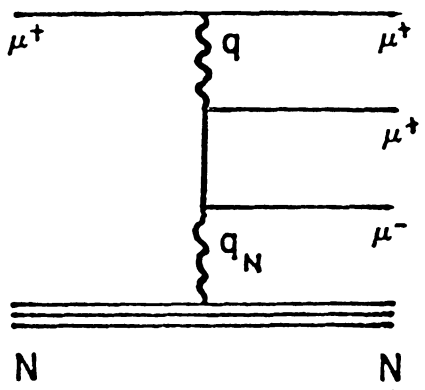

a. Bethe-Heitler Tridents

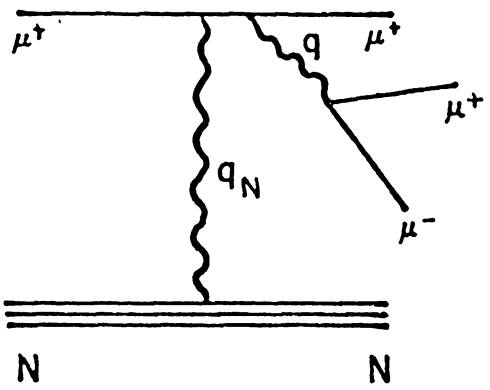

b. Bremsstrahlung/Pair Prod.

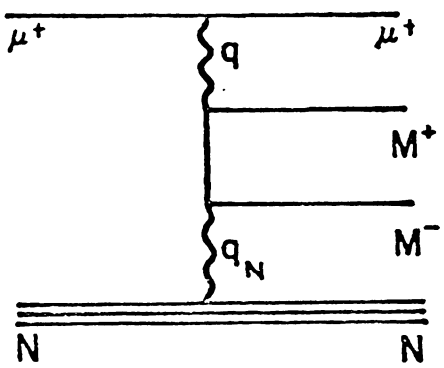

c. Heavy Lepton Pair Prod.

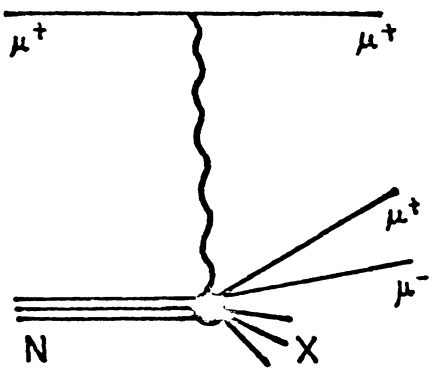

d. Deep Compton

Figure 1.14 QED Multimuon Diagrams

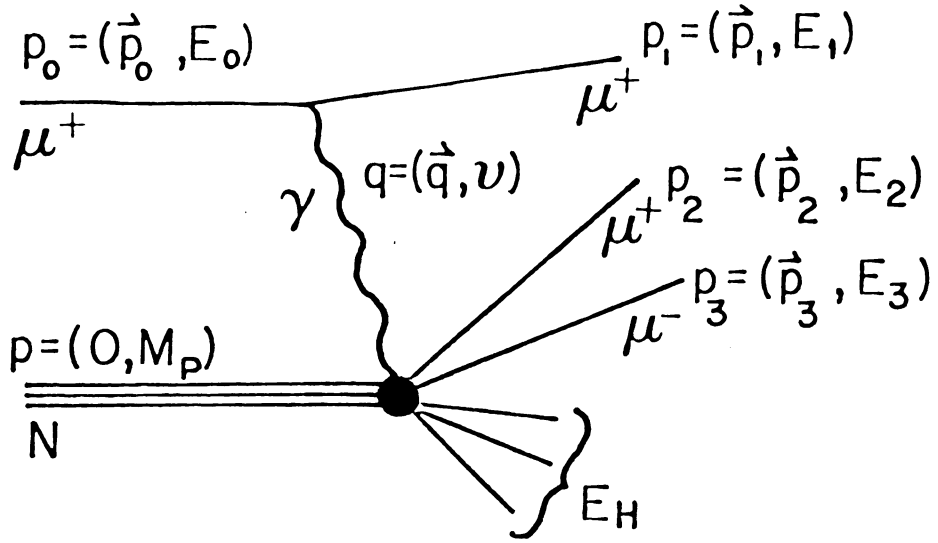

For dimuons:

p_1 = momentum of largest energy positive muon
= leading particle momentum

p_2 = momentum of negative or smallest energy positive muon

$\theta_{\gamma 2} = \cos^{-1}((\vec{p}_2 \cdot \vec{q})/|\vec{p}_2||\vec{q}|)$ = polar angle between second muon and virtual photon

$p_T = p_2 \sin\theta_{\gamma 2}$ = transverse momentum of second muon relative to the virtual photon direction

$\Delta\theta = \cos^{-1}((\vec{p}_1 \cdot \vec{p}_2)/|\vec{p}_1||\vec{p}_2|)$ = polar angle between final state muons

$\Delta\phi = \phi_1 - \phi_2$= azimuthal angle between final state muons

$M_{\mu\mu} = 4E_1E_2\sin^2(\Delta\theta/2)$ = apparent mass of final state muons

$E_m = E_0 - E_1 - E_2 - E_H = \nu - E_2 - E_H$
= missing energy

Inelasticity = $(E_0 - E_1 - E_2)/E_0$

Asymmetry = $(E_1 - E_2)/(E_1 + E_2)$

Figure 1.15 Multimuon Final State Kinematics

The first muon scattering experiment to observe multimuon final states (which could not be accounted for by conventional processes) was Fermilab experiment E26[12] (a Cornell-Michigan State-University of California collaboration). A total of 32 dimuons and 11 trimuons were observed in E26, using an earlier version of the apparatus used for E319 (the E26 apparatus is shown in Figure 1.16). In this Figure, P denotes the proportional chambers, S the spark chambers, T the trigger bank counters, and V denotes the halo and beam veto counters (halo veto counters are at the front of the target). E26 used a 1.94 meter long iron-plastic scintillator target, with an incident flux of 6.8×10^9 150 GeV positive and negative muons. The acceptance for the E26 apparatus was such that the minimum accepted muon energy was approximately 17 GeV (a muon had to traverse the entire apparatus to be found by the track reconstruction program, at least for dimuons, since track searching[50] began in the spark chambers at the downstream end of the magnetic spectrometer) and the minimum allowed angle was approximately 13 mR. The dimuon p_2 and p_T (relative to the virtual photon direction) data distributions for E26 are shown in Figures 1.17 and 1.18 (the E319 data distributions and calculated background curves are shown in Chapter V). The curves on Figure 1.17 and 1.18 are the calculated π/K decay, prompt muon production, and QED trident dimuon backgrounds for E26, labelled as: I) decay muon from pion and kaon production in the hadronic cascade following a deep inelastic muon interaction, II) prompt muons from the initial interaction via conventional processes, III) prompt muons produced in the hadronic cascade, IV) QED tridents with one muon undetected, and

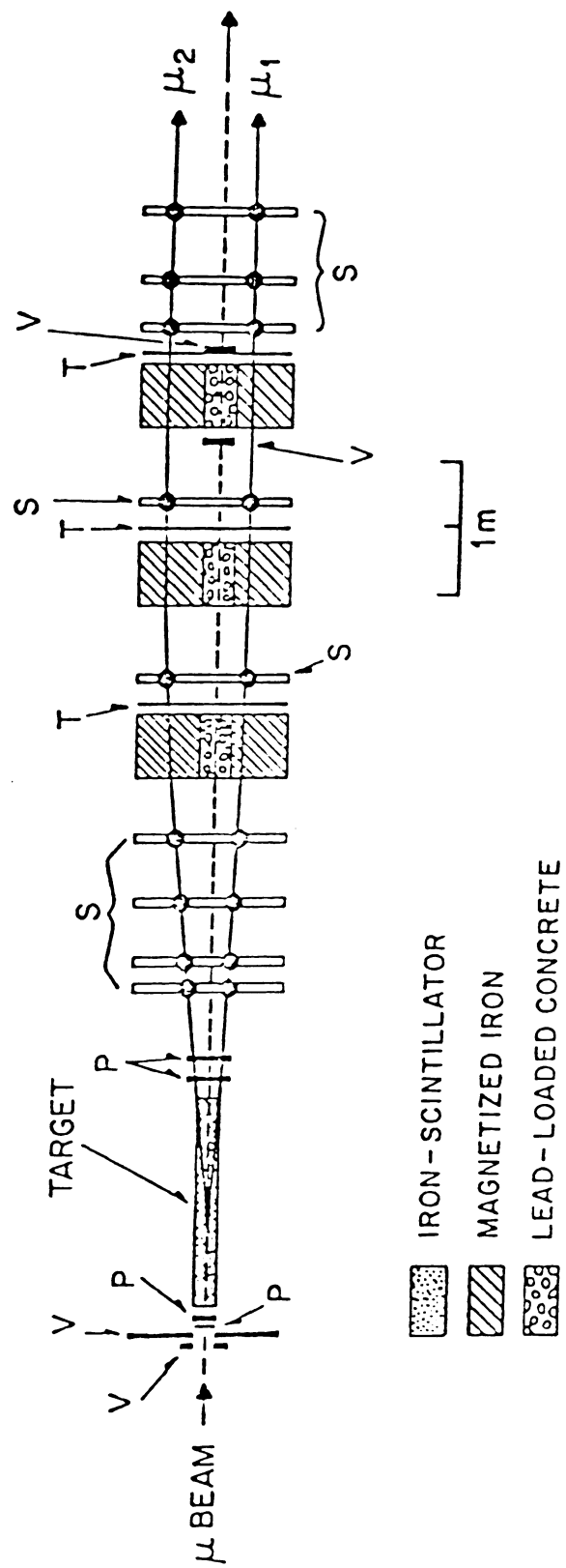

Figure 1.16 E26 Experimental Apparatus

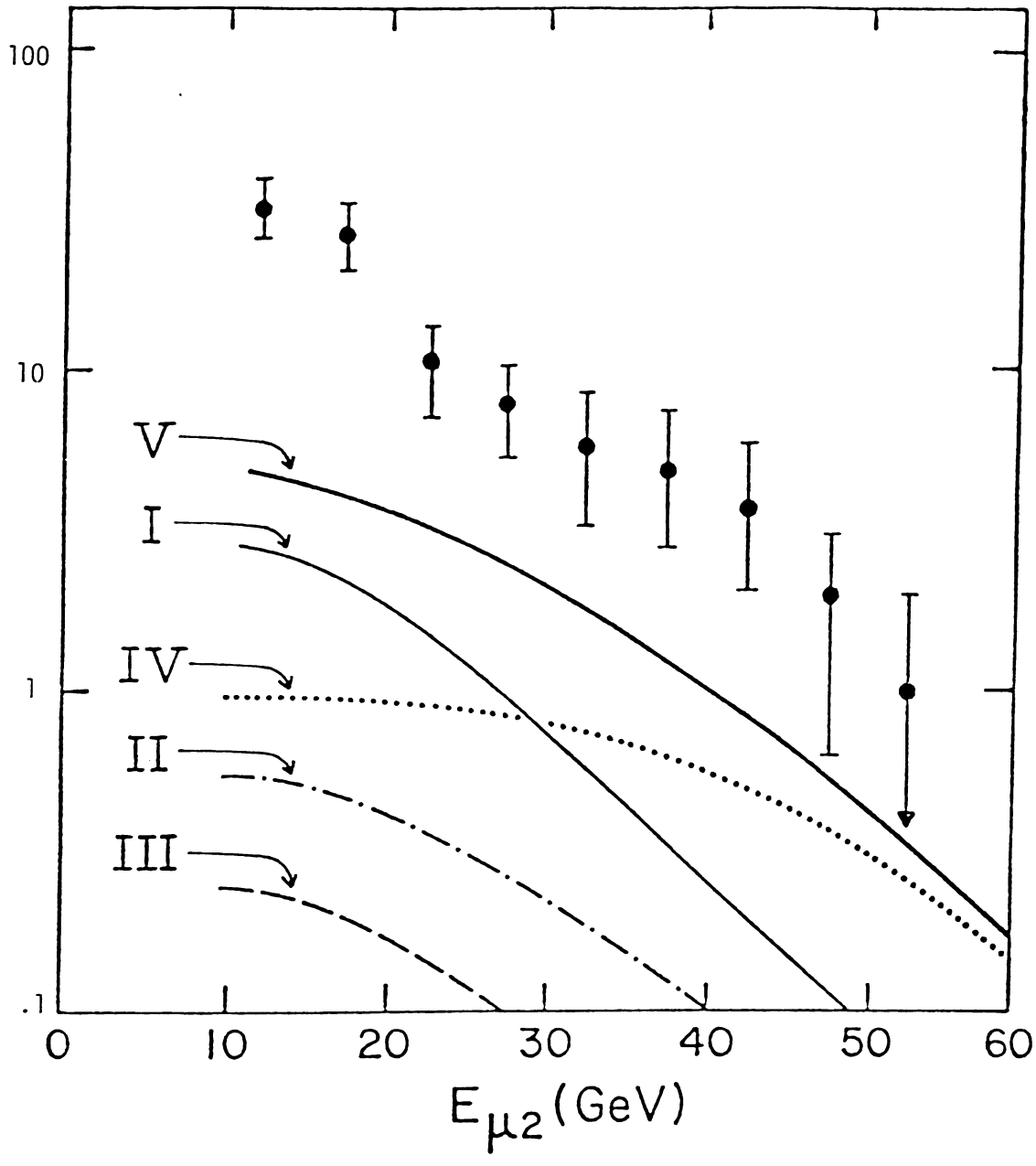

Figure 1.17 E26 Dimuon p_2 Distribution

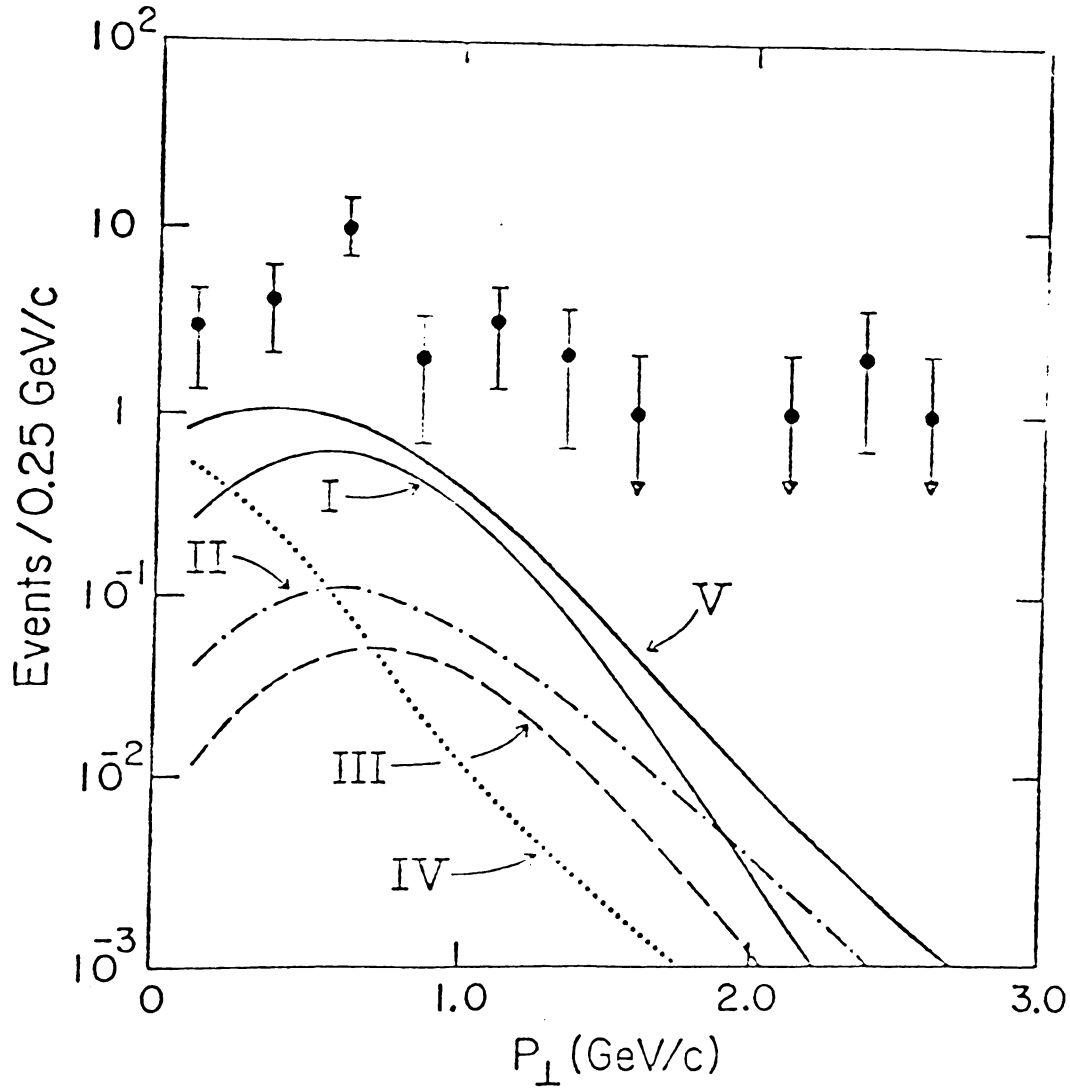

Figure 1.18 E26 Dimuon p_T Distribution

V) the total calculated background for the above mentioned processes. Plots of the variables Q^2, x, y, and W are shown in Figure 1.19 for the E26 data, comparing the "leading particle" (largest energy final state muon with the same sign as the incident muon) distributions for dimuon events with the scattered muon distributions for deep inelastic single muon scattering (these distributions are shown in Chapter V for the E319 final data sample).

The rate for two muon final states in E26 was measured to be greater than 5×10^{-4} times the rate for deep inelastic muon interactions ($\sim$ 25,550 deep inelastic single muon events passed the experimental cuts for an incident flux of 6.8×10^9 muons). The net cross section for dimuon events in E26, uncorrected for acceptance, was $5 \times 10^{-36} cm^2$/nucleon for the process $\mu N \rightarrow \mu\mu X$. The bulk of these events were not due to conventional background processes, and were thought to be due to associated charmed meson production and decay, although the relatively small size of the data sample prevented any definite conclusions from being reached.

Using the E319 data sample (449 found dimuons for an incident flux of 1.0974×10^{10} positive 270 GeV muons) and Monte Carlo simulations, a charm production cross section was calculated which had the apparatus acceptance removed (this process is described in Chapter V). This cross section is compared to a QCD calculation of charmed meson production, using the photon-gluon fusion model[51], the Feynman diagram for this process is shown in Figure 1.13. This process is the interaction of a virtual photon with a c or $\bar{c}$ quark from the nucleons quark-antiquark "sea", which is produced when a gluon inside a nucleon

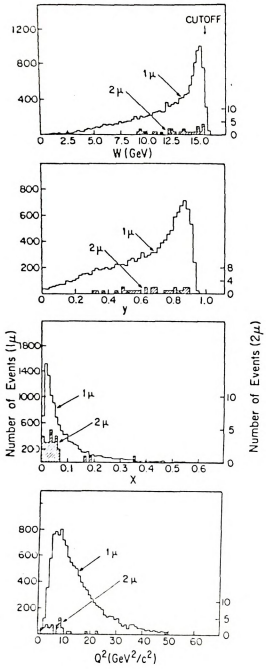

Figure 1.19 E26 Q^2, x, y, and W Distributions

breaks up into a $c\bar{c}$ pair. The scattered c and $\bar{c}$ quarks pick up other quarks from the quark-antiquark "sea", to materialize as D and $\bar{D}$ mesons, which can then decay semileptonically to yield one or two produced muons in the final state of a deep inelastic muon-nucleon interaction.

One of the major improvements of E319 over E26 (besides the much larger total luminosity and improved apparatus acceptance for dimuons), was the use of an iron-plastic scintillator sampling calorimeter[52], which made possible an accurate measurement of the energies of the hadronic showers accompanying deep inelastic muon interactions. Hadronic shower measurements were not possible for E26, due to hadronic shower leakage from the target, and the fact that the ADC's were set up so that they saturated for greater than five particles passing through a target counter (in E319, two ADC's were used per counter, giving a much larger dynamic range; each counter could measure from one to 300 particles passing through it). This allowed a measurement of the "missing energy" due to decay neutrinos, which was expected if the dimuon events were due to charmed meson production and decay (the missing energy measurements are discussed in Chapter V).

CHAPTER II

EXPERIMENTAL APPARATUS

2.1 Muon Beam

Muons used in our experiment were derived from the decays of secondary particles produced by the 400 GeV proton beam at Fermilab. The proton beam began in the pre-accelerator, where it was given a maximum energy of 750 KeV. The energy was then raised to 200 MeV in the linear accelerator, after which the protons were injected into the booster synchroton and raised to 8 GeV. These protons were used to fill the main ring, where they were R.F. boosted to energies of up to 400 GeV. Every 15-20 seconds the protons were delivered to the main beam switchyard as a 1.8 second long beam spill (with 2ns R.F. buckets every 18.8 ns), from where they could be sent to the proton, meson, or neutrino experimental areas. The accelerator is shown in Figure 2.1.

Upon entering the neutrino area, the proton beam was focused onto the "triplet train" production target, a 12" long, 0.75" diameter aluminum oxide cylinder in enclosure 99 of the neutrino line.

Pions, kaons ($\sim$ 10% of the number of pions), and protons of the desired energy were swept into a 300 m long evacuated decay pipe, while the remainder of the proton beam went to a beam dump. In the decay pipe, a large fraction of the pions and kaons decayed leptonically yielding muons and neutrinos. In enclosure 100 the charged particles were bent westward (28.68 mR) and focused into the N1 muon line, leaving the neutrinos to proceed down the neutrino line (NØ). In enclosure 101 the beam was again focused and bent

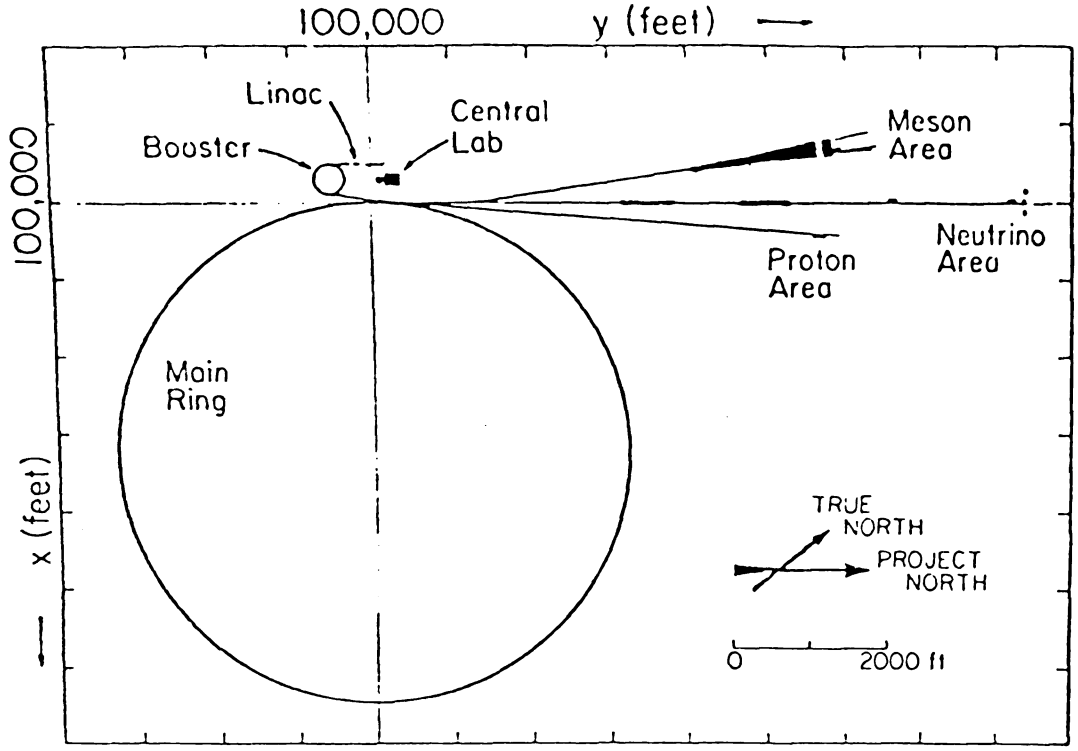

Figure 2.1. FNAL Accelerator and Experimental Areas

28.68mR eastward. The beam was bent back westward (28.68mR) in enclosure 102 and almost all of the strongly interacting particles (protons, pions, and kaons) were removed by 61 feet of polyethylene in the magnet apertures, yielding a μ/π ratio of $\sim 4 \times 10^6$. Multiple Coulomb scattering of the muons at this point caused many of them to diverge from the beam, which led to a large fraction of the halo muons seen at the front of the target in the muon lab. The muon beam was refocused in enclosure 103 and proceeded to enclosure 104 where the final momentum selection was made. The muons were bent eastward (28.68mR) by shimmed main ring dipoles and then entered the muon lab. The muon N1 beam line is shown in Figure 2.2.

Because the incoming muon energy was determined by its bend through the 1E4 dipoles (in enclosure 104), a precise knowledge of the magnetic field (both as a function of magnet current and distance along the beam axis) was necessary. This was obtained using an NMR probe and a gaussmeter. Results from these measurements are shown in Figure 2.3 and Table 2.1. The "effective length" of one magnet, defined as $\int B \cdot dl / B_{max}$, was found to be 18.64 meters.

Control of the magnet currents and polarities of the triplet train and N1 muon beam line was accessible to the neutrino line staff and experimenters through a remote terminal hooked to the MAC computer system controlling a CAMAC serial branch highway. The magnet settings for a typical 270 GeV $\mu+$ run are shown in Table 2.2.

Using the ionization and scintillation counters in the beam line, as well as our beam counters and proportional wire chambers, the beam was tuned to give the maximum number of useful beam muons, minimum number of halo muons (muons outside the beam which could strike the

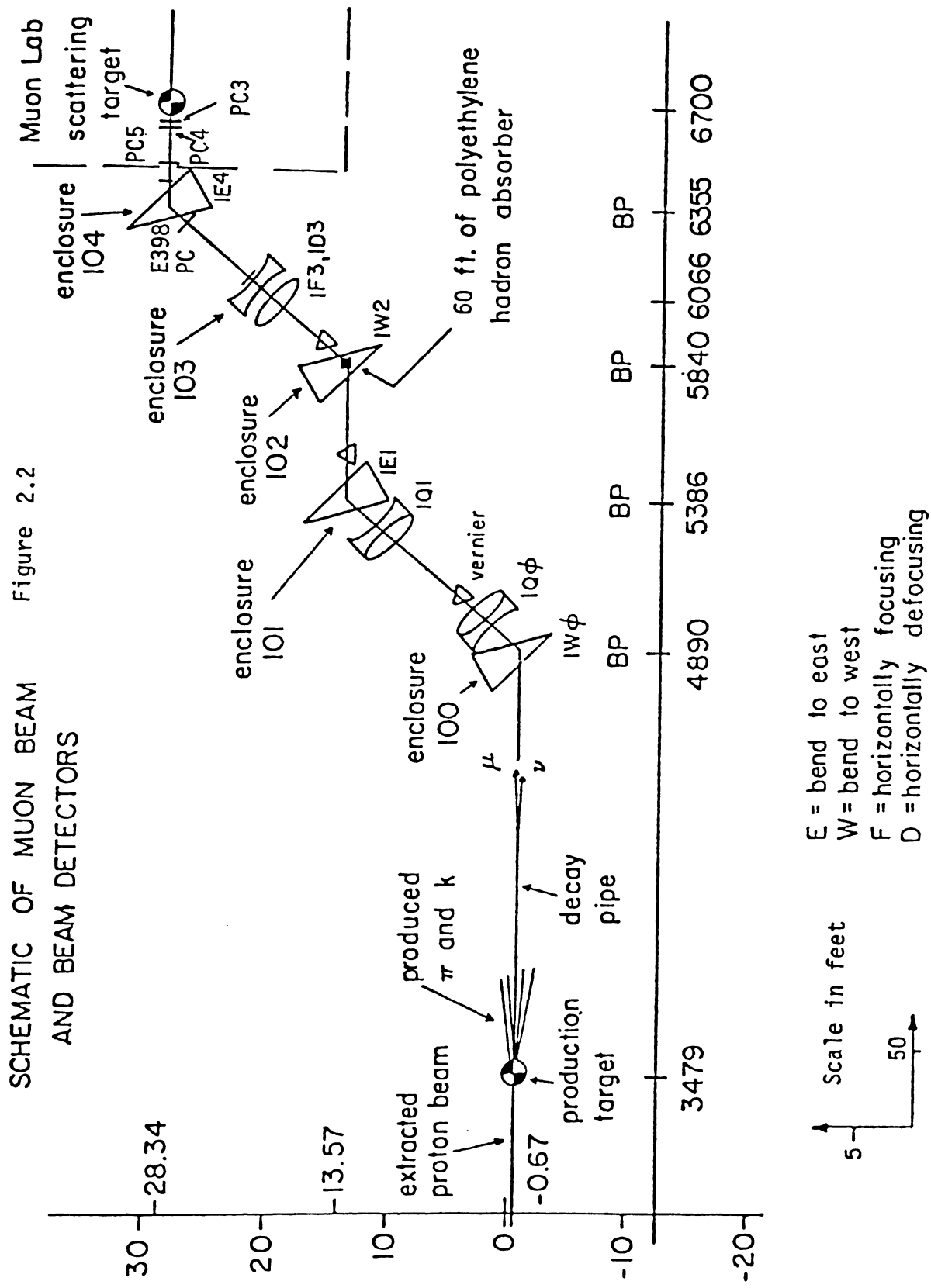
SCHEMATIC OF MUON BEAM AND BEAM DETECTORS
Muon Lab
scattering target
PC5
PC4
PC3
IE4
E398 PC
enclosure 104
enclosure 103
IF3,103
IW2
60 ft. of polyethylene hadron absorber
enclosure 102
IE1
IQ1
enclosure 101
vernier
IQφ
IWφ
enclosure 100
μ
ν
produced π and k
decay pipe
extracted proton beam
production target
BP
BP
BP
BP
BP
6700
6355
6066
5840
5386
4890
3479
28.34
13.57
-0.67
30
20
10
0
-10
-20
Scale in feet
5
50
E = bend to east
W = bend to west
F = horizontally focusing
D = horizontally defocusing

Figure 2.2

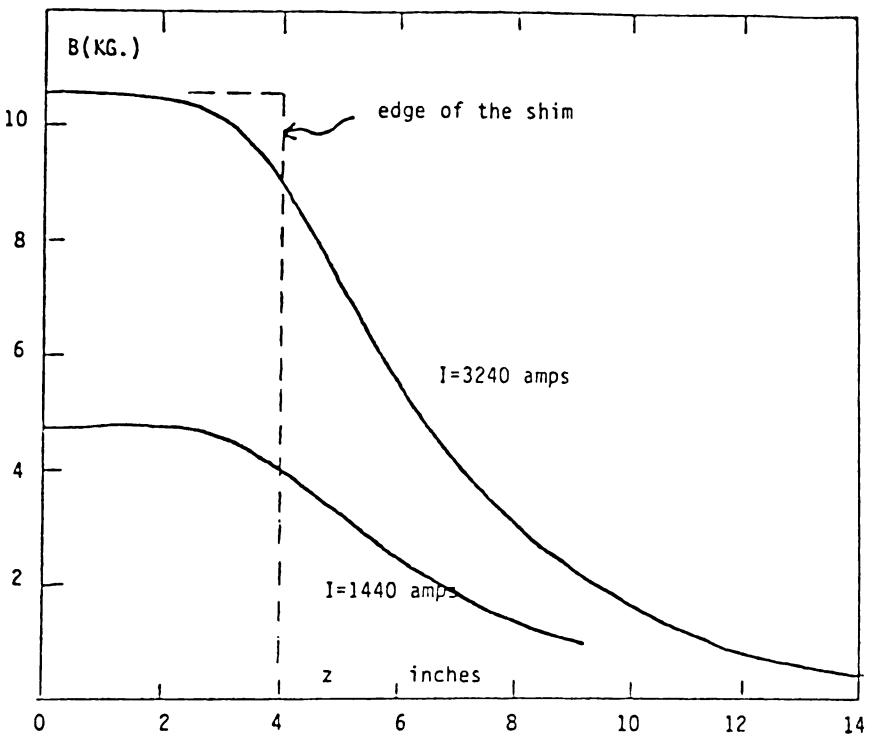

Figure 2.3. Magnetic field in 1E4 dipoles

Table 2.1 Calibration of the 1E4 Dipoles

$B(KG) = aI^2 + bI + c$; I = current(amps)

	Runs before 8/23/76	Runs after 8/23/76
a	$(-0.5964 \pm 0.6656) \times 10^{-8}$	$(-0.1714 \pm 0.6134) \times 10^{-8}$
b	$0.32892 \times 10^{-2} \pm 0.3015 \times 10^{-4}$	$0.33635 \times 10^{-2} \pm 0.2658 \times 10^{-4}$
c	-0.03107 ± 0.0273	-0.032787 ± 0.0273
χ^2/dof	0.10	0.10

Table 2.2 Magnet Currents for the Triplet Train and Muon N1 Beam Line

Magnet	Type	Setting(amps)	Reading(amps)
OUT		290	281-284
OVT		15	15.5
OHT		121	117.5
OFT1		96.2	92.5
OFT2		95.6	92.4
ODT		2777	2690
OPT		3102	2978
OPT3		3177	3060
1WO1	bend	0	4630
1WO2	bend	4332	4180-4190
1WO3	bend	4832	4630
1VO	pitch	25	106.25
1FO	focus	370	361.5
1DO	focus	370	350-353
1Q1	focus	4175	4000
1E1	bend	3862	3715-3720
1V1	pitch	120	8.125
1W2	bend	3712	3540
1F3	focus	940	918.747
1D3	focus	980	955
1E41	bend	4319.98	4237.48
1E42	bend	0	4230-4234

trigger counter banks), and an acceptable beam shape at the face of the target. For 10^{13} protons incident on the production target, the typical number of beam muons was 4-6 x 10^5 per spill. For the $\mu+$ data runs (the only data sample considered here), the average beam energy for data events was 268.6 GeV.

2.2 Apparatus Overview

The apparatus consisted of the following elements: the incident beam defining counters, the B and C counters, which guaranteed that the beam muon passed through the aperture of the 1E4 dipoles and the active area of the beam multiwire proportional chambers (MWPC's); the beam MWPC's and counter hodoscopes, which gave information on the incident muon's momentum and position at the face of the target; the target/calorimeter, which supplied the μ-nucleon scattering targets, and was used to measure the energy in hadronic showers, the interaction vertex, and helped to discriminate between single and multimuon final states; the hadron shield, just downstream of the target, which absorbed pions and kaons produced in the downstream end of the target and kept them from entering the magnetic spectrometer; the magnetic spectrometer, consisting of iron toroidal magnets, magnetostrictive wire spark chambers, and hadron MWPC's (upstream of the hadron shield), to measure the scattered muon(s) trajectory and hence determine its energy and angle at the end of the target; the trigger counter banks, three sets of counter banks located inside the spectrometer, used to ensure that the scattered muon passed through the active area of the spark chambers and was indeed a deep-inelastic scatter; the beam vetoes, three circular counters centered on the spectrometer axis used to reject events with an unscattered beam muon in time with a halo muon;

the halo veto, a set of counters similar to the trigger banks located just upstream of the target, used to ensure that in-time halo did not trigger the apparatus; the fast electronics, which generated standard logic pulses from counter information which were used to form the event trigger, fire the spark chambers, and generate all the necessary gates needed to read out the detector information for each event; and the CAMAC and mini-computer systems, which read out the detector information, digitized it, and wrote it onto magnetic tape for later off-line analysis.

A right-handed coordinate system was defined with the z-axis along the nominal spectrometer axis (pointing downstream), the x-axis pointing vertically upward, and the y-axis pointing to the right of the beam (east).

Each of these elements of the apparatus will now be considered in more detail. A diagram of the apparatus is shown in Figure 2.4. Z-positions of all the spectrometer and beam elements are shown in Table 2.3.

2.3 Beam Counters

Scintillation counters are specially treated plastic detectors which scintillate when a charged particle passes through them. The resulting light is then internally reflected down a light pipe, where it causes electrons to leave the surface of the cathode of a photomultiplier tube. This electron signal is then amplified by a dynode chain, which results in the final photomultiplier tube signal at the anode.

Two sets of scintillation counters were used to define the incident muon beam. The three B counters, located upstream,

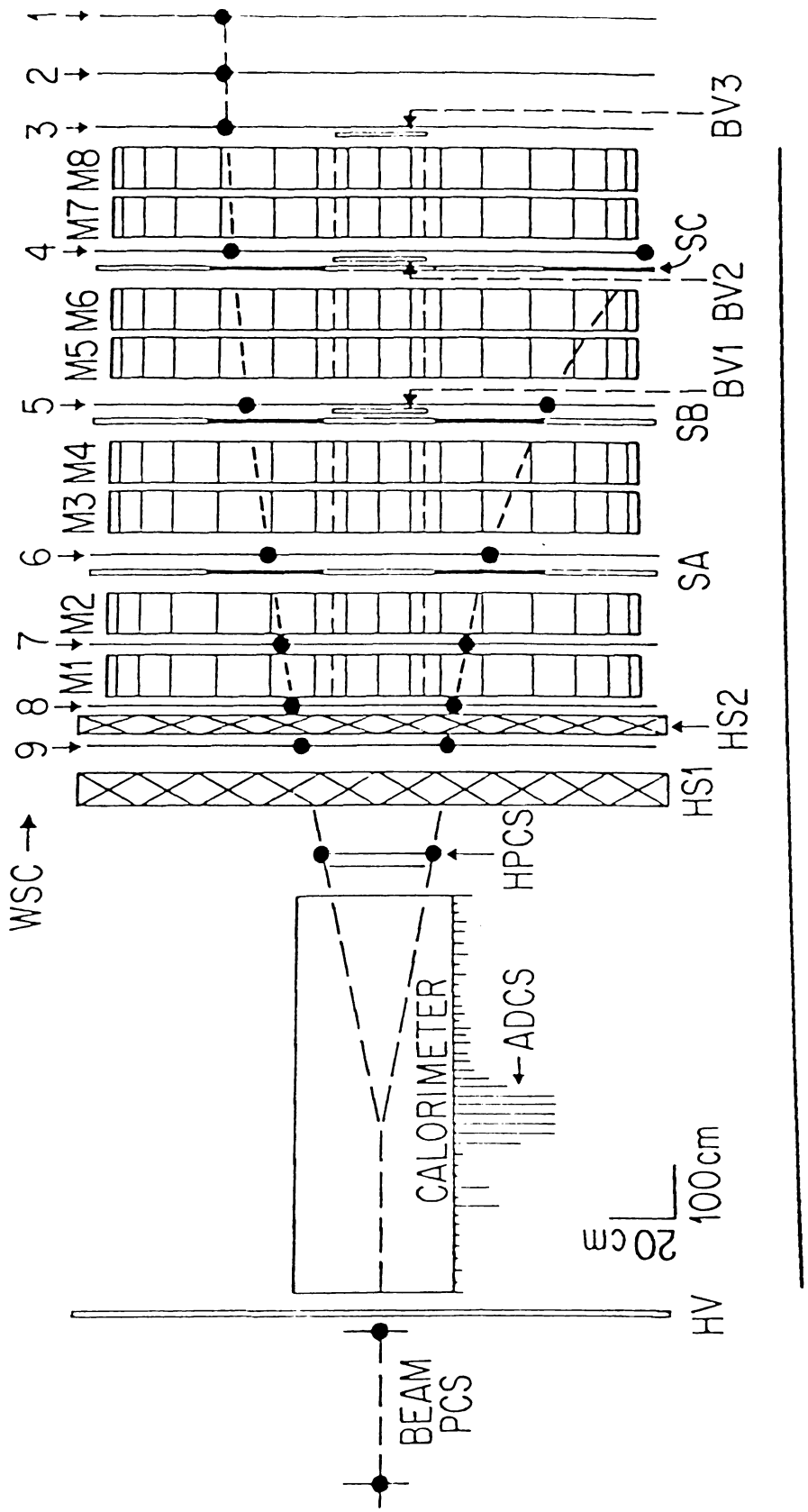

Figure 2.4. E319 Experimental Apparatus

Table 2.3. z-Positions of all E319 Equipment (cm)

Equipment					Position
E398	PWC1				-15512.95
		BH1			-15486.28
E398	PWC2				-8512.30
		BH2			-8485.63
			B1		-8450.00
			B2		-7800.00
			B3		-6460.00
E398	PWC3				-6393.49
E398	PWC4				-6393.49
		BH3			-6366.82
E319	PWC5				-3685.54
			C1		-3630.00
E398	PWC5				-3294.28
E398	PWC6				-3294.28
			C2		-525.00
E319	PWC4				-517.76
			C3		-490.00
				HV1	-480.00
				HV2	-400.00
E319	PWC3				-235.35
Target - Calorimeter					-165.74 to 574.14
E319	PWC2				625.32
E319	PWC1				649.77
Hadron - Shield I					736.76 to 798.51
		WSC9			848.68
Hadron - Shield II					869.63 to 902.65
		WSC8			922.02
			M1*		978.54 (79.70)
		WSC7			1035.37
			M2*		1092.68 (79.85)
				SA	1148.87
				SA'	1170.70
		WSC6			1201.42
			M3*		1282.70 (79.06)
			M4*		1370.33 (79.86)
				SB	1427.80
				SB'	1449.87

Table 2.3. Continued

Equipment				Position	
BV1				1464.79	
	WSC5			1478.92	
		M5*		1565.59	(79.46)
		M6*		1655.13	(80.02)
			SC	1710.53	
			SC'	1731.96	
BV2				1747.20	
	WSC4			1761.49	
		M7*		1822.77	(78.75)
		M8*		1911.19	(79.93)
BV3				1960.36	
	WSC3			1988.03	
	WSC2			2086.29	
	WSC1			2190.43	

*Values are center (length)

Key: PWC = Proportional-Wire-Chamber
BH = Beam Hodoscope
B = Beam Telescope B
C = Beam Telescope C
HV = Halo Veto Counters
WSC = Wire-Spark-Chamber
M = Magnet
BV = Beam Veto Counters
S = V Trigger Bank Hodoscopes
S' = H Trigger Bank Hodoscopes

To convert to FNAL coordinates, the Chicago Cyclotron Magnet Center in the MSU coordinate system is -920.125" = -2337.12 cm
FNAL System = 106523.83'

downstream, and in the middle of the enclosure 104 dipoles, were 0.25" thick x 3.5" (horizontal) x 2.5" (vertical) and covered the magnet apertures in enclosure 104 (the last beamline bend before the muon lab). The three C counters, located at the entrance of the muon lab and just upstream of the target, were 7.5" in diameter X 0.25" thick and were used to ensure the muons passage through the active area of the E319 beam proportional chambers. All B and C counters used Amperex 56AVP phototubes. Fast cables (speed of pulse propagation $\simeq$ 0.97c) were used to carry the photomultiplier tube signals of B_1, B_2, B_3, and C_1 to their discriminators in the muon lab (where they were clipped to three ns at the inputs), since these signals were the last to arrive and needed to form the event trigger. These counters had measured efficiencies of > 99% for our runs.

The energy of the incident muon can be calculated knowing the positions and angles (relative to the "nominal" beam axis) of the muon before and after the enclosure 104 dipoles. For this purpose, we had the use of three E98 (Chicago-Harvard-Illinois-Oxford muon scattering group) beam hodoscopes. These hodoscopes consisted of eight 1/16" thick counters; seven of which were 0.75" wide and one which was 1" wide (the eastmost counter which was labelled #1), with the entire hodoscope being centered on the magnet aperture. These were located downstream in enclosure 103, and upstream and downstream of the magnets in enclosure 104, all of these hodoscopes measured y (east-west) displacements only. Use of these hodoscopes allowed a 1% energy determination on an event-by-event basis.

2.4 Multiwire Proportional Chambers (MWPC's)

The E319 MWPC system (on loan from Cornell University) consisted of 12 planes (each with 2 mm wire spacing) combined in sets to yield five chambers. PC5 (at the entrance of the muon lab, near C_1) was an XY module with 96 wires/module and an active area of 19cm x 19cm. PC4 and PC3 were UVW modules (96 wires/module) located just upstream of the target (near beam counters C_2 and C_3), with the V and W modules rotated 120° clockwise from the U module looking in the positive z direction; for PC4 u was in the +x direction and for PC3 u was in the -y direction. The active area of these detectors was a 19cm diameter circle. PC2 and PC1 were located downstream of the target (before the hadron shield); PC2 was a UV module with 160 wires/module (active area 31.8cm x 31.8cm) and PC1 was an XY module with 192 wires/module (active area 38.2cm x 38.2cm). For the hadron PC's (PC2 and PC1) and all the spark chambers, $u \equiv (x + y)/\sqrt{2}$, $v \equiv (y - x)/\sqrt{2}$, and so $x = (u - v)/\sqrt{2}$, $y = (u + v)/\sqrt{2}$.

The anode planes of these PC's consisted of 20 micron thick gold-plated tungsten wires (tensioned to 50 grams) with 2 mm wire spacing, sandwiched between two three-mil thick aluminum foil high voltage planes, which were 0.25" from the anode plane. The outer windows of each module were 6 mil thick Kapton film. The pre-mixed "Magic Gas" used was: 20% Isobutane, 4% Methylal, 0.25% Freon 13B1, and the balance Argon. Typical high voltage was -4.5kV, which was adjusted for each chamber using a Zener diode divider chain with 70 volt steps.

Charged particles passing through the chambers knocked loose valence electrons from the gas molecules, which because of the large

electric field, were accelerated towards the nearest anode wire, causing an electron avalanche which induced a negative pulse on that wire. The signals on all wires were amplified and discriminated (threshold $\sim$ 5mV) at the chamber and sent differentially down 100 ohm ribbon cable (3 wires/signal; up, down, and ground) to avoid noise pickup and cross talk between channels.

Since the PC's ran continuously, the PC signals were latched into CAMAC latch cards only if a fast pre-trigger logic signal (called PC Strobe) was received. PC Strobe was used to generate a 10-20 ns wide PC Reset signal (which set all latch bits to zero), followed by a 100-120 ns wide PC Enable signal (any PC signals arriving at a latch input during this period caused the latch bit for that wire to be set to one). If a real trigger occured (later in time than the PC information was latched), a signal was sent, using fast cable, into the computer portacamp to gate off the PC Reset and Enable units, preventing a later beam track from being stored into the latches. Diagrams of the amplifier/discriminator cards and latch cards are shown in Figures 2.5 and 2.6. More details on the construction of the proportional chambers can be found in the thesis of Y. Watanabe.[1] See Table 2.4 for a summary of proportional chamber characteristics.

The other set of beam PC's used belonged to E98. These consisted of 6 planes with 96 wires each (with 12 wires/inch and an active area of 8" x 8") centered on the magnet aperture they were located near. Each anode plane consisted of 0.8 mil diameter stainless steel wires tensioned to $\sim$ 20 grams, sandwiched between two high voltage wire

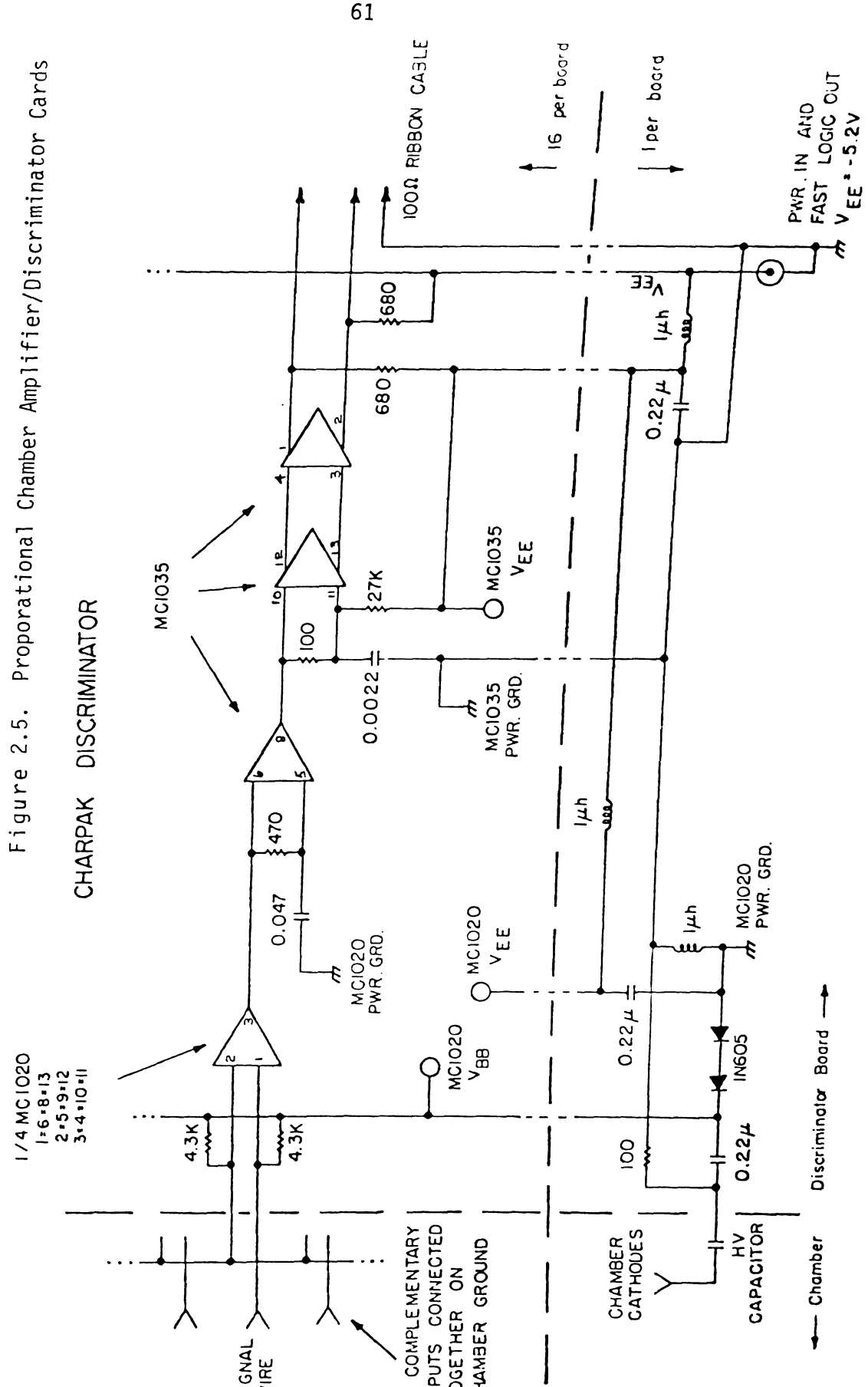

Figure 2.5. Proporational Chamber Amplifier/Discriminator Cards

CHARPAK DISCRIMINATOR

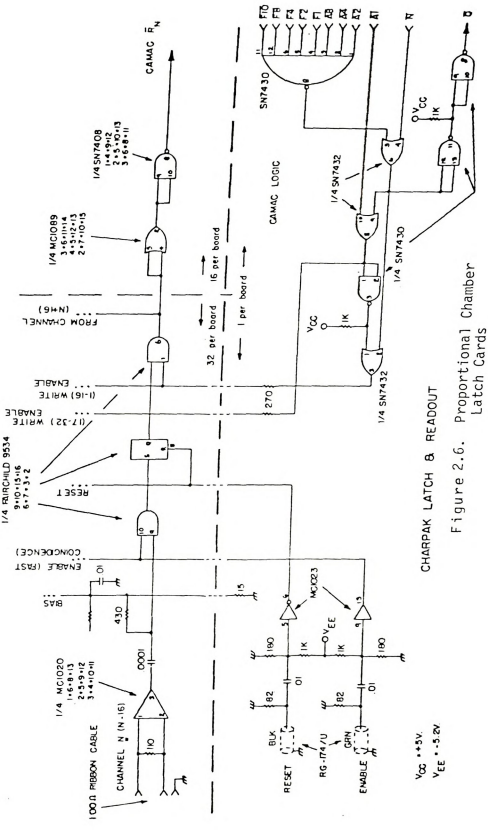

CHARPAK LATCH & READOUT

Figure 2.6. Proportional Chamber Latch Cards

Table 2.4 Proportional Chamber Information

PWC	Location (cm)	No. of Planes	Orientation*	Size of Planes Edge to Edge (cm)
A) E319 Proportional-Wire-Chamber (PWC)				
5	-3685.54	2	-X,-Y	19.2
4	-517.76	3	X, V', W'	19.2
3	-235.35	3	-Y, V, W	19.2
2	625.32	2	-U, V	32.0
1	649.77	2	-X, Y	38.4

*Sign indicates direction in which the numbered wires increase.

Wire spacing = 2.0 mm

Reset Pulse Width = 15 ns

Enable Pulse Width: PWC1, 2, 3, 4 (X, V') = 120 ns
PWC4W' = 86 ns
PWC5 = 80 ns

B) E398 PWC's			
1	-15512.95	Y	20.3
2	-8512.30	Y	20.3
3	-6393.49	Y	20.3
4	-6393.49	X	20.3
5	-3294.28	Y	20.3
6	-3294.28	X	20.3

Wire Spacing = 12 wires per inch

Reset Pulse width = 20 ns

Enable Pulse Width = 98 ns

planes composed of four mil thick stainless steel wires, which were 3/16" from the anode plane. The pre-mixed gas used was: 25% CO_2, 0.4% Freon 13B1, and the balance Argon; typical high voltage was -3400 volts. Operating very similarly to the Cornell chambers, these were read out using 100 ohm ribbon cable and latched into CAMAC latches in the computer portacamp. The E98 PC1 was located downstream of enclosure 103, PC2 was located upstream in enclosure 104, PC3 and 4 were located downstream of enclosure 104, and PC5 and 6 were located at the entrance of the muon lab. E98 PC4 and 6 measured x (up-down), all of the rest measured y coordinates (east-west). These PC's were not used for the 270 GeV μ+ runs because of a latch gate timing problem but proved useful in obtaining alignment constants for the beam hodoscopes located near them, which were used for E_0 measurements during the main data runs.

2.5 Calorimeter

The target/calorimeter was composed of 110 1-7/8" thick x 20" x 20" machined steel plates (weighing about 210 lbs each) with a 3/4" thick aluminum counter frame placed between sets of adjacent steel plates. Inside the frame was a 3/8" thick x 20" x 20" plastic scintillation counter (NE110), viewed above by an RCA 6342A phototube. See Table 2.5 for the average target density and radiation length. Each anode signal was fed via coaxial cable into an amplifier, where the signal was resistively split and fed into two amplifier channels, one with unity gain and one with a gain of $\sim$ 30. These 220 signals were digitized in Lecroy 2249A CAMAC analog-to-digital converters (ADC's). The 12 channel ADC's had 10 bit resolution (1 part in 1024), with a full

Table 2.5. Calculation of Average Target Density and Radiation Length

Material in Each Target Segment			
Material	Thickness t(cm)	Density ρ(g/cm^3)	L_{RAD} (cm)
Fe	1 7/8" = 4.7625	7.870000	1.76
Scintillator	3/8" = 0.9525	1.032000	42.90
Vinyl	2x.015" = 0.0762	1.390000	28.70
Al foil	4x.001" = 0.1016	2.700000	8.90
Air*	.363" = 0.9223	0.001205	30050.00

Total target thickness = 110 segments x 6.7237 cm/segment
= 739.6 cm

*Air gap in each segment varies--it has been adjusted here for agreement with the total measured target length.

$$\langle\rho\rangle = \frac{\sum_i t_i\rho_i}{\sum_j t_j} = 5.741 \text{ g/cm}^3 = 4246 \text{ g/cm}^2$$

$$\langle L_{RAD}\rangle = \frac{\sum_i t_j}{(\sum_i t_i/L_{RAD_i})} = 2.46 \text{ cm} = 14.1 \text{ g/cm}^2$$

scale signal corresponding to 256 pC of charge (an overflow bit was set if a larger pulse occured). The amplified phototube signals were stored only when they arrived in time with a 100 ns gate pulse derived from the event trigger signal.

The ADC pedestals (digitized signal for zero particles in a counter) were set to $\sim$ channel 7, while the single muon peak (digitized signal for a single minimum ionizing particle passing through a counter) was at $\sim$ channel 10 for the low gain (even numbered) ADC channels and $\sim$ channel 50 for the high gain (odd numbered) ADC channels. During the experiment, 38 pedestal runs and seven single muon peak runs were taken which were later used as inputs for the data analysis program (to be discussed in Chapter III).

The calorimeter was used to measure the energy of hadronic showers accompanying deep inelastic muon interactions. For each counter, the number of "equivalent particles" was defined as: (ADC channel number - ADC pedestal)/(single muon peak - ADC pedestal), which is equivalent to the number of minimum ionizing particles passing through that counter. For all counters with the number of equivalent particles above a certain threshold (15 equivalent particles), the number of equivalent particles was summed. By steering hadron beams (i.e. π^- beams of five energies ranging from 25 GeV to 225 GeV) of known energy into the calorimeter, and using the same algorithm to define a hadronic shower as was used for the data (using only events with one shower in the calorimeter), the sum of the number of equivalent particles in a shower was obtained, which yielded data giving a linear relationship between the number of equivalent particles in a shower and the energy of the

hadronic shower. In data events where a shower was present, the interaction vertex (ZADC) was taken as the first counter of the shower.

Care had to be taken in using the calorimeter information. Spark chamber noise, carried on the ground shield of the ADC gates, was able to reopen the ADC gates, allowing unwanted signals to be digitized. More information about this and the details of the calorimeter construction can be found in the thesis of Dan Bauer.[2]

2.6 Hadron Shields

To shield the front spark chambers from hadrons exiting the target, so that these chambers could be more easily used by the track finding routines, which began at the front of the spectrometer, two hadron shields ($\sim$ 84" high and 145" wide), composed of 2-3/8" thick unmagnetized steel plates, were located between the Hadron PC's and the first wire spark chamber (WSC), and between the first and second WSC's. The first hadron shield was $\sim$ 24" thick ($\sim$ 480 gm/cm^2 or 3.6 absorption lengths), while the second was $\sim$ 13" thick ($\sim$ 260 gm/cm^2 or 1.9 absorption lengths); so with $\sim$ 5.5 absorption lengths of total material, the probability of a hadron exiting the target and reaching the first magnet was $e^{-5.5}$ or 0.4%.

2.7 Spectrometer Magnets

Eight iron-core toroidal magnets were utilized for scattered muon(s) momentum analysis and to shield the trigger counter banks and spark chambers from penetrating hadrons exiting the target. Each magnet had a 12" ID, a 68" OD, and was $\sim$ 31" thick (actually four 7.75" thick low-carbon steel plates welded together at the edges). The magnets were radially wound with $\sim$ 460 turns of #8 wire, and run

at $\sim$ 35 amps, giving an average B field of 17 kgauss. Two old FNAL beam line power supplies were used to power the magnets, with odd numbered magnets being powered by one supply and even numbered magnets by the other. The radial dependance of the magnetic fields is shown in Table 2.6. Inside the magnet holes was an aluminum and copper shell through which low conductivity water was circulated to cool the magnets. Inside this shell, the magnet holes were filled with ilminite-loaded concrete, which prevented hadrons, which had exited the target, from striking the beam veto counters and thus vetoing an event.

The energy loss[3] per magnet (one magnet $\sim$ 620 gm/cm^2 or 4.6 absorption lengths) varied from 1.2 GeV for a 10 GeV muon to 2.3 GeV for a 250 GeV muon. For a muon traversing the entire spectrometer, the energy resolution was $\sim$ 9%. The average P_T due to the magnetic field was 0.4 GeV/c per magnet, while the average P_T due to multiple scattering in the magnet iron was $\sim$ 0.1 GeV/c per magnet.

The magnetic field shape was measured two ways in the previous experiment (E26):

1) A B-H curve of a small toroid made from the same batch as the large toroids was used to obtain B(r) vs r.

2) Small holes were drilled through a 7.75" plate of one of the spectrometer magnets and the induced current through a coil wound through this hole and the center magnet hole was measured.

These two methods agreed to $\sim$ 1%. Because of the hysteresis properties of iron, the magnets had to be degaussed (by varying the current direction and amplitude in many steps over several hours) before the muon data runs to ensure the same magnetic field shape as in E26.

Table 2.6. Fits to Toroid Magnetic Fields

Coefficients	a	c	d	f
M1,M3,M5,M7	12.20	19.92	-0.08357	0.0004346
M2,M4,M6,M8	12.07	19.71	-0.08270	0.0004301

Current = 35 Amps

Average Field = 17.09 kG M1,M3,M5,M7
17.27 kG M2,M4,M6,M8

$$B(r) = a/r + c + dr + fr^2$$

B in kG
r in cm

The average field measurements made using flux loop techniques in E319 agreed very well with similar measurements made in E26. Further details on magnet construction and magnetic field measurements can be found in the thesis of S. Herb.[4]

2.8 Spark Chambers

There were nine magnetostrictive readout wire spark chambers in the spectrometer. Each chamber consisted of two modules, with each module containing two orthogonal signal wire planes. The first module measured XY coordinates, while the second module, which was rotated 45° with respect to the first module, measured UV coordinates ($u \equiv (x + y)/\sqrt{2}$, $v \equiv (y - x)/\sqrt{2}$). The second module was necessary in order to remove XY match ambiguities when more than one track went through a chamber. The active region of a chamber was a 72" diameter circle (each module had an active area of 73" x 73"), slightly larger than the active area of the spectrometer magnets or trigger counter banks. The central region of the back five spark chambers had a 12" diameter dead region (a plastic patch between wire planes) in order to avoid recording beam tracks and tracks in the field free region of the spectrometer.

The signal wire planes were made of five mil diameter Be-Cu wires with a wire spacing of $\sim$ 0.7mm, tensioned to one lb/wire. The two high voltage planes were 25 mil thick x 80" x 80" aluminum sheets. The two orthogonal signal wire planes were separated from each other by $\sim$ 3/16" with a high voltage plane $\sim$ 0.25" from a signal plane on either side. The gas used was: 80% Neon, 17% Helium, 3% Argon, with $\sim$ 0.7 SCFH ($\sim$ 4% of the total flow) passed through isopropyl alcohol at 80° F.

The gas was purified and recirculated at the rate of ∿ 17 SCFH using an LBL recirculator[5] which had a cryogenic alcohol trap added to keep the liquid nitrogen gas traps from becoming clogged with alcohol. The alcohol was added because it limited spark currents (keeping one spark from getting all the available spark current) which helped improve the chambers' multiple track efficiency. The gas mixture was monitored periodically using a gas chromatograph.

The spark chambers were triggered by the main trigger signal, which fired a hydrogen thyratron causing the breakdown of the spark gaps located on each chamber, which caused a high voltage (∿ 7.5 - 8.5 kV) capacitor storage bank to be discharged across the chamber's high voltage planes about 200 ns after a trigger had occured. Spark breakdowns occured along the ion trails left by charged particles traversing the chambers, which induced pulses on the signal wires closest to the spark breakdown between the high voltage planes. To keep the memory time of the chambers short (actual value was ∿ one microsec), a DC +40 volt clearing field was applied to the high voltage planes to sweep out unwanted ion trails. Due to the large amount of charge necessary to fire a chamber, the LC spark gap circuit had to be recharged before the chamber could be refired. To allow sufficient time for this, another trigger was prevented from occuring by gating off the trigger module for 42 msec (the "dead time" of the spark chambers).

The current pulses traveling down the signal wires were grounded out at one end, and traveled perpendicularly across a magnetostrictive wire inside a plastic catheter (filled with argon to prevent wire

corrosion) at the other end. Induced acoustic stress waves traveled along this wire at $\sim 5.3 \times 10^5$ cm/sec and were picked up by a coil at one end of the magnetostrictive wire. Part of the chamber current was fired through fixed wires at the two ends of each wire plane (called fiducial wires). The difference of the arrival times of a pulse relative to the fiducials gave the distance along the wand at which the spark occured. The distance between fiducial wires was 184.15 cm for WSC 1-5 and 182.88 cm for WSC 6-9. The signals were amplified at the chamber and sent to discriminators, and were then differentiated and the peak determined using a zero-crossing peak detector. Output pulses were converted to 20 Mhz scaler counts in CAMAC 14-bit time digital converters (TDC's), which digitized the first eight sparks (including fiducials, unless missing) for each wand, setting an overflow bit for the ninth spark. All the time digitizers were started by the trigger signal, with the first fiducial usually at $\sim$ 700 counts, and the second fiducial usually at $\sim$ 8000 counts.

The spark gap circuit, the wand amplifier circuit, the zero crossing peak detector, and the time digitizer system are shown in Figures 2.7 - 2.10. Spark chamber characteristics are summarized in Table 2.7. Further detail on the construction and operation of the spark chamber system can be found in the thesis of C. Chang.[6]

2.9 Trigger Bank Counters

Six banks of counters (three groups of two each) were used to define a scattered muon in the active area of the spectrometer. These counters (which divided an $\sim$ 70" diameter circle into five

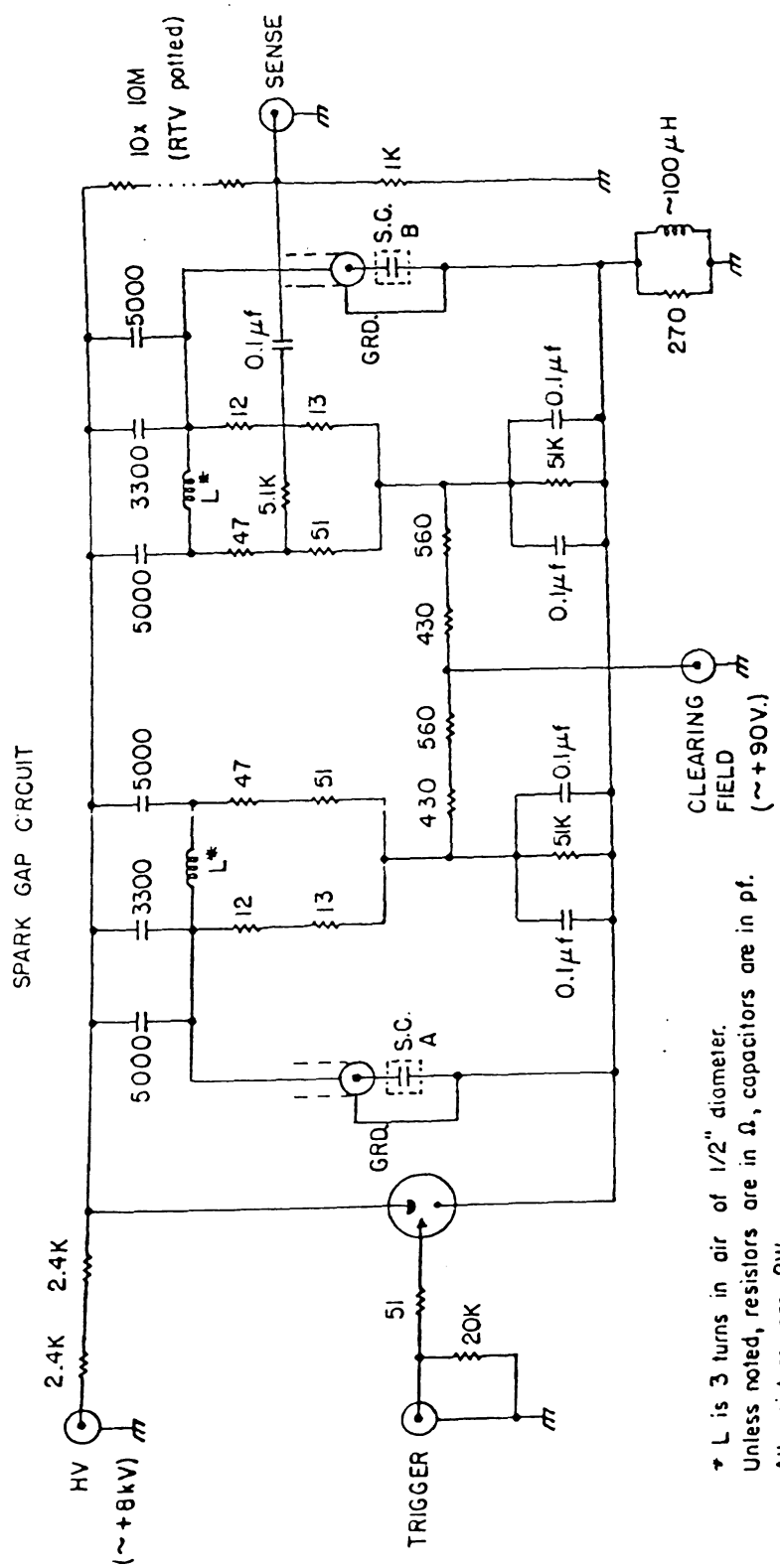

* L is 3 turns in air of 1/2" diameter.
Unless noted, resistors are in Ω, capacitors are in pf.
All resistors are 2W.
2 x 15Ω 2' long cables in parallel to each chamber.

Figure 2.7 Spark Gap Circuit

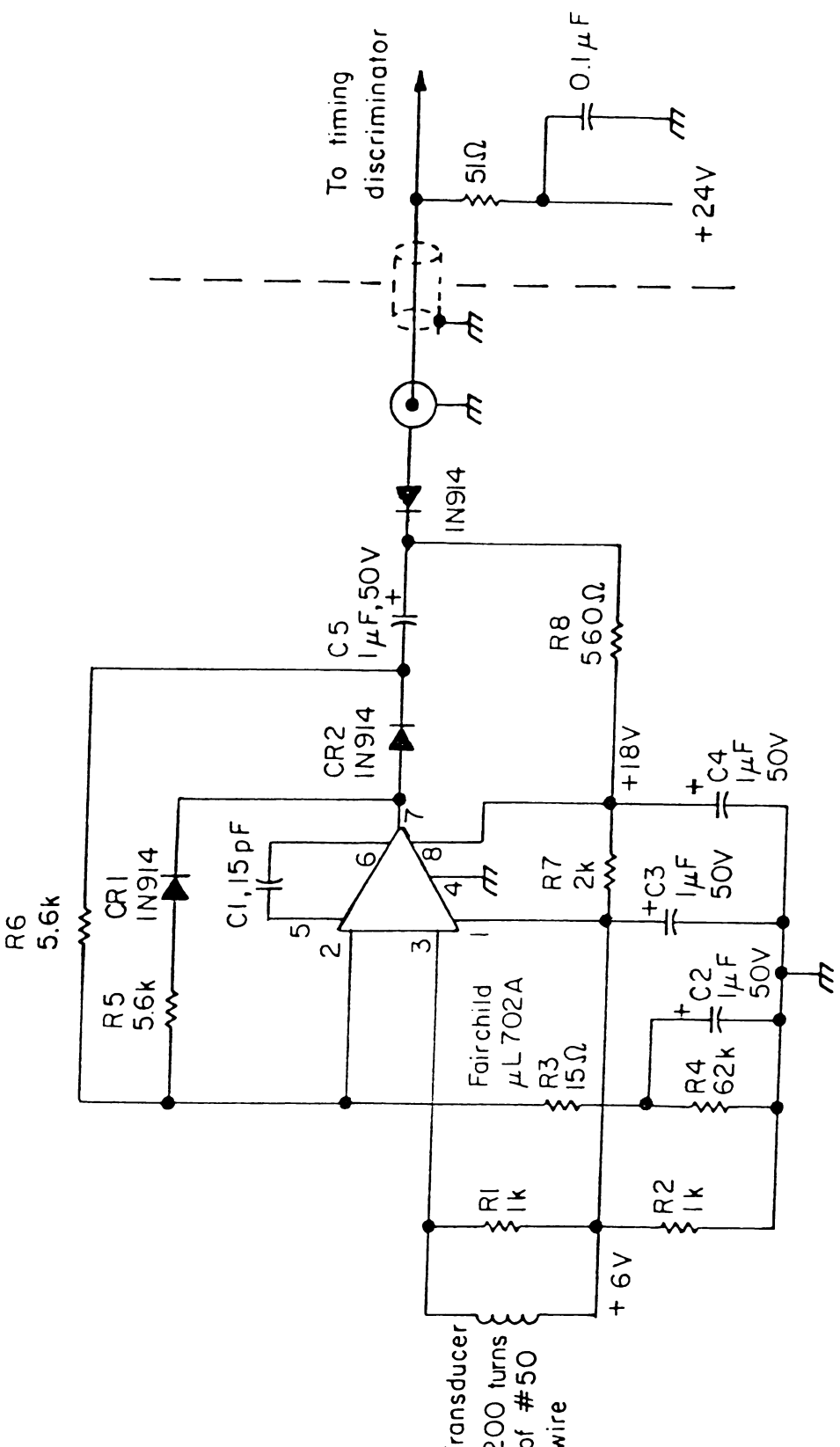

Wand Amp Circuit

Figure 2.8.

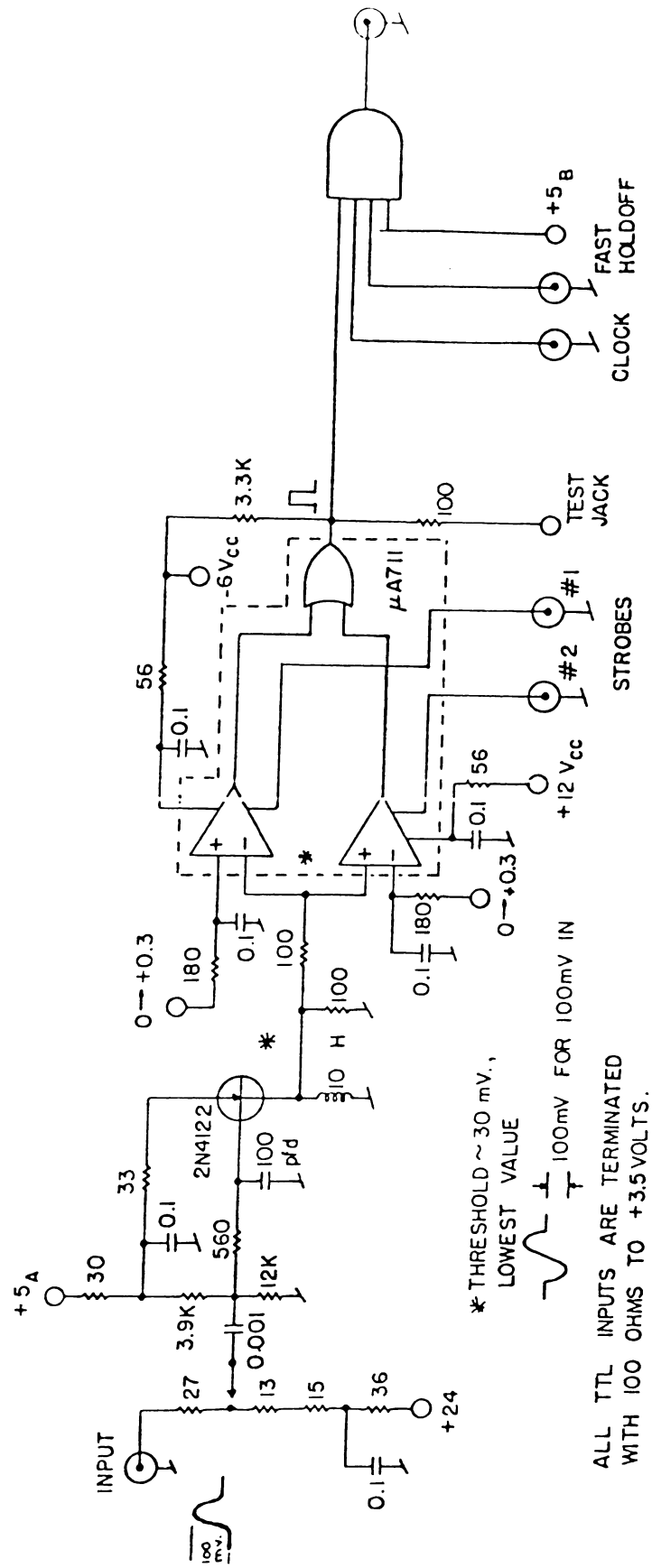

ZERO CROSSING PEAK DETECTOR

Figure 2.9.

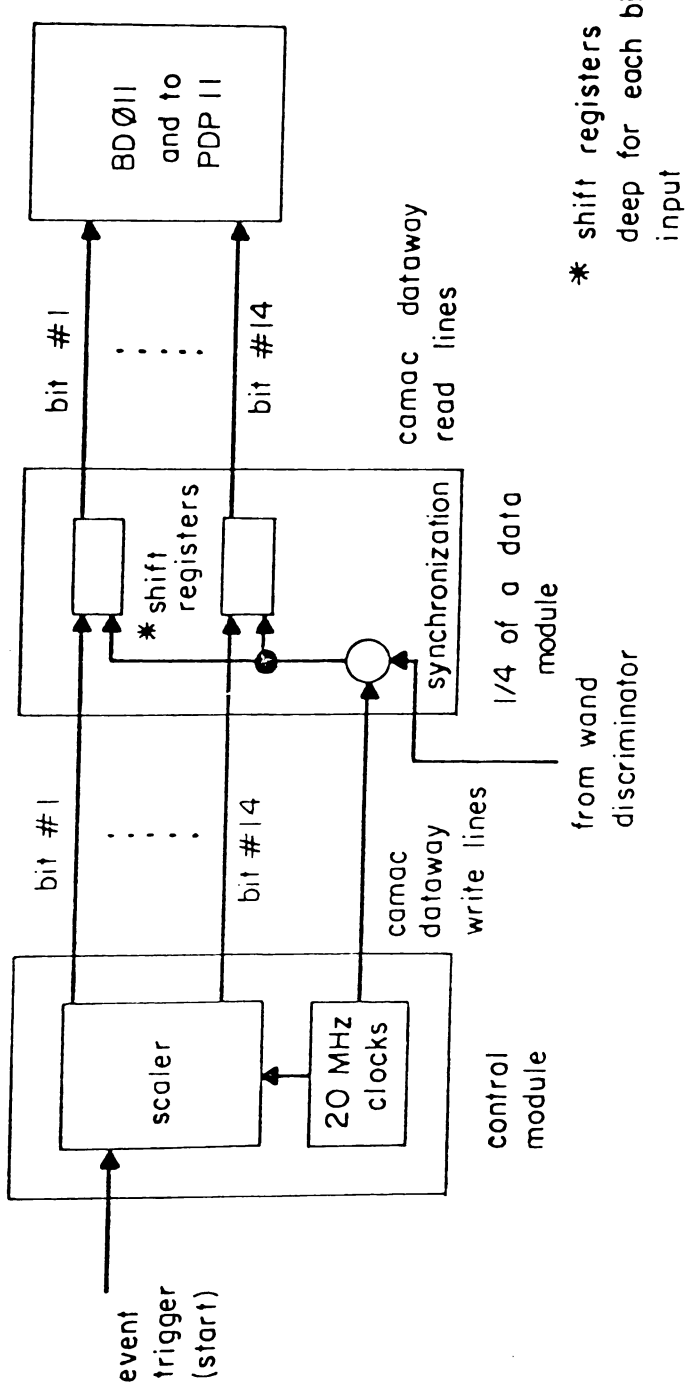

Simplified Schematic of Time Digitizer System

Figure 2.10

Table 2.7. Spark Chamber Properties

Active area 73" x 73"

Be-Cu wire 0.005" diameter spaced 0.7 mm apart

Fiducial wire separation 184.15 cm in WSC1-5
182.88 cm in WSC6-9

Gas mixture Ne-He 78-80%
Ar 2-3%
Alcohol 0.7 SCFH @80°F

Wand catheters contain Ar

Spark gaps contain N_2

Time from trigger signal to spark gap breakdown 220 ns

Wand Reversal* and Chamber High Voltage

Chamber	Reversal	H.V.	Chamber	Reversal	H.V.
1X	+		6X	-	
1Y	+	8.6 kV	6Y	-	8.6 kV
1U	-		6U	+	
1V	-		6V	+	
2X	-		7X	+	
2Y	-	8.4 kV	7Y	+	7.6 kV
2U	+		7U	-	
2V	+		7V	-	
3X	+		8X	-	
3Y	+	8.4 kV	8Y	-	7.8 kV
3U	-		8U	+	
3V	-		8V	+	
4X	-		9X	+	
4Y	-	7.6 kV	9Y	+	7.4 kV
4U	+		9U	-	
4V	+		9V	-	
5X	+				
5Y	+	7.2 kV			
5U	-				
5V	-				

* + means increasing time counted with increasing displacement

\- means decreasing time count with increasing displacement

horizontal or vertical slats) were located behind the second (SA and SA'), fourth (SB and SB'), and sixth (SC and SC') spectrometer magnets. The trigger banks are shown in Figure 2.11. Each slat of the trigger banks was viewed at each end by an Amperex 56AVP phototube, with both signals going into the parallel inputs of a discriminator. The outputs of all the discriminators were latched into a set of CAMAC discriminator coincidence registers (DCR's) so that in-time tracks could be distinguished from out-of-time tracks during later analysis. All of the counter slats in one bank were OR'ed together to form the logic signal for that bank, which was later used in forming the trigger signal. The horizontal trigger banks (SA, SB, and SC) were made up of 0.25" thick x 14" wide counters, having a 13.5" diameter circular hole in the center of the counter bank which was centered on the spectrometer axis. The vertical trigger banks were made up of 3/8" thick x 14.25" wide counters, with an overlap of 0.25" between counters, and a 12" diameter hole in the center of the counter bank which was centered on the spectrometer axis.

2.10 Halo Veto and Beam Veto Counters

Halo was defined as incident muons (at the face of the target) outside of a seven inch diameter circle (centered on the beam axis) and inside an $\sim$ 70" diameter circle (the approximate size of the halo veto and trigger bank counters). To detect in-time muons in this area (within $\pm$ 12.5 ns of a beam track) a halo veto counter bank (similar to a horizontal trigger bank with a 14" x 14" central hole, see Figure 2.12) was placed upstream of the target. To make the central hole smaller, a 20" x 20" counter, with a 7" diameter hole,

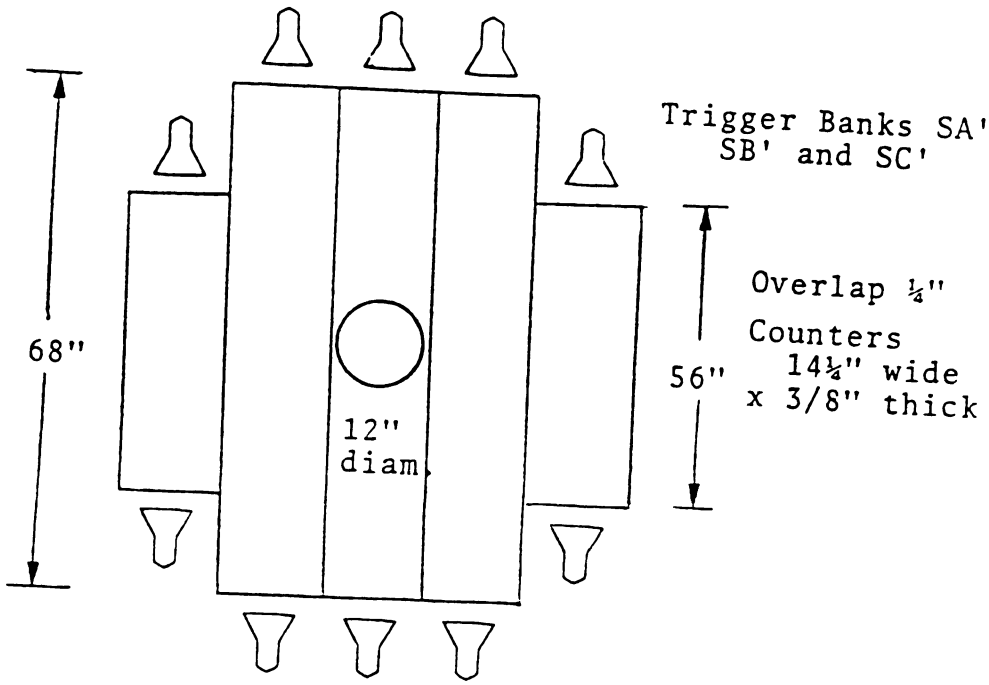

All phototubes are Amperex 56AVP

Figure 2.11. TBC Diagram

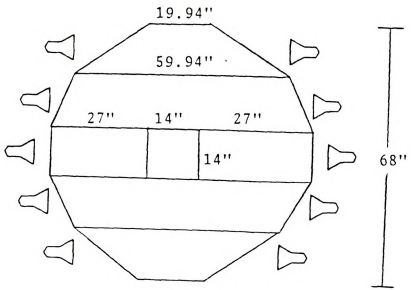

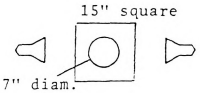

CORRECTION COUNTERS

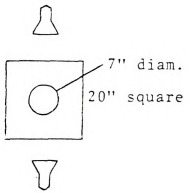

Figure 2.12. Halo Veto Diagram

was centered on the halo veto bank at $\sim$ the same z-position as C_3. All counter slats were viewed at each end by Amperex 56AVP phototubes, and fed into the parallel inputs of discriminators in DC Pass mode (in DC Pass mode, the dead time of the discriminator was almost zero). All of the discriminator outputs were "OR"ed to form the halo veto signal HV. This NIM logic signal was used as a trigger veto, since an in-time halo can hit all of the trigger banks, simulating a scattered muon. To measure the efficiency of this counter bank during data runs, a set of three 10" x 10" counters (called S_{tel}) was located at the approximate z-positions of the horizontal trigger banks. The ratio $(S_{tel} \cdot \overline{HV})/S_{tel}$ was measured to be $\sim 2.7 \times 10^{-4}$, indicating very good efficiency.

To ensure that a beam muon was scattered (due to a nuclear interaction) in the target by a large enough angle so that it entered the active area of the spectrometer, three beam veto counters were placed behind magnets four (BV_1), six (BV_2), and eight (BV_3) centered on the magnet axis. These counters were 3/8" thick x 12.5" diameter and were viewed by Amperex 56AVP phototubes. Phototube signals were discriminated in DC Pass mode (to eliminate dead time, since the beam rate was $\sim 10^6$ muons/spill). The beam veto signal was defined as $BV = (BV_1 + BV_2) \cdot BV_3$ and was used as a trigger veto. To ensure that hadrons exiting the target did not strike the beam vetoes and veto a good event, the magnet holes were filled with ilminite-loaded concrete (2.1 absorption lengths of material/magnet). The efficiency of these counters was measured using the ratio $(B \cdot \overline{BV})/B$, which was measured to be $\sim 10^{-4}$.

2.11 Fast Electronics and Trigger

For the purposes of triggering the apparatus and standardizing counter pulses, so they could be stored into CAMAC modules, a large array of NIM bins and associated discriminators, logic modules, and gate generators existed in the muon lab. All of the signals from the B and C counters, beam hodoscopes, halo veto, trigger bank, and beam veto counters were fed into discriminators, whose outputs were standard NIM pulses of fixed length (NIM pulses are defined as > -700 mV into 50 ohms). These pulses could then be stored into discriminator coincidence registers (DCR's), see Figure 2.13, and the signals themselves and various logical combinations could be counted in visual and CAMAC scalers, see Table 2.8.

To ensure that the apparatus was triggered only during the beam spill and also that a trigger did not occur before the previous one had been read into the computer, most of the fast electronics NIM bins were gated (either spill gated or event gated). The spill gated bins were turned on for the duration of the main ring beam spill, $\sim$ 1.8 seconds out of every 15 to 20 seconds (the gate unit for this was started and stopped using FNAL main ring ramp timing signals). Once a trigger occured, time had to be allowed to read out the counters, calorimeter, proportional chambers and spark chambers, but most of the time needed was used to recharge the spark chamber firing circuit; also, certain devices had to be shut off so that they did not overwrite previously stored information. Whenever a trigger occured, all event gated NIM bins were shut off for 42 msec (the "dead time" of the system), so that it was impossible to have another trigger until the previous one was stored in the computer and all devices were again ready. Since

	BIT	LATCH
DCR1	1	SAV-1
	2	SAV-2
	3	SAV-3
	4	SAV-4
	5	SAV-5
	6	SBV-1
	7	SBV-2
	8	SBV-3
	9	SBV-4
	10	SBV-5
	11	SCV-1
	12	SCV-2
	13	SCV-3
	14	SCV-4
	15	SCV-5
	16	---

	BIT	LATCH
DCR2	1	SAH-1
	2	SAH-2
	3	SAH-3
	4	SAH-4
	5	SAH-5
	6	SBH-1
	7	SBH-2
	8	SBH-3
	9	SBH-4
	10	SBH-5
	11	SCH-1
	12	SCH-2
	13	SCH-3
	14	SCH-4
	15	SCH-5
	16	---

	BIT	LATCH
DCR3	1	$B \cdot P_{evg}$
	2	$B \cdot S \cdot BV_{evg}$
	3	$B \cdot SD_{evg}$
	4	$B \cdot SL \cdot BV_{evg}$
	5	$B \cdot SH \cdot BV_{evg}$
	6	π_{evg}
	7	---
	.	.
	.	.
	.	.
	14	P.C. RESET
	15	---
	16	---

	BIT	LATCH
DCR4	1	BH 21
	2	BH 22
	3	BH 23
	4	BH 24
	5	BH 25
	6	BH 26
	7	BH 27
	8	BH 28
	9	BH 31
	10	BH 32
	11	BH 33
	12	BH 34
	13	BH 35
	14	BH 36
	15	BH 37
	16	BH 38

	BIT	LATCH
DCR5	1	BH 41
	2	BH 42
	3	BH 43
	4	BH 44
	5	BH 45
	6	BH 46
	7	BH 47
	8	BH 48
	9	---
	.	.
	.	.
	.	.
	16	---

	BIT	LATCH
DCR6	1	P.C. STROBE
	2	TH 1
	3	TH 2
	4	TH 3
	5	TH 4
	6	TH 5
	7	TH 6
	8	TH 7
	9	TH 8
	10	---
	11	---
	12	S TELESCOPE
	13	BV I
	14	BV II
	15	BV III
	16	---

Figure 2-13. DCR Latch Bits

Table 2.8. CAMAC Scaler Contents

Scaler No.	Scaled Quantity	Scaler No.	Scaled Quantity
1	B·BV1	19	--
2	B·BV2	20	B·P(EVG)
3	B·BV3	21	S(SPG)
4	$B\cdot\overline{BV}$(EVG)	22	SD(SPG)
5	B(SPG)	23	SL(SPG)
6	$B\cdot\overline{BV}$(SPG)	24	SH(SPG)
7	B(EVG)	25	SL(SPG,NV)
8	$B\cdot\overline{BV}\cdot$SA(EVG)	26	S(SPG,NV)
9	$B\cdot S\cdot\overline{BV}$(EVG)	27	SEM
10	$B\cdot SD\cdot\overline{BV}$(EVG)	28	SPILLS
11	$B\cdot SL\cdot\overline{BV}$(EVG)	29	B104
12	$B\cdot SH\cdot\overline{BV}$(EVG)	30	C
13	$B\cdot S\cdot\overline{BV}$(SPG)	31	$B\cdot B_d$
14	$B\cdot SD\cdot\overline{BV}$(SPG)	32	PCS
15	$B\cdot SL\cdot\overline{BV}$(SPG)	33	HV·S
16	$B\cdot SH\cdot\overline{BV}$(SPG)	34	TOTAL TRIGGERS
17	$B\cdot\overline{BV}_d$(EVG)	35	A.D.C. GATES
18	--	36	P.C. RESETS

EVG = GATED BY EVENT GATE
SPG = GATED BY SPILL GATE
SEM = PROTONS DIRECTED ON PRODUCTION TARGET
NV = NOT SELF VETOED
d = 60 ns Delay in Signal

a trigger cannot occur during this dead time, the flux (incident muons on target) was not accumulated during this time. To prevent the CAMAC and visual scalers from being fired by spark chamber noise, all scalers were inhibited by a 5 microsec pulse started by the trigger.

To get a trigger, a beam muon, not accompanied by an in-time halo muon (i.e. one within $\pm$ 12.5 nsec), had to pass through the active area of the beam counters. The beam signal was defined as: $B = B104 \cdot C \cdot \overline{HV}$, where $B104 = B_1 \cdot B_2 \cdot B_3$, and $C = C_1 \cdot C_2 \cdot C_3$. To ensure there was a scattered muon(s), two scattered muon signals were generated: $S \cdot \overline{BV}$ and $SD \cdot \overline{BV}$, where:

$$S = (SA + SA') \cdot (SB + SB') \cdot (SC + SC'),\ SD = (SA \geq 2 + SA' \geq 2) \cdot (SB \geq 2 + SB' \geq 2),\ BV = (BV_1 + BV_2) \cdot BV_3,$$

and $SA \geq 2$ means two or more slats of counter bank SA were hit. The two main event triggers were $B \cdot S \cdot \overline{BV}$ (the deep-inelastic trigger) and $B \cdot SD \cdot \overline{BV}$ (the so called "dimuon" trigger, implying two or more tracks passing through the active area of the SA, SA' and SB, SB' trigger bank arrays). The dimuon trigger was not very efficient for dimuons, since for many of the dimuon events the second muon passed inside the SA counters or exited the side of the spectrometer before the SB counters.

In order to extract useful information from the experiment, a Monte Carlo program, used to simulate the experimental data (described in Chapter IV), was needed. One of the most important, and sensitive, inputs to this was an unbiased (by apparatus acceptance) random sample of beam muons. For this purpose a third trigger existed: $B \cdot P$, which was the random overlap of a discriminated pulser signal and a beam

signal. Pulser triggers accounted for $\sim$ 5% of the events recorded. The final data trigger was: $T = (B_{evg} \cdot S \cdot \overline{BV}) + (B_{evg} \cdot SD \cdot \overline{BV}) + (B_{evg} \cdot P)$.

The signal used to latch the proportional chamber system was PC Strobe, which was $C \cdot (P + (SA + SA'))$. The C signal was used (instead of B) because a fast signal was needed, due to the small delay provided by the ribbon cable PC readout, while P + (SA + SA') was used since at least one of these signals had to be present for a trigger to occur. However, since this signal was not as restrictive as the trigger signal itself, there were many more PC Strobes than triggers. To ensure that a PC Strobe was not generated after the trigger, but before the event gate was turned off (resulting in latching the wrong beam track), a two microsec pulse inhibited the PC Strobe from firing once a trigger was generated. The trigger logic, the counter logic, and the gate logic diagrams are shown in Figures 2.14 - 2.16.

2.12 CAMAC System and Mini-Computer

Before any of the spectrometer information could be used, it had to be stored onto magnetic tape. This was done in a three step process. First, all relevant information (usually in the form of standardized logic pulses) was read into CAMAC modules, located in six serial-readout CAMAC crates located in the computer portacamp, and stored when the information arrived during a "live time" for that module. Trigger bank, beam hodoscope, and beam veto hits, as well as various triggers, were latched into 16 channel DCR's as either zero (no hit) or one (a hit), depending on whether or not the signals arrived in coincidence with the DCR 40 nsec gate. Hits from the PC's were read into CAMAC latches, which were first all set to zero (by PC Reset,

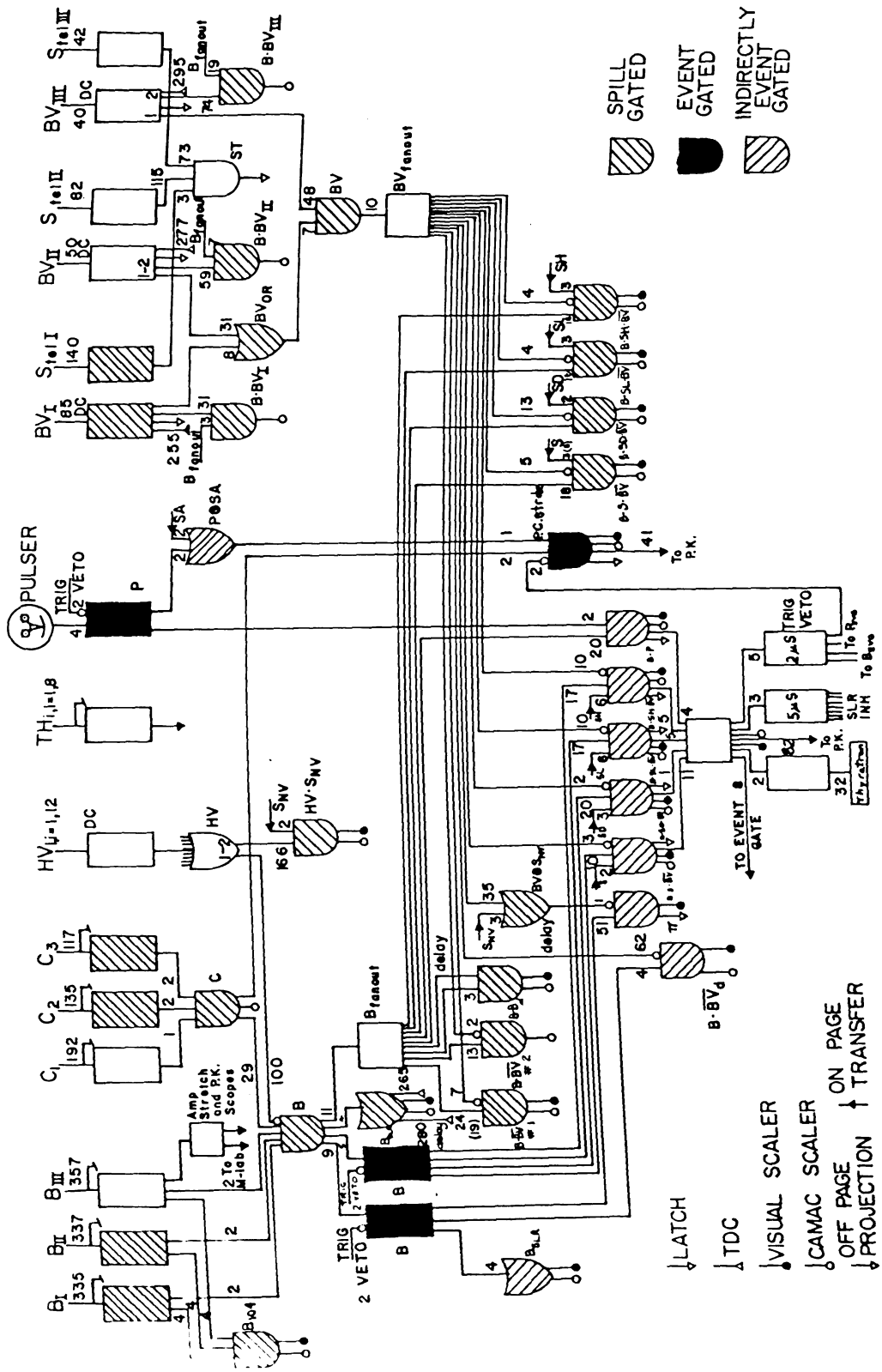

Figure 2.14. Trigger Logic Diagram

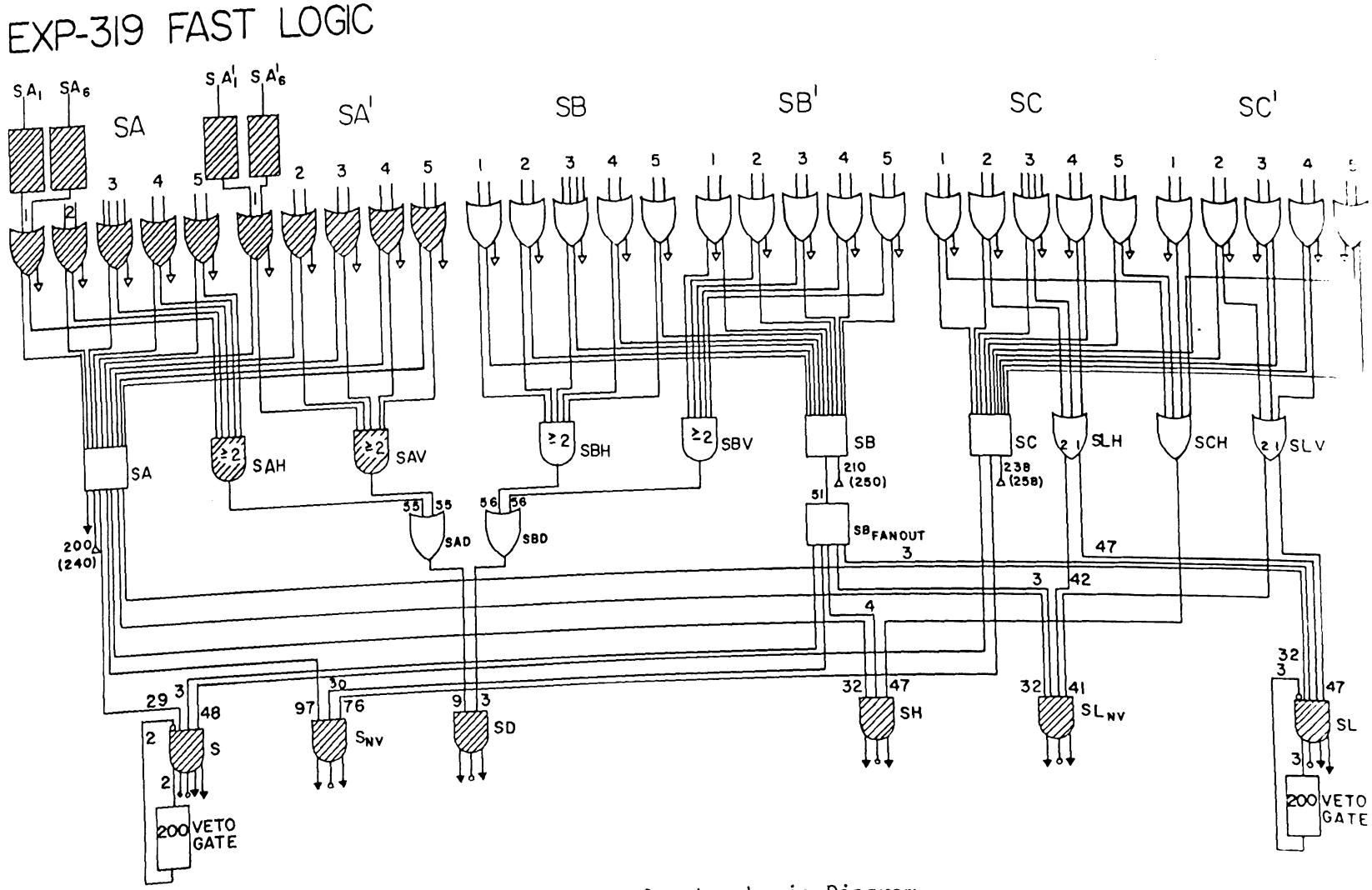

Figure 2.15. Counter Logic Diagram

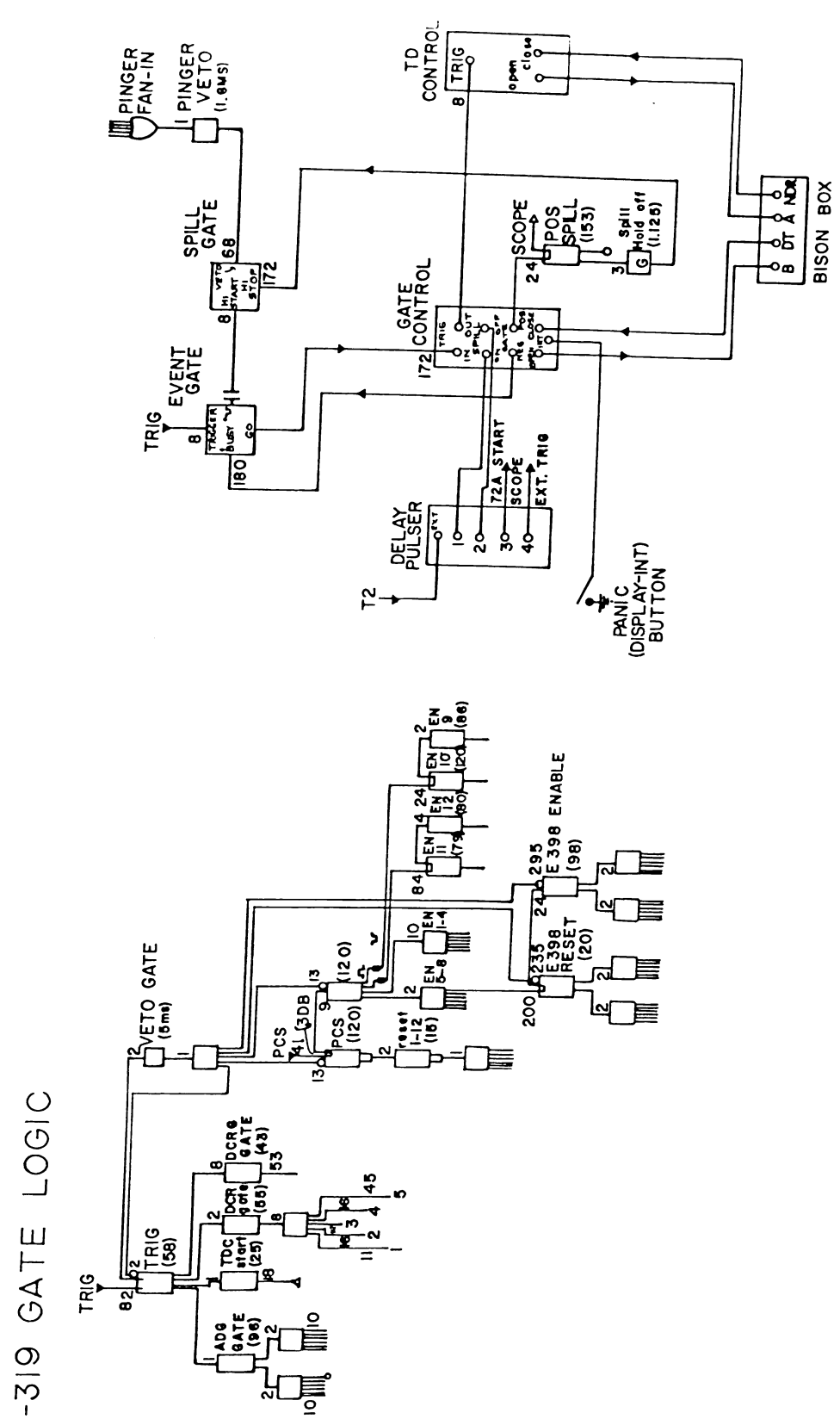

Figure 2.16. Gate Logic Diagram

a 10-20 nsec long pulse) and then to one if a PC pulse arrived during the PC Enable gate ($\sim$ 100 nsec long). Calorimeter signals (two/counter, unamplified and *30) were digitized in 12 channel ADC's for all signals arriving during the 100 nsec ADC gate. Standardized counter pulses, or logical combinations of pulses, were counted in 24-bit CAMAC scalers and visual scalers in the muon lab, which were gated off for five microsec once a trigger occured (to prevent spark chamber noise pickup). The spark chamber pulses were digitized using a 20 Mhz clock for the 36 spark chamber wands (with up to eight sparks/wand), using the trigger signal as a zero-time reference.

Once a trigger had occured, a 42 msec dead time was generated, and all of the CAMAC modules were serially read into the computer. The on-line computer used was a DEC PDP11/45 with a 32k memory (16 bit words). The CAMAC dataway was read out by a BDØ11 branch driver, and all information for one event was written to disk as a 768 word (16 bits/word) block. See Table 2.9 for the data event block format.

Finally, when four such data event blocks were accumulated on the disk, they were written onto a 9-track magnetic tape. About 10,000 triggers were written per tape during a typical data run. These primary tapes were copied (with four events/block going to two events/block) onto secondary 9-track tapes, and the primary tapes were stored in a tape vault at FNAL. Only the secondary 9-track tapes were used for the later off-line data analysis. More detail about the CAMAC and on-line systems can be found in the thesis of Bob Ball.[7]

Besides writing data events onto tape, the on-line system was used to monitor the workings of the various detectors and stability

Table 2.9. Primary Tape Event Block Structure

A) Overview

Words	Content
1-15	I.D. block
16-87	Scalers
88-179	E319 PWC's
180-215	E398 PWC's
216-220	DCR's 1-5
221-228	TDC's
229-456	ADC's
457	DCR 6
458-464	Not used
465-761	TD's
762-768	Not used

B) Detail--I.D. Block

Word	Content
1	Operator name
2	Run number
3	Event number
4	Date = 1000·(YR-1970) + Day
5	Time--high order 16 bits
6	Time--low order 16 bits Time = ((60·HR) + MIN)·7200
7	Tape number
8	Beam energy
9	Unused
10	Type of target
11	Unused
12	Beam spill number
13-15	CAMAC error flags

C) Detail--Scalers

Word	Content
16	High order 8 bits, scaler 1
17	Low order 16 bits, scaler 1
⋮	
86	High order 8 bits, scaler 36
87	Low order 16 bits, scaler 36

Table 2.9. Continued

D) Detail--E319 PWC's

Words	Chamber-Module	Physical Location of Wire, Lowest Numbered Word, Bit 1
88-99	1-1	West-most
100-111	1-2	Top-most
112-121	2-3	West-most
122-131	2-4	West-most
132-137	3-5	East-most
138-143	3-6	West-most
144-149	3-7	West-most
150-155	4-8	Bottom-most
156-161	4-9	East-most
162-167	4-10	West-most
168-173	5-11	Top-most
174-179	5-12	East-most

E) Detail--E398 PWC's

Words	Chamber
180-185	1
186-191	2
192-197	3
198-203	4
204-209	5
210-215	6

Table 2.10 Scaler Averages for a Single Run

Scaler	Interpretation	Average per run
$B \cdot S \cdot \overline{BV}_{evg}$ + $B \cdot SD \cdot \overline{BV}_{evg}$ + $B \cdot P$	standard trigger	7838
BDERR	branch driver errors	111.6
$B \cdot \overline{BV}_{delay}$	effective incident flux	$7.831 \times 10^{7}\mu$'s
$B \cdot S \cdot \overline{BV}_{evg}$	single muon trigger	7383
$B \cdot SD \cdot \overline{BV}_{evg}$	dimuon trigger	865
$B \cdot P_{evg}$	pulser trigger	376.7
$\frac{B \cdot S \cdot \overline{BV}_{evg}}{B_{evg}}$	event rate	0.90536×10^{-4}
$HV \cdot S_{nv}/B_{spg}$	halo	102.53%
B_{spg}/SEM	μ / p yield	5.44×10^{-8}
B_{spg}/no. of spills	incident μ's per spill	0.50272×10^{6}
B_{evg}/B_{spg}	dead time	46.56%
$B_{spg}/B_{spg}(104)$	beam tune	68.38%
average flux x #targets/cm^2	average luminosity per run	2.0×10^{35} cm^{-2}

of various rates and ratios of rates (and hence the data) from run to run. Histograms of the total number of hits in the DCR's (trigger bank and beam veto counters, and beam hodoscopes) showed not only that all of the counters and logic modules were working, but also if the beam distribution had changed during running. Histograms of PC hits and tables of PC hit multiplicities showed potential PC problems quickly, such as dead bits, and amp/disc card or latch card problems. Fiducial and spark count tables, as well as hit multiplicity/wand tables for the spark chambers helped monitor these devices. ADC histograms for all counters and an equivalent particle histogram for the calorimeter was also available. This information was printed out on a line printer and saved for each run, to help spot problems that might arise in the off-line analysis (covered in Chapter III). As an independent check of the CAMAC scalers, the visual scaler readings in the muon lab were recorded in the log books for each run, to ensure that the flux measurements for the experiment were reliable.

CHAPTER III

DATA ANALYSIS

3.1 Data Summary

The main data and calibration runs for E319[1] took place between March and September of 1976. Altogether, there were 594 runs, which were written onto 372 9-track magnetic tapes (with $\sim$ 10,000 events/tape). Runs 163-172 were the positive hadron calorimeter runs with 2/3 of the iron target in place, runs 173-177 used the entire iron target. Runs 222-394 were the 270 GeV μ+ data runs (the data sample considered in this thesis), while runs 395-426 were 270 GeV μ+ data runs using the 1/3 density target. Runs 427-466 were the 150 GeV μ+ data runs (also with the 1/3 density target). The main spectrometer calibration runs (using the Chicago Cyclotron Magnet, CCM, located upstream of our experiment in the E98[2] apparatus) were runs 467-478. Runs 479-542 were the 270 GeV μ- data runs, with runs 543-566 being the second main set of calorimeter calibration runs (using both positive and negative incident hadron beams). Finally, runs 567-583 and 591-594 were runs with incident 120 and 150 GeV positive pion beams (instead of a muon beam) using the same trigger and apparatus geometry as our main data runs. This data was analyzed using the CDC 6500 at MSU and the CDC 6600 and CDC Cyber 175 systems at FNAL.

3.2 Reconstruction Program Overview

The reconstruction program (called MULTIMU, and used for both the final single muon and multimuon data analysis) had the job of reading the data tapes, finding beam tracks, incident muon energy, energy of hadron showers in the calorimeter and interaction vertex using ADC information, decoding and accumulating scaler information,

finding spectrometer tracks (beginning with the four chambers just downstream of the target) and tracing these tracks through the spectrometer or until they exited the side or entered the field free region of the iron toroid magnets. At that time, all track (beam and spectrometer) and ADC information was written out to a secondary tape; also written out was a file of run and event numbers of events considered likely multimuon candidates and the scaler totals for that run. This secondary tape output was later read by the spectrometer track momentum fitting routines (called GETP and GETP2), which did a five parameter χ^2 minimization to get 1/p, theta in the x-z plane, theta in the y-z plane, and x and y at the position of spark chamber eight. Provisions were made for pulling up to two sparks from a spectrometer track and refitting its momentum if the initial fit was deemed bad (i.e. χ^2/degree of freedom > 5) due to improper spark selection. This information was written onto another tape, which included the information from the secondary tape and the momentum fit (as well as which sparks, if any, were pulled). This tape was used to get the kinematics of the multimuon final state events, as well as for the DATA and Monte Carlo comparisons for the single muon analysis.

One of the most important numbers needed for any data analysis was the number of incident muons at the target face that could have led to an interaction (i.e. the flux, which is necessary to get absolute rates or cross sections). For our experiment this was $(B \cdot \overline{BV}_d)_{evg}$. This scaler was event gated since muons arriving during the 42 msec dead time after each trigger could not have led to a trigger. Since the event triggers contained $\overline{BV}$, accidental

pulses from these counters or two beam muons in the same R.F. bucket could veto a good event. This was corrected using a $\overline{BV}$ signal delayed three R.F. buckets (or $\sim$ 60 nsec). The raw flux for the 270 GeV μ+ data was 1.2834×10^{10} incident muons. In our analysis, only events with one good beam track and events which were not pulser triggers were analyzed. Also, events with the branch driver error flags (event block words 13-15) non zero were not analyzed. A branch driver error occured whenever one of the CAMAC modules could not be read out by the branch driver during data taking. To account for these triggers the total raw flux was multiplied by the ratio of useful triggers/total triggers, with useful triggers defined as: total triggers - branch driver errors - pulser triggers - triggers without one beam track. The corrected total flux for the 270 GeV μ+ main data run was 1.0974×10^{10} incident muons.

Input files necessary for the running of the data analysis program included the spark chamber fiducials (for each separate run), ADC pedestal and single muon peak values for all counters, the 1E4 magnet current, and the z-positions of the calorimeter counters.

3.3 Alignment of the Apparatus

Placing the various proportional and spark chambers in the beam line did not guarantee that their centers were on the spectrometer axis (defined as the center line through the spectrometer magnets). In order to use the chamber information, these chambers had to be aligned relative to each other and the spectrometer axis. The four downstream E319 PC's (PC 1-4) and the four upstream spark chambers (WSC 9-6) were aligned using a straight-thru muon run (run 130) with the target removed and the magnets degaussed, as shown in Figure 3.1. Picking hits in two chambers (in one of the four views), a straight

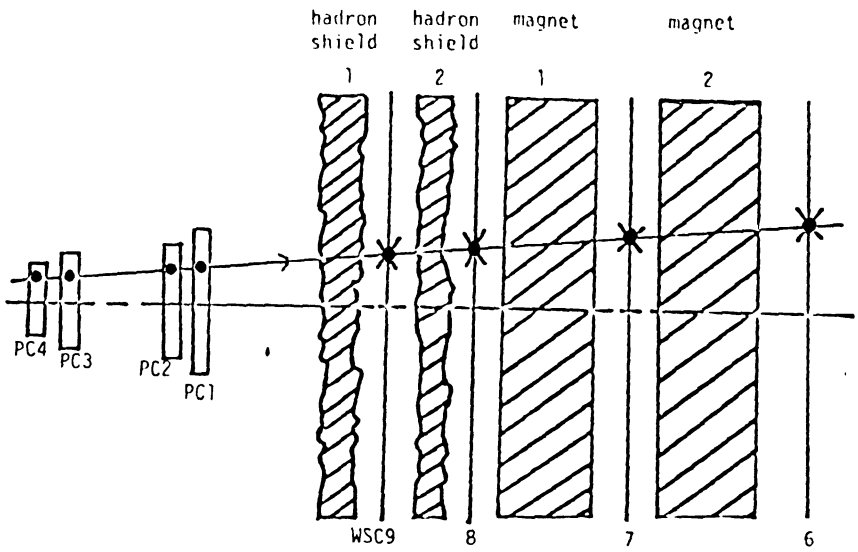

Figure 3.1 Aligning PC's and the front spark chambers

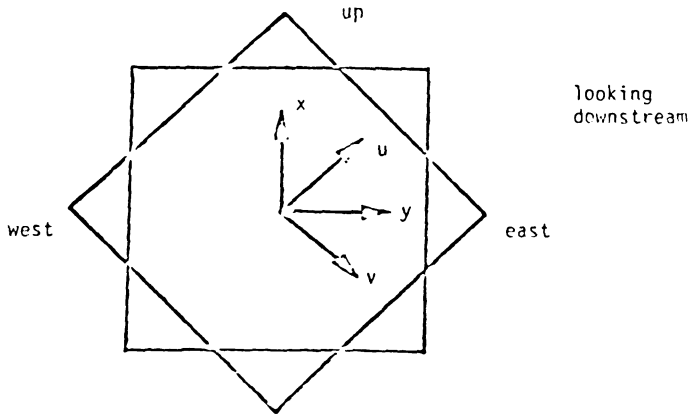

Figure 3.2 Spark Chamber Coordinate System

line was extrapolated through the remaining chambers and a histogram of actual hit minus predicted hit was produced. The mean of this histogram was subtracted from the actual hit coordinate for each chamber and the procedure was repeated until the change in alignment constants was less that 0.001 cm. This was done for each of the four views (X,Y,U, and V), shown in Figure 3.2. This procedure could not be used for the back five spark chambers, since their central regions had been deadened. Instead, runs 113-120 (with the magnets degaussed) were used, during which the muon beam was defocussed in enclosure 103 to spray muons over much of the aperture of the spectrometer. Using front lines in the upstream four spark chambers, histograms of actual hit minus predicted hit were obtained to get the alignment constants for the back five spark chambers in each view. This procedure was stopped when the alignment constants changed by less than 0.001 cm. Because of obstructing material in the beam line upstream of the target in the E98 apparatus, these runs could not be used to align PC5 at the entrance to the muon lab. For this purpose, a data run (run 363) was used, following the above procedure to get the alignment constants.

Once this was done, the chambers were aligned relative to each other (not necessarily with the spectrometer axis) in all four views, but the views did not agree on spark coordinates. The match distributions, defined by: $\Delta x_{match} = (u - v)/\sqrt{2} - x$ = x predicted -x actual, $\Delta y_{match} = (u + v)/\sqrt{2} - y$, $\Delta u_{match} = (x + y)/\sqrt{2} - u$, and $\Delta v_{match} = (y - x)/\sqrt{2} - v$, should have a mean of zero when histogrammed for the alignment runs but did not. This was accomplished by offsetting the x and y views in a linear manner in order to minimize the expression

$$\sum_{WSC,HPC} (\Delta x_{match})^2 + (\Delta y_{match})^2 + (\Delta u_{match} + \frac{az+b+cz+d}{\sqrt{2}})^2$$
$$+(\Delta v_{match} + \frac{az+b-cz-d}{\sqrt{2}})^2$$

with respect to a,b,c, and d. This gave the chamber offsets x shift = cz+d and y shift = az+b, where z was the chamber's z-position.

Next the chamber axis and spectrometer axis had to be aligned. For this purpose, the spectrometer magnets were turned on and a monoenergetic muon beam was deflected into the spectrometer. Dividing the face of the spectrometer into quadrants, the mean fit momentum of tracks through all four quadrants should agree (to within a few percent). The alignment constants were adjusted until this agreement was achieved and the average χ^2/degree of freedom for the momentum fit for each of the four quadrants was minimized. The final alignment constants are shown in Table 3.1.

3.4 Beam Track Reconstruction

Beam PC hits for each of the eight PC planes upstream of the target (96 wires/plane) were decoded from the 16-bit latch information and stored as spatial coordinates relative to the center of the PC plane (there were two UVW and one XY module in the muon lab used to define beam tracks). Up to 10 hits/plane were allowed. For clusters of hits (adjacent PC bits on), the average of the cluster was used as the hit coordinate. Next matches of three were looked for in the two UVW chambers. For UVW chambers, with the origin of the coordinate system at the center of the chamber, U+V+W=0 (allowing for chamber resolution). Taking all possible combinations of V and W hits (up to 10/plane) one at a time, hits were looked for in the U plane such that U+V+W<0.5 cm. If any were found, this was taken as a three point

Table 3.1 E319 Alignment Constants (in cm.)

Wands

	x	y	u	v
WSC 1	0.211	0.742	0.953	0.521
2	0.324	0.557	0.508	0.148
3	0.111	0.611	0.663	0.391
4	0.341	0.606	0.375	0.136
5	0.034	0.190	0.429	0.189
6	0.140	0.069	0.036	-0.142
7	-0.124	0.057	0.144	0.122
8	-0.020	0.206	0.255	0.316
9	-0.034	1.122	0.590	0.327

	x	y
E319PC 1	0.637	0.688
2	1.073	-0.115
3	0.438	0.324
4	-0.090	1.284
5	0.151	1.918

		y
E398 PC	1	0.0
	2	0.054
	3	0.476
	4	0.0
	5	-0.435
	6	0.0

match and was stored. The UVW coordinates were used to compute x and y for that match at that PC (alignment constants were then added). Up to 10 matches of three were allowed per UVW chamber. If no matches of three were found, all possible matches of two were looked for (up to 10/chamber) using all possible PC module combinations. For the XY chamber (PC5), each plane was decoded and stored as a spatial coordinate and as XY hits (with alignment constants added). If there were no two or three point matched hits in either of the UVW chambers, there can be no beam track (by our definition) and this event was skipped.

Beam tracks were looked for in a two cycle process. In the first cycle, tracks were looked for with all three chambers contributing (i.e. matches of 3-3-2, 3-3-1, 3-2-2, 3-2-1, 2-3-2, 2-3-1, 2-2-2, and 2-2-1). The second cycle picked up beam tracks where only the two UVW chambers contributed. For the first cycle, matched points in the two UVW chambers were projected in the x and y views (separately) to the XY module. If the slope of the projected line was >10mR or the extrapolated coordinate was the half width of PC5 + 2.5cm (an extrapolation window) this combination of matched points in the UVW chambers was skipped and the next set was looked at. If these cuts were passed, the PC hit closest to the extrapolated line in the x or y view was searched for (with a $\pm$ 2.5cm window cut being made). If a point passed the cut, we have a three chamber line in one view, which was saved as a beam track candidate (only three beam tracks were stored). Next two dimensional straight lines were fit through all lines found above in each view, using a linear least-squares algorithm with the resolution errors being taken as 0.1cm. If the fit failed, continue

with the next set of points in the UVW modules. For a line combination to have been accepted, the sum of the chi-squared of the fit for the x and y views must have been $\leq$ five and the fitted three dimensional beam angle must have been <10mR. Note that at this point, if there were two accepted beam tracks, this event was skipped, since we demand one and only one beam track for data events (which occurred for $\sim$ 90.4% of the 270 GeV μ+ data).

3.5 Beam Track Momentum

Using the E98 beam hodoscopes, the beam energy of the incident muon could be determined. Use of the E98 beam PC's will not be discussed, since these were not properly timed for the 270 GeV μ+ main data runs. First two of the three beam hodoscopes were decoded (only the downstream enclosure 103 y-hodoscope and the upstream enclosure 104 y-hodoscope were used). Given the beam track, the intercept and angle at the face of the enclosure 104 dipoles can be computed. Knowing the effective magnet length and magnetic field, all that was needed was one point in a hodoscope upstream of the enclosure 104 dipoles to determine the beam muon momentum. Order of preference for upstream beam information was: a) one hodoscope hit in BH1 and BH2, and b) one hodoscope hit in BH1 (downstream of enclosure 103). The geometry for the momentum measurement is shown in Figure 3.3.

Given the incoming angle, outgoing angle, effective magnet length, and radius of curvature of the track, it can be shown that[3]:

$$y_{disp} = \frac{\alpha}{p}\left(\frac{L}{2} + d\right) - \Theta\,(L + d) = \frac{\alpha}{p} A - \Theta\, C$$

where $\alpha = \Delta p_T$(in GeV/c) $= 0.03 \int B \cdot dl = 0.03\, B_{max}\, L_{eff}$, L = physical length of the magnet, d = distance between downstream end of the magnet and the y-measuring hodoscope, and Θ = angle of the track

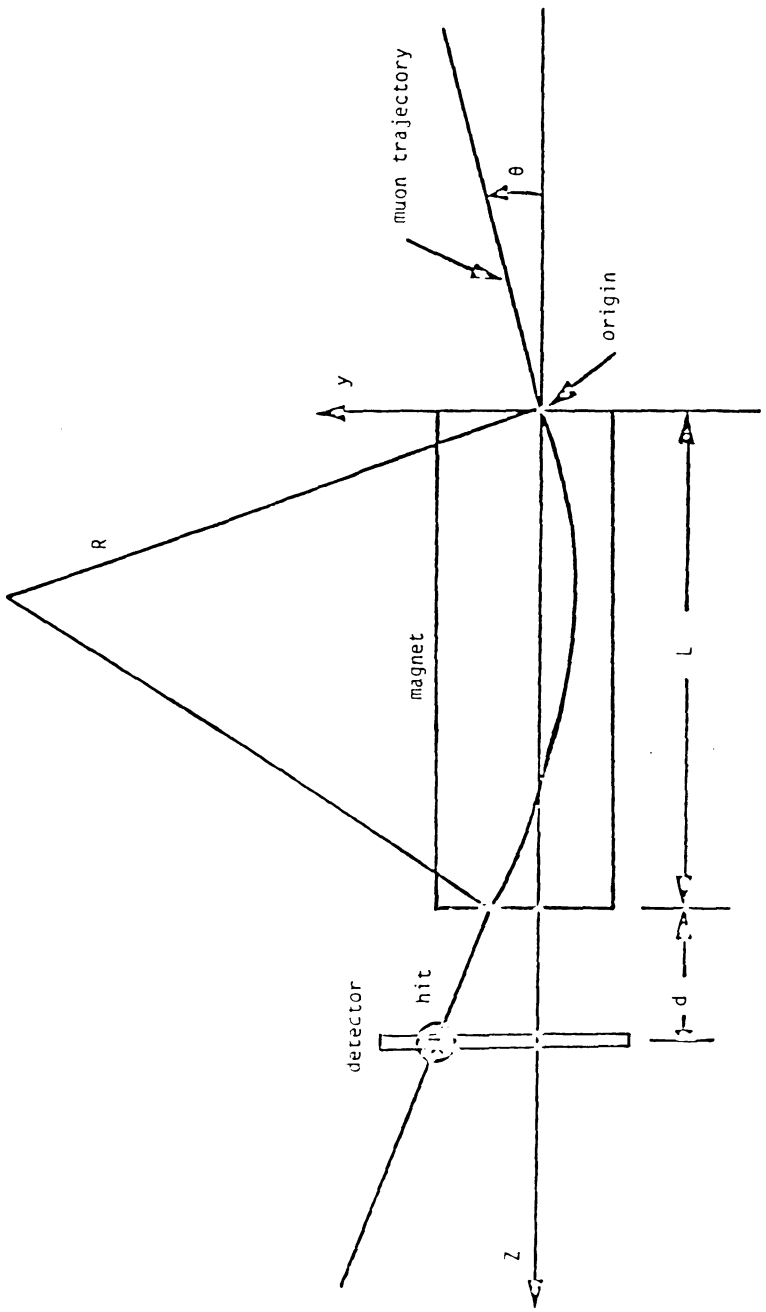

Figure 3.3 Geometry for Beam Momentum Fit

leaving the magnet.

For two hodoscopes, $y_1 = \alpha A_1/p - \theta C_1$ and $y_2 = \alpha A_2/p - \theta C_2$. Let y_1^m and y_2^m be measured hodoscope coordinates, and define a chi-squared for the track: $\chi^2 = (y_1 - y_1^m)^2/\sigma_1^2 + (y_2 - y_2^m)^2/\sigma_2^2$. Minimizing this chi-squared (i.e. set $\partial\chi^2/\partial(1/p)=0$) and solving for $1/p$ yields:

$$1/p = \frac{A_1 y_1^m + A_2 y_2^m + \theta(A_1 C_1 + A_2 C_2)}{A_1^2 + A_2^2} .$$

Similarly, for one available hodoscope upstream of enclosure 104, we obtain:

$$1/p = \frac{A_1 y_1^m + \theta A_1 C_1}{A_1^2} = \frac{y_1^m + \theta C_1}{A_1} .$$

If there was not enough information to determine the beam momentum, it was set to 270 GeV (this occurred for $\sim$ 6.5% of the 270 GeV μ+ data).

3.6 Calorimeter Analysis

First all raw ADC readings were converted into equivalent particles, defined as: number of equivalent particles = (ADC reading - pedestal)/(single muon peak-pedestal), for both the high and low gain ADC channels. All ADC channels were in order except channels 95 and 96 (counter 48), which belonged to counter zero at the front of the calorimeter. If there was a peak or pedestal problem for a run the number of equivalent particles was set to -1 for that counter. Raw ADC readings $\geq$ channel 1023 were set equal to 1024 (i.e. ADC overflow).

Next showers were looked for in the calorimeter (i.e. hadronic showers downstream of a deep-inelastic scatter) and the shower length (in counters) and beginning counter number for up to five showers was stored. A shower was defined as $\geq$ four consecutive counters (allowing for a lapse of one counter) with $\geq$ 15 equivalent particles/counter in

the high gain ADC channels. Finally, the last two counters were examined and if they had > 30 equivalent particles in them, a flag was set which indicated a "leaky" shower, but the event was not cut.

Next the hadronic energy deposited in each shower was determined and stored. The number of equivalent particles for each counter in a shower was summed, using the high gain channels, if unsaturated (raw ADC reading < channel 1023), and the low gain channels otherwise. This sum was then converted into an energy using a quadratic fit of the hadronic energy vs number of equivalent particles from the pion calibration runs (runs 173-177). The calibration obtained[4] was: energy (GeV) = 0.122 X 10^{-5} (eq part)^2 + 0.0517 (eq part) + 2.704 (χ^2/degree of freedom = 0.013 for 5 calibration points). Also, ZADC was defined as the average of the starting point of all of the showers present (up to five). To ensure that tails of showers were included in the showers, the two counters before and after the shower were included in the equivalent particle sum.

3.7 Spectrometer Track Reconstruction

A schematic of the track reconstruction program MULTIMU is shown in Figure 3.4. First the hadron PC's were decoded. The bits of the HPC latch information (192 bits per plane for the XY planes, 160 bits per plane for the UV planes upstream of the XY planes) were decoded and stored as real coordinates (relative to the center of the PC plane) with alignment constants added. Clusters of hits (adjacent bits on) were averaged over and the first 10 hits/plane were stored, plus an overflow bit was set for each plane with > 10 hits/plane.

Next the spark chamber time digitizers were decoded. Each of the nine spark chambers had four view (i.e. four wands), each view

```
Initialization
┌─ Read next trigger from tape
│  Decode and accumulate scalers
│  Decode discriminator latch bits
│  Front line finding procedure
│       Get beam muon track
│       Get WSC spark coordinates
│       Get hadron PWC spark positions
│       Find all possible 3-point lines in upstream four
│            chambers in all views, allow 20 lines per
│            view
│       Apply single-view line cuts
│       Demand good lines in minimum two views
│  Get muon beam track energy
│  Get hadron shower energy and vertex, if present
│  Match front lines from separate views
│     ┌─ Apply vertex cuts
│     │  Set up track tracing matrix
│     │  Trace to next downstream chamber and adjust
│     │       matrix.  Iterate through all remaining
│     │       chambers.
│     └─ Iterate for all track candidates
│        Apply quality cuts and eliminate duplicate tracks
│  Output acceptable tracks
└─ Iterate for all triggers until run end
   Print accumulated statistics
```

Figure 3.4. MULTIMU Program Organization

having up to eight scaler words. Non-zero scalers for each wand were looped through one at a time. If the scaler reading was within $\pm$ 15 counts of the first or second fiducial from the fiducial file, the scaler reading was used as the fiducial (first or second) for this wand for this event. If a first or second fiducial was not found amongst the scaler readings, the value from the fiducial file (average fiducial for this run) was used. All scaler readings below the first fiducial and above the second fiducial were rejected at this point. Next clusters of sparks were looked for. If adjacent sparks were closer than 10 counts, they were considered part of a cluster of sparks and were averaged together. Scaler values were then converted to real coordinates (relative to the center of the spark chambers) using the fiducials, and alignment constants were then added, giving coordinates relative to the spectrometer axis. Up to eight hits/view were stored, along with the number of sparks in each view.

Next front lines were looked for, view by view, in each of the four views. For this purpose, the hadron PC's were treated as one chamber with four views. Since the front chambers were not all 100% efficient (in fact WSC8 XY did not work for most of the experiment) and since the HPC's could be swamped by a hadron shower leaking from the end of the target, the HPC's, WSC9, 8, and 7 were used to look for front lines, even though WSC7 was behind one magnet and would not give a strictly straight line. Front lines of three sparks each were looked for in the HPC's and WSC9, 8, and 7. There were four possible combinations: Type 1 = HPC, 9, 7; Type 2 = 9, 8, 7; Type 3 = HPC, 8, 7; and Type 4 = HPC, 9, 8. If an HPC plane had > 10 hits, then only type 2 lines were used for this view. All types of possible

tracks were looped over, skipping any types which had one of the three modules with zero hits in that view.

After picking a spark in the most upstream chamber and another in the next downstream chamber, the expected coordinate in the third chamber was predicted by extrapolating a straight line using the upstream two sparks. Then a window for spark search was formed in the third chamber. The form of this window was: WIN = 0.0005 ABS $(PRED)^2$ + 0.165 ABS(PRED) + 0.5, and WIN = 10cm if 50cm < ABS(PRED) < 75cm, WIN = 20cm if ABS(PRED) > 75cm. The form of this window was determined by looking at dimuon events found by an earlier, less restrictive front line finding program called PASSI (the first stage in the development of MULTIMU). The main reason this was necessary was that when WSC7 was used as the downstream chamber, low energy tracks bent sufficiently that front lines were not found very efficiently, unless we made use of the fact that low energy tracks are usually at fairly high radii in the front chambers used in forming this window. Looping over all sparks in the third chamber, a window was formed as spark $\pm$ WIN. If the predicted hit was within this range, a front line had been found. For all "front lines" (up to a maximum of 50) the spark positions were stored and the fit slope and intercept at z=0 was calculated (for front lines using WSC7, only the two upstream sparks were used for line fitting; for type 4 lines, all three upstream sparks were used for line fitting in this view).

Each fit front line then had to pass a set of cuts. Its slope must have been less than 234mR (maximum angle to pass through WSC7 for a track originating at the end of the target). Fitted lines must have been within the target area in at least one of three places, at

the front, middle, or back of the target (i.e. | coordinate | < 25.4cm for XY, < 35.9cm for UV at one of the above mentioned z positions). The two dimensional z-intercept of the extrapolated beam track and the front line (i.e. ZVERTEX) must lie in the vicinity of the target, the cut made was: -2500cm < ZVERTEX < 2500cm. For type 2 lines (WSC 9, 8, 7) with < 10 hits in the HPC's (i.e. no overflows), an additional cut was made. If the extrapolated line passed through the active area of the HPC, it was demanded that a PC hit existed within $\pm$ 1cm. If not, this front line was cut.

For each view, if more than one front line existed, a search was done to look for and eliminate duplicate lines. A double loop was done over all front line combinations, comparing slopes and intercepts. If the slope difference was $\leq$0.0005 or the intercept difference was $\leq$ 0.5cm, the lines were considered to be duplicates and one was eliminated. Type 4 lines were preferentially kept first, after which the preferred order was type 1, type 2, and type 3. For the event analysis to continue, $\geq$ two views must have had at least one front line each.

Once front lines were found, the second main part of MULTIMU began, track finding in the spark chambers. Matches of two of the four possible front line views (i.e. six combinations in all; U-V, Y-V, X-V, Y-U, X-U, and X-Y) were looked for and for each good two-view match, tracks were searched for in the spectrometer (back seven chambers) with up to 10 good spectrometer tracks allowed. A loop was done over all match types (with at least one front line in each of the two views), then a dual loop over all lines to be matched in the two views looked at. For each matched three dimensional front line, ZMIN and DMIN cuts were made. Given the slopes and intercepts

(at z=0) of the beam track and current front track, the distance of closest approach (DMIN) and z position at which this occurred (ZMIN) were calculated.[5] These two tracks were not expected to intercept (at least in three dimensions) due to multiple scattering in the seven meter long iron target. It was demanded that ZMIN (interaction vertex found using beam and spectrometer tracks) was between -250cm and +600cm for the current front track. For dimuon events, a simple DMIN cut was found to lose too many low E', high angle tracks (probably because multiple scattering was a larger effect for low energies), so the DMIN cut made was a linear function of the radius (at WSC8), DMIN $\leq$ MIN ($0.15R_8$(cm) + 2.0cm; 10cm). Also, if ZADC existed for this event, it was required that | ZADC - ZMIN | $\leq$ 400cm.

Given the slopes and intercepts of the front three dimensional track (at WSC8), the problem was to trace the track through the spectrometer, accounting for bending in the magnets, and muon energy loss and multiple scattering in the iron toroids, and to predict and find sparks in the back seven spark chambers. Simple rectangular windows were formed in each chamber about the predicted spark position (the size of which was determined by multiple scattering and measurement errors in all upstream magnets and chambers) for each view, and sparks were searched for. Sparks found this way for each view were matched to form three dimensional points (with a match window of 1.2cm). The multiple scattering in the toroids caused correlated deviations (due to the magnetic fields), so it was convenient to form a smaller, hourglass shaped window cut, which increased the probability of finding and matching correct sparks and decreased the spark search area. Further spark searching was terminated if the predicted spark position

exceeded the magnet radius, the track crossed the spectrometer axis, or if two consecutive chambers had no sparks. If many matched sparks were found, the spark closest to the predicted position was kept. Once matched points were found for chambers downstream of a magnet, an estimate of the tracks momentum was made using a simple chi-squared minimization (similar to the simple method used to get an initial momentum guess for the main momentum fitting algorithm, to be described later) assuming the bending in a magnet took place at its center (the "impulse" approximation). This momentum estimate was then used to obtain the predicted spark position in the next downstream chamber.

At this point, further cuts were imposed to eliminate bad tracks. These included a chi-squared cut (to minimize the difference between predicted and actual spark position), a number of degrees of freedom cut, a DMIN cut, a cut on the average match code for sparks in the back seven spark chambers (which helped to eliminate halo and improperly matched track segments), and a cut to ensure that the track was outside the magnet holes (i.e. $r > 15.24$cm) at least for one chamber in the spectrometer. A summary of all cuts made can be found in Tables 3.2 - 3.5.

To eliminate duplicate tracks (i.e. tracks with x and y positions within two mm at half of the chambers) another empirically developed cut was made. Now that all identical tracks were eliminated, each track was written to an output tape whose format is given in Table 3.6. Further information on the track finding algorithm for the spectrometer tracks and the hourglass window cut can be found in the thesis of Dan Bauer.[6]

Table 3.2. Acceptable Three-Point Line Types

Type	Included Chambers
1	HPC,WSC9,WSC7
2	WSC9,WSC8,WSC7
3	HPC,WSC8,WSC7
4	HPC,WSC9,WSC8

HPC = Hadron Proportional Wire Chamber

Table 3.3. Single-View Line Cuts

Cut	Description
1	Line slope less than 234 mRad
2	Extrapolated line within target bounds at one of upstream edge, middle, or downstream edge
3	Intersection with beam track line (projected) within -2500 cm $< z < 2500$ cm

Table 3.4. Vertex Cuts

Cut	Description
1	Z position of minimum separation from beam track (ZMIN) within $-250 < z < 600$ cm
2	Minimum separation from beam track (DMIN) less than $0.15 \cdot R + 2.0$; R is track radius at WSC8
3	ZADC = z-position of hadron shower $\lvert$ZADC-ZMIN$\rvert$ < 400 cm (when shower present)

Table 3.5. Track Quality Standards

Standard	Description
1	Average chamber match code* greater than 2.80
2	Track outside of toroid hole region at a minimum of one chamber
3	One parameter+ χ^2/degree of freedom less than 10.0

+This is a primitive χ^2 fit to 1/E' based on equal weights for all chambers.

*Each chamber is assigned a match code on the basis of which module views contribute to the spark position for the track. The match codes are summed and divided by the number of contributing chambers to get the average for the track. Match codes are assigned as follows:

Contributing Chambers	Match Code	Contributing Chambers	Match Code
XYUV	4.0	XY	2.5
XY V	3.8	X U	2.4
XYU	3.6	YU	2.3
YUV	3.4	X V	2.2
X UV	3.2	Y V	2.1
		UV	2.0

Table 3.6. MULTIMU Output Tape Format

Words	150 Words/Track Content
1	100,000·Run# + Event# (I)
2	Track# (1 to 10) (I)
3	Value of scaler $B \cdot \overline{BV}_d$(EVG) (I)
4	Found x-coord. PWC5
5	Found x-coord. PWC4
6	Found x-coord. PWC3
7	0.0
8	Found x-coord. HPC
9	Found x-coord. WSC9
⋮	⋮
17	Found x-coord. WSC1
18	Same as words 4-17, except for y-coords.
⋮	⋮
31	
32	Match Code PWC5
33	Match Code PWC4
34	Match Code PWC3
35	0.0
36	Match Code HPC
37	Match Code WSC9
⋮	⋮
45	Match Code WSC1
46	0.0
⋮	⋮
53	0.0
54	X-component of beam momentum E_o
55	Y-component of beam momentum E_o
56	Z-component of beam momentum E_o
57	Extrapolated x-position of beam track at z = 0
58	Extrapolated y-position of beam track at z = 0

Table 3.6. Continued

Word	Content
59	x-component scattered muon momentum guess (E')
60	y-component scattered muon momentum guess (E')
61	z-component scattered muon momentum guess (E')
62	Extrapolated x-position of scattered muon track at z = 0
63	Extrapolated y-position of scattered muon track at z = 0
64	One parameter χ^2
65	Degrees of freedom
66	ZADC
67	Shower energy
Words 68 - 71 measured at WSC8	
68	Angle from z-axis in x-z plane
69	Angle from z-axis in y-z plane
70	x-position
71	y-position
72	E' guess
73	θ guess
74	Packed word with number of HPC wires hit in each plane (I)
75	Packed word with total number of WSC sparks for each chamber (I)
76	Packed word with truncated match codes from PWC's 5-3 and HPC (I)
77	Number of spectrometer tracks this event (I)
78	Number of beam muon tracks (I)
79	DCR1 contents (I)
80	DCR2 contents (I)
81	DCR3 contents (I)
82	DCR4 contents (I)
83	DCR6 contents (I)

Table 3.6. Continued

Word	Content
84	Average Match Code
85	DMIN guess
86	ZMIN guess
87	Packed number of accepted lines/view (I)
88	Packed number of found lines/view (I)
89	8 - J or 0 [Track leaves spectrometer at WSCJ] (I)
90	Packed, truncated match codes from WSC1-9 (I)
91-150	Packed ADC counts (I)

(I) Indicates integer value; otherwise stored as floating point value.

The single muon track finding efficiency of MULTIMU was checked by a comparison with an independent reconstruction program called VOREP.[7] A visual scan study[8] was made of events missed by one program and found by the other for low q^2 ($\leq$ 8 GeV^2/c^2) and high q^2 ($\geq$ 40 GeV^2/c^2) regions. The inefficiency of MULTIMU was found to be < 10% except at very high q^2 (due to tracks missing the HPC's and/or low front spark chamber efficiencies). A second check was done using a very efficient version of MULTIMU called PASSOUT, which used combinations of two (instead of three) front chambers to get front lines, allowed more track combinations, and had less restrictive cuts. PASSOUT was run on 28 data tapes (only for the events MULTIMU missed) which yielded 3820 extra events (or $\sim$ 7% more than from MULTIMU). The shape of the ratio (PASSOUT - MULTIMU)/MULTIMU is shown in Figures 3.5 - 3.6.

3.8 Spectrometer Track Momentum Fitting

What was desired from the momentum fitting routines were the best values of p and Θ for the spectrometer track given. This was done by defining a chi-squared and minimizing it with respect to five parameters (1/p, Θ_{x-z}, Θ_{y-z}, x, and y at WSC8). In order to define a chi-squared, a knowledge of the fitted spark positions was needed, i.e. given the momentum obtained and initial $\Theta_{x,y}$ and x, y values at WSC8, we wanted to be able to predict the spark positions in the downstream WSC's. This was done using the ZZ array (described later). Given these ZZ's, a chi-squared was defined, which when minimized, gave the best possible values of the five desired parameters. The usual definition of chi-squared, $\sum (\delta x_i^2/\sigma_i^2 + \delta y_i^2/\sigma_i^2)$ ignored the fact that downstream in the spectrometer, multiple scattering and energy loss in the iron

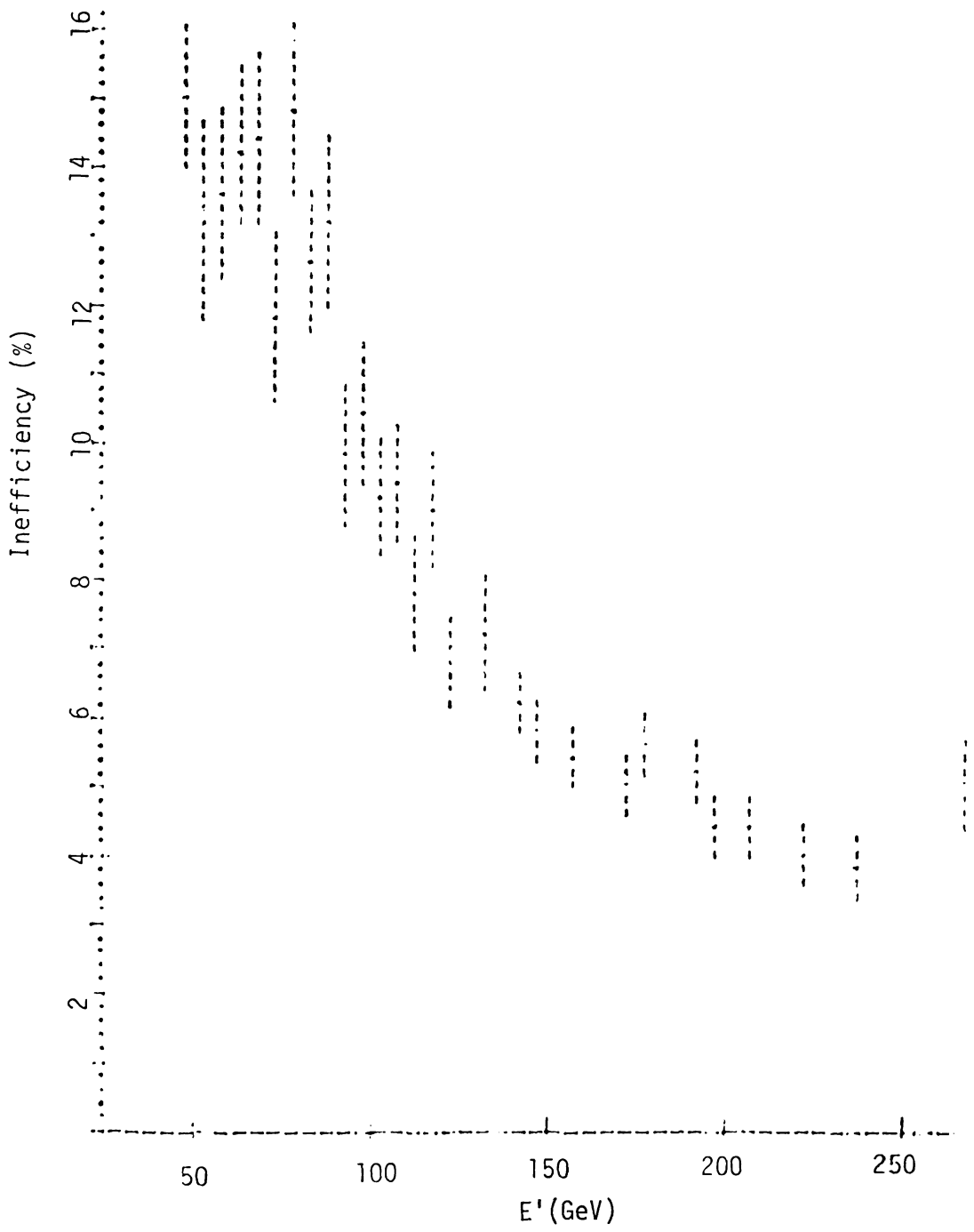

Figure 3.5 Reconstruction Inefficiency vs Energy

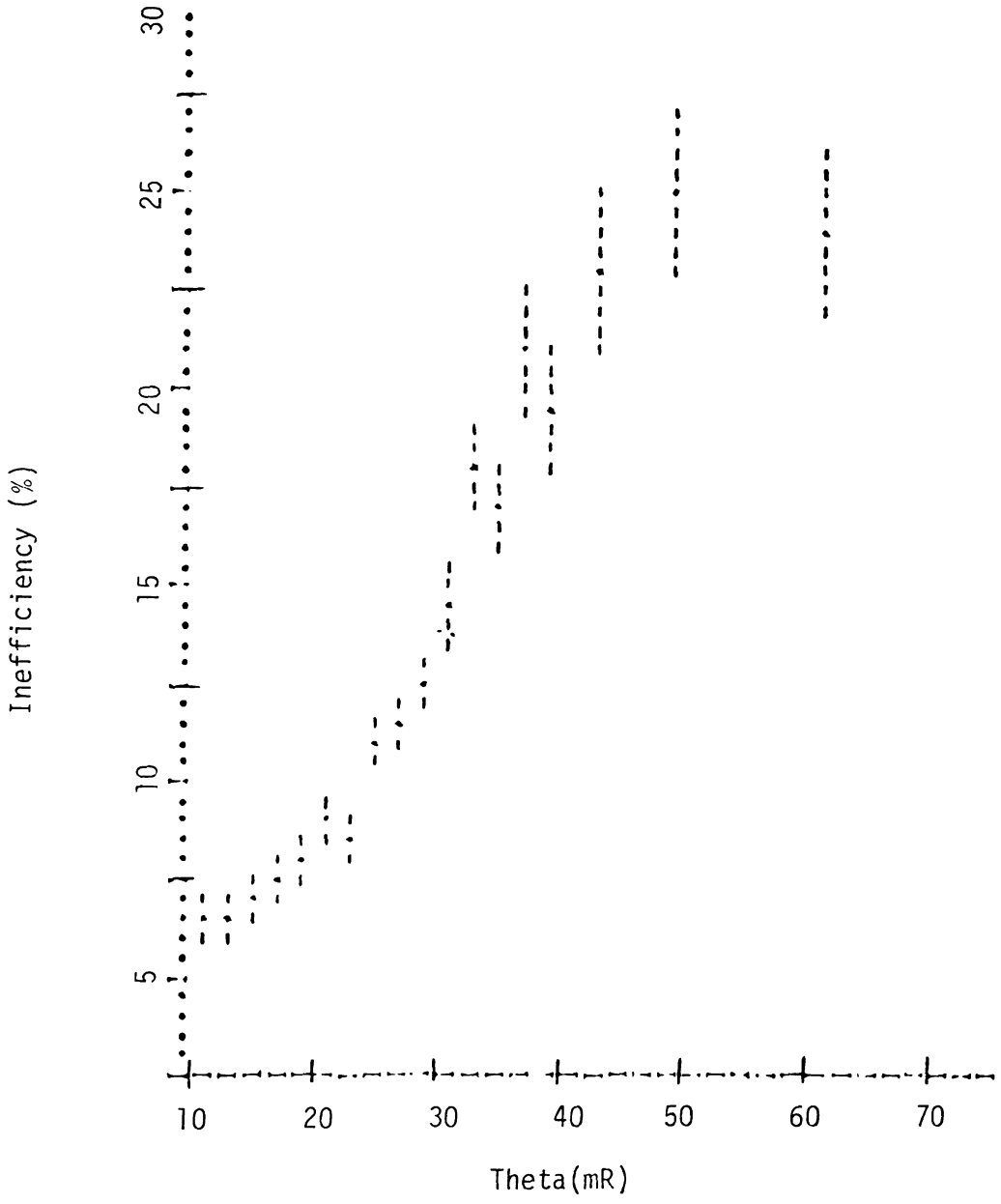

Figure 3.6 Reconstruction Inefficiency vs Theta

toroids made the spark deviations larger, also a multiple scattering upstream caused a larger deviation in the downstream WSC's (i.e. deviations in the WSC's were correlated).

Each magnet the muon traversed gave it a P_T kick of 0.03 $\int$ Bdl (p in GeV/c, B in kGauss, l in meters). Using the impulse approximation (make all of the bending take place at the center of a magnet) and starting at the front of the spectrometer (at known x, y, Θ_x, Θ_y) with knowledge of the z-positions of all magnets and chambers, and the magnetic field, spark positions could be predicted at each chamber. However, there was multiple scattering and the magnetic field depended on x and y, which complicated the situation.

Instead, a power series expansion for the spark coordinates was made in powers of 1/p from an infinite momentum track. Let $x = c_0 + c_1k + c_2k^2$ and $x' = c_0' + c_1'k + c_2'k^2$, where $k = e\,B_o/(3335.64p)$, and set up similar equations for y and y'. To be determined were the values c_0, c_1, c_2, c_0', c_1', and c_2' (the elements of the ZZ array).

For a muon traversing a magnet (traveling into the page for Figure 3.7) $\Delta\vec{p}$ (GeV/c) = 0.03 $\Delta\vec{L}$ (meters) x $\vec{B}$ (kGauss), which for $B_z = 0$ (azimuthal B field) gives: $\Delta p_x = 0.03\,(-L\,B_y)$ and $\Delta p_y = 0.03\,(L\,B_x)$, where L is the thickness of a magnet. The changes in slope were:

$$\Delta x' = \Delta p_x/p = (-0.03\ LB\cos\phi)/p = -f(r)kL\cos\phi \text{ and}$$

$$\Delta y' = \Delta p_y/p = (0.03\ LB(-\sin\phi))/p = -f(r)kL\sin\phi.$$

If we now expand in a Taylor series about r_0, k_0, and ϕ_0 (the values of r, k, and ϕ for the infinite momentum track), we get:

$$-\Delta x'/L = kf(r)\cos\phi = kf(r_0)\cos\phi_0 + f(r_0)\cos\phi_0\,(\partial k/\partial p)\Delta p + kf'(r_0)\cos\phi_0\Delta r + kf(r_0)\,\Delta(\cos\phi)\big|_{\phi=\phi_0} + \ldots$$

After some algebra, it can be shown that:[9]

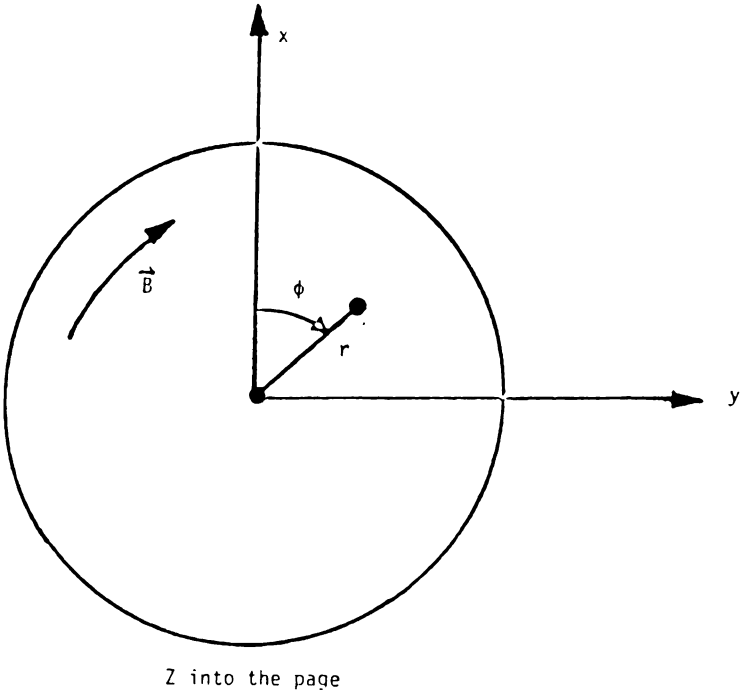

Figure 3.7 Geometry of Spectrometer Magnet Bends

$$\Delta r = r - r_0 = k(x_0\, x_1 + y_0\, y_1)/r_0 \equiv k r_1,\ \Delta(\cos\phi) = k(x_1/r_0 - x_0 r_1/r_0^2) \equiv k \sin\phi_0;\ \text{and so}$$

$$-\Delta x'/L = kf(r_0)\cos\phi_0 + k^2(f'(r_0)\, r_1 \cos\phi_1 + f(r_0)\sin\phi_1 + f(r_0)\cos\phi_0(-\Delta p/\alpha)),$$

where $r_0 = (x_0^2 + y_0^2)^{\frac{1}{2}}$, $\sin\phi_0 = x_0/r_0$, $\cos\phi_0 = y_0/r_0$, $\sin\phi_1 = (x_1 r_0 - x_0 r_1)/r_0^2$, $\cos\phi_1 = (y_1 r_0 - y_0 r_1)/r_0^2$, and $\alpha = eB/3335.64$.

Using these equations, the change in x-slope caused by a magnet was calculated (similarly for y). So starting at the front of the spectrometer, we can calculate the change in slope (and also position) as the track traversed the spectrometer. This information was used to define the ZZ array, where:

$$X(\text{at } WSC_i) = ZZ(i,1,1) + k\, ZZ(i,1,2) + k^2\, ZZ(i,1,3)$$
$$Y(\text{at } WSC_i) = ZZ(i,2,1) + k\, ZZ(i,2,2) + k^2\, ZZ(i,2,3).$$

So given p (and hence k), spark positions in all spectrometer chambers could be predicted.

The chi-squared used was defined by:

$$\chi^2 = \sum_{\substack{i,j \\ i<j}} Y_{ij}^{-1}\ (\delta x_i \delta x_j + \delta y_i \delta y_j)$$

where δx_i was the residual at chamber i and Y_{ij} was the error matrix, i.e. it took into account the correlations in the chambers due to multiple scattering as well as the measurement error of each chamber. The measurement error at z due to a magnet at ξ was: $\Delta x|_z = \theta_{ms}(z - \xi)$, where $\theta_{ms} = (\theta_{ms}^2)^{\frac{1}{2}} \simeq (0.015/p)(L/1.77)^{\frac{1}{2}}$ for iron, L being the length of the magnet in cm and p was in GeV/c. A typical error term looked like:

$$\Delta x_i \Delta x_j = (\theta_{ms})_i\ (z_i - \xi)(\theta_{ms})_j (z_j - \xi).$$

The full Y_{ij} contained a summation over all magnets upstream of both the i and j chambers. Also, for i=j, the spark chamber resolution σ_i must be included. Assuming that the energy loss in a magnet was small (so that the same 1/p could be used for all θ_{ms}), we can take θ_{ms} out of the summation to get:

$$Y_{ij} = \theta_{ms}^2 \sum_m (z_i - \xi_m)(z_j - \xi_m) + \delta_{ij}\sigma_i^2$$

with $z_i > \xi_m$ and $z_j > \xi_m$

$$\theta_{ms}^2 = (0.014/p)^2 \, (L/1.77) \, (1 + 1/9 \log (L/1.77))$$

$$= 1.228 \times 10^{-2}/p^2 \text{ for one magnet (78.74cm)}$$

and σ_i = 0.1cm for the spectrometer spark chambers.

Since $Y_{ij} = \langle \delta x_i \delta x_j \rangle$, we expect the chi-squared per degree of freedom to be about one. This was the chi-squared used for the back seven spark chambers (called χ^2 back).

For the HPC's and WSC9 and 8, chi-squared was defined as:

$$\chi^2_{\text{front}} = \sum_{\text{HPC,9,8}} \frac{\delta x_i^2 + \delta y_i^2}{\sigma_f^2 + \text{extra term}}$$

σ_f was 0.2 cm, and the extra term was due to multiple scattering in the hadron shields, and was equal to $(3.575\text{cm}/p)^2$ for WSC9 (muon traversed one hadron shield) and $(15.282\text{cm}/p)^2$ for WSC8 (muon traversed both hadron shields and the gap between them), and where $\delta x_i = x_{act} - x_{pred} = x_{act} - (\theta_x z + x_0)$.

At this point, we have a way of getting the predicted coordinates in the front chambers (straight line fit using θ_x, θ_y, x, and y at WSC8 to get coordinates at HPC, WSC9 and 8) and the back seven chambers (using the ZZ array and p). We also have a chi-squared,

which, when minimized, will give us the five parameters we seek (1/p, Θ_x, Θ_y, x, and y at WSC8).

Fitting was done by the programs GETP and GETP2 (which were modified versions of the E26 fitting program called FINAL,[10] see Figure 3.8). First the ZZ array was set up using a momentum guess of $E_0/2$ (i.e. 135 GeV) in subroutine TRACE. Using these ZZ's, the predicted sparks in the back chambers were used (in subroutine MINRC) to find a better guess of p by minimizing a one parameter chi-squared which was only a function of 1/p (MULTIMU guesses for Θ_x, Θ_y, x, and y at WSC8 were used, since these should be fairly accurate). The chi-squared was defined as: $\sum (x_{act} - x_{pred})^2 + (y_{act} - y_{pred})^2$, and minimizing this gave a momentum value which was usually within 10-20% of the final momentum value obtained by minimizing the multi-parameter chi-squared. If $|p| > 400$ GeV, it was set to 400 GeV. TRACE was called again with the new momentum guess, setting up new ZZ's and predicted spark positions. MINRC was called again and a new momentum guess obtained, minimizing the same one parameter chi-squared. If $|p| > 400$ GeV, it was set equal to 400 GeV. Also, if the momentum guess was < 50 GeV, it was multiplied by 1.25, since earlier analysis showed that the chi-squared minimization had troubles if the initial guess fell on the lower side of the chi-squared curve (especially for low momentum tracks). Subroutine CORR set up the Y_{ij} array and inverted it to get Y_{ij}^{-1}. Next PFIT was called, which controlled the actual multiparameter chi-squared fit. CHIOV computed the chi-squared from Y_{ij}^{-1} and ZZ arrays set up before entry into PFIT. Total $\chi^2 = \chi^2_{front} + \chi^2_{back}$ and number of degrees of freedom, NDOF = $NDOF_{front}$ (2x number of front chambers) + $NDOF_{back}$ (2x number of

Initialize

Read next event

First order guess at E'

Guess E' = pc = $1/E_o$ and set up matrix ZZ to give fit track positions at all chambers

One parameter χ^2 fit to guess a better p

Adjust ZZ matrix for new p

Verify p is in reasonable range of values

Set up error matrix YY and invert it

Determine an accurate E'

Calculate χ^2 using YY^{-1}

Set up partial derivatives of χ^2 with respect to five fit parameters to get matrices XX (first derivatives) and ZX (second derivatives). Solve matrix equation XX = ZX·ΔAP for ΔAP which are the changes to be made to five fit parameters.

Adjust ZZ matrix

Determine error matrix YY; invert it and find χ^2

Iterate until p changes by less than 1% between steps

If necessary (χ^2/degree of freedom >5) pull spark to get best improvement of χ^2

Write track to output tape

Iterate for all tracks until run ends

Figure 3.8. GETP and GETP2 Program Organization

back chambers) - 5(number of parameters in the fit). Next CDXB was called, which calculated the changes in the five parameters (1/p, Θ_x, Θ_y, x, and y at WSC8) which would minimize the above chi-squared.

If we expand χ^2 about its minimum (i.e. RC = RC_0, $\Theta_x = \Theta_{x0}$,...) we have:

$$\chi^2\ (RC,\ \Theta_x,\ \Theta_y,\ x,\ y) = \chi^2\ (RC_0,\ \theta_{x0},\ \theta_{y0},\ x_0,\ y_0) +$$

$$\frac{\partial\chi^2}{\partial RC}\,\Delta RC + \frac{\partial\chi^2}{\partial\Theta_x}\,\Delta\Theta_x + \frac{\partial\chi^2}{\partial\Theta_y}\,\Delta\Theta_y + \frac{\partial\chi^2}{\partial x}\,\Delta x + \frac{\partial\chi^2}{\partial y}\,\Delta y\ .$$

At the minimum, $\partial\chi^2\ (RC_0,\ \Theta_{x0},\ \Theta_{y0},\ldots)/\partial RC = 0$, and similarly for the partial derivatives with respect to Θ_x, Θ_y, x, and y. Taking partial derivatives of the above equation, we get the set of equations:

$$\frac{\partial\chi^2}{\partial RC} = \frac{\partial^2\chi^2}{\partial RC^2}\,\Delta RC + \frac{\partial^2\chi^2}{\partial RC\partial\Theta_x}\Delta\Theta_x + \ldots + \frac{\partial^2\chi^2}{\partial RC\partial y}\Delta y$$

and similar equations for the other four partial derivatives, which gives the matrix equation:

$$\begin{bmatrix} \frac{\partial\chi^2}{\partial RC} \\ \frac{\partial\chi^2}{\partial\Theta_x} \\ \frac{\partial\chi^2}{\partial\Theta_y} \\ \frac{\partial\chi^2}{\partial x} \\ \frac{\partial\chi^2}{\partial y} \end{bmatrix} = \begin{bmatrix} \frac{\partial^2\chi^2}{\partial RC^2} & \frac{\partial^2\chi^2}{\partial RC\partial\Theta_x} & \cdots \\ \frac{\partial^2\chi^2}{\partial RC\partial\Theta_x} & \frac{\partial^2\chi^2}{\partial\Theta_x^2} & \\ \vdots & & \ddots \end{bmatrix} \begin{bmatrix} \Delta RC \\ \Delta\Theta_x \\ \Delta\Theta_y \\ \Delta x \\ \Delta y \end{bmatrix}$$

or (XX) = (ZX)(DEL).

What was wanted were the deltas (i.e. the changes of the five parameters necessary to minimize χ^2), which were gotten as (DEL) = $(ZX^{-1})(XX)$. CDXB calculated the deltas, and added these to the old values of RC, Θ_x, Θ_y, x, and y to get the new values. Next TRACE was called to set up the new ZZ's and CORR to set up the new Y_{ij}^{-1}, with the new values of the five parameters. If Δp was < 1%,

the final χ^2 was computed and the fit stopped. Otherwise, CDXB, TRACE, and CORR were called again, and Δp was again checked. This loop could be gone through up to five times, but usually only two or three times were necessary. Once $\Delta p < 1\%$, the final χ^2 and NDOF were calculated and PFIT was exited. Finally, the muon's energy loss[11] in the hadron shields was added to the fit momentum, giving the muon's momentum at the end of the target.

So far it has been assumed that all of the sparks fed to the fitting routines were the correct sparks (this was true most of the time). However, the track finding routines occasionally found a bad spark which made the χ^2 of the fit large, and which made the fitted momentum and angle values suspect. Since it took a lot of computer time to find the correct spark each time (especially when there were lots of extra sparks in the WSC's), it was decided an easier solution was to shut off sparks if a bad χ^2 was obtained during momentum fitting. A few different algorithms were tried, but the best, and most reliable method found, was to remove sparks from the fit, one at a time, and keep track of the fit with the best χ^2, this one being chosen as the fitted track. Spark pulling was skipped (the first time) if: the $\chi^2/DOF < 10$ and $DOF \leq 7$, $\chi^2/DOF < 5$, or if only one spark in the spectrometer. If a spark was pulled, all of the fit information was stored into the output block (see Table 3.7) and the number of the chamber shut off was loaded into word 73 of the output block (this word was zeroed at the start of fitting).

Next, a check was made to see if the momentum fit worked. The fit failed if: $p = 39.147$ (p was set to 30 GeV if no one-parameter χ^2 minimum was found, this was multiplied by 1.25 and the energy loss

Table 3.7. GETP and GETP2 Output Tape Format

Words	150 Words/Track Content
1	Same as for MULTIMU
⋮	⋮
31	
32	0.0
33	Fitted x-coordinate HPC
34	Fitted x-coord. WSC9
⋮	⋮
42	Fitted x-coord. WSC1
43	Same as words 32-42 for y coords.
⋮	⋮
53	Word 46 set = -1024.0 if track is not fit
54	Same as for MULTIMU
⋮	
58	
59	x-component of scattered muon momentum E' from the fit
60	y-component of E'
61	z-component of E'
62	Extrapolated x-position of scattered muon track at z = 0
63	Extrapolated y-position of scattered muon track at z = 0
64	χ^2 of the momentum fit
65	Degrees of freedom
66	ZADC
67	Shower Energy
68	θ_x, angle of scattered muon track from z-axis in x-z plane
69	θ_y, same as word 68 for y-z plane
70	Same as word 62
71	Same as word 63

Table 3.7. Continued

Words	Content
72	Chamber shut off by GETP2 or zero
73	Chamber shut off by GETP or zero

Value in words 72 and 73 is 16-J where WSCJ or HPC (J=10) is turned off

74	Same as for MULTIMU
⋮	⋮
150	

in the hadron shields was added in), $p > 500$ GeV, or NDOF < 1. If the fit failed, output block words 46 and 73 were set to -1024.

It was possible to get two bad sparks in a track (we never observed a track with three bad sparks). If the first fit had not failed (as defined above) and χ^2/DOF > 10, then the entire fitting routine was run again (after having shut off any spark pulled the first time) and each spark left was pulled one at a time. If a spark was pulled the second time, the number of the chamber turned off was written into word 72 of the output block (which was zeroed before the program was run).

It was assumed that the angle of the spectrometer track at WSC8 was the same as at the end of the target, i.e. the effect of multiple scattering due to the hadron shields was small.

3.9 Spectrometer Momentum Calibration

The momentum fitting algorithms were calibrated using two methods, the first entailed using the Chicago Cyclotron Magnet (part of the E98 apparatus located upstream of our experiment in the muon lab) to deflect a monoenergetic muon beam (of known energy) into the active region of the spectrometer, while the second used a Monte Carlo program (MCP, an updated and modified version of the E26 Michigan State single muon Monte Carlo program[10]) to generate simulated hits in the spectrometer chambers, which were fed into a momentum analysis program similar to the data momentum fitting routines.

For the CCM runs (a large aperture air gap dipole which was the magnet for the University of Chicago Cyclotron), the target was removed (to reduce multiple scattering and muon energy loss) and muon beams of 250, 200, 150, 100, and 50 GeV were deflected into the spectrometer

aperture. Since these muons missed the E319 beam proportional chambers, a modified beam momentum routine had to be used to get the incident beam muon momentum using only the E98 beam hodoscopes and proportional chambers. Because of PC latch gate timing problems, the beam momentum was not available on an event-by-event basis, so the average beam momentum for each run was used instead. A further complication was that deflected muons could pass through iron and lead walls in the downstream E98 apparatus (energy loss in these walls had to be subtracted from the incident muon energy). Figure 3.9 shows the layout of the CCM and downstream iron and lead walls, Table 3.8 gives the characteristics of the iron and lead walls in the E98 apparatus.

For a monoenergetic muon beam incident on the spectrometer, the radius of curvature of the tracks through the spectrometer should be the same. Because of multiple scattering in the iron toroids, a plot of radius of curvature would be smeared out from a nice narrow peak into a gaussian distribution. So for these runs, 1/E' (which is proportional to the radius of curvature of a track) was histogrammed and fit to a gaussian distribution[7]. The width of this distribution gave the 1/E' resolution of the spectrometer, while the mean 1/E' was compared to $1/E_0$ (after energy loss corrections). A sample histogram and gaussian fit for the 250 GeV calibration run is shown in Figure 3.10, while the results of the calibration are shown in Table 3.9.

For the Monte Carlo calibration, MCP (to be described in Chapter IV) was run to generate muons incident on the spectrometer face with E' = 250, 200, 150, 100, and 50 GeV, and at Θ = 20, 25, and 30 mR. Each of these muons was traced through the spectrometer, taking

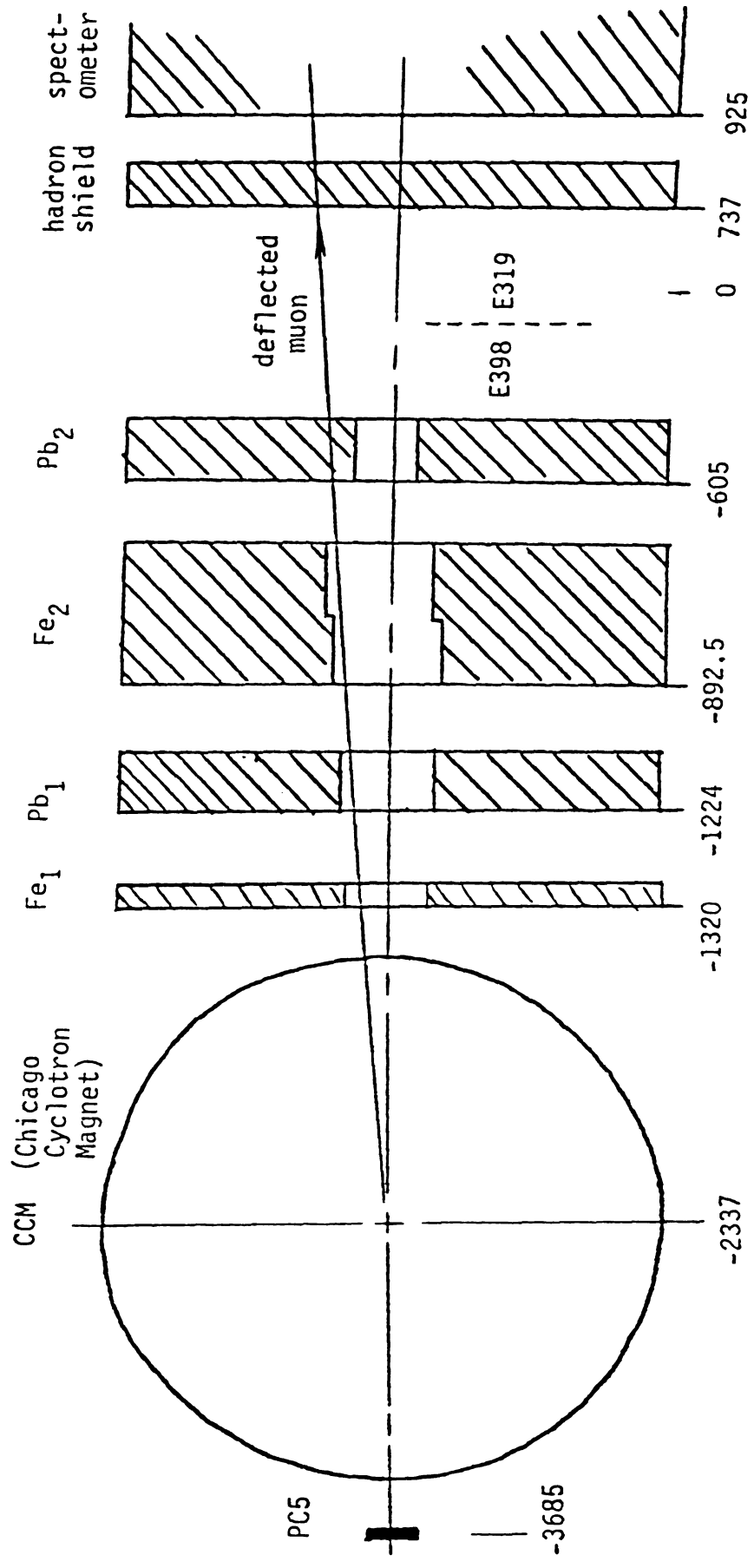

Figure 3.9. Layout of E398 and E319 apparatus during the spectrometer calibration

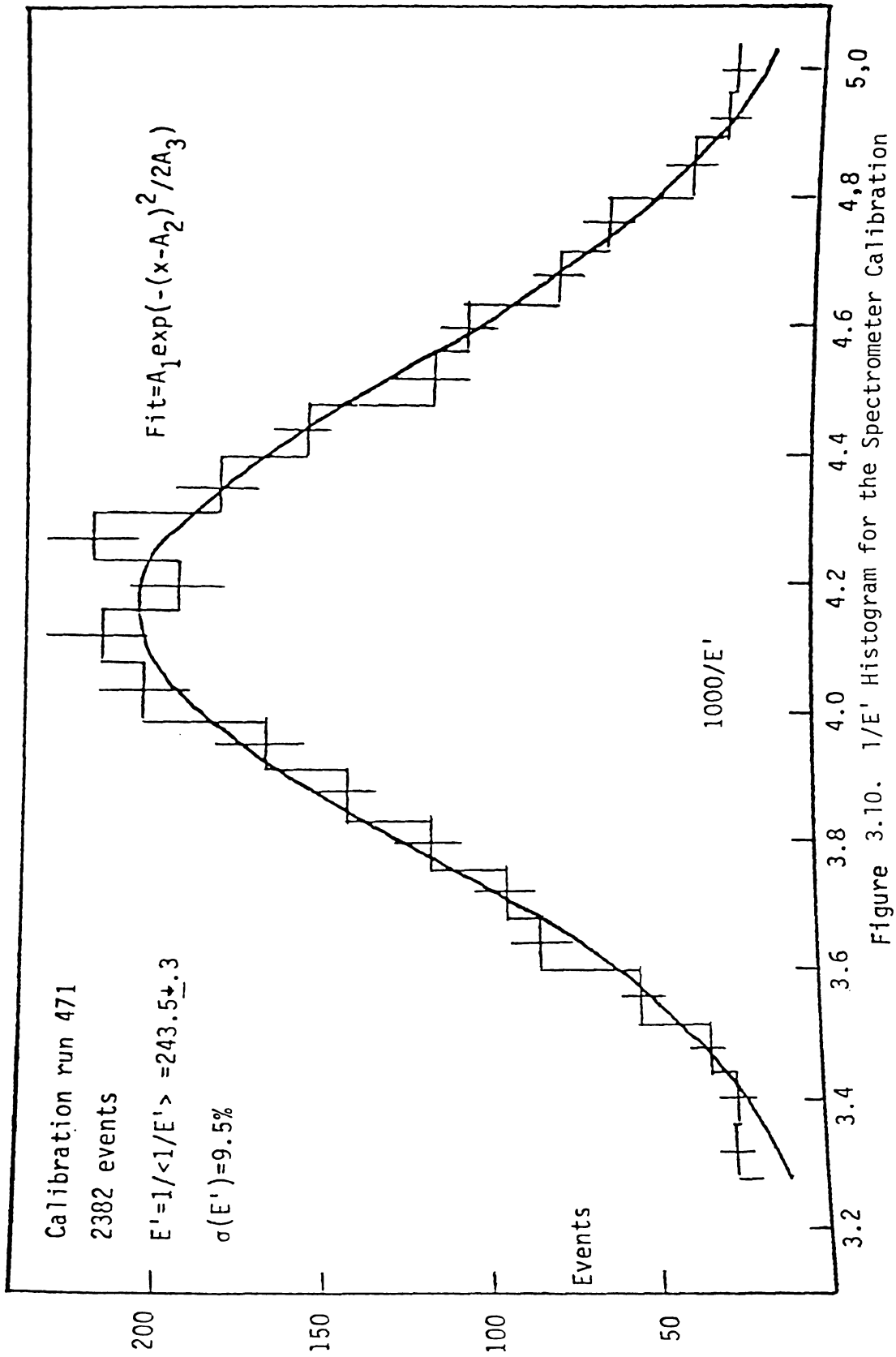

Figure 3.10. 1/E' Histogram for the Spectrometer Calibration

Table 3.8 Apertures in the E98 Walls

Fe_1 20cm thick, all muons through this aperture, z = -1320cm

Pb_1 41.3cm thick, aperture: 40.6cm wide x 38.2cm high, z = -1224cm

Fe_2 (Rochester cyclotron magnet iron used for hadron filter)
aperture: 160.6cm thick x 90.6cm high x 90.6cm wide
upstream edge: z = -892.5cm

Pb_2 2 slabs of Fe: 1.27cm thick, aperture: 15.9cm wide x 13.4cm high

Pb: 20.98cm thick, aperture: 19cm x 19cm, upstream edge:
z = -605cm

Table 3.9

Calibration of the Spectrometer using the CCM

RUN NO.	NOMINAL ENERGY	E_0 (GeV)	$1/\langle 1/E' \rangle$ (GeV)	$\sigma(E')$	EVENTS	$(E_0 - E')/E_0$
471	250	248.4±1.0	243.5±0.3	9.5%	3488	2.0%
470	200	200.3±0.5	199.3±0.3	9.4%	5528	0.5%
468	150	149.5±0.4	149.3±0.2	8.9%	3098	0.13%
469	150	149.1±0.4	148.6±0.3	9.1%	2954	0.35%
comb	150	149.4±0.4	149.0±0.2	9.0%	6052	0.25%
473	100	98.9±0.24	96.3±0.2	9.4%	6055	2.6%
474	50	47.56±0.14	45.89±0.08	9.3%	2665	3.5%

Table 3.10

Calibration of the Spectrometer using MCP

E(MC)	E(reconstructed)	$\sigma(E)$	EVENTS	(E(MC)-E(RE))/E(MC)
250	251.83±0.17	1.8%	699	-0.7%
200	201.36±0.21	1.6%	228	-0.7%
150	150.91±0.08	1.4%	631	-0.6%
100	100.56±0.08	1.2%	223	-0.6%
50	49.51±0.04	1.2%	274	+1.0%

account of energy loss and bending in the magnets, but the multiple scattering in the toroids was "turned off" (which accounts for the low values of energy resolution in Table 3.10). The hits in the spark chambers were written onto a simulated data tape. After these spark coordinates were smeared by a gaussian distribution (whose width was given by the instrinsic spark chamber resolution), they were fit using the data momentum fitting routines. From this, a plot of E' (incident) vs E' (reconstructed) was obtained, which was fit to a straight line. From this plot, a correction factor for the fitting routine energy loss subroutine (PLOSS) was obtained, and this factor was adjusted until the actual and reconstructed energies agreed to better than 1%. Results of this are shown in Table 3.10.

All of the above calibrations were for positive muons only (which bent inward in the spectrometer magnets) and for tracks which traversed all the spectrometer magnets and chambers. Also, because of the limited range of E' and Θ used for these runs (which were done primarily for the single muon analysis), another calibration was needed for the multimuon analysis. For this purpose, two large MCP runs (50,000 generated events for positive muons and 50,000 events for negative muons) were made, with E' thrown at a scattering point in the target (events were thrown uniformly over the target length) between 5 and 300 GeV, and theta thrown between 5 and 160 mR. These events were written to tape and momentum fit, after the spark chamber hits had been smeared. About half of the events were momentum fit and histograms were obtained for the 1/E' resolution (defined as $\Delta = (1/E'_{fit} - 1/E'_{act})/(1/E'_{fit})$ for the 100 bins the E' - Θ plane was divided into. Results of this analysis are shown in Tables 3.11 -

Table 3.11. Data Positive Muon I/E' Shifts (in %)

E' (GeV)	0	16	32	48	64	80	96	112	128	144	160
300	-9.9	-3.5	0.1	-6.8	-11.7	-22.7	-26.8	-35.1	—	—	
270	-4.3	0.2	1.9	0.6	-7.0	-7.5	-19.3	-16.3	—	—	
240	-0.1	1.7	3.8	2.4	3.0	-2.4	-7.7	2.1	-15.0	-7.8	
210	2.6	3.0	3.9	4.9	6.0	3.4	13.3	0	2.8	13.3	
180	3.2	3.9	6.0	8.0	8.2	12.9	16.0	14.4	19.0	13.8	
150	2.2	3.9	4.9	6.7	10.3	16.1	19.1	19.0	21.6	26.7	
120	2.7	3.9	4.6	8.6	13.7	18.0	20.9	26.0	29.7	45.4	
90	4.2	3.4	5.7	8.5	11.2	20.4	27.2	42.1	48.9	48.6	
60	23.0	4.6	7.0	7.8	10.0	19.7	48.1	60.9	68.7	60.8	
30	16.0	4.9	7.9	8.5	11.5	13.6	17.5	28.7	54.9	55.1	

θ (milliradians)

Table 3.12. Data Positive Muon I/E' Widths (in %)

E' (GeV)	0–16	16–32	32–48	48–64	64–80	80–96	96–112	112–128	128–144	144–160
300	17.1	8.6	9.2	12.1	18.4	28.1	28.0	26.9	–	–
270	13.9	8.9	10.4	10.8	16.1	18.2	30.2	27.5	–	–
240	12.1	8.7	8.9	10.9	15.4	21.8	26.5	19.1	1.7	5.0
210	10.8	8.3	8.1	10.2	17.5	22.0	20.6	24.3	23.8	23.2
180	12.3	9.0	8.1	11.4	17.4	20.4	22.0	27.3	13.3	8.9
150	11.9	8.1	8.7	11.1	18.1	23.7	25.0	25.4	23.3	22.9
120	12.4	9.6	8.9	11.2	17.4	26.4	29.7	29.9	24.8	12.1
90	15.8	9.9	8.3	10.2	15.9	30.5	34.5	32.5	27.8	24.5
60	2.5	9.5	9.0	9.8	12.7	32.9	50.8	55.3	27.2	27.5
30	2.7	21.9	12.5	10.2	12.6	15.5	25.7	38.7	49.6	23.7

θ (milliradians)

Table 3.13. Data Negative Muon I/E' Shifts (in %)

E' (GeV)	0	16	32	48	64	80	96	112	128	144	160
300	-3.5	-5.7	-0.9	-10.9	-16.2	-20.8	-19.9	-38.4	—	—	
270	-2.2	-0.8	-0.6	-5.0	-0.9	-13.7	-17.5	-23.5	—	—	
240	-1.1	2.2	2.8	2.4	1.2	-0.5	-3.5	-4.4	-10.6	-12.5	
210	0	3.4	4.0	6.2	4.8	5.6	15.6	-6.6	-3.5	15.1	
180	3.3	4.1	4.6	8.5	9.3	11.3	14.6	13.4	20.8	9.1	
150	1.8	3.7	5.1	6.0	12.2	17.3	21.4	25.9	19.2	39.1	
120	2.0	3.1	5.7	6.8	15.9	21.7	26.0	30.7	44.3	36.7	
90	1.7	3.2	5.0	9.1	12.1	23.7	28.9	41.0	56.7	52.7	
60	-0.7	3.5	5.2	7.6	10.4	34.2	47.1	66.5	70.5	66.0	
30	-2.8	4.7	7.6	9.7	12.3	16.1	29.8	39.6	41.3	56.7	
0											

θ (milliradians)

Table 3.14. Data Negative Muon I/E' Widths (in %)

E' (GeV)	0	16	32	48	64	80	96	112	128	144	160
300											
	11.8	10.8	8.2	14.8	22.5	26.9	18.1	30.3	–	–	
270											
	13.4	9.6	10.6	13.7	21.8	23.4	32.1	24.7	–	–	
240											
	14.0	9.7	10.0	13.8	15.6	19.2	28.3	29.0	17.6	8.5	
210											
	12.8	9.2	10.4	12.6	17.4	20.2	15.1	31.9	21.5	5.0	
180											
	10.7	9.5	9.6	14.6	23.0	24.7	24.7	24.6	12.0	14.9	
150											
	11.7	9.3	10.2	15.9	22.4	25.3	21.9	22.9	31.3	7.9	
120											
	11.7	9.4	9.6	15.2	23.5	27.0	27.1	30.9	17.3	19.6	
90											
	11.1	9.9	10.1	13.2	22.7	35.9	35.6	40.0	18.7	25.7	
60											
	11.3	9.9	10.5	13.2	21.0	48.3	51.0	28.6	15.8	19.3	
30											
	21.8	11.2	12.0	15.3	21.8	23.0	34.7	35.1	35.3	27.6	
0											

θ (milliradians)

3.14. The calibration E' shifts were applied to the multimuon data, while the 1/E' resolution (obtained from a gaussian fit of the 1/E' histograms) was used in the multimuon Monte Carlo simulations.

3.10 Multimuon Analysis

Because the event finding program MULTIMU was not perfect at finding multimuons (to keep from losing good events, some bad events with a halo muon or a stale beam track in the front WSC's were selected) the final selection of good multimuon data events was made on the basis of a visual scan of the "dimuon" triggers selected by MULTIMU. For each run, a file of run and event numbers was written by MULTIMU, which was used to create a scan file from the original tapes. This information was displayed on a Tektronix graphics terminal (format similar to Figure 2.4). For each of the four views, all sparks were shown on the spark chambers and up to 10 hits per HPC plane. Also shown were hits in the beam PC's, raw high and low gain ADC readings (shown as 110 small "thermometers", with an extra bar to show ADC overflows), trigger bank and beam veto hits. The general philosophy of scanning was to: a) examine at least two views (usually U and V) of the spectrometer for any evidence of two or more tracks, when in doubt, look at all four views; frequently halo and stale beam tracks forced this to be done, b) if two or more tracks were seen, make sure they were "live" by examining the hadron PC's and the trigger bank counters, c) the ADC's should show two (or more) particles after the shower (or just a step from one to $\geq$ two) with only one particle incident; this was a very reliable clue to multimuon events, and d) the vertex of the tracks should be consistent in all views and within the target, although this was hard to judge on the

display screen.

The events chosen were then second scanned (by more experienced scanners) and events still considered likely candidates were plotted on 8" x 11" paper using a calcomp plotter. The events were then classified as one of the following: 1A good trimuon; 1B questionable trimuon; 2A good dimuon; 2B questionable dimuon; 3 dimuon with one track in the spectrometer hole; 4 other unusual events (not multimuons); and 5 not a multimuon. Once all of the plots for the events were available, graduate students went through all of the plots (at least twice) and picked out all of the good events (reclassifying the events if necessary). The results of the momentum fitting for the spectrometer tracks were examined, especially the χ^2/DOF, NDOF, and spark deviations for the fitted tracks.

Of the final sample of 412 (out of 449 found) dimuons that could be momentum analyzed, $\sim$ 1/3 - 1/2 had to have at least one of the spectrometer tracks "fixed" because the initial momentum fit looked suspect (χ^2/DOF large, NDOF too small to be realistic, spark deviations very large, and/or an unreasonable momentum value) or else a momentum fit (without fixing the track) was not possible at all. Some of the tracks had to be fixed because of one bad spark, which pulled off the momentum fit, but not by enough for the χ^2 spark pulling, built into the momentum routines, to catch. Some tracks needed extra sparks (especially high momentum tracks very near the toroid holes and low momentum tracks which exited the spectrometer side after only one or two magnets) to help the momentum fitting routines get a more reasonable fit, and sometimes the matching routines found the wrong track (hooking the front of one track to the back of another track). So

in each of the four views, the "obvious" tracks were drawn in on the calcomp plots (care being taken to simulate bending in the magnets as best as possible for chambers with no sparks). These sparks were measured using a magnifying glass and a machinist's ruler. Sometimes an entire track was remeasured, sometimes just one or two sparks on a track. These corrections were read into a file and used to modify the original MULTIMU output block for that track, after views were matched (leading to matched hits) and alignment constants were added in. These tracks were then run through the fitting routines and the two stages of spark pulling (the same as for the tracks that were not fixed). All "good" events were merged into the final dimuon file to yield our final sample of 412 dimuons with complete kinematic information.

The track fixing procedure was checked by measuring normal fit events and the momentum of the "fixed" track came out within 10% of the nominal value, consistent with our $\sim$ 9% (at best) momentum resolution.

To check the scanning and multimuon reconstruction efficiencies, two μ+ data tapes (runs 280 and 363, which represented about 1.5% of the total 270 GeV μ+ data sample) were mass scanned, i.e. all triggers on these tapes, except pulser triggers and triggers with Branch Driver errors, were scanned. Nineteen multimuons were found in this mass scan, compared with 12 multimuons found by MULTIMU. However, requiring that all scattered muon energies were $\geq$ 5 GeV gave only 13 mass scan events giving MULTIMU a 92.3% efficiency for finding multimuons (83 $\pm$ 5% for dimuons, 96 $\pm$ 5% for trimuons).

Since most of the data was analyzed by two multimuon finding

programs (PASSI, which had very loose cuts, found only front lines, and wrote out a large number of possible multimuon events; PASSII or MULTIMU, which had more restrictive cuts, found spectrometer tracks and wrote out a much smaller file of multimuon candidates), the events found in PASSI which were not found in PASSII scanning was a measure of the scanning efficiency. This was found to be 25 dimuons (5.6%) and eight trimuons (12.5%). Also, about 9.5% of the total MULTIMU events (1.6×10^4 events) were rescanned yielding average efficiencies of 77.8% for dimuons and 89.7% for trimuons. The total scanning efficiencies were $(83.9 \pm 5)\%$ for dimuons and $(92.6 \pm 5)\%$ for trimuons. Combining the reconstruction and scanning efficiencies gives the total event finding efficiencies, $(70 \pm 7)\%$ for dimuons and $(89 \pm 7)\%$ for trimuons. The total raw dimuon and trimuon data rates were scaled by these efficiencies in order to compare to Monte Carlo predicted rates and for the purpose of cross-section measurements (to be discussed in Chapter V).

CHAPTER IV

MONTE CARLO SIMULATIONS

4.1 Monte Carlo Overview

The main job of the Monte Carlo programs was to take a "known" physics process (i.e. a certain model or cross section), and using experimental inputs (i.e. the incoming muon beam distribution, target and spectrometer geometry, E' and Θ resolution of the spectrometer, and geometric hardware and program software cuts) to predict the final experimentally measured data distributions and rates for that specific model.

For E319 two main Monte Carlo programs existed (plus various special purpose versions), which were begun in E26. The first one, called MCP, was used for the single muon analysis of E26[1] and the analysis of the first published single muon data of E319[2]. A cross-section table was used to throw E' and Θ in the nucleon rest frame of the scattering nucleon instead of the weighting scheme used in MUDD (the second main Monte Carlo, developed by A. Van Ginneken of Fermilab for the E26 multimuon analysis[3]). The step size used for tracing through the spectrometer magnets was variable (depending on the momentum of the particle being traced) to ensure that energy loss, multiple scattering, and bending in the toroid magnetic fields was done to very high precision. The coordinates of the spectrometer track at each chamber were written onto an output tape which was used as the input to a momentum fitting program (one very similar to the one used to fit the data). In this way, the "experimentally" measured E' and Θ for the MCP events was the result of fitting the smeared

sparks (the same procedure as used for the data), which should account for any systematic energy or angle shifts introduced into the data distributions as a result of the momentum fitting procedure used.

The second Monte Carlo, called MUDD (for $\mu \rightarrow D\bar{D}$), was used for all of the multimuon analysis (calculations of rates and kinematic distributions for multimuon final states due to π/K cascade decays, "prompt" muons, and QED tridents; also calculations of kinematic distributions for $D\bar{D}$ production and decay, and to extract a cross-section from our dimuon data for $D\bar{D}$ production). A single muon version of this program was used for the final analysis of the single muon data[4] and for comparisons to Quantum Chromodynamics (QCD) calculations[5] for deep inelastic muon scattering. Instead of using a cross section table (and throwing away generated events by comparing the ratio of the cross section in an E', θ bin/total cross section to a random number) as was done in MCP, MUDD generated a weight for each event, which was proportional to the cross section for the E' and θ thrown. Also, since MUDD did not write out tracks, E' and θ resolutions were inputs to the program (these were found using very large MCP runs, as described in Section 3.9).

The parts of MUDD dealing with the propagation of a muon through the target (incident beam distribution, energy loss and multiple scattering in the iron) and spectrometer (bending due to magnetic fields, energy loss and multiple scattering in the iron, geometric trigger and veto demands, and MULTIMU software cuts) were the same for all of the versions of the multimuon Monte Carlos and will be described first.

4.2 MUDD Main Routines

First the beam routine was called to get E_0, Θ_x, Θ_y, x, and y for the beam muon at the front face of the target. For the QED and $D\bar{D}$ programs, a beam tape (format shown in Table 4.1) was read, which consisted of pulser triggers from the μ+ data tapes which had PC Resets. These values were smeared by a gaussian distribution with a sigma of 0.1 GeV for E_0, 0.01mR for Θ_x and Θ_y, and 0.01 cm for x and y. These sigma values were much smaller than the experimental resolution in these variables, and the smearing was done mainly to smooth these distributions, since the number of good pulser triggers was small. For the π/K and prompt muon program, which was run on the IBM computers at the Argonne National Laboratory, the total E_0, Θ_x, Θ_y, x, and y distributions (at the target face) were fit with gaussians (using the CERN library fitting routine FUMILI). The means and sigmas of these fitted distributions are shown in Table 4.2.

Next the z-position of the muon interaction (ZINT) was randomly thrown uniformly over the entire length of the target (737.7cm), and the three momentum components, x, and y at the target face were stored (these were needed later to make the MULTIMU software ZMIN and DMIN cuts). From this point on each particle (incident muon and produced muon(s)) was characterized by its three direction cosines (DCX = p_x/p, DCY = p_y/p, and DCZ = p_z/p), total momentum p (or energy E), and the x, y, and z of the muon at a particular step in the apparatus. The incident muon was then stepped through the target (with energy loss and multiple scattering being accounted for; these processes will be described in detail later) up to the interaction point, where the

Table 4.1. Beam Tape Format

Word	Contents
1	run number
2	trigger number
3	Θ_x (beam)
4	Θ_y (beam)
5	x intercept (at z = 0)
6	y intercept (at z = 0)
7	$\chi^2(x)$ straight line fit to beam track
8	$\chi^2(y)$
9	DCR packed with information of trigger type and PC reset
10	E_o (measured)

Table 4.2. Incident Muon Beam Fitted Parameters

Quantity	Fitted Mean	Fitted Width (σ)
E_o (GeV)	269.589	3.475
Θ_x (mR)	0.060	0.409
Θ_y (mR)	-0.292	0.367
x (cm)	1.397	2.593
y (cm)	-1.123	3.044

number of steps taken was ZINT/5 cm, which was forced to be an integer between one and ten.

At this point the incident muon was scattered (an E' and θ were selected and the necessary weights calculated; how this was done will be described in detail later) and other muons (one or two, depending on the particular process) were generated, complete with their energies, angles, and weighting factors. This part of the Monte Carlo programs will be described later for the various production models. For each muon, subroutine TRAMP was called with the muon's momentum, spatial coordinates, direction cosines, and charge (+1 for positive muons, -1 for negative muons).

In TRAMP, the muon was stepped through the remainder of the target and the spectrometer in five cm steps, simulating energy loss and multiple scattering for the iron traversed during that step (not always five cm of iron, i.e. when leaving the target, or entering or leaving a magnet or hadron shield), and the bending of particle trajectories due to spectrometer magnetic fields.

Initially, subroutine HITORM was called with the current spatial coordinates of the muon, which determined the material index for the particle. The material index was: 0 for air, 1 for the iron target (ρ = 5.76 gms/cm^3), 2 for spectrometer iron (ρ = 7.86 gms/cm^3), 3 for magnet hole concrete (ρ = 4 gms/cm^3), and 4 for the muon outside the maximum radius or at the end of the spectrometer (i.e. radius > 86.36 cm or z > 2135 cm). The length of iron traversed was calculated (for the next 5 cm step), as well as the x and y components of the magnetic field. If a muon traversed magnetized iron, MFTR was called,

which calculated the new direction cosines for the muon (using $\Delta\vec{p}(GeV/c) = 3 \times 10^{-4} \Delta\vec{L}$ (cm) x $\vec{B}$(kgauss)) and normalized them (i.e. $DCX^2 + DCY^2 + DCZ^2 = 1$). Next the current x, y, and z were incremented (for the 5 cm three dimensional tracking step), and a check was made to see if the muon had stepped through one of the eight z-positions where its radius was checked (elements of the ZZL array: 1 for HPC, 2 for WSC9, 3 for WSC8, 4 for WSC7, 5 for SA', 6 for SB' and BV_1, 7 for SC' and BV_2, 8 for BV_3). At these z-positions checks were made to see if the muon passed through a trigger bank, beam veto counter, or a front spark chamber where MULTIMU software cuts were made. If the z position was not near one of these, multiple scattering and energy loss was done for the iron traversed and the program went back to HITORM and did the next 5 cm step.

If the muon was near HPC, then the momentum, direction cosines, and coordinates at the end of the target were stored (for use by the DMIN - ZMIN routines), and the "true" experimental E' was calculated using the spectrometer resolution tables. Multiple scattering and energy loss were accounted for and the program returned to HITORM.

If the muon was at WSC9 or WSC8, x and y coordinates were stored and the angles of the track in the x and y-views were calculated using the direction cosines at the end of the target. For the MULTIMU software cuts, an array called NP2(n), where n = number of the muon, existed (no software cuts leaves NP2(n) = 0). If the angle in the x or y view was > 234 mR, NP2(n) = 1.

At this point it should be mentioned that E_0 was measured at the front of the target, E' at the end of the target, and θ was calculated

using the incoming and outgoing muon tracks outside the target. This was done in the Monte Carlo because this was the only way these quantities could be measured for the data.

The scattering angle was computed as $\cos^{-1}((\vec{p}_0 \cdot \vec{p}')/|\vec{p}_0|\ |\vec{p}'|)$, and the theta resolution was then simulated. Using MCP, events were generated over the entire allowed range of E' and Θ (0-300GeV and 0-160mR) and the quantities $\Delta\ 1/E' \equiv (1/E'_{fit} - 1/E'_{act})/(1/E'_{act})$ and $\Delta\Theta = \Theta_{act} - \Theta_{fit}$ were loaded into a 10 x 10 E'- Θ plane. Each bin of this plane yielded a gaussian-like histogram (as expected), so each histogram was fit to a gaussian and the mean and width of the distribution was written out to a table (shown in Tables 4.3 - 4.10) for positive and negative muons and for 1/E' and Θ resolution. For the Θ resolution, the Θ_{MUDD} value was shifted by the theta offset read from the theta resolution table, and a value was randomly chosen from a gaussian distribution with a sigma given by the theta resolution table.

The MULTIMU DMIN and ZMIN cuts were made next. Using the momentum components and coordinates at the front of the target for the incoming muon, and the momentum components and coordinates at the end of the target for the muon being traced, the three dimensional distance of closest approach of the tracks (DMIN) and the z position at which this occured (ZMIN) were calculated. It was demanded that DMIN be less than min(0.15 R(WSC8) cm + 2.0cm, 10cm), if not NP2(n) was set to two. It was demanded that ZMIN be in the range -84.3 cm to 765.74cm (i.e. from 84.3 cm in front of the target to 28 cm behind the target), if not NP2(n) was set to three. The ZDIFF cut demanded

Table 4.3. Monte Carlo Positive Muon I/E' Shifts (in %)

E' (GeV)	0	16	32	48	64	80	96	112	128	144	160
300	-2.2	1.8	5.7	5.5	8.1	10.2	17.3	10.7	–	–	
270	0.9	2.8	.5.4	2.1	7.5	4.7	18.7	16.6	–	–	
240	0.4	2.0	3.7	4.1	4.3	4.4	6.4	15.1	22.6	15.0	
210	1.8	2.7	3.5	4.9	6.6	3.9	6.4	6.3	6.7	43.2	
180	-1.0	2.7	3.9	5.2	1.0	4.2	8.4	4.4	6.4	10.8	
150	-0.5	3.1	4.4	5.0	6.6	5.3	9.6	6.2	2.6	-66.0	
120	-0.8	3.0	3.4	7.3	6.0	1.8	2.8	4.9	-2.1	3.2	
90	-8.8	1.3	4.6	7.1	7.4	5.9	8.3	1.6	10.8	-60.0	
60	-20.0	1.2	5.8	6.7	7.3	8.2	6.5	3.4	3.5	11.4	
30	-25.3	0.3	4.7	7.1	8.5	9.6	9.2	3.7	-5.2	-15.3	
0											

θ (milliradians)

Table 4.4. Monte Carlo Positive Muon I/E' Widths (in %)

E' (GeV)	0	16	32	48	64	80	96	112	128	144	160
300	12.7	9.9	11.2	14.7	33.7	31.6	59.3	25.4	—	—	
270	15.7	10.0	8.3	12.2	24.6	27.8	39.6	41.0	—	—	
240	13.4	8.6	10.1	12.7	22.3	35.4	47.5	42.8	41.6	43.0	
210	12.0	9.1	9.6	12.5	18.9	37.4	39.3	46.9	51.5	22.5	
180	13.4	9.0	9.7	12.6	24.1	32.9	39.7	47.7	64.5	62.1	
150	12.1	8.9	9.2	12.6	19.2	30.2	42.2	45.9	48.9	50.6	
120	11.4	9.6	8.4	12.7	19.2	28.7	23.6	38.3	64.3	32.2	
90	13.7	10.1	9.3	11.4	16.4	18.6	25.5	30.9	80.6	18.0	
60	20.5	10.0	9.4	10.8	15.6	17.5	20.9	32.6	58.9	51.3	
30	5.9	20.1	13.3	11.4	13.7	18.9	22.5	25.4	31.9	13.7	
0											

θ (milliradians)

Table 4.5. Monte Carlo Negative Muon I/E' Shifts (in %)

E' (GeV)	0	16	32	48	64	80	96	112	128	144	160
300	3.3	2.8	3.2	3.3	12.9	13.2	22.3	32.9	–	–	
270	1.0	3.1	3.7	4.0	7.6	9.8	11.3	-6.2	–	–	
240	0.1	1.8	3.3	3.2	2.6	4.0	8.8	9.2	13.1	76.9	
210	-0.1	2.1	2.8	4.7	4.0	4.5	12.5	10.3	-0.6	-26.9	
180	-2.9	2.4	3.8	6.1	3.2	4.1	9.2	2.7	7.8	10.4	
150	1.5	2.7	3.0	2.8	6.1	3.4	4.8	-1.4	17.3	-4.5	
120	-0.2	2.0	3.9	2.4	2.2	4.7	1.8	-1.5	3.3	26.4	
90	-1.0	1.9	3.6	5.6	3.0	2.2	6.6	1.7	8.1	-0.1	
60	-2.0	2.5	2.7	4.0	4.1	0.3	-1.0	0.6	8.6	7.9	
30	-6.3	2.5	4.9	5.7	4.6	4.9	2.6	3.2	5.4	8.2	
0											

θ (milliradians)

Table 4.6. Monte Carlo Negative Muon I/E' Widths (in%)

E' (GeV)	0	16	32	48	64	80	96	112	128	144	160
300	14.0	10.7	11.1	19.8	25.0	40.5	39.9	16.7	–	–	
270	11.2	10.6	10.1	17.5	33.8	36.8	41.8	32.9	–	–	
240	13.4	10.2	11.4	18.7	29.3	34.1	38.4	47.0	43.6	14.3	
210	12.6	10.0	10.3	15.9	25.5	37.0	46.7	47.6	48.5	16.2	
180	13.4	9.0	10.9	17.9	26.9	36.5	44.1	43.8	61.6	6.1	
150	13.3	9.7	10.4	15.1	24.3	32.3	40.8	46.9	52.2	34.7	
120	11.0	9.6	10.6	15.4	23.8	28.6	34.3	43.8	84.2	9.8	
90	12.9	9.1	11.0	15.5	21.1	26.7	36.7	45.0	61.2	56.7	
60	10.4	10.2	11.1	14.4	19.6	26.4	30.0	53.4	60.3	26.6	
30	16.6	12.5	14.6	17.0	20.5	26.6	41.1	48.4	51.0	33.9	
0											

θ (milliradians)

Table 4.7. Monte Carlo Positive Muon θ Shifts ($X10^{-4}$mR)

E' (GeV)	0	16	32	48	64	80	96	112	128	144	160
300	2	2	2	1	0	1	4	2	—	—	
270	3	3	2	3	2	1	2	3	—	—	
240	2	3	2	2	2	1	3	2	-2	2	
210	3	3	2	2	3	3	3	1	4	2	
180	1	2	2	2	2	2	1	0	2	-1	
150	2	3	2	2	2	2	2	1	4	6	
120	2	2	3	2	3	2	3	3	3	7	
90	-2	2	1	1	4	3	4	5	2	-5	
60	-5	0	1	3	2	6	3	1	-2	-2	
30	16	-8	-4	1	-2	2	-4	6	1	12	
0											

θ (milliradians)

Table 4.8. Monte Carlo Positive Muon θ Widths ($X10^{-4}$mR)

E' (GeV)	0	16	32	48	64	80	96	112	128	144	160
300	6	5	6	5	5	7	9	10	–	–	
270	5	5	6	6	6	6	8	10	–	–	
240	5	6	6	6	6	8	8	7	10	11	
210	5	6	6	6	7	8	10	8	11	10	
180	6	6	7	8	8	9	9	10	10	6	
150	8	8	8	7	7	8	10	8	9	9	
120	8	8	10	10	10	10	8	10	10	11	
90	11	11	11	11	12	12	10	12	11	13	
60	19	14	16	17	17	15	16	17	13	14	
30	13	37	34	28	31	26	29	26	32	24	
0											

θ (milliradians)

Table 4.9. Monte Carlo Negative Muon θ Shifts ($X10^{-4}$mR)

E' (GeV)	0	16	32	48	64	80	96	112	128	144	160
300		2	2	2	4	4	4	3	2	–	–
270		3	3	2	3	3	4	3	-1	–	–
240		2	2	3	2	3	2	4	3	2	2
210		2	3	2	2	3	3	4	3	3	1
180		2	3	3	3	2	3	3	3	6	5
150		3	2	2	2	3	3	4	2	2	2
120		2	2	2	3	3	3	3	3	3	9
90		0	4	1	2	2	2	3	4	5	3
60		0	0	2	5	4	2	6	4	3	8
30		-11	0	6	2	5	0	4	2	0	0
0											

θ (milliradians)

Table 4.10. Monte Carlo Negative Muon θ Widths ($X10^{-4}$mR)

E' (GeV)	0	16	32	48	64	80	96	112	128	144	160
300	5	5	5	5	6	7	8	9	–	–	
270	5	5	5	5	7	6	7	10	–	–	
240	5	6	5	6	8	7	8	9	11	12	
210	6	7	6	6	7	8	9	8	12	12	
180	7	7	6	7	8	8	9	10	12	10	
150	8	7	7	8	8	8	8	9	13	11	
120	8	9	9	9	9	9	10	10	11	14	
90	11	11	11	11	12	11	12	11	11	11	
60	16	14	17	16	15	15	15	15	12	14	
30	26	36	35	33	34	33	28	22	32	17	

θ (milliradians)

that | ZMIN - ZINT | $\leq$ 400 cm, if not NP2(n) was set to four. Once these cuts were done, the program returned to HITORM and continued tracing.

If the muon was at WSC7, the spark positions (smeared by a gaussian distribution with a sigma of 0.1 cm) were stored, and the expected spark coordinates at WSC7 were computed using a straight line extrapolated through the sparks in WSC9 and 8. The MULTIMU window cuts were then done for the x and y views. Window sizes for each view were defined as: WIN = A |expected coord|^2 + B |expected coord| + C, where A = 5 x 10^{-4}, B = 0.165, and C = 0.5. If 50 cm $\leq$ |expected coord| $\leq$ 75 cm, WIN was set to 10 cm; and if |expected coord| > 75 cm, WIN was set to 20 cm. Now if the extrapolated coord > the actual coord + WIN, or the extrapolated coord < the actual coord - WIN, NP2(n) was set to five.

If the muon was at the position of a trigger bank, and if the radius was > 15.24 cm, the trigger bank bit (for this trigger bank and track) was set to one. The track was then extrapolated to the z-position of the nearest beam veto and a BV hit was recorded if the radius was < 15.88 cm (again for this track and beam veto). To make veto checking easier, the beam veto hit for the second track was the "OR" of the beam veto hit for the first and second particle for each beam veto, similarly for the third track, the hit was the "OR" of the hits for the first and third track hits for each beam veto.

Once the above checks were made, the muon continued through the apparatus, losing energy and multiple scattering in the iron, bending in the magnets, and hitting or missing trigger banks and beam vetoes, until the last beam veto, at the end of the apparatus, was reached.

This ended the tracking part of MUDD for this track.

The beam veto hits were then checked, to see if this event was vetoed. For muon number one, only particle one vetoes were looked at, for particles two and three we look at 1-2 and 1-3 multiple particle vetoes as well as single particle vetoes. And for muon number three, we look at 1-2-3 particle vetoes. The veto definition was: (> 1 hit in BV_1 OR > 1 hit in BV_2) AND > 1 hit in BV_3, with allowances made for multiple particle vetoes, as described above. When a veto occured, the trigger code (NMP(n), for muon n) was set to two (the default value was five) and the next section of code, which checked triggering requirements, was skipped.

The hardware trigger was checked next. For each muon, the bits for hits in the three trigger banks (SA, SB, and SC) were added up. If this sum was $\geq$ three, NMP(n) was set to one (i.e. single muon trigger) and the rest of the trigger checks were skipped. For a muon to be momentum analyzable, it had to pass through at least one magnet. If the radius was > 15.24 cm at WSC7, SA, SB, or SC, the muon was momentum analyzable and NMP(n) was set to three. A check for multiple particle triggers was done, summing the trigger bank hits for the first and second particle if the second muon was being traced, and the first, second, and third particle if the third muon was being traced. If (number of SA hits $\geq$ 1 AND number of SB hits $\geq$ 1 AND number of SC hits $\geq$ 1), we set NMP (2 or 3) to one (i.e. this particle satisfied the single muon trigger requirement). Next the dimuon trigger was checked, and if (number of SA hits $\geq$ 2 AND number of SB hits $\geq$ 2), NMP (2 or 3) was set to one (i.e. this particle satisfied

the dimuon trigger criteria).

Since the largest resolution effect was the 1/E' resolution (which for a fully penetrating track was $\sim$ 9%, compared to $\sim$ 1% for the E_0 resolution and $\sim$ 2% for the θ resolution) and since the number of events traced and accepted tended to be small (due to the computer time needed to trace tracks and the low spectrometer acceptance), the 1/E' resolution function would not have been sampled very well if 1/E' was chosen as one point from a gaussian of width given by the 1/E' resolution sigma table. Without using the technique described below, the E' and associated kinematic spectra (i.e. Q^2, ν,...) would have had very large bin-to-bin variations. Effectively what was done was to use six points on the 1/E' gaussian distribution instead of the one usually used when an "experimentally" measured quantity (like θ) was chosen from its gaussian distribution. Starting with a table of the integrals of a normalized gaussian distribution,[6]

$$\int_0^z \frac{1}{\sigma\sqrt{2\pi}} \exp \; - \tfrac{1}{2} \left(\frac{x - \mu}{\sigma}\right)^2 \; dx,$$

where μ = mean of the distribution, σ = standard deviation of the distribution, 60 values were obtained for z between 0 and 6 σ in steps of 0.1 σ. We randomly pick three values from this gaussian distribution, between zero and 1σ, 1σ and 2.6σ, and 2.6σ and 5.9σ. Each of these was weighted by the integral of this part of the gaussian versus the total area of the gaussian (0.341345 for 0 to 1σ, 0.15399 for 1σ to 2.6σ, and 0.004665 for 2.6σ to 5.9σ). The gaussian distribution is symmetric about the origin, so that the

three values on the "high side" of the gaussian have three corresponding values on the low side. Hence, each time the entire range of the 1/E' resolution function was sampled, instead of just the most probable part. The same total weight is achieved (since the sum of the weights = 1) for each event but with much smoother kinematic spectra. The resulting six values of E' were stored for each event being traced (also their weights).

If at this point the first (scattered) muon was being traced, the single muon histograms were called and tracking was begun for the second muon. If the second muon was being traced, tracking was begun for the third muon. If the program was on the third muon, all three muons had been traced through the spectrometer until their values of NMP(n) had been set to one (trigger), two (veto), three (momentum analyzable), or five (none of the above). An index was defined, NCODE = 25 (NMP(1)-1) + 5 (NMP(2)-1) + NMP(3), and the NGO array was checked to see if this was a trigger combination which would lead to a dimuon or a trimuon (one of the muons must have NMP = 1, and at least one other muon must have NMP = 3 or 1; the remaining muon could have any value for NMP for the $D\bar{D}$ Monte Carlo, it could even be a veto since the branching ratio for the process being considered would prevent this muon from occuring a certain part of the time). By convention, the first muon was always the scattered muon, the second muon was the positive produced muon, and the third muon was the negative produced muon.

If muon one was not momentum analyzable (i.e. NMP(1) = 5) or if E'_{fit} for muon two was > E'_{fit} for muon one, then the particle one

and two arrays were interchanged, NCODE was recalculated, and a bit was set to keep track of the switch. Experimentally there was no way of knowing, except by the muons charges, which muon of a dimuon was the scattered muon, so if both muons of a dimuon event were positive, the "leading particle" (number one) was chosen as the muon with the largest momentum (for both the data and Monte Carlo events). Due to the fact that all of the processes calculated had branching ratios (except the QED processes), a dimuon event was the most probable outcome for the three muon process being looked at (i.e. a particle 1-2 or 1-3 dimuon), while a trimuon event resulted only occasionally ($\propto$ branching ratio squared).

A loop was done over all six of the E_1' values (these were generated during the 1/E' resoultion). All of the relevant single muon scattering variables were defined: Q^2, ν, x, ω, y, and W. Inside this loop was a loop over all six values of E_2', and if NMP(2) was = 1 or 3 and $E_2' > 5$ GeV, relevant dimuon kinematics were defined: P_T^2 (with respect to the virtual photon direction), inelasticity, $M_{\mu\mu}$ (the invariant mass of the pair), and asymmetry $((E_1 - E_2)/(E_1 + E_2))$. At this point subroutine COMB was called with the values for: x, Q^2, W, P_T^2, $M_{\mu\mu}$, η, $\Delta\Theta$, p_2, $\Delta\phi$, y, asymmetry, and a weight, part of which was the E_1' gaussian weight, the E_2' gaussian weight, the branching ratio (for $D\bar{D}$ calculations), the cross section weights, and the E_1' and Θ_1 throwing weights. A loop was next done over the six values of E_3', if NMP (3) = 1 or 3. If $E_3' > 5$GeV, the same dimuon kinematics as above were calculated, and subroutine COMB was again called (this time the weight contained the E_3' gaussian weight). Inside this loop,

if NMP(2) = 1 or 3 and E_2' > 5GeV, trimuon kinematics were calculated and subroutine COMB was called for these events with the appropriate weights. Once all possible combinations were taken care of, particles one and two were exchanged (if they were exchanged in the first place) and the next beam muon was chosen, the entire procedure being repeated until a preset number of incident muons had been traced or the computer time used exceeded a preset limit. At this time all of the stored histogram arrays, final run statistics, and tables were printed and/or written to disk.

A brief description of subroutine COMB will finish up this section. This routine was called with the histogram number, weight for the event, value of the variable, and NCODE. Using this information, the appropriate bin number of the histogram storage array was computed (all histogram arrays were 20 bins) and the weight for the event was added to that bin of the histogram. All events which would have underflowed or overflowed the allowed range of a histogram were skipped. When the single muon histograms were called for the first particle (scattered muon), the sum of the total single muon weight was accumulated, which yielded the total number of scattered single muons accepted by the apparatus for the given incident flux. This number ($\sim$ 560,000) corresponded very closely with the data value and also was the same for all the Monte Carlo programs (which were run on different computers).

4.3 Muon Energy Loss and Multiple Scattering

Energy loss by muons passing through matter is due to four physical processes: a) ionization of atomic electrons, b) brems-

strahlung (emission of real photons), c) electron pair production, and d) nuclear interactions. The fourth process is very small at our energies, and was neglected.

The ionization energy loss is due to interactions of the muon with atomic electrons. For particles heavier than the electron, the average energy loss is given by the Bethe-Block equation[7]

$$-\frac{dE}{dx} = \frac{2\pi n z^2 e^4}{mv^2}\left(\ln\left(\frac{2mv^2 W_{max}}{I^2(1-\beta^2)}\right) - 2\beta^2 - \delta - u\right)$$

where n is the material electron number density, I the ionization potential, W_{max} the maximum energy transfer to the electrons, u a screening function for inner shell electrons, and δ a density function due to polarization of the material by the muons passage. The energy loss distribution for a muon traversing a finite thickness of material is a very broad, asymmetric distribution, which is shown in Figures 2.71 and 2.72 of Rossi.[8] Following Rossi's method and using the values of Sternheimer[9] and Joseph[10], a most probable energy loss ε_p was selected:

$$\varepsilon_p = \frac{At\rho}{\beta^2}\left(B + 1.06 + 2\ln\frac{p}{m_\mu} + \ln\frac{At\rho}{\beta^2} - \beta^2 - \delta + S\right)$$

$$A = \frac{2\pi N_0 e^4 \beta^2}{m_e v^2 \rho} = 7.15\times10^{-5}\ \frac{GeV}{g/cm^2} \quad \text{(for iron)}$$

$$B = \ln\frac{m_e}{I^2} = 15.64$$

$$\delta = \begin{cases} 0.0443\ \beta^2\ (\frac{E}{m_\mu})^{1.73} & ;\ \frac{E}{m_\mu} < 4 \\ 10^{(0.043\ -\ 0.730(x-1)\ -\ 0.188(x-1)^2)} & \\ \qquad + 2\ \ln \frac{E}{m_\mu}\ -\ 4.3 & ;\ 4 < \frac{E}{m_\mu} < 100 \\ 2\ \ln \frac{E}{m_\mu}\ -\ 4.3 + (3.8 + 3.33\times10^{-4}(\frac{E}{m_\mu})^2)^{-1} & \\ & ;\ \frac{E}{m_\mu} > 100 \end{cases}$$

$$x = \log_{10} \frac{E}{m_\mu} \qquad b = \lambda = 1.48$$

$$S = \frac{1}{4} \frac{W^2}{E_\mu^2} \qquad W = \frac{E_\mu^2}{m_\mu} / (\frac{2m_\mu}{m_e} + \frac{E_\mu}{m_\mu})$$

$$\Delta_0 = \frac{0.3 Z m_e b t \rho}{A \beta^2}$$

Fits to Rossi's distribution, divided into four regions, were made in terms of $x = (\epsilon_p - E)/\Delta_0$ (see Table 4.11) and the probability of each region contributing to the energy loss computed. Once one of these regions was selected (using a random number), the ionization energy loss was computed.

The energy loss due to muon bremsstrahlung, the emission of a real photon by a muon, was modeled after the work of Tsai.[11] The

Table 4.11. Fits to Ionization Loss

Region 1: Probability fraction 0.094

$$f(x) = 0.4662\ e^{(x+1.878\cdot10^{-4})\cdot0.4662}$$

$$-4.0 \leq x < -0.75$$

Region 2: Probability fraction 0.378

$$f(x) = \frac{1}{(2\pi)^{\frac{1}{2}}}\ e^{\left(\frac{-x^2}{2\cdot0.9705^2}\right)}$$

$$-0.75 \leq x \leq 0.75$$

Region 3: Probability fraction 0.453

$$f(x) = 0.003672\cdot x - 0.08318 + 0.61186/x - 0.25295/x^2$$

$$0.75 < x \leq 9.0$$

Region 4: Probability fraction 0.075

$$f(x) = \frac{1}{x^2}$$

$$9 < x < \frac{E_o - \varepsilon_p - m_\mu}{\Delta_o}$$

$$x = \frac{E-\varepsilon_p}{\Delta_o}$$

ε_p and Δ_o defined in the text

probability of a bremsstrahlung occuring is:

$$P(E) = \frac{N_A}{A} \rho t \, \sigma_B$$

where

$$\sigma_B = \int \frac{d\sigma_B}{dy} \, dy = \frac{\alpha^3}{m_\mu{}^2} \int \frac{1}{y} \, F(y) dy$$

$$F(y) = (\frac{4}{3} - \frac{4}{3} y + y^2)(z^2(\phi_1 - \frac{4}{3} \ln z - 4f(z)) + z(\psi_1 - \frac{8}{3} \ln z))$$

$$f(z) = 1.202 \, (\frac{z}{137})^2 - 1.0369 \, (\frac{z}{137})^4 + \frac{1.008(\frac{z}{137})^6}{(1+(\frac{z}{137})^2)}$$

$$y = \frac{\text{photon energy}}{\text{muon energy}} \quad .$$

where $\alpha = 1/137$, and ϕ_1 and ψ_1 are the Bethe-Heitler screening functions. Energy loss due to this process occured $\sim$ 2% of the time, so a random number was used to see if this energy loss was to be computed. If so, y was selected to conform to the differential cross section and the energy loss was taken as yE_0.

The energy loss due to the production of electron pairs was computed using only the average energy loss (since straggling for this process is small), given by the formula of Richard-Serre[12]

$$\frac{dE}{dx} = \frac{N}{A}\,\frac{m_e}{m_\mu}\,\frac{(\alpha z r_e)^2}{\pi}\,E_0(19.3\ \ln\frac{E}{m_\mu} - 53.7\ f)$$

$$; \ E_0 < 20 \text{ GeV}$$

$$f = (\frac{16}{9}\ln\frac{183}{z^{1/3}} + 1)/(\frac{16}{9}\ln\frac{E_0}{m_\mu} - \frac{14}{9} + \ln 2)$$

$$; \ E_0 > 20 \text{ GeV}$$

where r_e = 2.8 fm and f is due to screening by atomic electrons. The total energy loss was taken as the sum of these three contributions.

As a muon passes through matter, it is scattered in the Coulomb field of the nuclei making up this material. Many such scatters occur per cm of material traversed, and lead to the deflection of the muon from its initial trajectory. For a large number of particles traversing a finite thickness of material, the angular scatter at the end of the material has a gaussian shape, with the width of the distribution[13] (projected onto a plane) being:

$$\theta_{rms}^{plane} = \frac{0.015 \text{ GeV/c}}{p\beta}\sqrt{\frac{L}{L_{rad}}}$$

where p is the particle's momentum (in GeV/c), βc its velocity, L the length of material passed through, and L_{rad} the radiation length of the material.

4.4 Throwing and Weighting Variables

Before the models and cross sections needed to calculate the event rates and kinematic distributions for the main dimuon sources are described, a brief description of how variables were thrown, and their corresponding weights calculated, is in order. For certain variables, for example E' and θ for deep inelastic scattering, there is no way of knowing what E' and θ should be for each simulated event. But since the cross section for this process is known, E' and θ are thrown using random numbers over their entire range (from lower to upper limits) and the cross section and apparatus acceptance give the proper kinematic spectra for these variables. In certain cases, where the actual data distribution is very peaked over only a small part of the entire range available for a variable (e.g. Q^2 or θ), a lot of computer time is wasted sampling the entire variable range uniformly. Instead, most of the sampling should be done where most of the events are, in the case of θ, near the spectrometer hole and at small θ ($d\sigma/d\Omega \propto \theta^{-4}$, so $d\sigma/d\theta \propto \theta^{-3}$). To do this, the variable is chosen according to some probability distribution (and possibly different distributions in different regions of the variable's range) and a weight is applied, so that a histogram of the weighted thrown distribution is uniform. This is done using the following fundamental principle:[14]

If $p(x)dx$ is the probability of x lying between x and $x + dx$, with $a \leq x < b$, and $\int_a^b p(\xi)d\xi = 1$, then $r = P(x) = \int_a^x p(\xi)d\xi$ determines x uniquely as a function of r; moreover, if r is uniformly distributed on $0 \leq r < 1$, then x falls with frequency $p(x)dx$ in the interval $(x, x + dx)$.

As a trivial example, suppose we want to throw the interaction vertex uniformly on the interval a<z<b. In this case, $p(z)dz = cdz$, normalization of the integral implies that $c = 1/(b - a)$. So $r = P(z) = \int_a^z p(\xi)\, d\xi = (z - a)/(b - a)$. Solving this for z yields: $z = a + r^*(b - a)$. Hence, once a suitable random number generator is available, we can bias the throwing of variables any way necessary to optimize the Monte Carlo running. For each event, there is an associated weight: WT = probability of occurance/probability of throwing $\propto$ cross section/probability of throwing. For example, E' in the nucleon rest frame was thrown uniformly from 0.2 GeV up to the incoming muon energy, i.e. $E' = E_{min} + r(E_{max} - E_{min})$, and since $P(E') = 1/(E_{max} - E_{min})$, the weight for this event is: $WT(E') = 1/P(E') = E_{max} - E_{min}$.

As a final example, consider the θ throwing for deep inelastic muon scattering. What was desired was to sample mostly low θ (since the cross section is proportional to θ^{-3}), near the toroid hole; but for dimuons, we must sample inside the toroid hole because of the possibility of cooperative triggering. Also, a fairly large range of θ must be covered, since the Lorentz transform to the lab frame from the nucleon rest frame can make a large rest frame angle into a small lab angle. Events occuring at the front of the target can be accepted with a much smaller scattering angle than events occuring at the end of the target. The theta throwing was divided into two regions. For 0.1 mR < θ < 12 mR, the probability function used was $p_1(\theta)d\theta = c_1\theta^2 d\theta$, which throws most of the events near the edge of the toroid holes (since most small angle events are not accepted). For 12 mR < θ < 150 mR, the probability function used was $p_2(\theta)d\theta =$

$c_2\theta^{-2}d\theta$ (since $d\sigma/d\theta \propto \theta^{-3}$, high θ events were well sampled). First it must be decided, given a random number r*, which of the two theta regions to select from, and once a particular region is chosen, a theta (and associated weight) must be selected given a second random number r. Given $p_1(\theta)d\theta = c_1\theta^2 d\theta$ for $0 < r^* < \ell_1$, normalization gives us $c_1 = 3/(b^3 - a^3) = 1{,}736{,}112$. Next set $r = \int_a^\theta c_1\xi^2 d\xi = (\theta^3 - a^3)/(b^3 - a^3)$, solving for theta gives $\theta_1 = (a^3 + r(b^3 - a^3))^{1/3}$. The weight is: WT_1 = 1/probability of throw = $1/(\ell_1/1)c_1\theta_1^2$, the ℓ_1 in the denominator is because θ_1 is not thrown all the time. For the second region, $p_2(\theta)d\theta = c_2\theta^{-2}d\theta$ for $\ell_1 < r^* < 1$, normalization gives $c_2 = ab/(b - a) = 0.0130435$. Next set $r = \int_a^\theta p_2(\xi)d\xi = ab/(b - a)*(1/\theta - 1/a)$, solving for theta gives $\theta_2 = (a^{-1} - r(a^{-1} - b^{-1}))^{-1}$, where a is the lower theta limit and b is the upper theta limit for this region. The weight is: WT_2 = 1/probability of throw = $1/(\ell_2/1)c_2\theta^{-2}$, where $\ell_2 = 1 - \ell_1$. To fix ℓ_1 and ℓ_2 (and hence WT_1 and WT_2), demand continuity of the weights at θ = 12 mR and use the fact that $\ell_1 + \ell_2 = 1$. This gives the condition: $1/c_1\ell_1(0.012)^2 = (0.012)^2/c_2(1 - \ell_1)$, or $\ell_1 = 0.26596$ (and hence $\ell_2 = 1 - \ell_1 = 0.73404$). So if a random number selected is < 0.26596, we select theta according to $p_1(\theta)$, if not, we select theta according to $p_2(\theta)$ and use the appropriate weights.

4.5 π/K and Prompt Muon Model

The π/K background consisted of four parts: 1) the second muon produced by the decay of a pion (before it interacted or was absorbed in the target) in the hadronic shower of a deep inelastic muon scatter, 2) the second muon produced by the decay of a kaon in the hadronic

shower of a deep inelastic muon scatter, 3) the second muon was a "prompt" muon[15] ($\mu/\pi \sim 10^{-4}$) produced at the initial interaction point, and 4) the second muon was a "prompt" muon produced in a second or higher generation hadronic interaction in the target. These background processes gave only dimuons (i.e. the first muon was the scattered incoming muon, while the second muon came from the π/K decay or prompt muon source). Since all of the cross sections for these processes are known, the program gave absolute rates (after acceptance) as well as kinematic distributions. The hadronic shower calculations were done using CASIM[16] (written by A. Van Ginneken at Fermilab to do shielding calculations).

The inclusive muoproduction cross section for pions ($\mu + p \rightarrow \mu + h^{\pm} + x$) was taken to be (based on E98 hadron production data[17]):

$$\frac{d\sigma}{dx'dp_T^2} = k \exp(-3.25\,|x'|) \exp(-b(p_T^2 + M^2)^{\frac{1}{2}})$$

where x' is the longitudinal pion momentum in units of its maximum values (i.e. $x' = p_{11}^*/(p_{max}^{*2} - p_T^2)^{\frac{1}{2}}$), p_{11}^* was the hadron's longitudinal CM momentum, p_{max}^* was the maximum value this momentum can have, and p_T is the momentum transverse to the virtual photon direction. The values used for b and M were: b = 6 and M = 0.8, which were consistent with the E98 hadron data. The value of k was fixed by demanding that $\int\int (d\sigma/dx'dp_T^2)dx'dp_T^2$ be equal to the observed pion multiplicity[18] (for large Q^2): $m_\pi = 0.18 + 0.75 \log S - 0.075 * \log Q^2$, where Q^2 is the square of the virtual photon's four momentum and S is the center of mass energy of the photon-nucleon system. The x' selection function was: $S(x') = c \exp(a\,x')$*

exp (-3.25 |x'|), where a was 6 for -1 < x' < 0 and 2 for 0 < x' < 1; c was a normalization constant determined by:

$c^{-1} = \int_{-1}^{0} S(x')dx' + \int_{0}^{1} S(x')dx' = T + U$. The range of x', (-1,0) or (0,1), was first selected by comparing a random number to cT. Once a range for x' was selected, it was thrown as:

$$x' = \log\{1 - r\,(1 - \exp(-3.25 - a))\}/(3.25 + a) \qquad x' \leq 0$$
$$x' = -\log\{1 - r\,(1 - \exp(-3.25 + a))\}/(3.25 - a) \qquad x' > 0$$

The p_T dependence of the cross section was not well suited to random selection. Instead, the selection function used was:

$$S_1(p_T^2)dp_T^2 = k_1 \exp(-4p_T^2)dp_T^2 \qquad p_T \leq 0.5 \text{ GeV/c}$$
$$S_2(p_T)dp_T = k_2 \exp(-p_T)dp_T \qquad p_T > 0.5 \text{ GeV/c}$$

with $k_2 = k_1 \exp(-0.5)$.

For $p_{T,max} \leq 0.5$ GeV, k is given by: $k_1 = 4/(1 - \exp(-4p_{T,max}^2))$, and p_T^2 is thrown as: $p_T^2 = -\log(1 - 4r/k_1)/4$.

For $p_{T,max} > 0.5$ GeV, normalization gives:

$$k_1^{-1} = (1 - \exp(-1))/4 + \{1 - \exp(-(p_{T,max} - 0.5))\}\exp(-1).$$

As was done for x', the range of P_T was first determined by comparing a random number with $k_1(1 - \exp(-1))/4$. Selection within each range leads to:

$$p_T^2 = -\log\{1 - r(1 - \exp(-1))\}/4 \qquad p_T \leq 0.5 \text{ GeV/c}$$
$$p_T = -\log\{\exp(-0.5) - r(\exp(-0.5) - \exp(-p_{T,max}))\} \qquad p_T > 0.5 \text{ GeV/c}$$

The weight for the entire pion momentum selection was:

$$WT = (d\sigma/dx'dp_T^2)/S(x')\ S(p_T^2).$$

A brief description of the methods used in CASIM[19] will now be given. This program was used to simulate internuclear hadronic cascades, making extensive use of weighting techniques. Each genera-

tion of a shower was represented by a single particle, weighted in such a manner that the properties of the cascade were reproduced on the average, or equivalently, over many incident particles. When a hadron was "born" from the nuclear interaction of the representative hadron of the previous generation, the relevant parameters, i.e. kind (i), momentum (p), and angles (Ω) were randomly chosen from a selection function $S(i,p,\Omega)$. The particle was weighted according to the inclusive distribution of the production model:

$$W(i,p,\Omega) = S^{-1}(i,p,\Omega) \quad dN(i,p,\Omega)/dpd\Omega$$

Since only one particle represented all outgoing secondaries, the normalization was: $\sum_i \int S(i,p,\Omega)\, dpd\Omega = 1$.

Weighting techniques were also used in calculating the collision distance r. In the case of a constant mean free path, λ, this distance was distributed according to $\lambda^{-1}\exp(-r/\lambda)$.

The input data needed to describe particle production were the nine inclusive distributions: $pA\rightarrow p$, $pA\rightarrow n$, $pA\rightarrow\pi$, $nA\rightarrow p$, $nA\rightarrow n$, $nA\rightarrow\pi$, $\pi A\rightarrow p$, $\pi A\rightarrow n$, $\pi A\rightarrow\pi$, where A represents any nucleus (Be to Pb) and π represents $\pi^+ + \pi^-$. The differential cross section for these various processes was obtained using the Hagedorn-Ranft (thermodynamic) model[20], with parameters from the H. Grote, R. Hagedorn, and J. Ranft "Atlas of Particle Spectra" paper.[21] Tables of shower multiplicity and inelasticity for incident nucleons and incident pions (for Be, Al, Cu, and Pb targets) were stored, values for all other materials were obtained from these tables by interpolation.

For our purposes, two components of muons were produced, the

usual decay muons and "prompt" muons.[15] The latter were assumed to have a production cross section equal to 10^{-4} of the pion yield everywhere. The production of two muon components was simulated every time a pion was generated during the Monte Carlo runs. This pion then represented: 1) a prompt muon of identical momentum and direction but with the weight reduced by a factor of 10^{-4}, and 2) a decay muon with direction and momentum randomly selected using the full decay kinematics and with the weight calculated assuming the pion traveled one collision length before interacting.

Since this program was run at the Argonne National Laboratory, the table of E' resolution was not used, instead, the 1/E' resolution of the scattered muon was taken as 10% and the resolution of the produced muon was taken as 12%.

4.6 QED Trident Model

Since the muon is a charged lepton, it is possible for it to emit a virtual photon (in the nuclear field, which helps to conserve momentum and energy) which can couple to a $\mu^+\mu^-$ pair, yielding a three muon final state (two muon if one of the muons is stopped in the target or lost because of very large lab angles). The Feynman diagrams for this are shown in Figure 4.1. The muon pair production cross section from the diagrams where a quark radiates, which is the virtual Compton process, is expected to be much smaller than the cross section for the process where a muon radiates, and in our calculations was ignored.

For a lepton of incident four momentum p_1 which produces a pair of leptons with four momentum p_3 (opposite charge) and p_4 (like

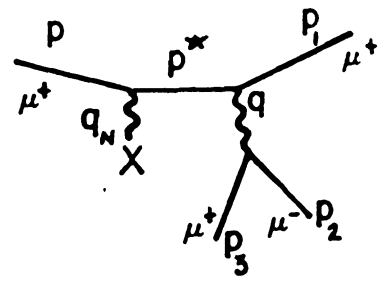

a. time-like

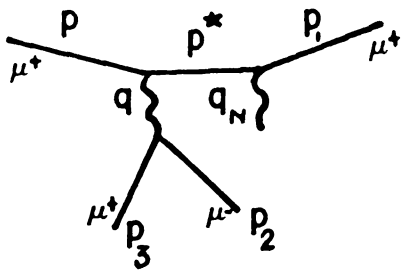

b. time-like

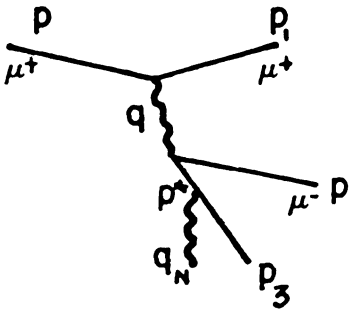

c. space-like

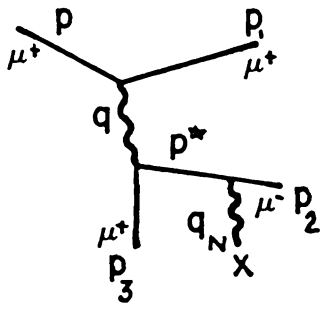

d. space-like

Figure 4.1 Feynman Diagrams for QED Tridents

charge) in the field of a heavy spin-zero nucleus (total charge Z, form factor $F(q_N^2)$), leaving a scattered lepton of four momentum p_2, the differential cross section is:[22]

$$\frac{d^5\sigma}{dE_2 dE_3 d\Omega_1 d\Omega_2 d\Omega_3} = \frac{Z^2}{2} F^2(q_N^2) \frac{\alpha^4}{2\pi^4} \frac{|\vec{p}_2||\vec{p}_3||\vec{p}_4|}{|\vec{p}_1|} \frac{1}{q_N^2} \sum_{\text{spins}} |M|^2$$

where $q_N = p_1 - p_2 - p_3 - p_4$ is the four momentum transfer to the nucleus. The incident lepton is assumed to be unpolarized and the spins of the final state particles are not observed. For muon tridents (all of the particles in the final state are muons), M is the sum of the four amplitudes of Figure 4.1 minus the four amplitudes with p_2 and p_4 exchanged.

The computer code used was written by Brodsky and Ting,[22] and calculated the amplitudes directly, instead of the usual reduction of spin sums into traces. The code itself calculates differential cross sections for tridents, muons or electrons producing muon or electron pairs for a spin zero nucleus, assuming zero nuclear recoil (i.e. only elastic tridents are looked at).

To get a qualitative look at tridents,[23] simply ignore all of the complicated terms in the numerator and consider only the effects of the denominator. Then the square of each amplitude makes a contribution to the cross section that looks like:

$$d\sigma_d \sim \frac{Z^2 F^2(q_N^2)}{q_N^4} \frac{1}{q^4} \frac{1}{(p^{*2} + m^2)^2}$$

where p* is the momentum of the virtual muon. Clearly the cross section is largest in the regions of phase space where a term in any

of the denominators of the matrix elements gets very small. This implies that there are essentially only four regions of phase space where the trident differential cross section is not vanishingly small: 1) a lepton is collinear with the virtual photon $\vec{q}$; in this case, $p^{*2} + m^2$ nearly vanishes for some diagrams, 2) a lepton of like charge is collinear with the incident particle; in this case, the spacelike virtual photon four momentum squared is small, 3) two leptons of opposite charge are collinear in the final state; this means that the timelike virtual four momentum squared is minimized, and 4) q_N, the nuclear recoil, is collinear with the incident lepton; this being the configuration in which q_N^2 takes on its minimum value when one of the final state lepton momenta is varied while the other two lepton momenta remain fixed.

Since these cross sections are extremely small, even in the regions of phase space where they are largest, it was very important to choose the selection functions for the momenta and angles of the second and third muons so that mostly the above mentioned regions of phase space were sampled. Even so, very long Monte Carlo runs were necessary to get adequate sampling of all of the available phase space to ensure a reliable answer.

For our purposes, it was important to look at incoherent scattering (from individual nucleons) as well as coherent scattering (virtual photon interacts with the entire nucleus). For incoherent scattering, Z^2 was replaced by Z and the nuclear form factor[24] for iron was replaced by the elastic nucleon (i.e. proton) form factor (the "dipole" fit[24]). More details on the QED trident calculations can be found in the thesis

of Dan Bauer.[25]

4.7 $D\bar{D}$ Production Model

The model adopted for associated charmed-meson production was that of Bletzacker and Nieh (BN)[26], the same model used for the E26 analysis.[3] The BN model was applied to the $D\bar{D}$ pair, rather than to single D production (as was done in BN), since it was desired to keep track of trimuon events and this helped to simulate the D and $\bar{D}$ correlations somewhat better. The production cross section was taken as:

$$\frac{d^3\sigma}{dxdyd\vec{p}_3} = (8\pi\alpha^2 M E_0 q^{-4})\ F_{ch}\ (x,y)\ f(\vec{p})$$

where $y = (E_0 - E')/E_0 = \nu/E_0$, E_0 is the incident energy, α the fine structure constant ($\sim 1/137$), M the nucleon mass, and $\vec{p}$ the momentum of the $D\bar{D}$ pair. The structure function $F_{ch}(x,y)$ was assumed to be:

$$F_{ch}(x,y) = A(q^2/(q^2 + 4M_D^2))\ ((S - S_0)/S)^3\ e^{-10x'}\ (1 + (1 - y)^2)$$

where A is a normalization constant, M_D = 1.86 GeV, S is the square of the invariant mass of the virtual photon-nucleon system, S_0 is the threshold for $D\bar{D}$ production, and $x' = (q^2 + 4M_D^2)/2M\nu$. The inclusive $D\bar{D}$ momentum distribution was taken to be (assuming factorization): $f(p) = N \exp(-az)\exp(-bp_T^2)$, where N is a normalization factor, $z = p_z/\nu$, with p_z the longitudinal and p_T the transverse (with respect to the virtual photon direction) $D\bar{D}$ momentum. The previously found E26 values of a = 1 and b = 0.25 have been used for this analysis; results showing the model dependence of the p_T kinematic spectra versus the choice of a and b are shown in Chapter V.

The invariant mass of the $D\bar{D}$ system was chosen from a theoretical

distribution for associated production from the Hagedorn-Ranft paper[27] on statistical thermodynamics of strong interactions. In this paper, they develop a model, using statistical thermodynamics and relativity, to describe certain features (e.g. final state multiplicities, energies, and angular distributions of produced secondaries) in high energy hadron-hadron collisions. They give the invariant mass distribution for two "fireballs" moving along the z-axis in opposite directions with equal speed γ, with the rest frame of the fireball being primed coordinates and the CM frame having unprimed coordinates. Each fireball emits one particle (D or $\overline{D}$) with mass m_1 and m_2 respectively, with thermodynamic spectra in the fireball rest frame:

$$f_i(\varepsilon')d^3p' = \exp(-\varepsilon_i'/T)d^3p'$$

$$\varepsilon_i' = (\vec{p}'^2 + m_i^2)^{\frac{1}{2}}$$

In the CM frame the invariant mass $(p_1 + p_2)^2$ of this pair has a certain value M^2; the distribution function being given by:

$$f(M^2,\gamma) = \int d^3p_1'd^3p_2' \; \delta(M^2 - m_1^2 - m_2^2 - 2\varepsilon_1\varepsilon_2 + 2\vec{p}_1 \cdot \vec{p}_2) \; *\exp\,(-(\varepsilon_1' + \varepsilon_2')/T)$$

for $\gamma = 1$, primed and unprimed coordinates become the same, in this case the z-axis is no longer defined, we first keep $\vec{p}_1$ fixed and choose the z-axis parallel to $\vec{p}_1$, using polar coordinates for $\vec{p}_2$ and integrating over cos Θ gives:

$$f(M^2,\gamma=1) = \int_{m_1}^{E} d\varepsilon_1\varepsilon_1 \exp\,(-\varepsilon_1/T)\left[(1 + \frac{\varepsilon_2^-}{T}) \exp\,(-\varepsilon_2^-/T) - (1 + \frac{\varepsilon_2^+}{T}) \exp\,(-\varepsilon_2^+/T)\right]$$

with

$$\varepsilon_2^{\pm} = \frac{\varepsilon_1}{2m_1^2}\,(M^2 - m_1^2 - m_2^2)\pm$$

$$\frac{1}{2m_1^2}\left[(\varepsilon_1^2 - m_1^2)\left[M^2(M^2 - 2m_1^2 - 2m_2^2 + (m_1^2 - m_2^2)^2\right]\right]^{\frac{1}{2}}$$

which was solved numerically. T was taken as 150 MeV (the asymptotic maximum temperature of the thermodynamic model ($\sim m_\pi$)). The decay of the $D\bar{D}$ pair was assumed to be isotropic in the $D\bar{D}$ rest frame, keeping track of the correlations between the two D's.

The decay of the D's was assumed to occur via their two principal semileptonic decay modes: $D \to K\mu\nu$ and $D \to K^*\mu\nu$, with the total branching ratio being taken as 10%[28] (the decay mode $D \to \pi\mu\nu$ was ignored, since it is at the 6% level relative to the kaon decay modes). Following SLAC data on D decay[28], 40% of the decays were assumed to be $K^*(890)\mu\nu$ and 60% were assumed to be $K\mu\nu$.

The energy spectrum of the muon (for the K decay) in the rest frame of the D was obtained from the matrix element:

$$< K(p') \mid J_\lambda \mid D(p) > = f_+(p + p')_\lambda + f_-(p - p')_\lambda \ .$$

For $m_\mu = 0$, so that f_- does not contribute, and treating f_+ as a constant, we obtain:[29]

$$\frac{1}{\Gamma_{D\to K\mu\nu}} \quad \frac{d\Gamma}{dE_\mu} = \frac{96\ f(E_\mu)}{I_k\ M_D^6}$$

where: $I_k = 1 - 8m^2 + 8m^6 - m^8 - 12m^4 \ln(m^2)$; $m = \frac{m_K}{m_D}$

$$f(x) = x^2(m_D^2 - m_K^2 - 2m_D x)^2/(m_D - 2x).$$

For the decay $D\to K^*\mu\nu$, the hadronic current has a matrix element of the form:

$$< K^*(p',\varepsilon)|J_\lambda|D(p)> = a\varepsilon_\lambda + b(p\cdot\varepsilon)(p + p')_\lambda + c(p\cdot\varepsilon)(p - p')_\lambda + ig\varepsilon_{\lambda\alpha\beta\gamma}p^\alpha p'^\beta \varepsilon^\gamma,$$

for the approximation $m_\mu = 0$ the c term does not contribute. Neglecting the b and g terms (whose contribution is only $\sim$ 15%), and keeping

only the a term yields:

$$\frac{1}{\Gamma_{D\to K^*\mu\nu}} \frac{d\Gamma}{dE_\mu} = \frac{96 f^*(E_\mu)}{I_K^* M_D^6}$$

where: $I_K^* = 1 + 72r^4 - 64r^6 - 9r^8 + (36r^4 + 48r^6) \ln (r^2)$

$$f^*(x) = \frac{x^2(m_D^2 - m_{K^*}^2 - 2m_D x)^2}{(m_D - 2x)} \left[1 + \frac{2m_{K^*}^2}{m_D(m_D - 2x)}\right]$$

and $r = m_{K^*}/m_D$.

Decay modes of the form $D\to K(n\pi)\mu\nu$, with $n \geq 1$, were ignored in this analysis.

Once the incoming muon had been traced to the interaction point, it was transformed from the lab frame to the nucleon rest frame, the frame where the nucleon struck by the virtual photon was at rest. The Fermi motion of the nucleon within the iron nucleus was generated according to a simple Fermi gas model:[30] $f(\vec{p}) = p^2/\left[1 + \exp((p^2 - p_f^{\,2})/2mkT)\right]$, with p_f = 260 MeV and kT = 8 MeV. In the nucleon rest frame, the outgoing scattered muon's E' and θ were thrown, as discussed in Section 4.4. Some kinematics were defined (i.e. $\nu = E_0 - E'$, Q^2, $x = Q^2/2m\nu = 1/\omega$, and $W^2 = m^2 + 2m\nu - Q^2$, where m = the nucleon mass) and elastic events were cut (i.e. demand $W^2 > (m_p + m_\pi)^2$ and $\omega > 1$; also since a $D\bar{D}$ pair must be produced, demand $W^2 > (m_p + 2m_D)^2$). The deep inelastic muon scattering cross section[2] was calculated:

$$\frac{d^2\sigma}{dE'd\theta} = \frac{8\pi\alpha^2}{(q^2)^2}\frac{E'}{y} \sin\theta \cos^2\frac{\theta}{2} \nu W_2 * \left[1 + 2\tan^2\frac{\theta}{2}(1 + \nu^2/q^2)/(1 + R)\right]$$

where the structure function W_1 was eliminated using:

$$\frac{W_2}{W_1} = (1 + R)/(1 + \nu^2/q^2).$$

For our analysis, R was taken to be equal to 0.25.[31] Since an iron target was used (A = 26, N = 30), an "average" νW_2 was used, defined as νW_2 = (26 νW_2(proton) + 30 νW_2(neutron))/56. For the proton νW_2, the "Stein" fit[24] was used:

$$\nu W_2^p = \sum_{n=3}^{7} a_n (1 - 1/\omega')^n$$

where $\omega' = 1/x' = (2m\nu + m^2)/q^2 = 1 + W^2/q^2$, and $a_3 = 1.0621$, $a_4 = -2.2594$, $a_5 = 10.54$, $a_6 = -15.8277$, and $a_7 = 6.7931$. For neutrons, we used:

$$\nu W_2^n = \nu W_2^p (1.0172 - 1.2605/\omega' + 0.73723/\omega'^2 - 0.34044/\omega'^3)$$

which was a fit from low energy SLAC data.[32]

To account for the scaling violation,[1] νW_2 was modified to the form

$$\nu W_2 = \nu W_2(\text{Stein}) \left(\frac{Q^2}{3}\right)^{b(x)}$$

where $b(x) = 0.16895 + 0.5777 \ln(1 - x)$ for iron[33] (using a fit to SLAC-MIT and E98 μp data).[34]

From the photon kinematics, the scattering angle for the virtual photon was calculated and ϕ was thrown uniformly over the interval $(0, 2\pi)$. Using the Hagedorn invariant mass distribution, the mass of the $D\bar{D}$ pair was selected between its minimum value ($2M_D$) and its maximum value ($W - m_p$). The weights for the deep inelastic cross section and the BN model were set up. For the deep inelastic scatter, the total weight was: WT = cross section * (N_{AV}* target

density * target length * incident flux) * WT(E' selection) * WT (Θ selection). The first part of this weight is the single muon scattering event rate (i.e. rate = cross section * luminosity). The scattered muon was transformed from the nucleon rest frame to the lab frame, and TRAMU was called to trace this muon through the rest of the apparatus.

The maximum momentum of the $D\bar{D}$ pair (as seen in the CM of the $D\bar{D}$ and p system) was computed and p_T of the pair was selected in the CM frame. The selection function used was:

$$S_1(p_T) = k \qquad p_T < 1 \text{ GeV/c}$$
$$S_2(p_T) = kp_T^{-1} \qquad 1 \text{ GeV/c} \leq p_T \leq p_{max}$$

where only one normalization constant was necessary (since $S_1 = S_2$ at $p_T = 1$). Normalization gave $k^{-1} = (1 + \log p_{max})$, so the corresponding weights were:

$$WT_1 = S_1^{-1}(p_T) = (1 + \log p_{max}) \qquad p_T < 1 \text{ GeV/c}$$
$$WT_2 = S_2^{-1}(p_T) = p_T(1 + \log p_{max}) \qquad p_T > 1 \text{ GeV/c}$$

To determine which selection function was to be used, a random number was compared with $1/k(1 + \log p_{max})$. Using $S_1(p_T)$, p_T was selected as: $p_T = r$; while for $S_2(p_T)$, p_T was selected as: $p_T = p_{max}^{r}$, where r is a random number.

Next the p_T and $z(= E_2/\nu)$ dependence of the cross section was accounted for. For p_T :

$$\frac{d\sigma}{dp_T} = 2bp_T \exp(-bp_T^2)/(1 - \exp(-bp_{max}^2))$$

where five cross sections (and weights) were set up, corresponding to b = 0.25, 0.5, 1.0, 2.0, and 3.0. For the histograms and weights, b = 0.25 (the E26 values) was used, but the p_T and z array were stored

for the five values of b and the corresponding five values of a. After computing $p_{L,max}$ and $p_{z,max}$ (and hence $z_{max} = p_{z,\ max}/E_\gamma$) the z dependence of the cross section was accounted for:

$$\frac{d\sigma}{dz} = a\ \exp(-az)/(1-\ \exp(-az_{max}))$$

where again five cross sections (and weights) were set up, corresponding to a = -1, 0, 1, 2, and 3. For the weights and histograms, a = 1 (the E26 value) was used.

After calculating the momentum and γ of the $D\overline{D}$ pair with respect to the proton in the nucleon rest frame, the angles of the pair relative to the virtual photon were computed. Assuming an isotropic decay of the $D\overline{D}$ pair into a D and $\overline{D}$ meson in the pair's rest frame, the D's direction cosines were computed and subroutine CHADK was called, which gave momentum, direction, and a weight (due to the Llewellyn Smith[29] inclusive decay cross section) for the decay muon. Using the direction cosines of the $\overline{D}$ meson, subroutine CHADK was again called, giving the decay muon's momentum, direction, and weight. The direction cosines of the two decay muons were calculated in the nucleon rest frame and then transformed back to the lab frame. Finally, subroutine TRAMU was called for each of these muons, which were traced through the rest of the apparatus.

4.8 Other Model Calculations

Using a set of simple cuts[25] to simulate our experimental apparatus a group of theorists[35] at the University of Wisconsin did Monte Carlo calculations of the rates and distributions expected for our experiment. They calculated electromagnetic production from bremsstrahlung and Bethe-Heitler (photon-photon fusion) processes for a)

the quark-parton model (inelastic recoil), b) coherent proton target recoil, and c) coherent iron target recoil; hadronic final state interactions; and vector meson production. They then compared these processes with multimuon final states resulting from charm ($c\bar{c}$) production (using the photon-gluon fusion model,[36] calculated in the framework of quantum chromodynamics).

Instead of tracing individual events, the calculated rates were obtained by integrating the differential cross section (using standard computer trace techniques) over the final state phase space that was consistent with a set of cuts which reproduced (to a remarkable extent) our experimental cuts and vetoing and triggering requirements. Without the cuts, the background processes swamped out the charm signal (as would be expected), but with the cuts (especially the veto requirement), the charm signal was found to be at least two orders of magnitude larger than the background signals.

Comparison[25] of our QED calculations (with the same simple cuts) as used above with those of Barger et al. show that the simple cuts were a very good approximation to the actual experimental conditions. Their rate calculations, as well as a description of the photon-gluon fusion model used, will be given in the next chapter.

CHAPTER V

CHARM CROSS SECTION AND CONCLUSIONS

5.1 Multimuon Data Sample

For the purposes of this analysis, only dimuon events from the 270 GeV μ+ main data runs will be considered[1], since this was the largest block of data, and the only data sample to undergo the track fixing procedures described in Chapter III. Also, it was the only data sample that was published.[2] A total of 449 dimuons was found, of which 324 were opposite sign pairs (OSP's) and 125 were same sign pairs (SSP's), with a total corrected incident flux of 1.094×10^{10} 270 GeV positive muons. Of these dimuon events, 412 were momentum analyzable (298 OSP's and 114 SSP's). Folding in the track finding and scanning efficiencies ($\sim$ 70%) yielded an expected sample of 644($\pm$ 55) dimuons, or $\sim 5.9 \times 10^{-8}$ dimuons per incident muon. The rates and average kinematics for the 270 GeV μ^- and 150 GeV μ+ (run with 1/3 the normal target density) data are comparable[1] with the above data sample, showing that dimuon production does not seem to depend on the incident particle's charge or energy (at least in the energy range covered).

Kinematic distributions for E_1 (the energy of the "leading" muon), E_2 (the energy of the "produced" muon), Q^2 (the four momentum transfer squared of the virtual photon), x (the fraction of the momentum of the nucleon carried by the quark struck by the virtual photon), W (the total CM energy of the virtual photon-nucleon system), P_T (the momentum of the produced muon transverse to the virtual photon direction), E_2/ν (the fraction of the final state "hadronic" energy carried by the produced muon), $\Delta\theta$ (the polar angle between the scattered and produced

muons), $\Delta\phi$ (the azimuthal angle between the scattered and produced muons), $(E_1 - E_2)/(E_1 + E_2)$ (the energy asymmetry of the final state muon pair), $M_{\mu\mu}$ (the apparent invariant mass of the final state muon pair), and $(E_0 - E_1 - E_2)/E_0$ (the inelasticity of the dimuon event, or percent of the energy of the final state not visible as final state muons) are shown in Figures 5.1 - 5.12. These plots represent the kinematic distributions for the 412 momentum analyzable events scaled up to the 644 events expected for the experiment (found number of dimuons/finding efficiency). The curves on these plots are the E319 Monte Carlo calculated backgrounds for: a) π/K internuclear cascade decay and prompt muon production (solid curve), and b) elastic QED tridents (dashed curve), which will be described later. Average kinematic values for the 412 momentum analyzable events of the 270 GeV μ+ dimuon sample are shown in Table 5.1.

Since apparatus acceptance is largely responsible for the shapes of the kinematic distributions shown, a more revealing way to look at these distributions is to compare the spectra of the leading particle of dimuon events (the largest energy positive muon of the final state muons) to that of deep-inelastic single muon interactions. Using this approach, the acceptance effects due to the scattered muon can be removed. In order to get a relatively pure sample of deep-inelastic single muon events, a set of cuts, shown in Table 5.2, were imposed on the 270 GeV μ+ data. These cuts ensured that the scattered muons were not in the region of the spectrometer near the magnet holes and that enough spark chambers contributed to the momentum fit to give realistic fit values for the muon's momentum and angles. Many of the events cut were due to beam muons with

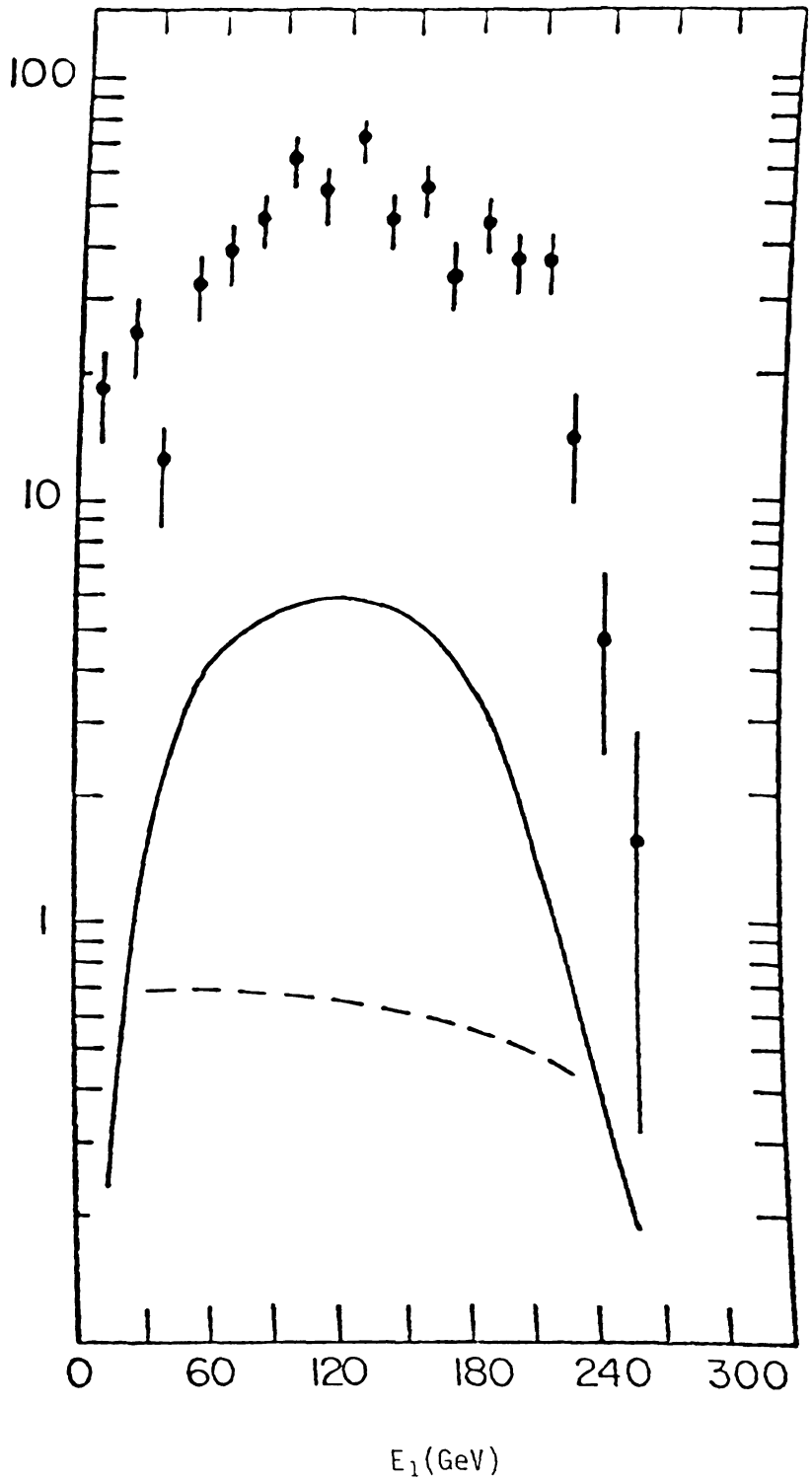

Figure 5.1 Dimuon E_1 and Background Curves

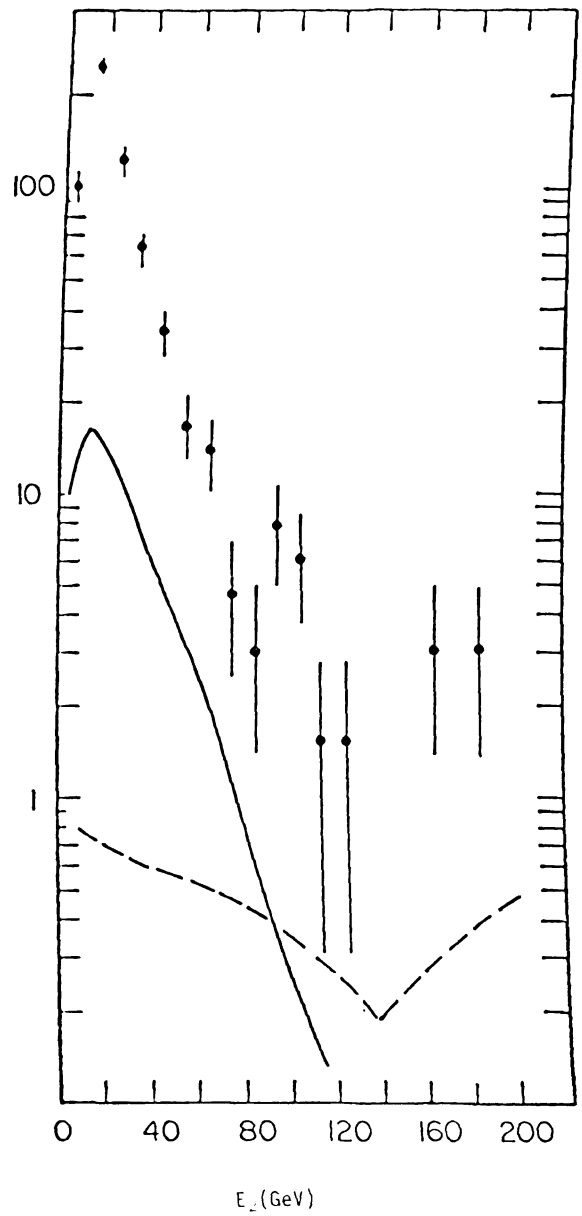

Figure 5.2 Dimuon $E_\perp$ and Background Curves

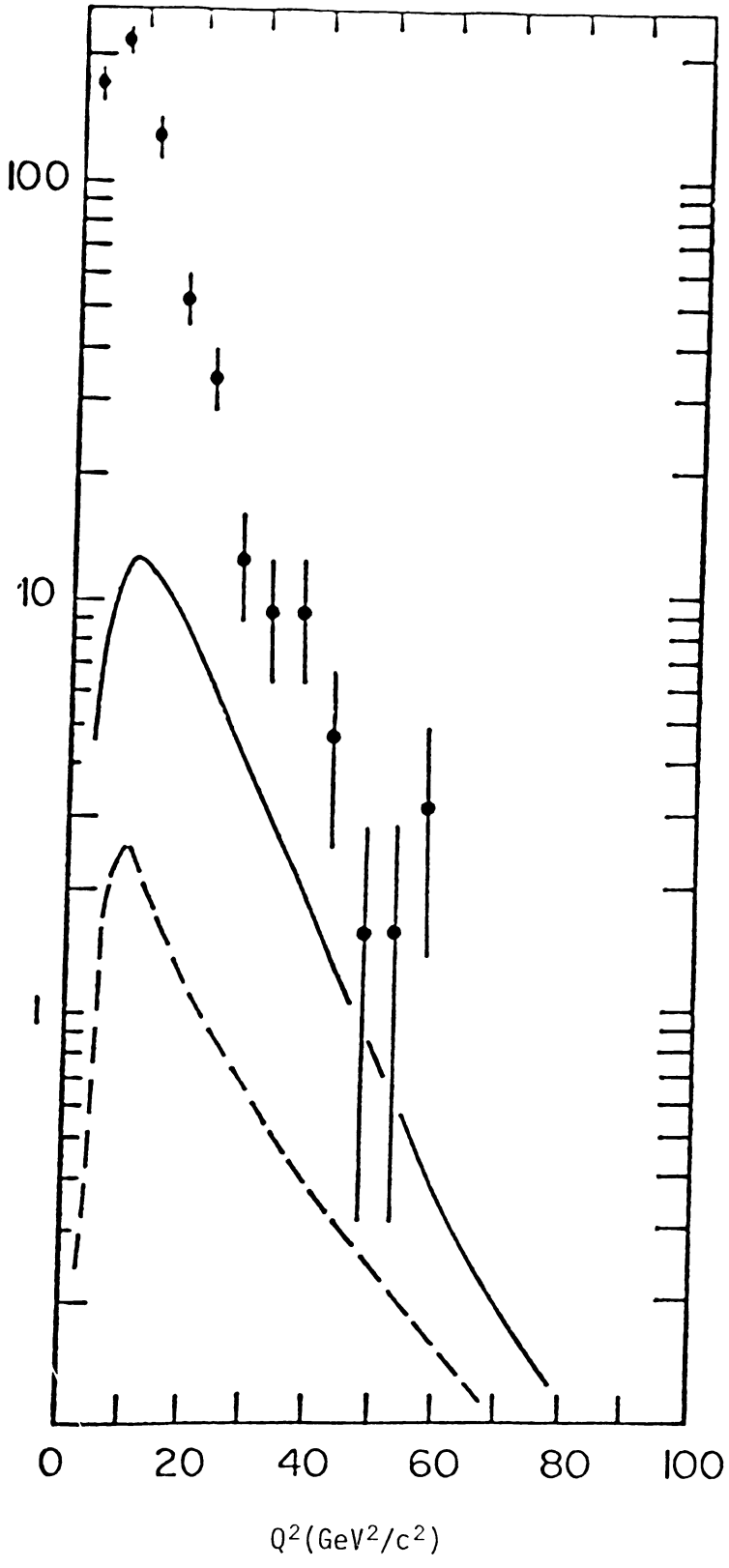

Figure 5.3 Dimuon Q^2 and Background Curves

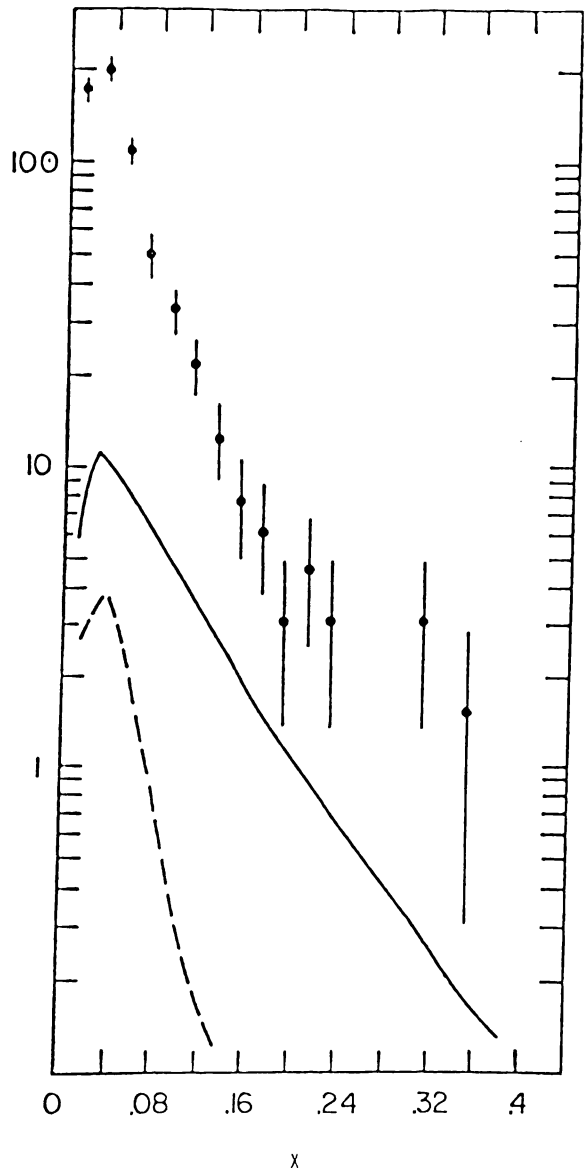

Figure 5.4 Dimuon X and Background Curves

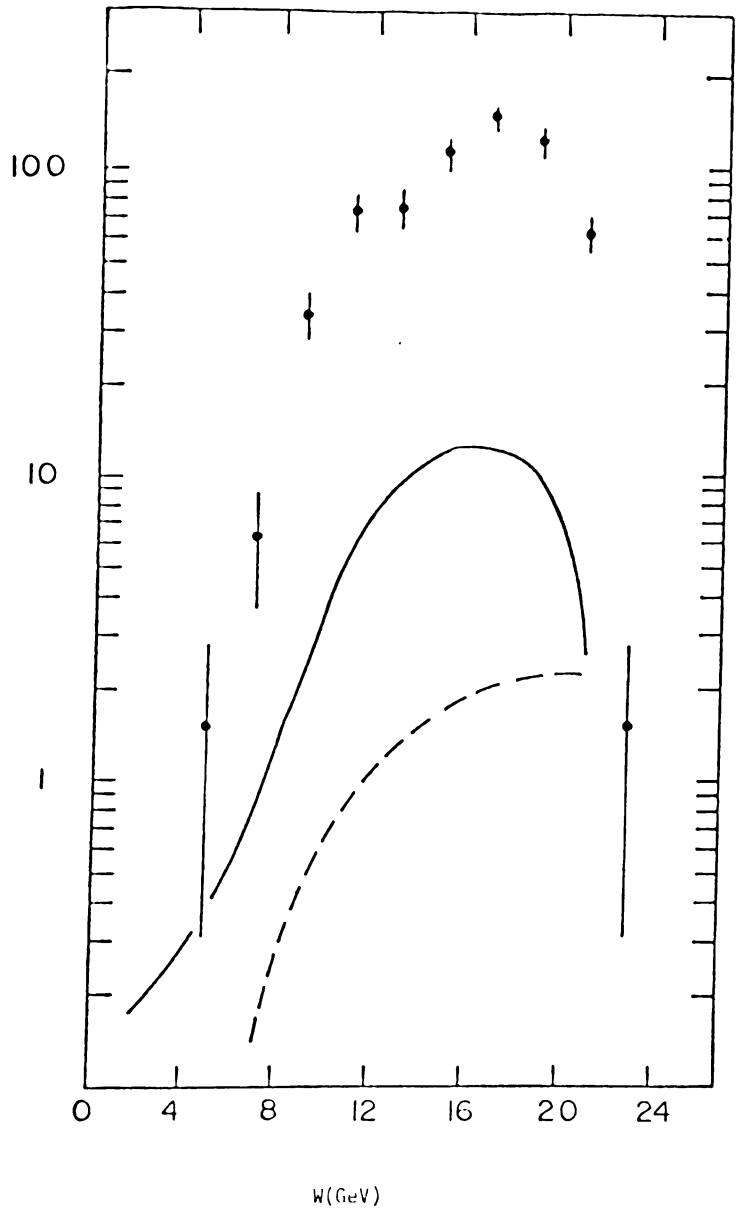

Figure 5.5 Dimuon W and Background Curves

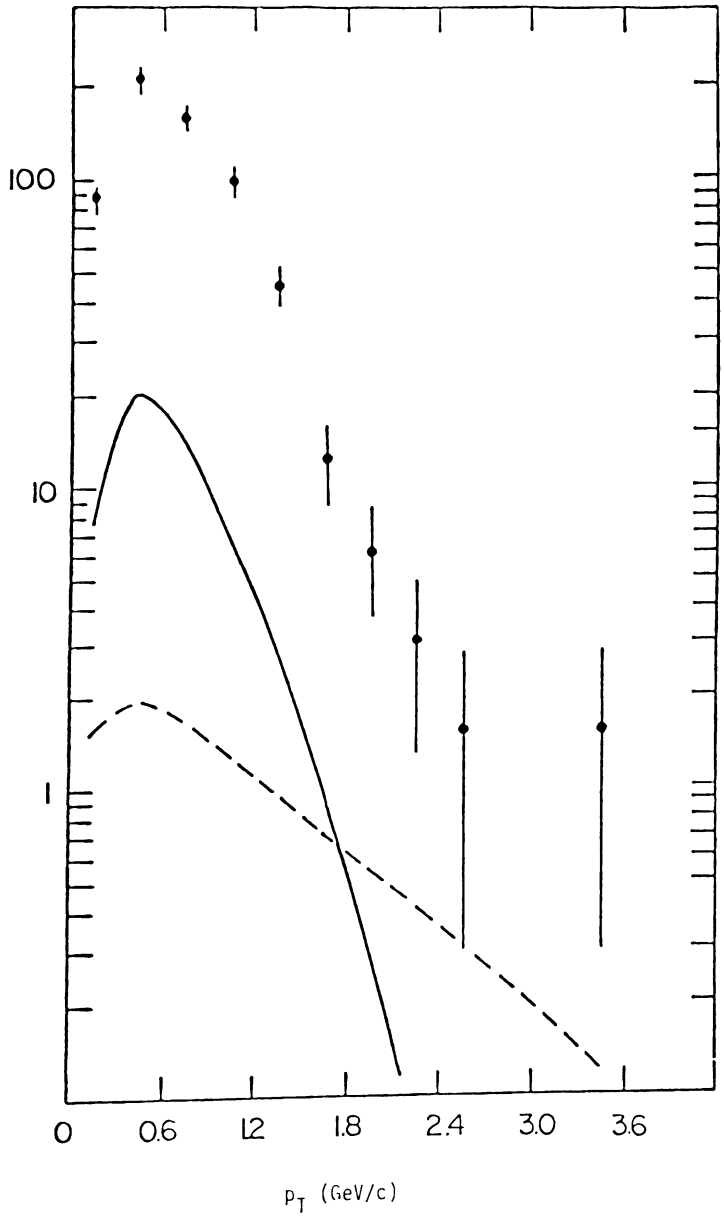

Figure 5.6 Dimuon p_T and Background Curves

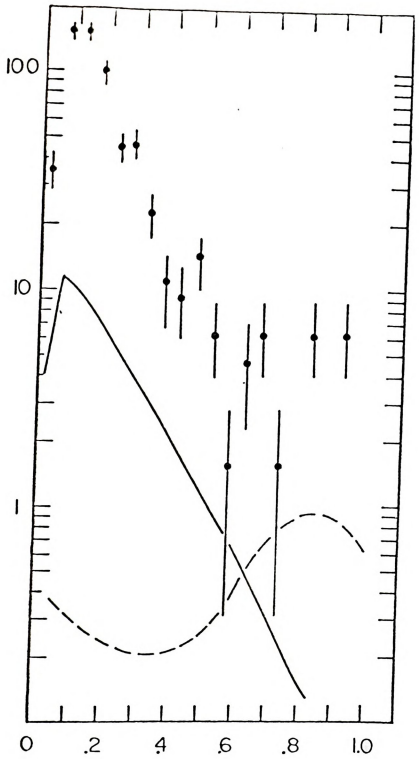

Figure 5.7 Dimuon E_2/ν and Background Curves

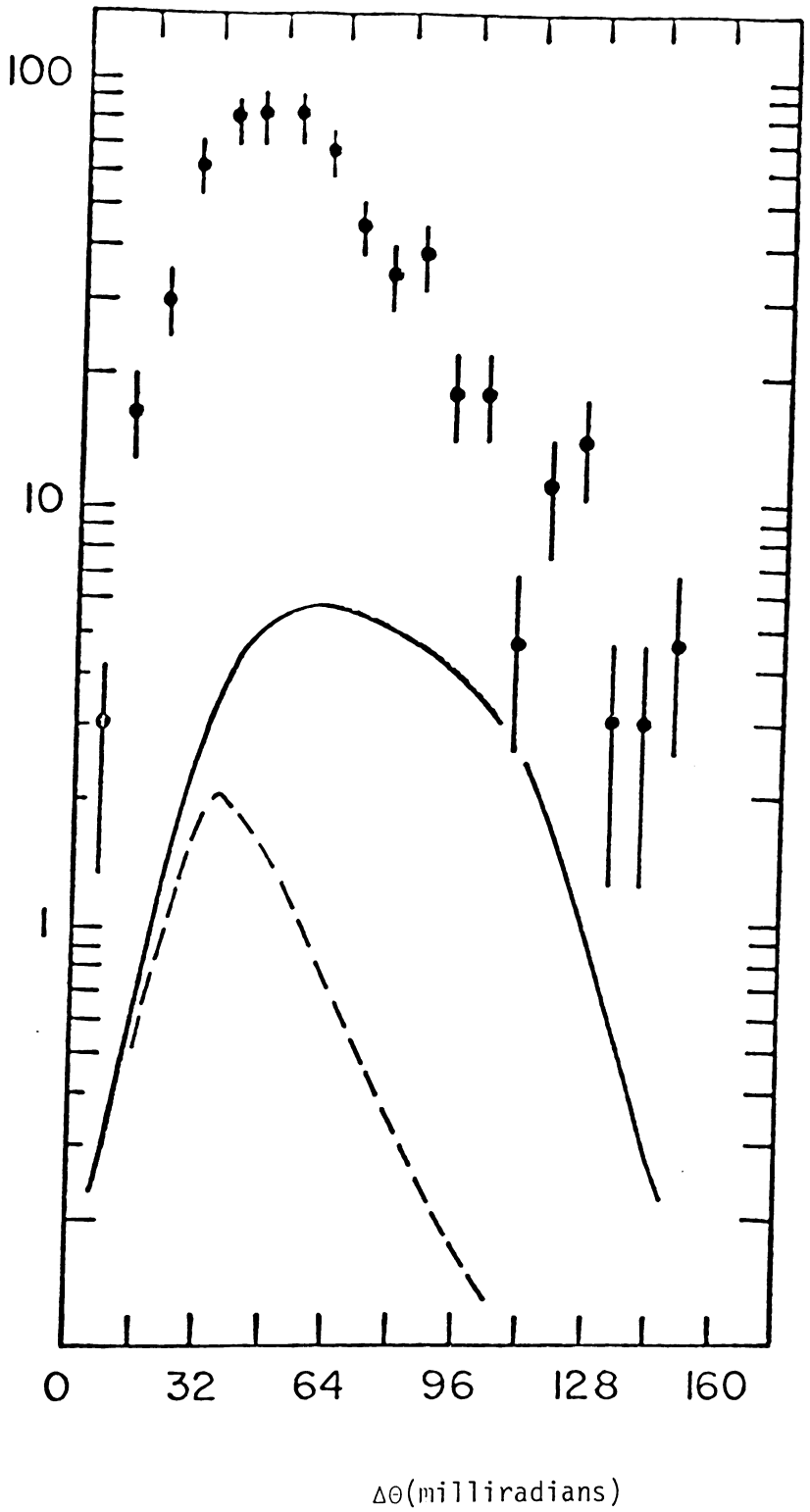

Figure 5.8 Dimuon Δθ and Background Curves

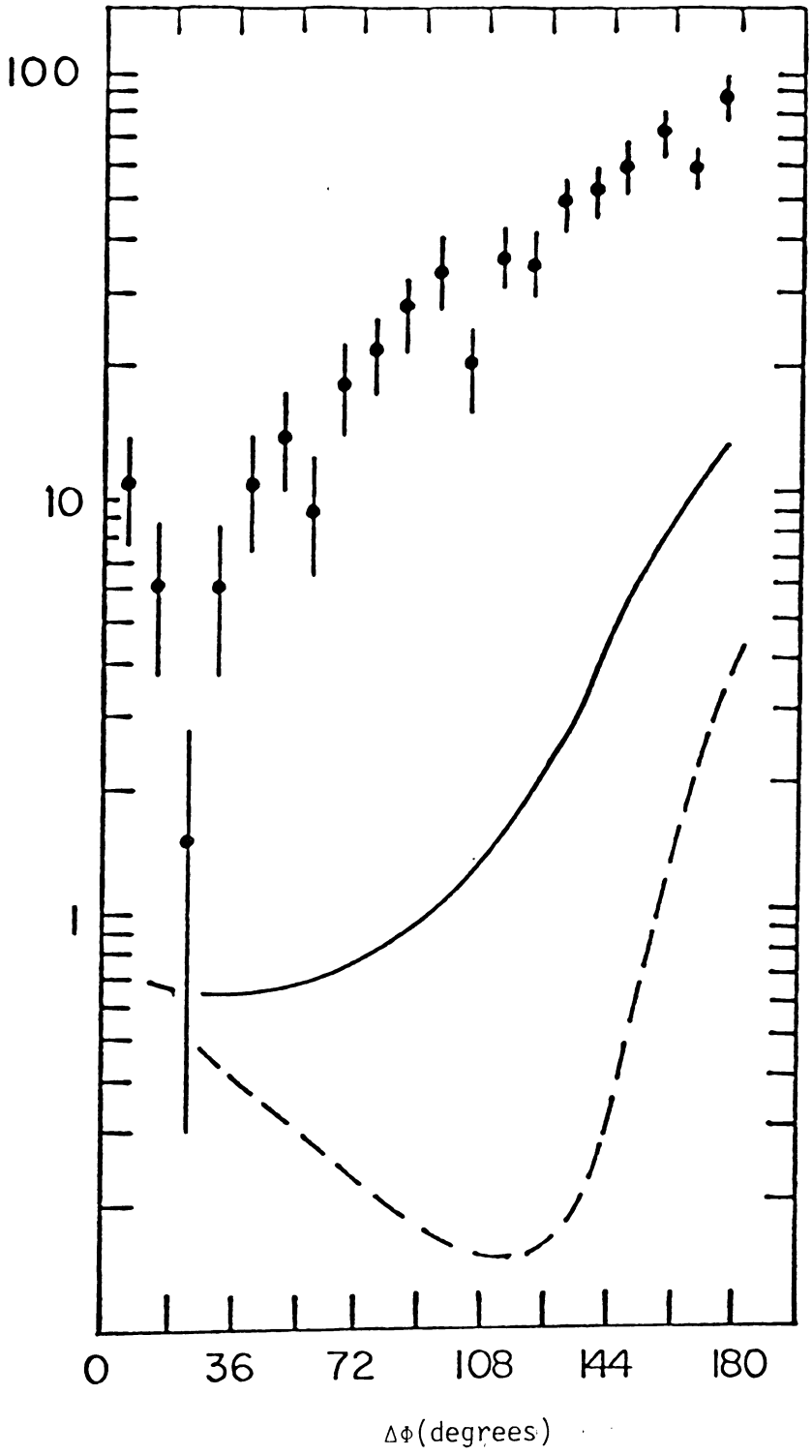

Figure 5.9 Dimuon $\Delta\phi$ and Background Curves

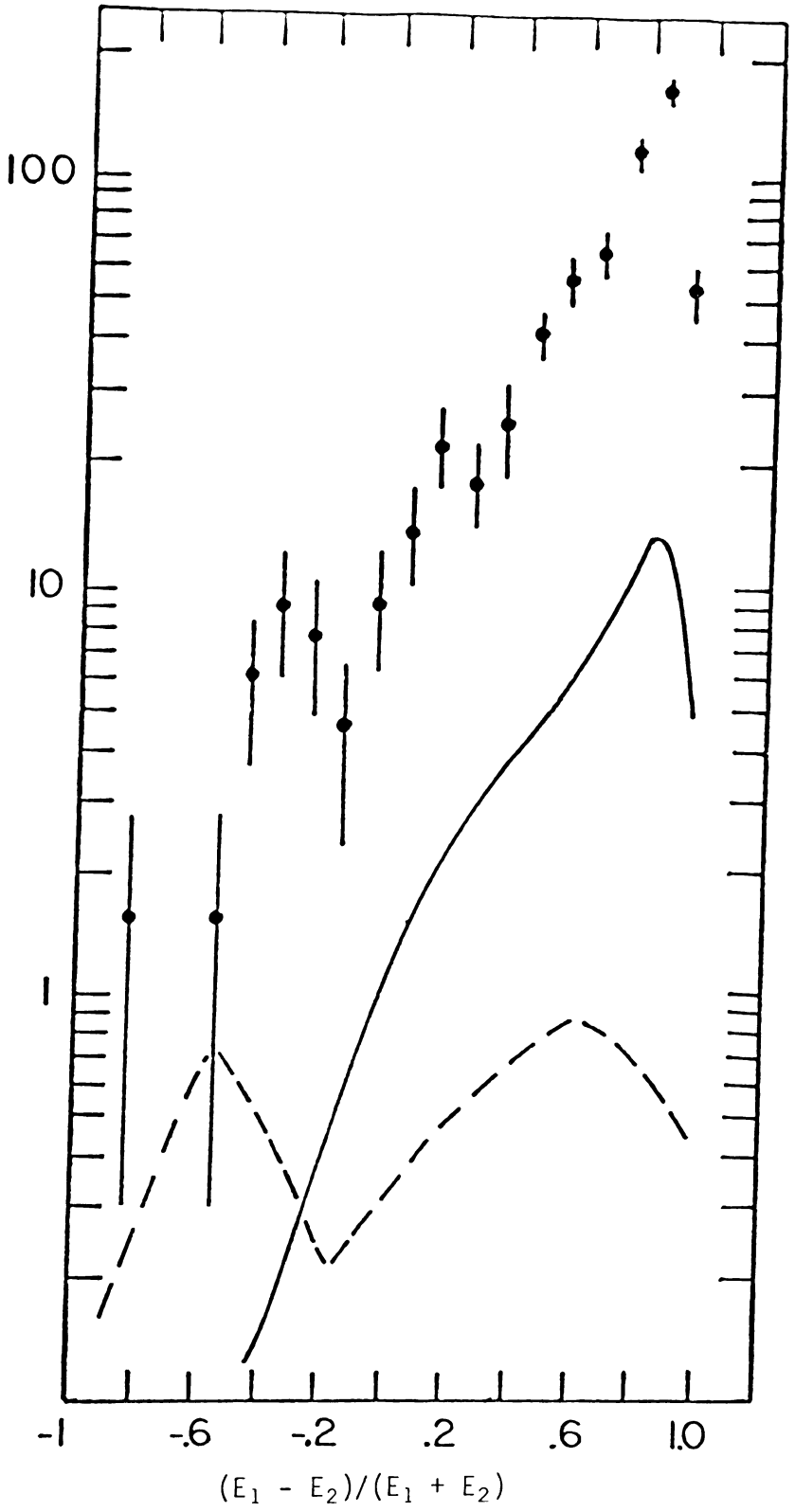

Figure 5.10 Dimuon Asymmetry and Background Curves

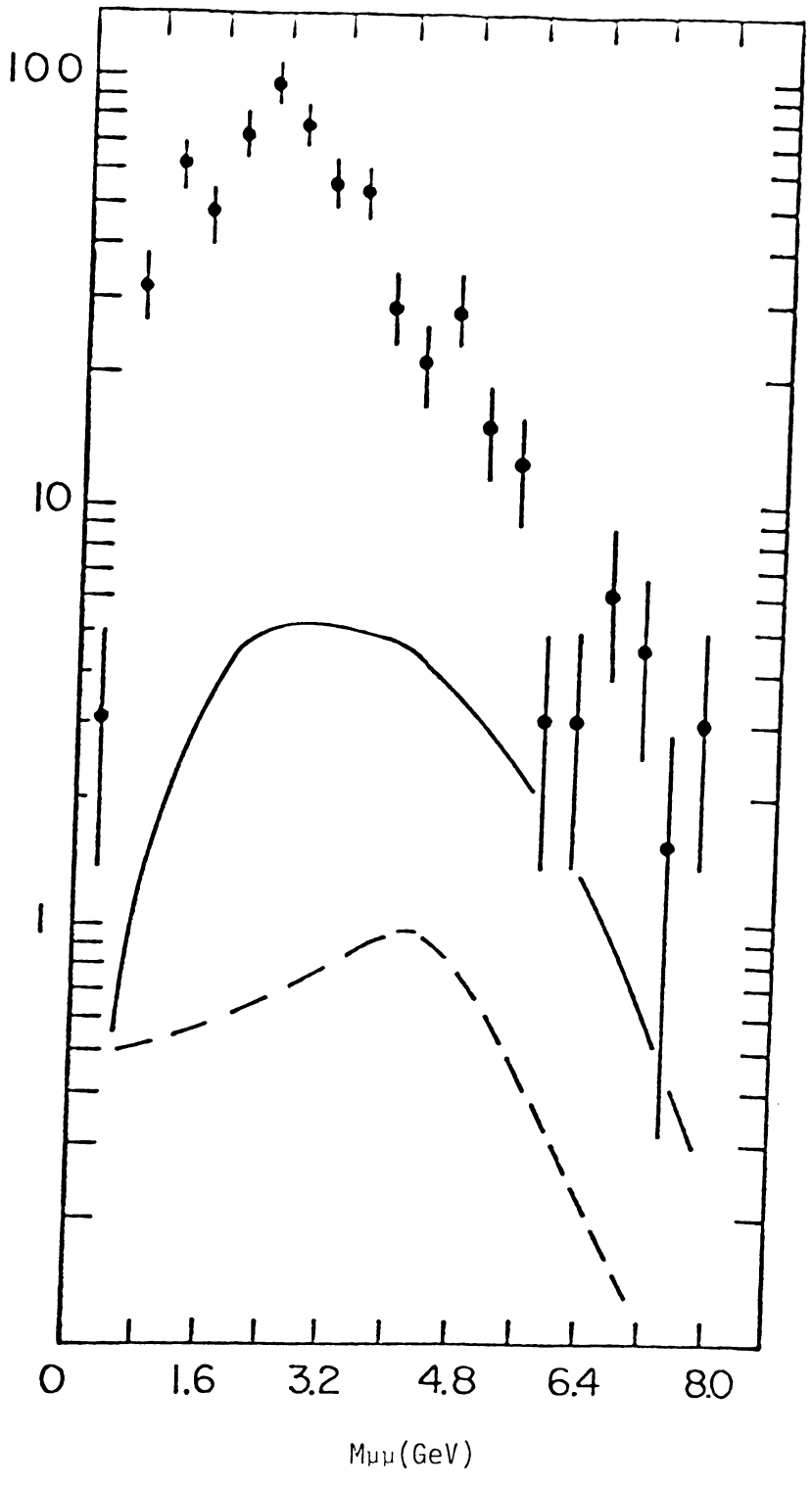

Figure 5.11 Dimuon Mμμ and Background Curves

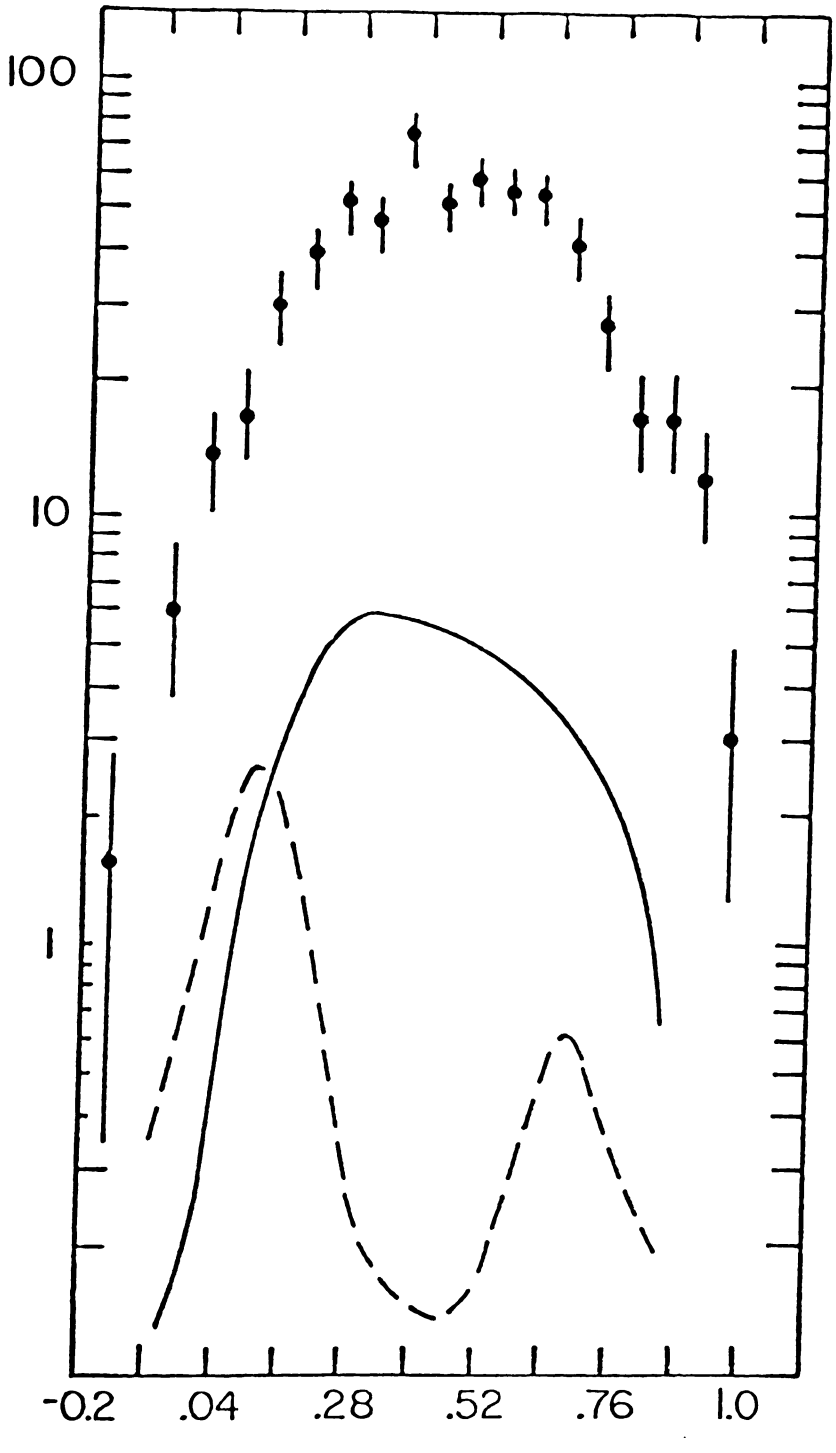

Figure 5.12 Dimuon Inelasticity and Background Curves

Table 5.1. Dimuon Kinematic Averages

	OSP	SSP	Total Dimuon
E_0	269.5 GeV	269.4 GeV	269.5 GeV
E_1	120 GeV	143 GeV	127 GeV
E_2	26.8 GeV	23.6 GeV	25.9 GeV
θ_1	19.4mR	18.5mR	19.1mR
θ_2	38.7mR	57.6mR	43.9mR
Q^2	10.2 GeV^2/c^2	11.8 GeV^2/c^2	10.7 GeV^2/c^2
ν	149.5 GeV	126.0 GeV	143.0 GeV
x	0.041	0.064	0.047
y	0.555	0.468	0.531
ω	43.6	29.3	39.6
W	16.1 GeV	14.6 GeV	15.7 GeV
$P_T(_2)$	0.66 GeV/c	0.85 GeV/c	0.71 GeV/c
$\Delta\theta$	51mR	69mR	56mR
$\Delta\Phi$	124°	133°	127°
$M\mu\mu$	2.39 GeV/c	3.33 GeV/c	2.65 GeV/c
E_1/E_2	7.13	10.06	7.94
inelasticity	0.458	0.385	0.438
E_2/ν	0.183	0.202	0.188
asymmetry	0.584	0.679	0.611
ZADC	239.3 cm	251.7 cm	242.7 cm

Table 5.2. Single Muon Data Cuts

	Cut	% cut by this cut alone	%cut by this cut and not cut by a previous cut
1.	$0 <$ Beam Angle < 2mR	0.7	0.7
2.	$0 <$ Beam Radius < 10 cm	0.08	0.01
3.	243 GeV $<$ Beam Energy $<$ 297 GeV	0.5	0.1
4.	-300 cm $<$ ZMIN < 700 cm	0.9	0.9
5.	$0 <$ DMIN < 5 cm	1.2	1.0
6.	$0 < \chi^2/\text{DOF} < 10$ (for momentum fit)	0.7	0.6
7.	DOF $\geqslant 9$ for momentum fit	20.2	18.1
8.	Radius at Trigger Banks > 15.24 cm	37.0	24.7
9.	Radius at Beam Vetoes > 15.88 cm	12.3	0.3
10.	5mR $< \theta, <$ 1 Rad	9.8	0.1
11.	10 GeV $< E_1 <$ 300 GeV	7.7	1.7
12.	1 GeV$^2/c^2 < Q^2 <$ 500 GeV$^2/c^2$	8.5	0.0
13.	Good Momentum Fit	3.4	3.3

Total cut $\sim$ 51.5%

very large incident radii and angles, which, due to multiple scattering in the target, were deflected into the active aperture of the spectrometer without having undergone a deep inelastic interaction. These cuts also removed halo muons which were very close to the beam region but which did not fire the halo veto counters. Using these cuts on the single muon sample yielded a total of 4.18×10^5 deep inelastic interactions ($\sim$ 51.5% of the initial sample failed to pass these cuts). Similar cuts applied to the leading particle of the dimuon sample yielded 245 events (based on scaling the number of events after cuts from the 412 dimuon sample to the expected total number of 644 dimuons). Using the corrected numbers after cuts, the ratio of dimuon to single muon events was $(5.9 \pm 0.6) \times 10^{-4}$, see Table 5.3. Average kinematic values for the 270 GeV $\mu+$ single muon data (after cuts) are shown in Table 5.4.

Plots comparing Q^2, x, W, and y for the single muon sample after cuts (solid line), the raw dimuon sample (dashed line), and the raw dimuon sample after cuts (cross-hatched) are shown in Figure 5.13. The numbers on the left of each plot refer to the single muon curve, while the numbers on the right side of each plot refer to the dimuon curves. The leading particle distributions for dimuon events are peaked at larger values of W and y than the single muon distributions, suggesting that more energy had to be available at the hadronic vertex for dimuon events than for single muon events. This was to be expected if the dimuon events were due to the production and semileptonic decay of heavy particles (i.e. charmed mesons) at the hadronic vertex. The leading particle distributions for dimuon events are also peaked at higher Q^2 and lower x than the single muon distributions, which suggest

Table 5.3. Single Muon Rates

Event Type	Number Before Cuts	Number After Cuts
1. Single Muon (corrected)	8.87×10^5	4.18×10^5
2. Dimuon		
a. Momentum Analyzable	412 ± 20	157 ± 8
b. Corrected	644 ± 61	245 ± 23
3. Trimuons		
a. Momentum Analyzable	36 ± 6	8 ± 1
b. Corrected	72 ± 13	16 ± 3

Using the corrected numbers after cuts yield:

Dimuon Rate/Single Muon Rate = $(5.9 \pm 0.6) \times 10^{-4}$

Trimuon Rate/Single Muon Rate = $(3.8 \pm 0.7) \times 10^{-5}$

Table 5.4. Single Muon Kinematic Averages

Kinematic Variable	Average After Cuts
E_0 (Beam Energy)	269.1 GeV
θ_0 (Beam Angle)	0.69mR
E_1 (Scattered Energy)	162.8 GeV
θ_1 (Scattered Angle)	18.2mR
Q^2 (4-Momentum Transfer Squared)	12.9 GeV^2/c^2
ν (Energy Transfer)	108.2 GeV
x (Bjorken Scaling Variable)	0.084
y (ν/E_0)	0.411
ω ($1/x$)	22.2
W (cm Energy)	13.3 GeV
DMIN	0.58 cm
ZMIN (z of interaction using tracks)	113.0 cm
ZADC (z of interaction using calorimeter)	111.3 cm
EHAD (energy in hadron shower)	86.2 GeV
χ^2/DOF (for momentum fit)	1.23
NDOF (for momentum fit)	12.9

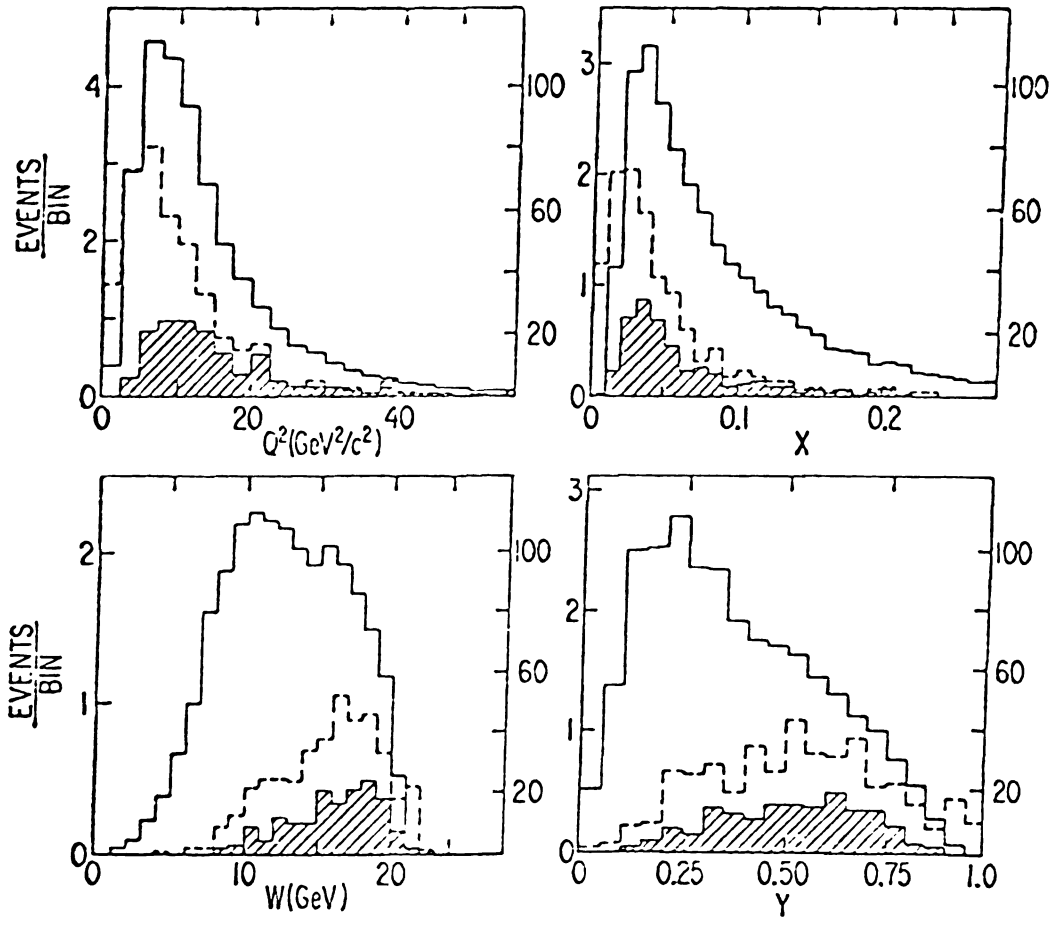

Figure 5.13 Single Muon and Leading Particle Distributions

that the virtual photon scattering may be occurring off sea quarks (i.e. c or $\bar{c}$ quarks) rather than valence quarks (i.e. u and d quarks), since sea quarks occur at much lower x values than do valence quarks.

Finally, the calorimeter information for the dimuon sample will be considered. The calorimeter vertex information is summarized in Table 5.5 for the 270 GeV μ+ data sample. As expected, most of the events were accompanied by hadronic showers in the calorimeter, which would be the case if the second muon were the result of the production and semileptonic decay of a heavy particle (and is inconsistent with elastic QED trident production or vector meson production and decay). The interaction vertex (ZADC) found using calorimeter information is shown in Figure 5.14 for single muon data and Figure 5.15 for the dimuon sample. The ZADC distribution is peaked further downstream for dimuons than for single muon interactions, since the high angle, low energy produced muons have a much higher acceptance when produced further downstream in the target. If the dimuon events were due to incident beam pion interactions or decays, the dimuon ZADC distribution would have been expected to peak near the front of the target (which it did not), or if the dimuon events were due to nuclear cascade pion decays (pions produced in the hadronic showers of deep inelastic muon interactions), the dimuon ZADC distribution would have been expected to peak near the end of the target (which was not observed).

The ADC's can be used to indicate how many particles were in the target before and after the interaction vertex. Using the high gain ADC's, the average number of particles in the calorimeter before and after the hadronic shower was computed, the results of which are shown in Figure 5.16 for deep inelastic single muon scattering and in

Table 5.5. Dimuon Calorimeter Vertex Information

	Total	Hadronic Shower	Leptonic Vertex	Uncertain
Found OSP	324	300	17	7
Found SSP	125	117	6	2
Found Dimuon	449	417	23	9
Momentum Analyzable OSP	298	280	14	4
Momentum Analyzable SSP	114	107	5	2
Momentum Analyzable Dimuon	412	387	19	6

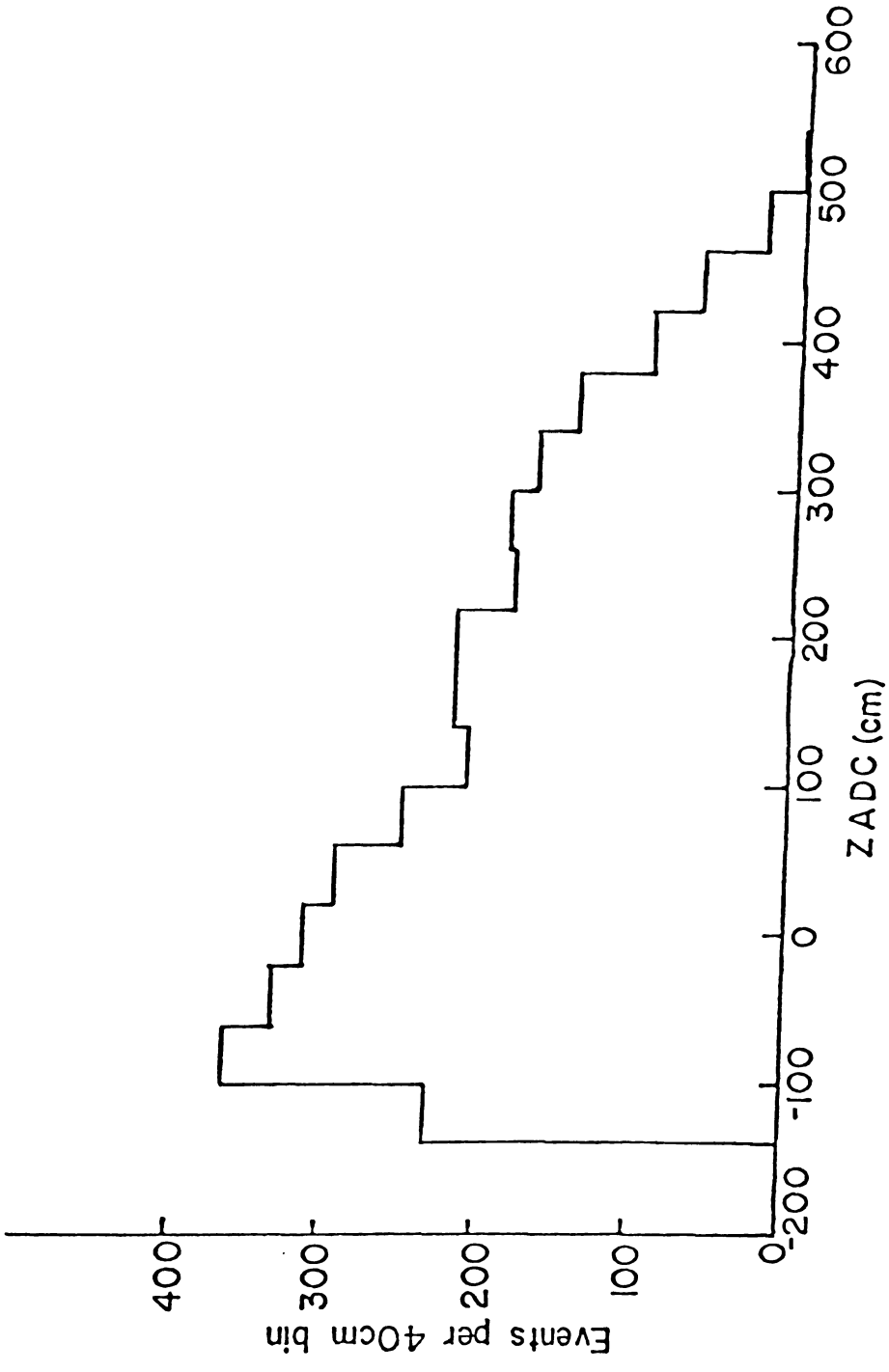

Figure 5.14 Single Muon ZADC Distribution

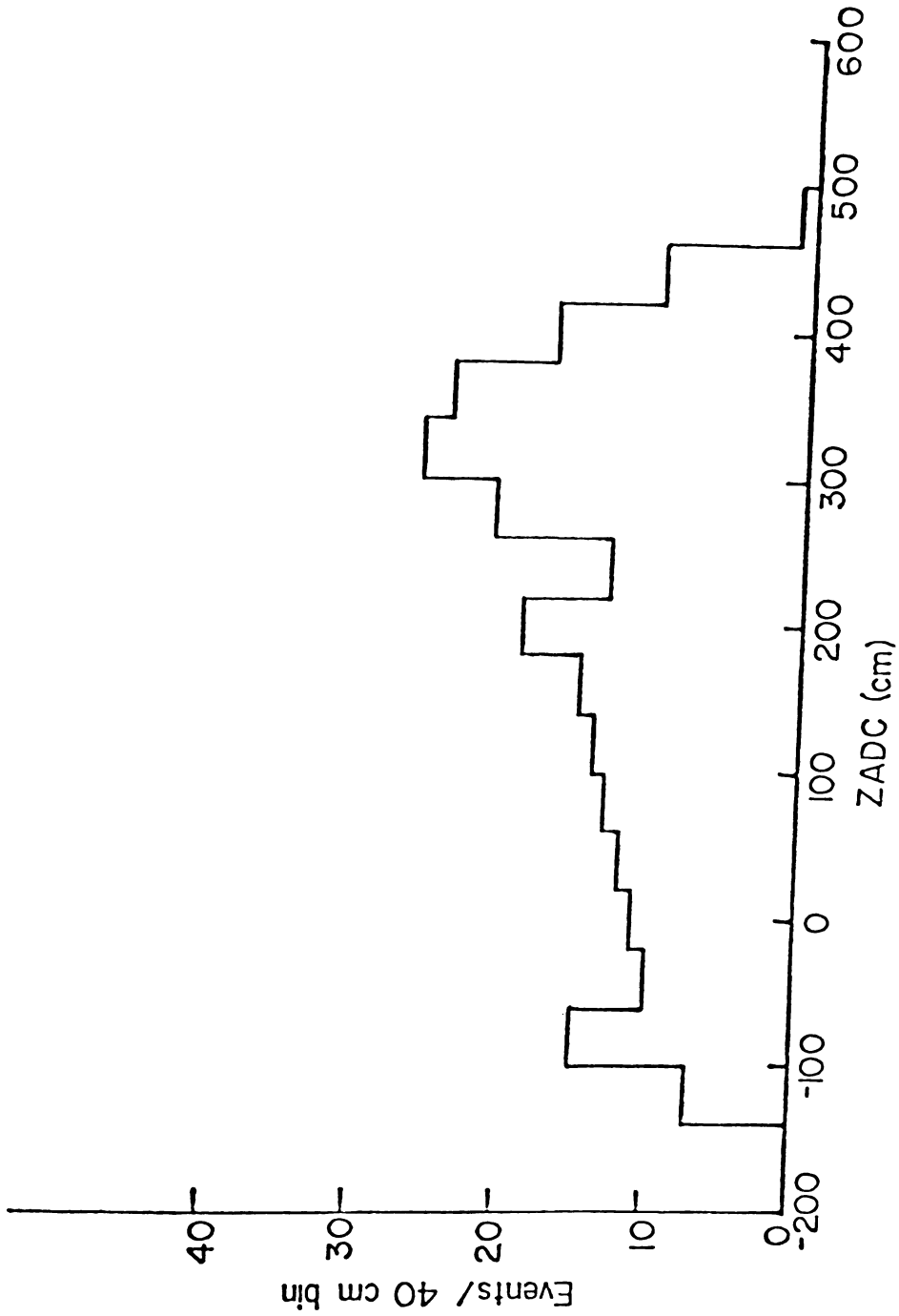

Figure 5.15 Dimuon ZADC Distribution

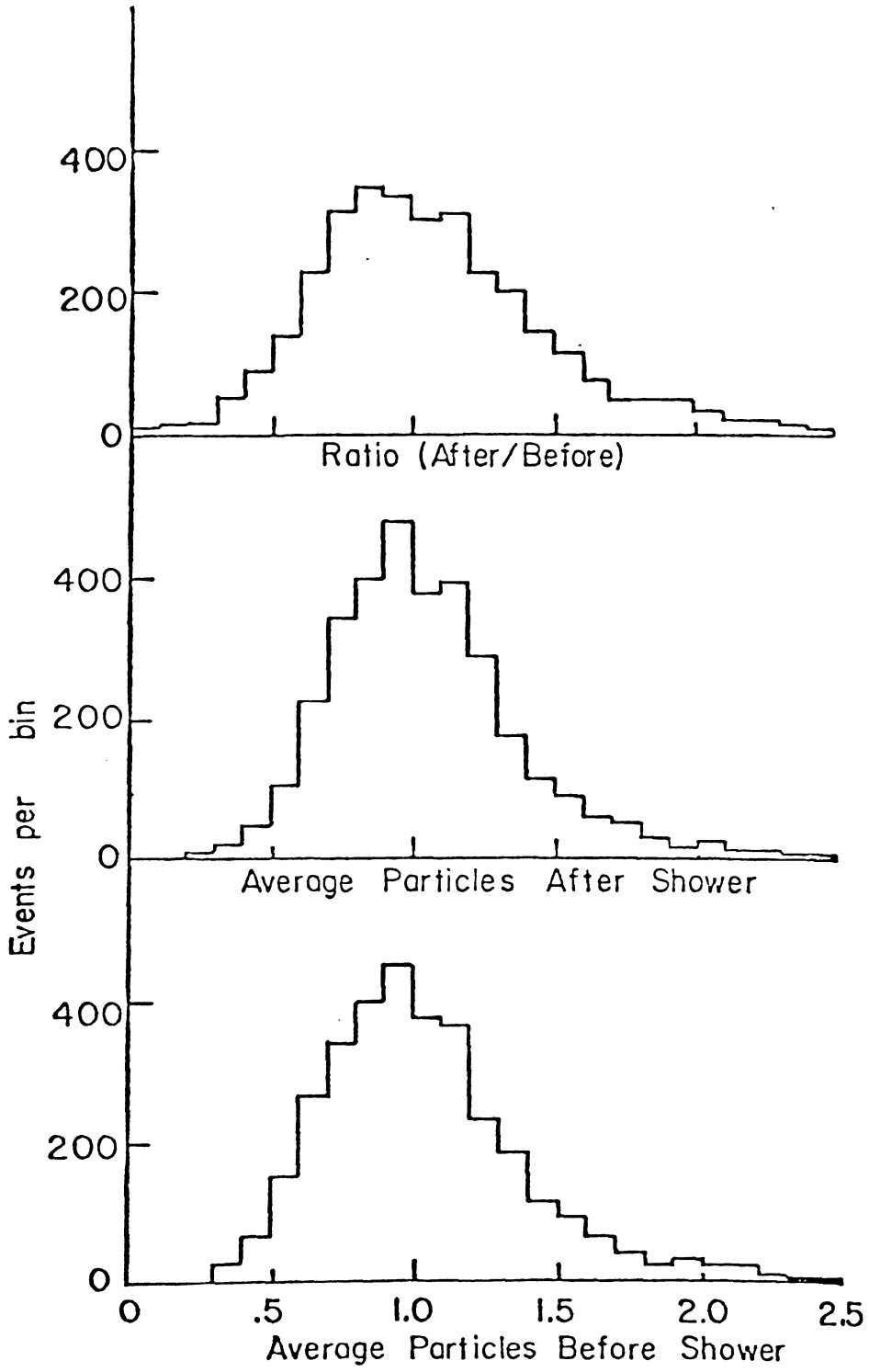

Figure 5.16 Single Muon Calorimeter Distributions

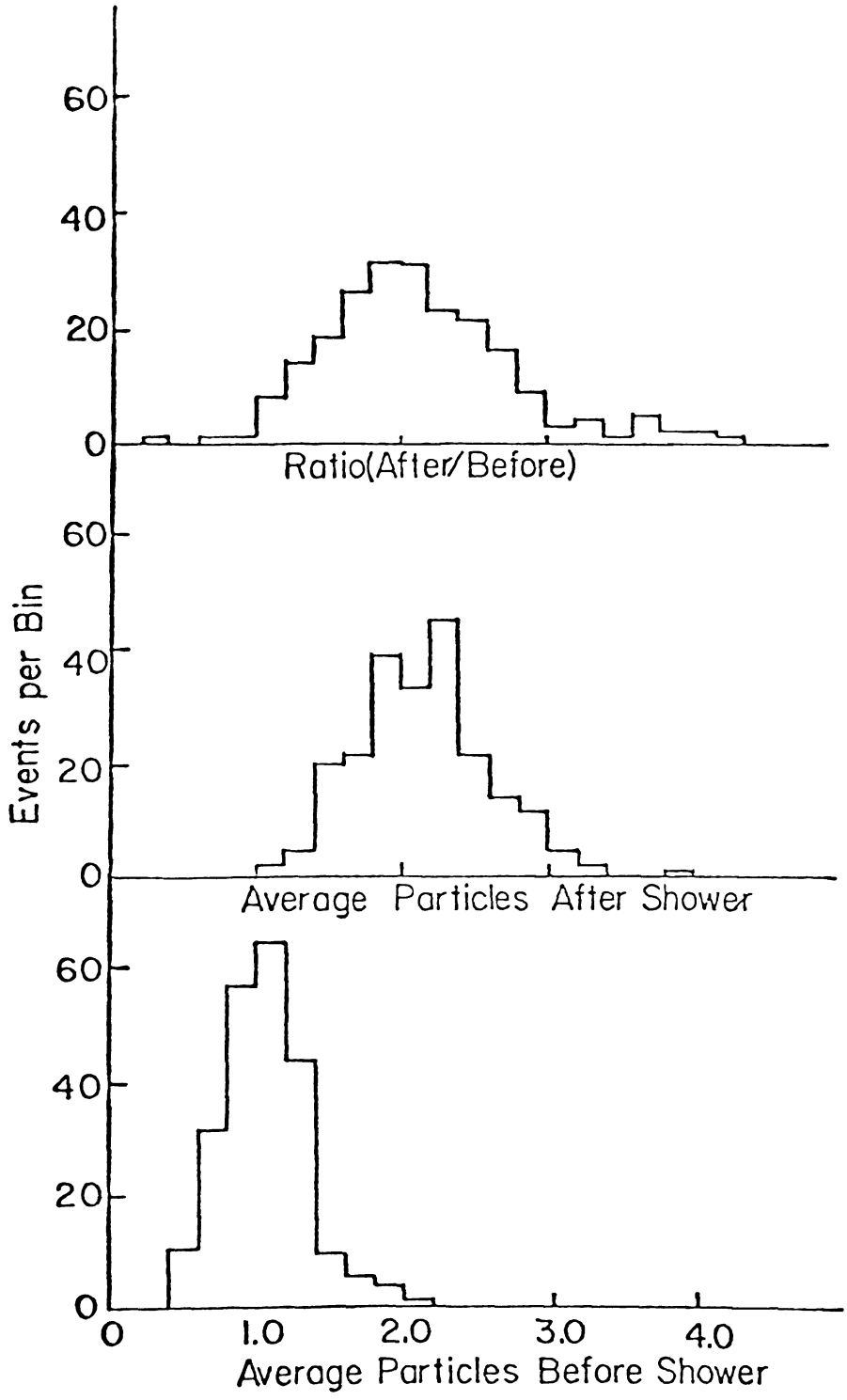

Figure 5.17 Dimuon Data Calorimeter Distributions

Figure 5.17 for the dimuon sample. The single muon distributions show peaks at one particle before and after the hadronic shower, while the dimuon distributions show peaks at one particle before and two particles after the hadronic shower.

If the dimuon events were due to the production and semileptonic decay of heavy particles (i.e. charmed mesons), then, on the average, there should be a missing energy due to decay neutrinos which are not measured in the calorimeter or spectrometer. To check this, we first look at the single muon sample, where no missing energy was expected. Defining $E_m = (E_0 - E_1) - E_H = \nu - E_H$, where the average energy loss of the incoming muon has been subtracted from E_0 (which was measured at the front of the target) and the average energy loss for the scattered muon has been added to E_1 (which was measured at the back of the target), we obtain the distribution shown in Figure 5.18. The mean of this distribution is (2.7 ± 2) GeV, and its width σ is (22.5 ± 5) GeV. Given the average spectrometer resolution ($\Delta E/E \sim$ 10%) and the calorimeter resolution[1] ($\Delta E_H/E_H \propto 1/(E_H)^{\frac{1}{2}}$, which averages 10-15%), the expected width of the missing energy distribution was $\sim$ 20%, consistent with the above results. The single muon distribution was consistent with zero missing energy and had a width consistent with the combined spectrometer and calorimeter resolutions. For the dimuon events, we define $E_m = E_0 - E_1 - E_2 - E_H = \nu - E_2 - E_H$, where all muon energies were again corrected for energy losses in the target. This distribution for the dimuon events is shown in Figure 5.19; the mean dimuon missing energy being 5.9 GeV, with a peak value of (10 ± 4) GeV and a width σ of about 30 GeV.

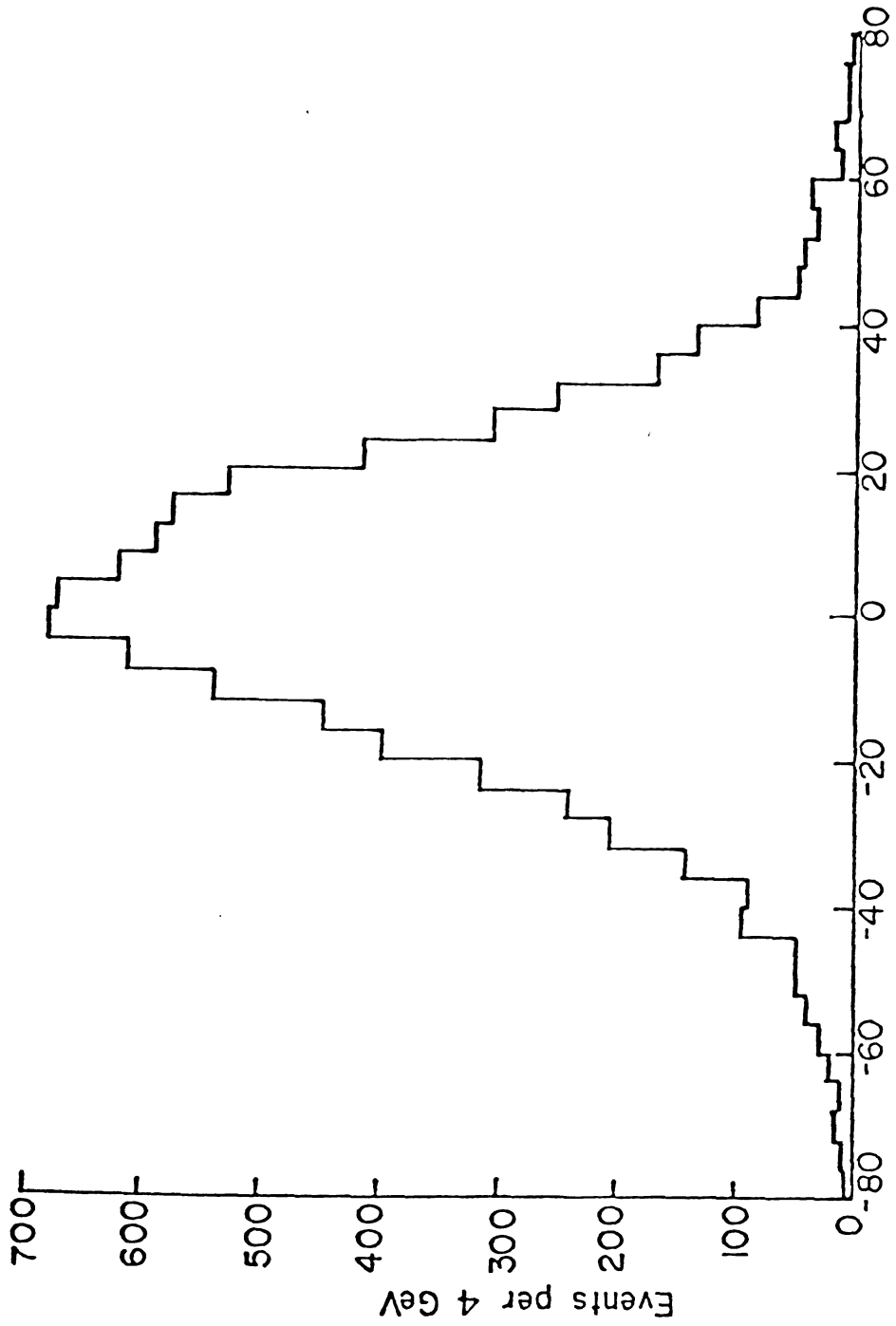

Figure 5.18 Single Muon Missing Energy Distribution

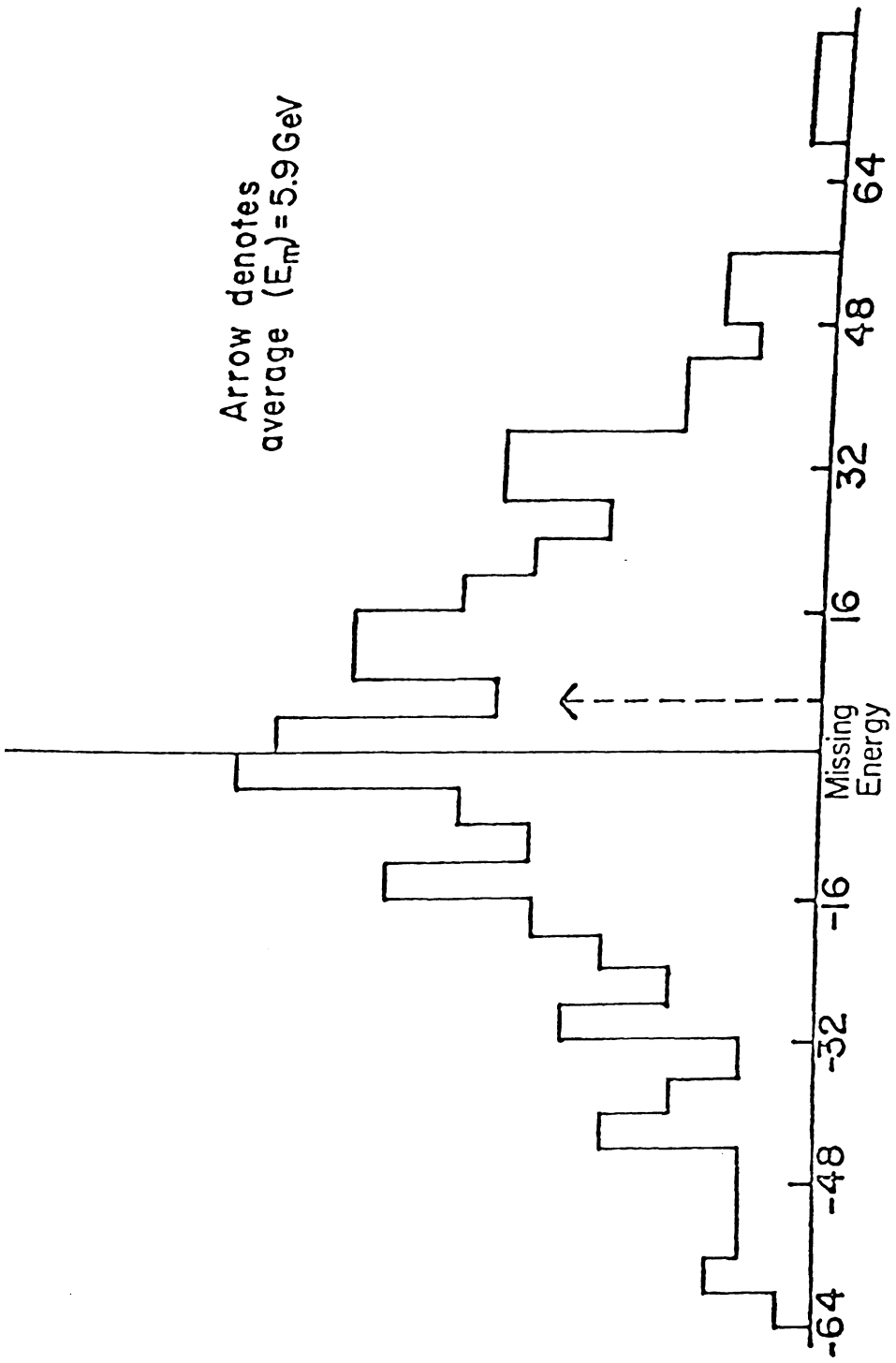

Figure 5.19 Dimuon Data Missing Energy Distribution

More information can be obtained by looking at the missing energy (E_m) versus the hadronic energy (E_H) for these two data samples. This is shown for single muons in Figure 5.20 and for dimuons in Figure 5.21. The single muon missing energy was consistent with zero, except at very large hadronic energies, where the scattered muon energy becomes very small (i.e. poor spectrometer resolution) and the hadronic energy becomes very large (poor calorimeter resolution due to shower leakage from the calorimeter). The dimuon distribution shows an increase of missing energy with hadronic energy, consistent with the production and decay of heavy particles (which yield neutrinos which are not accounted for in our energy measurements).

5.2 Monte Carlo Results

In this section, the results of the Monte Carlo calculations performed for E319 will be shown. The π/K internuclear cascade decay and prompt muon production backgrounds, calculated using CASIM[3], yielded a total of 55.8 dimuon events after acceptance (30.4 events from pion decays, 8.1 events from kaon decays, 10.8 events from prompt muon production at the interaction vertex, and 6.5 events from prompt muon production in the nuclear cascade). The kinematic distributions for these events are shown as the solid curves of Figures 5.1 - 5.12. The elastic QED trident background, calculated using the computer code of Brodsky and Ting[4], yielded a total of 10.3 dimuon events after acceptance. This background was severely suppressed for our experiment by the beam veto counters, which vetoed most of the possible events with very low angle produced muons. The kinematic distributions for this process are shown in Figures 5.1 - 5.12 as the dashed curves.

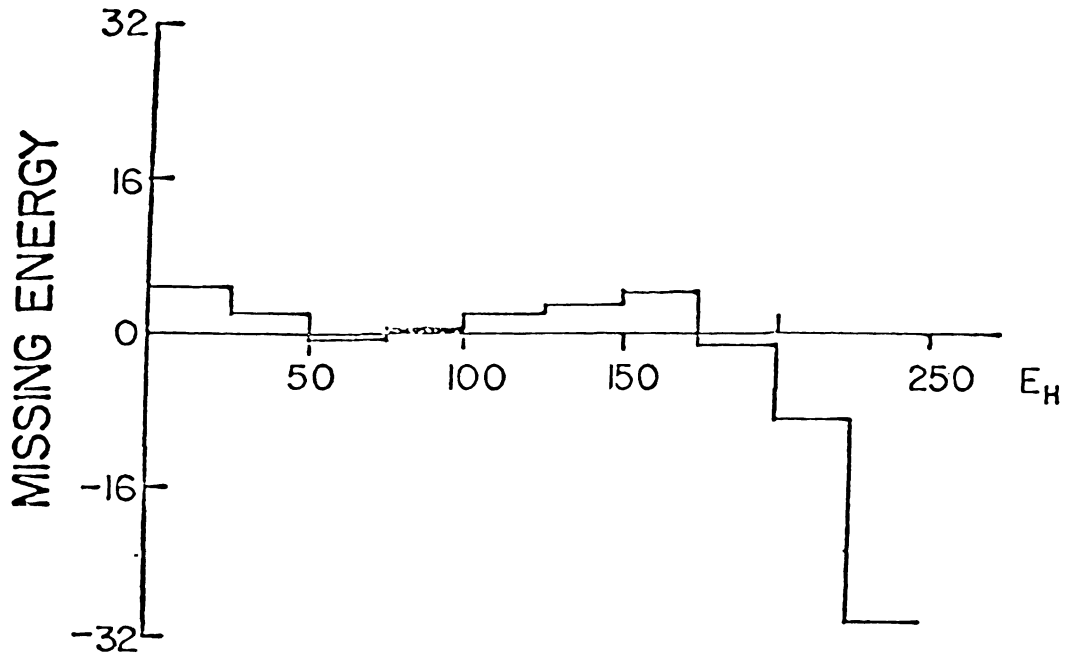

Figure 5.20 Single Muon Missing Energy versus Hadronic Energy

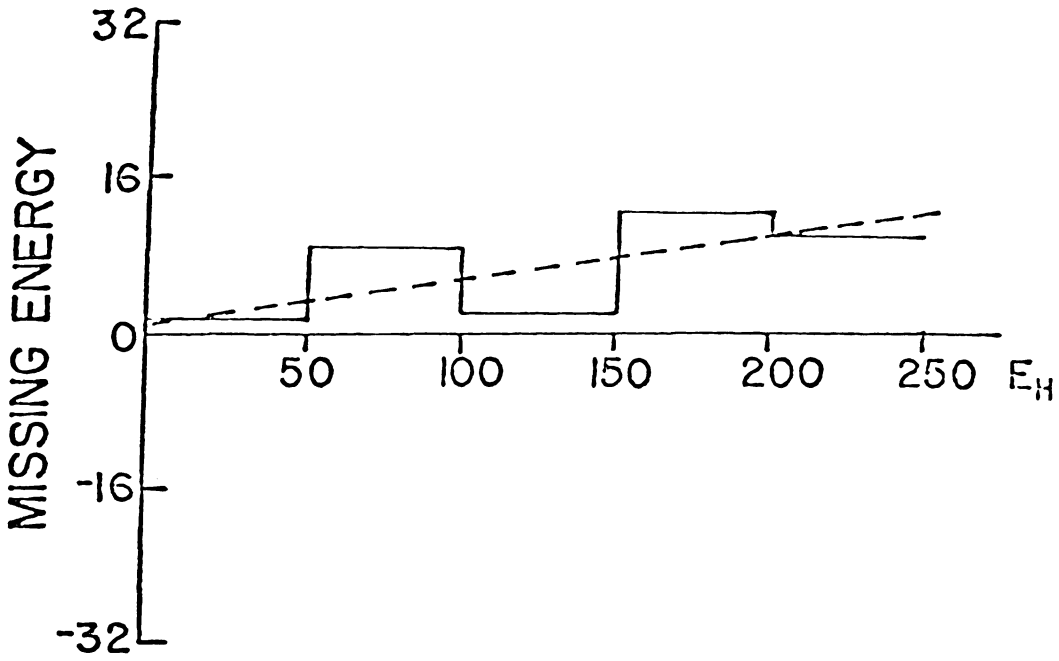

Figure 5.21 Dimuon Data Missing Energy versu Hadronic Energy

These backgrounds were the largest which could yield dimuon events. Independent calculations[5] of vector meson production (i.e. ψ mesons) and leptonic decay showed this background to be extremely small (even before acceptance cuts were applied). A look at the E319 trimuon data[1] in the region of the $\psi(3100)$ yielded $\sim 6 \pm 3$ trimuon events which could be ψ's, hence the ψ's contribution to the dimuon sample was expected to be vanishingly small.

Assuming that all of the remaining data events were due to the associated production and semileptonic decay of charmed mesons (i.e. D and $\bar{D}$ mesons), the above backgrounds were subtracted (bin by bin) from the scaled raw dimuon distributions (shown in Figures 5.1 - 5.12) to obtained the data distributions (shown in Figures 5.22 - 5.33) for charmed events. These distributions can be compared with our Monte Carlo predictions (using the Nieh[6] model) which are shown as the solid curves in Figures 5.22 - 5.33. The $D\bar{D}$ curves have been normalized to the number of data dimuon events (corrected for finding efficiency) minus the above mentioned backgrounds, since the Nieh model is unnormalized and does not yield absolute rates. All of the above distributions were calculated with the choice of Nieh model parameters a = 1 and b = 0.25. The $D\bar{D}$ model predicted 12 trimuon events, given the above normalization of the dimuon data. To show the Nieh model's relative insensitivity to the choice of model parameters, the P_T spectra for five values of the parameter b (which fixed the P_T behaviour of the production model) are shown in Table 5.6.

5.3 P_T Acceptance and Charm Cross Section

Once the total number of dimuons due to charm production was known, as well as the total luminosity for the experiment, the cross

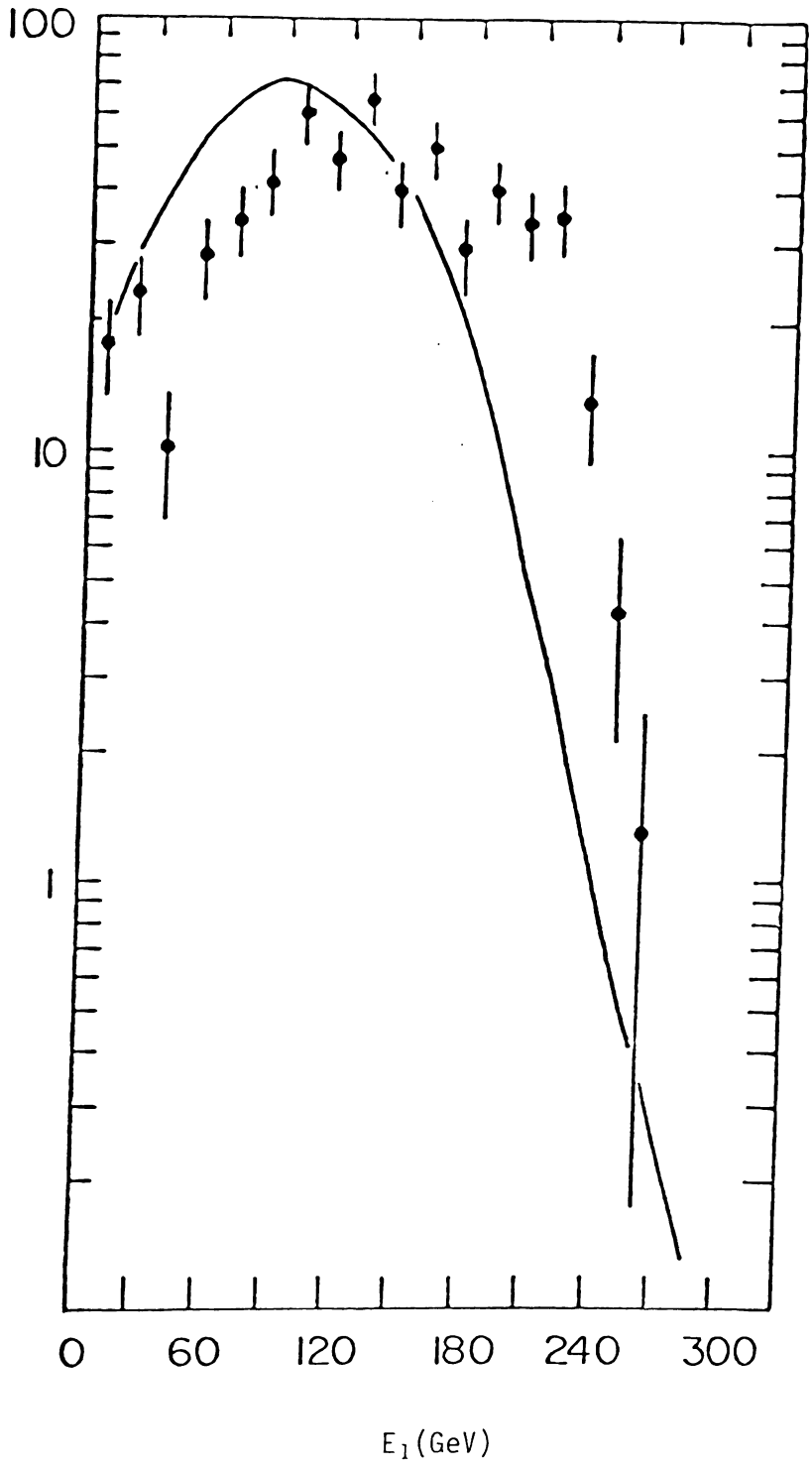

Figure 5.22 Dimuon Subtracted E_1 and $D\bar{D}$ Model Curve

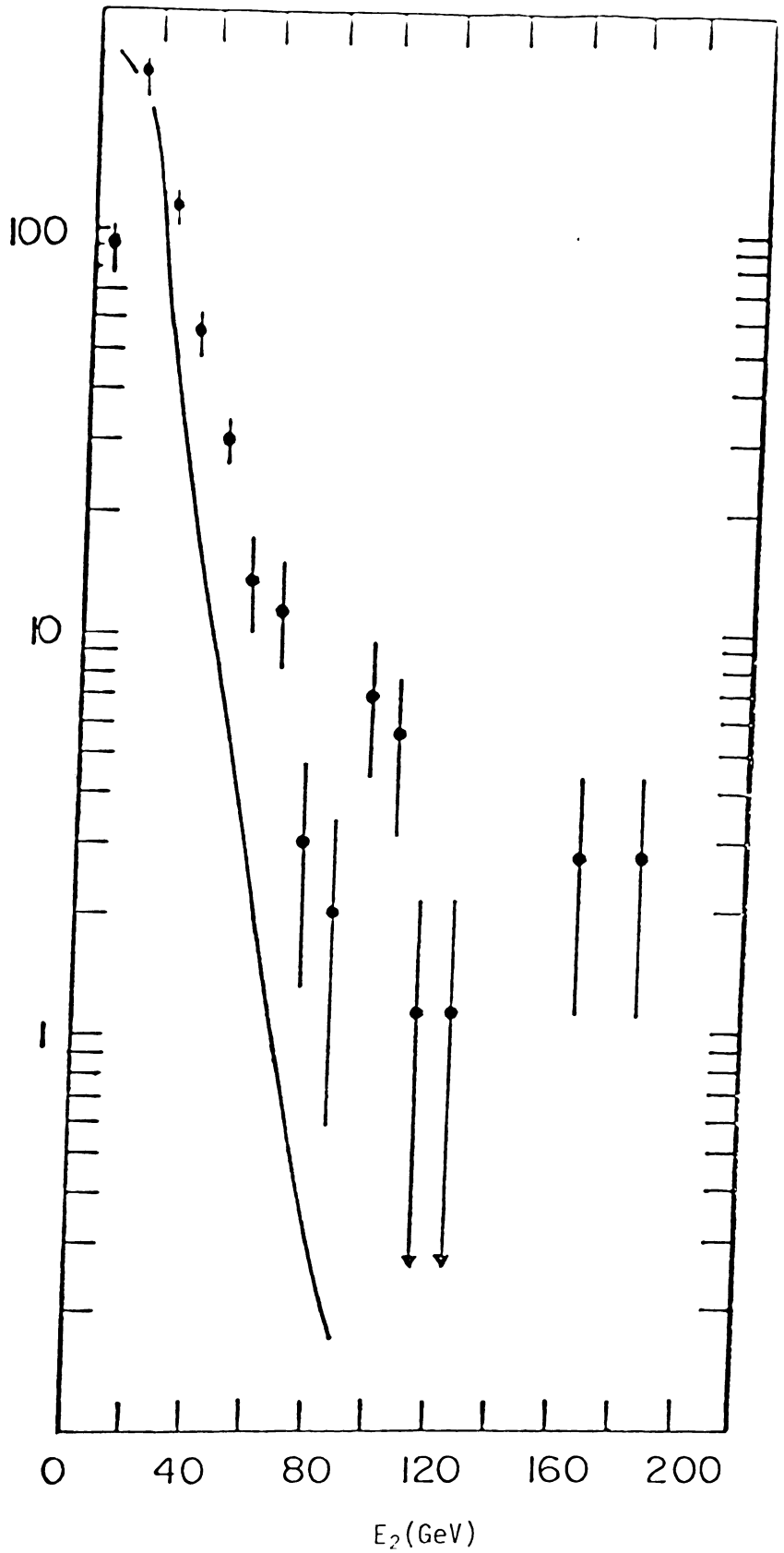

Figure 5.23 Dimuon Subtracted E_2 and $D\bar{D}$ Model Curve

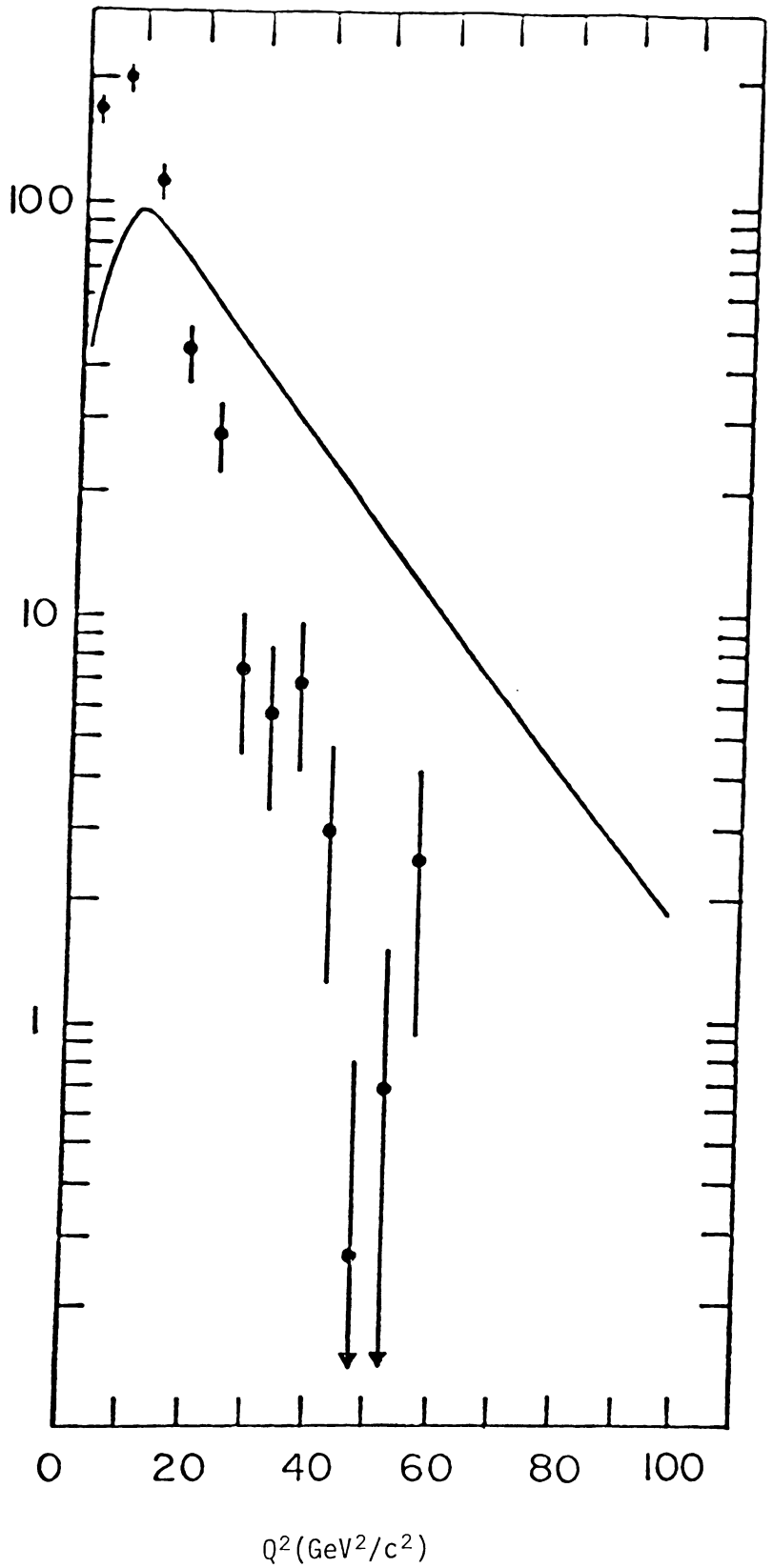

Figure 5.24 Dimuon Subtracted Q^2 and $D\bar{D}$ Model Curve

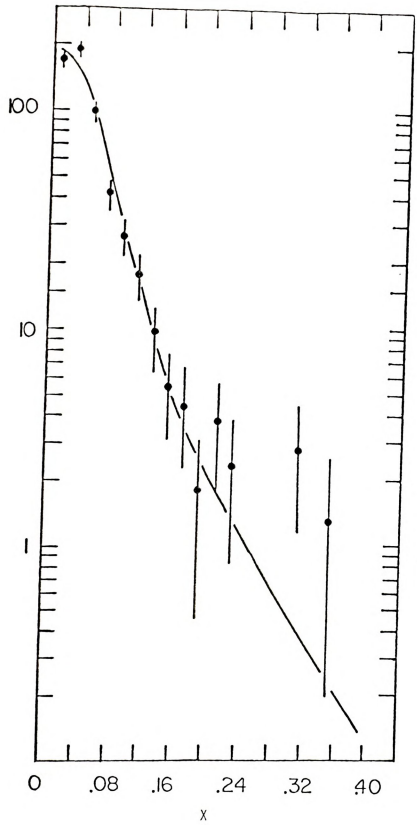

Figure 5.25 Dimuon Subtracted x and $D\bar{D}$ Model Curve

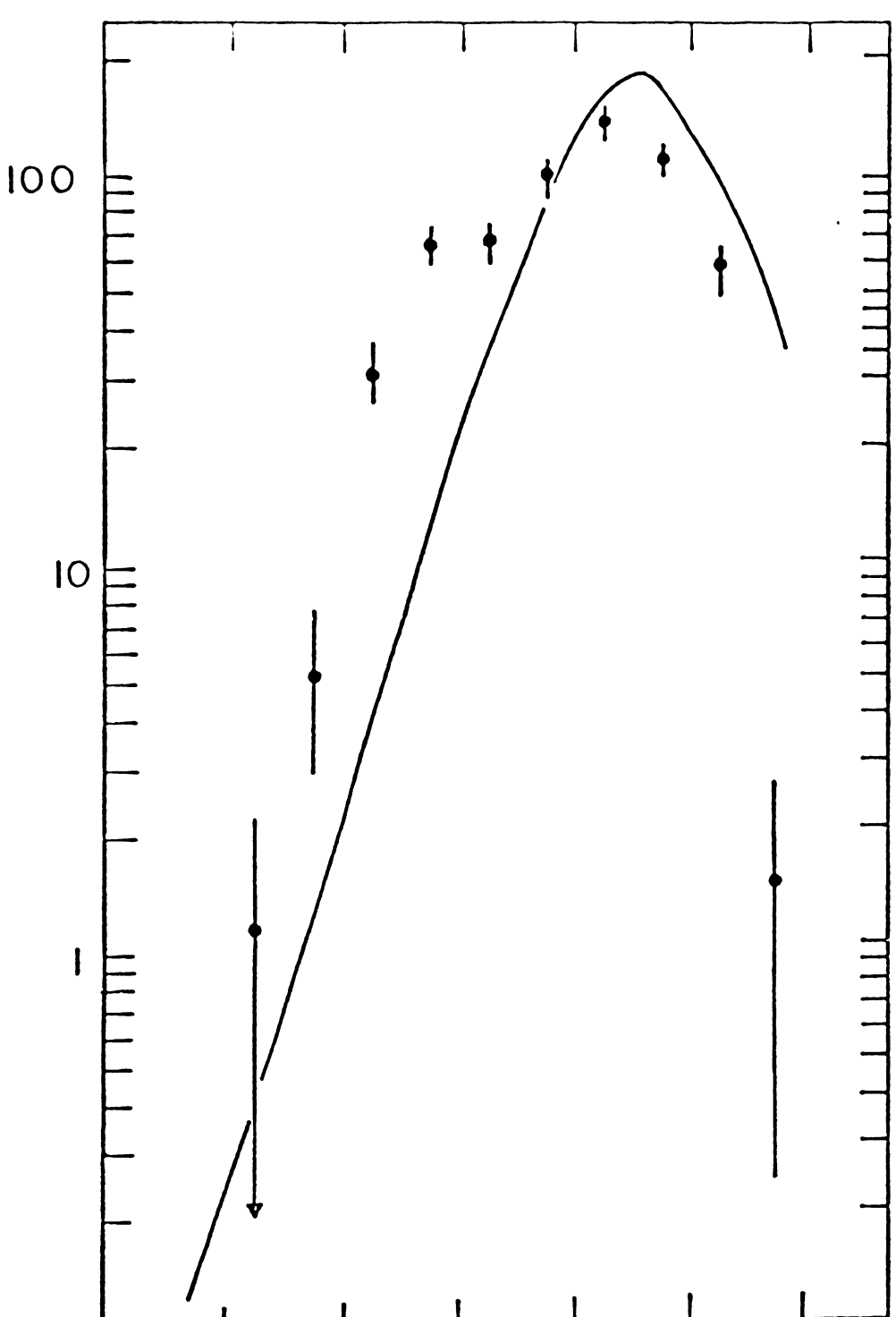

Figure 5.26 Dimuon Subtracted W and $D\bar{D}$ Model Curve

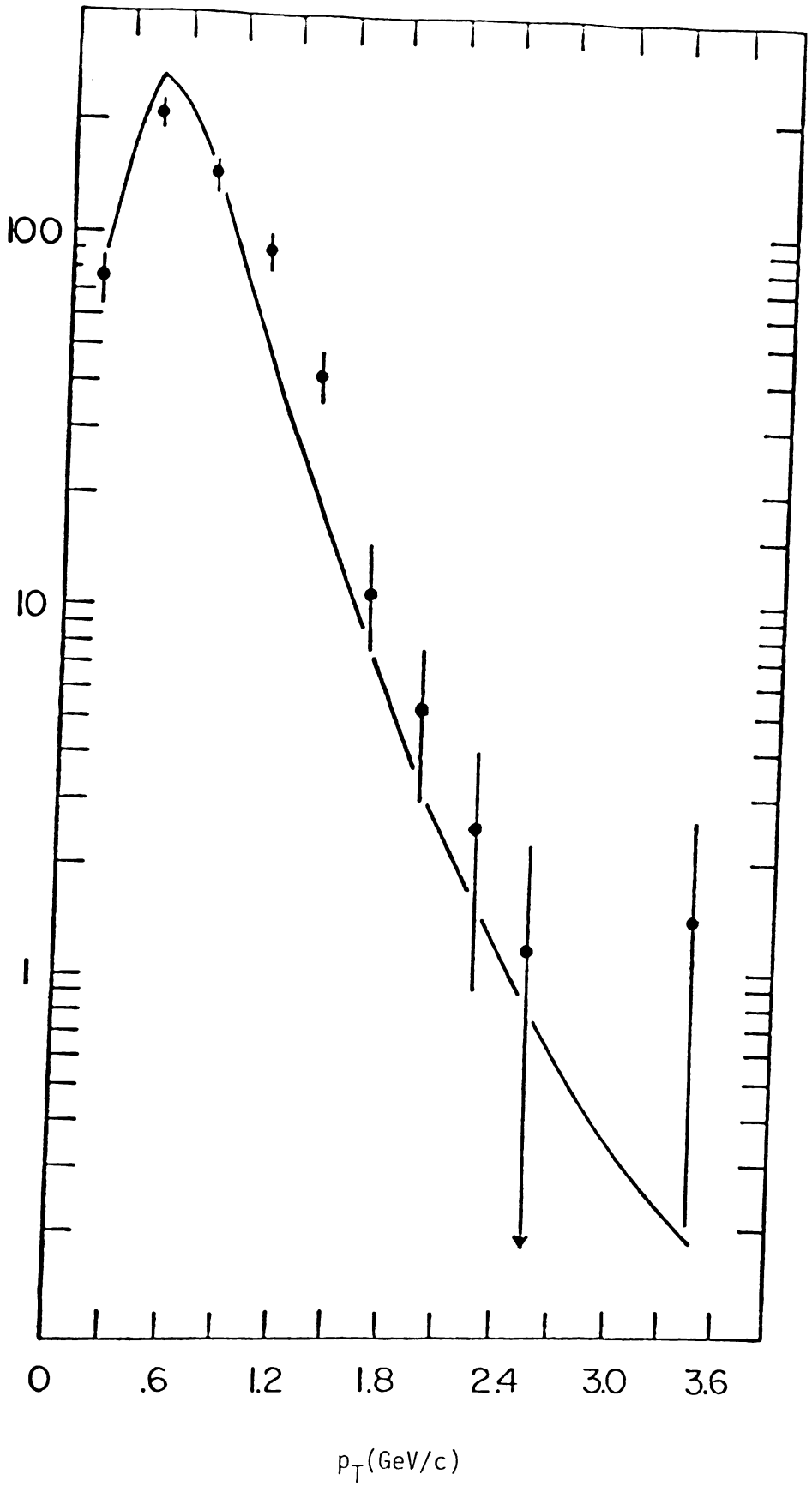

Figure 5.27 Dimuon Subtracted p_T and $D\bar{D}$ Model Curve

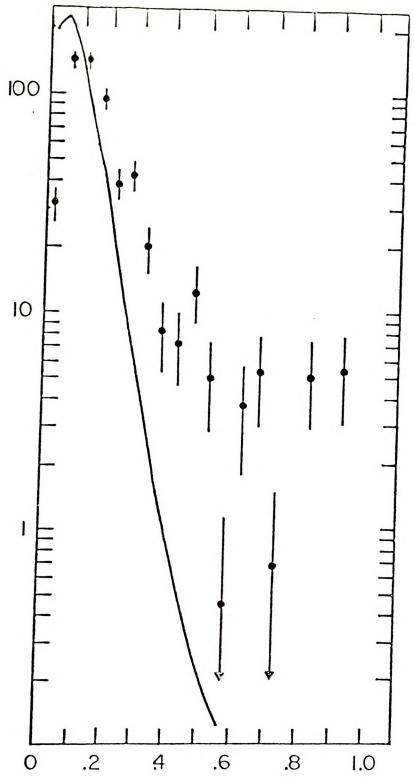

Figure 5.28 Dimuon Subtracted E_2/ν and $D\bar{D}$ Model Curve

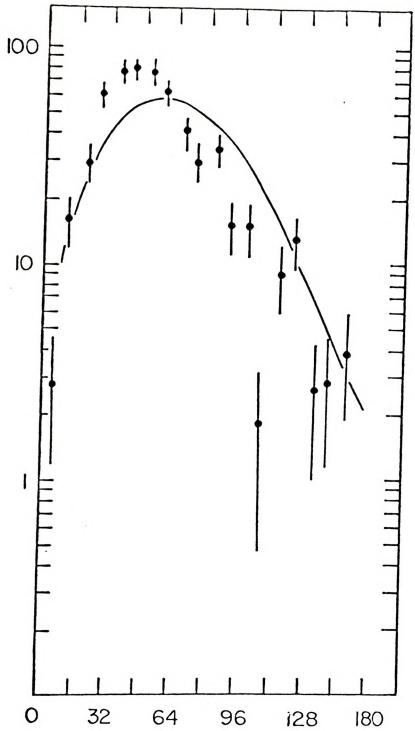

Figure 5.29 Dimuon Subtracted $\Delta\theta$ and $D\bar{D}$ Model Curve

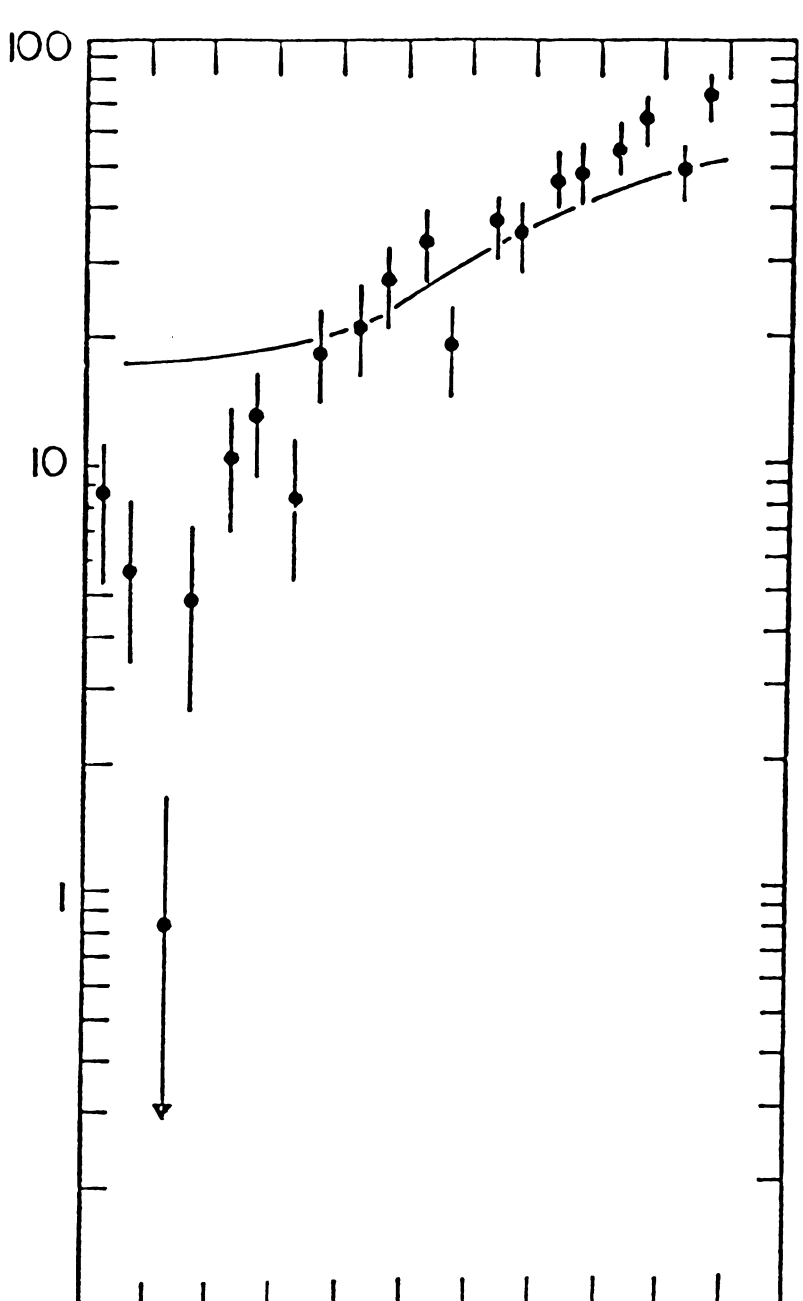

Figure 5.30 Dimuon Subtracted $\Delta\phi$ and $D\bar{D}$ Model Curve

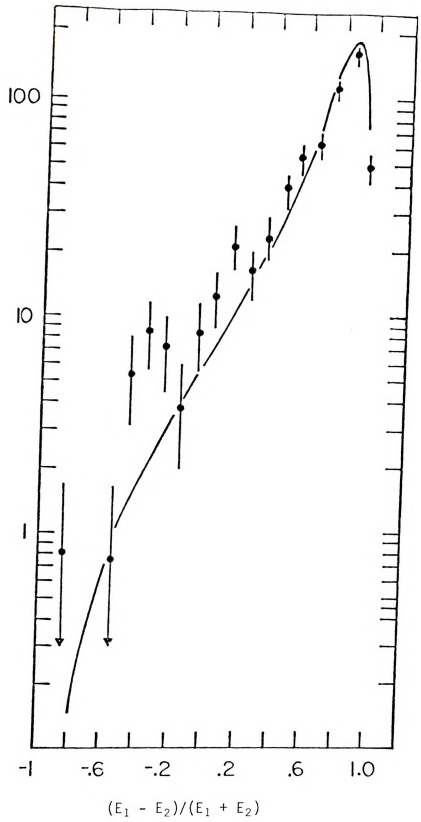

Figure 5.31 Dimuon Subtracted Asymmetry and $D\bar{D}$ Model Curve

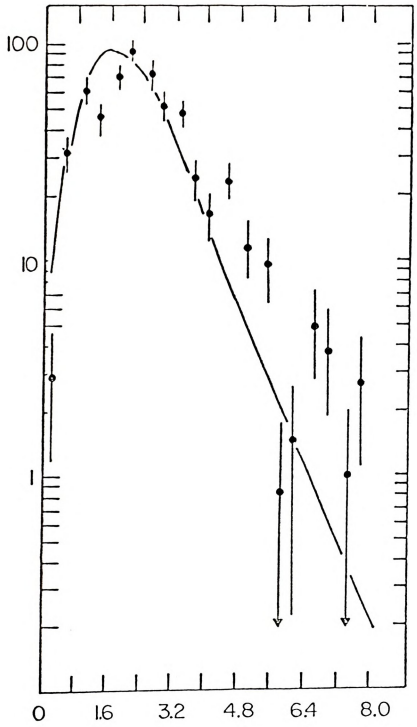

Figure 5.32 Dimuon Subtracted $M_{\mu\mu}$ and $D\bar{D}$ Model Curve

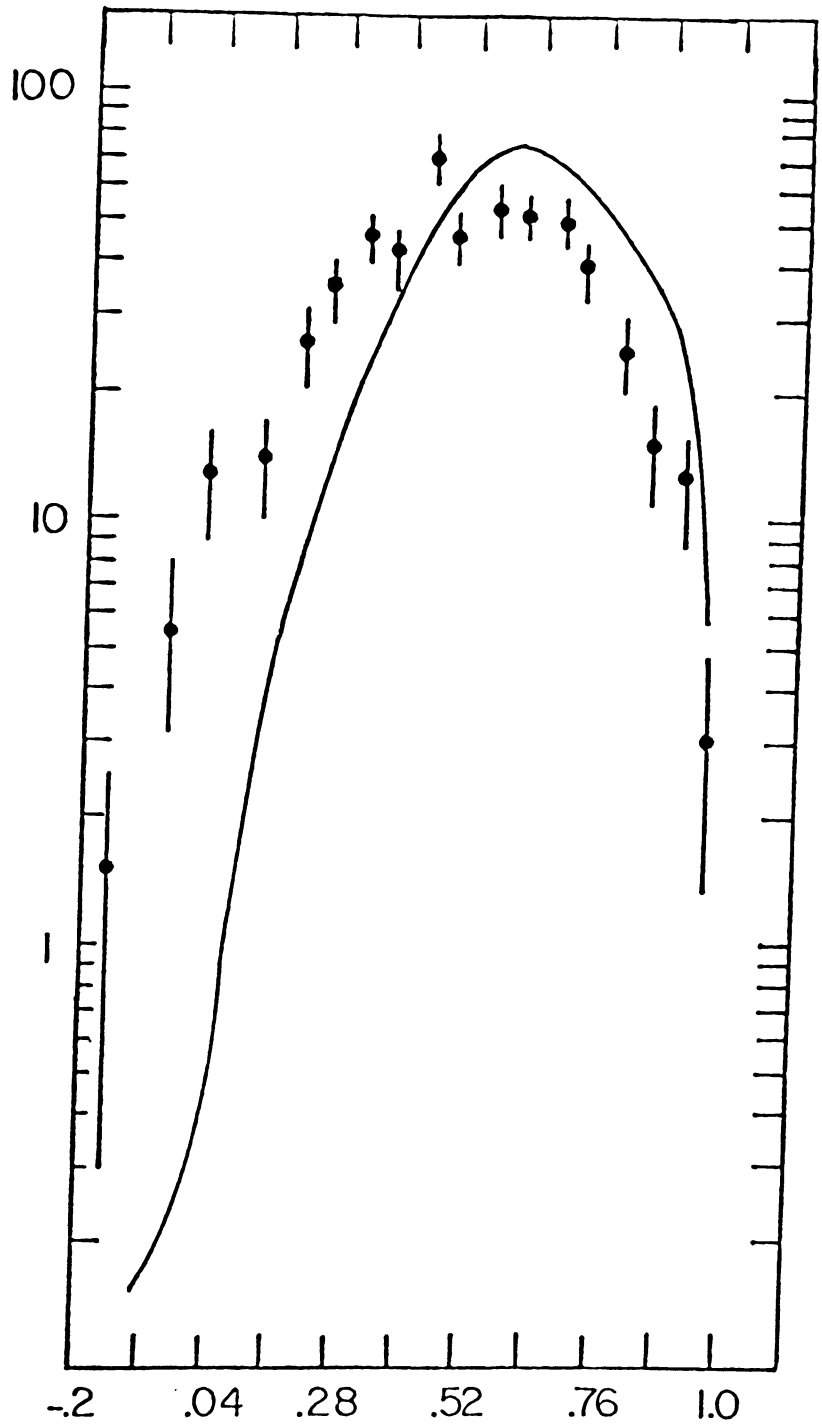

Figure 5.33 Dimuon Subtracted Inelasticity and $D\bar{D}$ Model Curve

Table 5.6. Dependence of P_T Spectra on Model Parameters (a=1)

P_T (GeV/c)	b=0.25	b=0.5	b=1.0	b=2.0	b=3.0
0-0.3	85.2	89.0	91.2	92.9	94.2
0.3-0.6	268.1	275.3	279.7	282.4	283.7
0.6-0.9	142.1	138.2	135.6	134.5	134.1
0.9-1.2	50.3	46.8	44.6	42.8	41.8
1.2-1.5	18.1	16.1	15.1	14.2	13.6
1.5-1.8	7.4	6.5	6.1	5.8	5.6
1.8-2.1	3.2	2.8	2.6	2.4	2.2
2.1-2.4	1.5	1.3	1.2	1.2	1.1
2.4-2.7	0.77	0.70	0.68	0.66	0.64
2.7-3.0	0.45	0.42	0.43	0.42	0.38
3.0-3.3	0.26	0.24	0.24	0.23	0.22
3.3-3.6	0.18	0.15	0.13	0.11	0.11
3.6-3.9	0.11	0.10	0.09	0.08	0.08
3.9-4.2	0.08	0.07	0.06	0.06	0.05
4.2-4.5	0.04	0.04	0.03	0.03	0.03
4.5-4.8	0.04	0.03	0.03	0.03	0.02
4.8-5.1	0.03	0.03	0.04	0.04	0.03
5.1-5.4	0.03	0.03	0.03	0.02	0.02
5.4-5.7	0.04	0.03	0.01	0.01	0.01
5.7-6.0	0.02	0.02	0.01	0.01	0.01

section for charm production can be calculated as: $\sigma \cdot B\mu$ = event rate/luminosity, where $B\mu$ is the branching ratio for $D \rightarrow K\mu\nu$ or $D \rightarrow K^*(890)\mu\nu$ (taken as 10% based on SLAC data) and the luminosity is the number of target nucleons/cm^2 * incident muon flux. However, this cross section was uncorrected for acceptance, and since our acceptance was very low (even in the best acceptance regions), was an almost meaningless number. For E319, we unfolded this acceptance (using the $D\bar{D}$ Monte Carlo and the Nieh model for $D\bar{D}$ production and decay described in Chapter IV) and have obtained the total number of events expected <u>without</u> acceptance, thus calculating the total $D\bar{D}$ cross section times leptonic branching ratio. To do this, use was made of the P_T (transverse momentum of the produced muon with respect to the virtual photon direction) spectrum, since there were no explicit cuts made on P_T in the Monte Carlo (i.e. this acceptance should extrapolate smoothly to $P_T = 0$). Also, the P_T spectrum seemed to be fairly well fit by the Nieh model, and was fairly insensitive to the choice of model parameters used. The Nieh model was used only to calculate the P_T acceptance; the experimental P_T spectrum was used to calculate the expected event rate without acceptance. Once the differential cross section was unfolded, it was summed for all P_T values to get the total cross section. To show that the acceptance obtained was <u>not</u> critically model dependent, Tables 5.7 and 5.8 show the P_T acceptance using the decay modes $D \rightarrow K\mu\nu$ and $D \rightarrow K^*\mu\nu$, respectively. For the final data unfolding, the P_T acceptance shown in Table 5.9 was used, which is a weighted average of the $D \rightarrow K^*\mu\nu$ and $D \rightarrow K\mu\nu$ values. The first columns in Tables 5.7 - 5.9 show the number of accepted events in each P_T bin, the second columns show the number of generated

Table 5.7. P_T Acceptance for $D \rightarrow K\mu\nu$

P_T (GeV/c)	Accepted P_T	Generated P_T	Acceptance (%)
0-0.3	74.7	4567.5	1.64 ± 0.60
0.3-0.6	256.9	1846.8	13.91 ± 2.22
0.6-0.9	152.8	886.3	17.24 ± 3.32
0.9-1.2	57.8	381.3	15.15 ± 3.06
1.2-1.5	21.8	192.2	11.36 ± 4.36
1.5-1.8	9.2	78.2	11.83 ± 4.20
1.8-2.1	4.0	43.5	9.15 ± 4.19
2.1-2.4	1.9	15.6	12.06 ± 2.71
2.4-2.7	1.0	8.9	10.86 ± 3.58
2.7-3.0	0.49	6.1	8.06 ± 3.74
3.0-3.3	0.30	2.1	14.37 ± 2.77
3.3-3.6	0.23	2.8	8.13 ± 5.22
3.6-3.9	0.12	1.1	11.49 ± 5.19
3.9-4.2	0.08	0.46	16.56 ± 5.79
4.2-4.5	0.04	0.40	10.84 ± 5.39
4.5-4.8	0.04	0.23	15.97 ± 6.70
4.8-5.1	0.05	0.26	17.20 ±16.26
5.1-5.4	0.03	0.28	11.03 ±11.59
5.4-5.7	0.02	0.29	6.12 ± 5.56
5.7-6.0	0.02	0.17	11.89 ± 6.74

Table 5.8. P_T Acceptance for $D \rightarrow K^* \mu \nu$

P_T (GeV/c)	Accepted P_T	Generated P_T	Acceptance (%)
0-0.3	102.1	6792.2	1.50 ± 0.47
0.3-0.6	288.9	2868.1	10.07 ± 3.64
0.6-0.9	128.2	1018.5	12.59 ± 1.87
0.9-1.2	39.7	388.3	10.24 ± 3.30
1.2-1.5	12.8	107.5	11.93 ± 2.02
1.5-1.8	4.7	55.7	8.45 ± 3.95
1.8-2.1	2.2	30.6	7.03 ± 3.89
2.1-2.4	0.90	9.9	9.03 ± 5.61
2.4-2.7	0.50	6.5	7.71 ± 4.48
2.7-3.0	0.40	3.1	12.92 ± 8.18
3.0-3.3	0.20	2.0	9.82 ± 6.29
3.3-3.6	0.10	0.82	12.62 ± 6.59
3.6-3.9	0.09	0.50	18.36 ±13.34
3.9-4.2	0.07	0.88	8.41 ± 7.92
4.2-4.5	0.04	0.30	12.93 ± 5.64
4.5-4.8	0.03	0.25	13.62 ± 7.94
4.8-5.1	0.02	0.21	8.05 ± 4.98
5.1-5.4	0.02	0.16	15.22 ± 9.71
5.4-5.7	0.07	0.08	82.16 ±87.24
5.7-6.0	0.01	0.38	3.90 ± 6.81

Table 5.9. Total P_T Acceptance for the D $\overline{D}$ Model.

P_T (GeV/c)	Accepted P_T	Generated P_T	Acceptance (%)
0-0.3	85.7	5457.4	1.58 ± 0.40
0.3-0.6	269.7	2255.3	12.37 ± 1.97
0.6-0.9	143.0	939.2	15.38 ± 2.13
0.9-1.2	50.6	384.1	13.18 ± 2.26
1.2-1.5	18.2	158.3	11.59 ± 2.74
1.5-1.8	7.4	69.2	10.48 ± 2.97
1.8-2.1	3.2	38.3	8.30 ± 2.96
2.1-2.4	1.5	13.3	10.85 ± 2.77
2.4-2.7	0.78	7.9	9.60 ± 2.80
2.7-3.0	0.46	4.9	10.00 ± 3.97
3.0-3.3	0.26	2.1	12.55 ± 3.02
3.3-3.6	0.18	2.0	9.93 ± 4.10
3.6-3.9	0.11	0.85	14.24 ± 6.18
3.9-4.2	0.08	0.63	13.30 ± 4.70
4.2-4.5	0.04	0.36	11.68 ± 3.94
4.5-4.8	0.04	0.24	15.02 ± 5.12
4.8-5.1	0.03	0.24	13.54 ± 9.96
5.1-5.4	0.03	0.23	12.71 ± 7.97
5.4-5.7	0.04	0.20	50.55 ±78.06
5.7-6.0	0.02	0.25	8.70 ± 4.87

events in each P_T bin (the first and second columns have been normalized so that the total number of events accepted was 577.9 and the ratio of the accepted events/generated events remained the same in each bin), while the third columns show the P_T acceptance and error.

The basic $D\bar{D}$ Monte Carlo was modified to keep track of the generated P_T's and to record these before any of the hardware or software cuts were made which decided which events would be accepted and before any tracking through the spectrometer was done. For the second and third traced muons (i.e. the decay muons from D decays), the scattered muon was chosen as the positive one with the largest momentum, and it was used, along with the incident muon, to define the virtual photon direction. Using this, and the momentum of the less energetic positive or negative muon, P_T was calculated. The momentum resolution for the scattered and the produced muons was done exactly the same as for the accepted events, using the same weighting schemes to call the histogram storage arrays. After the generated weighted events were stored, the cuts were made as usual and histograms called for the accepted events.

To get the cross section, the raw data distribution for P_T was multiplied by a factor to raise its nomalization to the total number of events expected without finding inefficiencies (i.e. 412 events were momentum analyzable out of 449 found dimuons, but track reconstruction and scanning efficiencies raise the expected number to 644 events). The Monte Carlo calculated elastic QED trident dimuon, π/K cascade decay, and prompt muon production differential event rates were subtracted bin by bin from the above P_T spectrum.

The P_T acceptance was then unfolded, bin by bin, by dividing the background subtracted renormalized raw data distribution by the P_T acceptance. This is shown in Table 5.10, and gives a total $D\bar{D}$ cross section of (3.2 ± 0.8) nanobarns per nucleon (assuming $\sigma_{Fe} = A^{1.0} \sigma_p$, i.e. no nuclear shadowing; and assuming a muon branching ratio for D decays of 10%). The error in the cross section was calculated by combining in quadrature the three most important error terms: a) the statistical errors for the raw data sample ($\sim\sqrt{N}$), b) the data renormalization error of 8.5%, and c) the statistical error in the acceptance calculation. We have neglected the errors for the π/K, elastic QED, and prompt muon background subtractions, which were small. Note that this error does not account for any differences that may occur in the P_T acceptance if we had changed the a or b parameters of the Nieh model (however, these changes would be small for a reasonable range of a and b parameters).

5.4 Comparison With Theory

In the framework of quantum chromodynamics (QCD), heavy quark production estimates have been made on the basis of the photon-gluon fusion model.[7] The heavy produced quarks can then decay semi-leptonically to produce multimuon events.

In the calculations of Barger et al.[5] a scaling on-shell gluon distribution $G(x) = 3(1 - x)^5/x$ was assumed, where x is the nucleon momentum fraction carried by the gluon in an infinite momentum frame. A constant gluon-heavy quark coupling constant was assumed with scale set by the heavy quark mass:

$$\alpha_s = \frac{12\pi}{(33 - 2n) \ln (4m_Q^2/\Lambda^2)}$$

Table 5.10. Unfolding the P_T Kinematic Spectra

P_T (GeV/c)	Raw Data	Corrected Data	QED Background	π/K Prompt μ	Subtracted Data	$\frac{\text{Data}}{\text{Acceptance}}$	Error
0-0.3	56	87.8	1.55	7.82	78.38	4958.92	1352.8
0.3-0.6	143	224.1	1.98	20.37	201.71	1671.23	350.8
0.6-0.9	103	161.4	1.70	16.61	143.08	952.46	146.3
0.9-1.2	63	98.7	1.20	7.08	90.43	711.59	155.2
1.2-1.5	29	45.4	1.01	2.48	41.95	362.12	103.2
1.5-1.8	8	12.5	0.59	0.93	11.01	107.99	42.0
1.8-2.1	4	6.3	0.67	0.29	5.31	64.98	32.8
2.1-2.4	2	3.1	0.54	0.08	2.52	23.65	14.1
2.4-2.7	1	1.6	0.36	0.04	1.17	12.55	9.8
2.7-3.0			0.23	0.03			
3.0-3.3			0.14	0.02			
3.3-3.6	1	1.6	0.13	0.02	1.42	14.95	13.5
3.6-3.9			0.08	0.01			
3.9-4.2			0.06	0.01			
4.2-4.5			0.03				
4.5-4.8			0.02				
4.8-5.1			0.01				
5.1-5.4	1	1.6	0.007		1.56	12.58	13.3
5.4-5.7							
5.7-6.0							
Total	412	644	10.33	55.79	577.89	8887.15	2233.7

where n is the effective number of quark flavors and $\Lambda \sim 0.5$ GeV. For the charmed quark, they take $m_c = 1.87$ GeV $= m_D$ in order to get the correct $D\bar{D}$ threshold. With n = 4, this gives $\alpha_s = 0.37$. For b quark production, it was assumed that $m_b = 5$ GeV, n = 5, and $\alpha_s = 0.27$. A c-quark to D-meson fragmentation function[8] D(z) = constant, was chosen, where $z = E_D/E_C$ in the lab frame and D(z) was normalized to give one D-meson per c-quark; plus a transverse momentum distribution $dN/dP_T^2 \sim \exp(-3(m_D^2 + P_T^2)^{\frac{1}{2}})$. For the semi-leptonic decay of the D-meson, equal proportions of $D \rightarrow K^*(890)\mu\nu$ and $D \rightarrow K\mu\nu$ were taken with matrix elements obtained from Barger et al.[9] The semileptonic branching ratio was taken as 10%. Figure 5.34 shows their resulting $c\bar{c}$ and $b\bar{b}$ production cross sections from the photon-gluon mechanism versus incident muon energy E. The calculated μN cross section at E = 270 GeV was $\sigma(c\bar{c}) \sim 5$ nanobarns, which agrees fairly well with the number obtained in the last section.

5.5 Conclusions

An experiment was performed at the Fermi National Accelerator Lab using a positive 269 GeV muon beam incident on a 7.38 meter long iron-plastic scintillator target. With an incident flux of 1.0974×10^{10} muons (total luminosity of $2.8 \times 10^{37}/cm^2$), 449 events with two muons in the final state were observed. Applying the track reconstruction and scanning efficiency of $\sim$ 70% gave the expected number of dimuons (644) for this experiment. Subtracting the Monte Carlo calculated π/K cascade decay and prompt muon production (total of 56 events) and elastic QED tridents (total of 10 events) backgrounds yielded 578 dimuons which were attributed to associated charmed meson production and semileptonic decay. Using a $D\bar{D}$ Monte

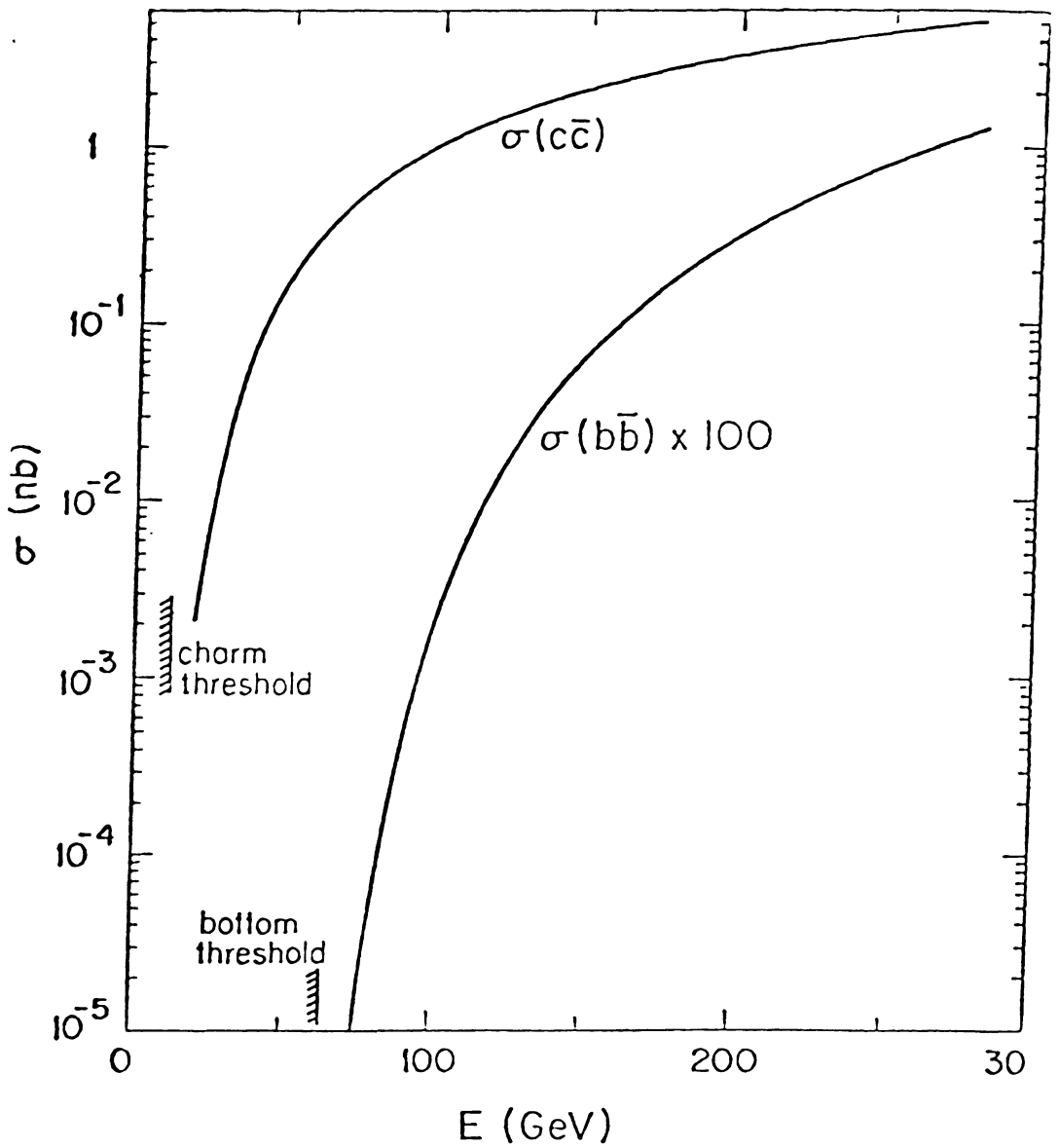

Figure 5.34 Calculated $\sigma(c\bar{c})$ for the Photon-Gluon Fusion Model

Carlo, based on the Nieh production model, the P_T (transverse momentum of the produced muon with respect to the virtual photon direction) acceptance was calculated and used to unfold the background subtracted renormalized data dimuon P_T spectra yielding the total number of dimuon events expected for the experiment without apparatus acceptance. This number of events was used to calculate the cross section for associated charm production, which was (3.2 ± 0.8) nanobarns per nucleon. This cross section compares with a calculated cross section, based on the photon-gluon fusion model of QCD, of ~ 5 nanobarns per nucleon for our incident energy.

Use of the beam veto counters in our experiment, which vetoed events with small angle muons entering the spectrometer, successfully reduced the large expected[5] electromagnetic and non-charm hadronic backgrounds to a point where the charm signal was dominant for dimuon events. Dimuon event finding was necessarily slow due to the large number of events that had to be visually scanned, the chief reason for this being the inefficiency of the front spark chambers and the lack of an efficient dimuon trigger. Use of proportional chambers (which have much shorter memory times, can handle higher rates, and have very good multi-track efficiencies) instead of spark chambers, optimization of trigger bank and veto locations for dimuon data, and utilization of an efficient dimuon trigger would have greatly enhanced our experiment. This has been done for the third generation muon experiments which have taken data recently at Fermilab[10] and CERN,[11] and which should yield at least an order of magnitude larger data sample for future analysis.

REFERENCES

REFERENCES

Chapter I

1. M. Gell-Mann and Y. Ne'eman, The Eightfold Way, Benjamin, New York, 1964.
2. O. W. Greenberg et al., Physics Reports 32C (1977) 70.
3. R. Feynman, Statistical Mechanics, Benjamin, Reading, Mass., 1972.
4. D. Perkins, Introduction to High Energy Physics, Addison-Wesley, Reading, Mass., 1972.
5. J. D. Bjorken et al., Physics Letters 11 (1964) 255.
6. C. Quigg, Fermilab-CONF-78/37-THY, April 1978; M. K. Gaillard et al., Reviews of Modern Physics 47 (1975) 277.
7. J. E. Augustin et al., Physical Review Letters 33 (1974) 1406.
8. J. J. Aubert et al., Physical Review Letters 33 (1974) 1404.
9. G. S. Abrams et al., Physical Review Letters 33 (1974) 1453.
10. M. L. Perl et al., Physical Review Letters 35 (1975) 1489.
11. S. W. Herb et al., Physical Review Letters 39 (1977) 252.
12. C. Chang et al., Physical Review Letters 39 (1977) 519; K. W. Chen et al., Physical Review Letters 40 (1978) 1417.
13. D. Bauer et al., Physical Review Letters 43 (1979) 1551.
14. R. Hofstadter, Nuclear and Nucleon Structure, Benjamin, New York, 1963.
15. M. B. Einhorn, Fermilab-Lecture-75/1-THY/EXP, 1975; H. J. Lipkin, Lie Groups For Pedestrians, North Holland Publishing Co., Amsterdam, 1966; F. E. Low, Symmetries and Elementary Particles, Gordon & Breach, New York, 1967.
16. V. Barnes et al., Physical Review Letters 12 (1964) 204.
17. S. Weinberg, Scientific American, Volume 244, Number 6 (1981) 64.
18. W. Chinowsky, Annual Reviews of Nuclear Science 27 (1977) 393.
19. C. D. Anderson et al., Physical Review 51 (1937) 884, 54 (1938) 88; J. C. Street et al., Physical Review 52 (1937) 1003.
20. W. Pauli, Handbuch der Physik 24 (1933) 1,233.
21. F. Reines et al., Physical Review 113 (1959) 273.
22. G. Danby et al., Physical Review Letters 9 (1962) 36; M. Block et al., Physics Letters 13 (1964) 86.
23. J. J. Sakurai, Advanced Quantum Mechanics, Addison-Wesley, Reading, Mass., 1967.

24. J. Iliopoulos, An Introduction to Gauge Theories, CERN 76-11, Geneva, 1976.

25. J. D. Jackson, Classical Electrodynamics, Wiley and Sons, New York, 1975.

26. P.A.M. Dirac, Proceedings of the Royal Society A117 (1928) 610.

27. C. D. Anderson, Physical Review 43 (1933) 491;
P. Blackett et al., Proceedings of the Royal Society A139 (1933) 699.

28. V. Barger et al., Nuclear Physics B73 (1974) 269.

29. S. Weinberg, Physical Review Letters 19 (1967) 1264.

30. C. Y. Prescott et al., SLAC-PUB-2148, July 1978.

31. N. Cabibbo, Physical Review Letters 10 (1963) 531.

32. S. Glashow et al., Physical Review D2 (1970) 1285.

33. G. Goldhaber et al., Physical Review Letters 37 (1976) 255;
I. Peruzzi et al., Physical Review Letters 37 (1976) 569.

34. R. Brandelik et al., Physics Letters 70B (1977) 132.

35. W. Braunchweig et al., Physics Letters 67B (1977) 243.

36. A. Benvenuti et al., Physical Review Letters 34 (1975) 419, 597;
B. Barish et al., Physical Review Letters 34 (1975) 538.

37. S. Stein et al., Physical Review D12 (1975) 1884.

38. L. Hand, Proceedings of the 1977 International Symposium on Lepton and Photon Interactions at High Energies, Hamburg, 1977.

39. J. D. Bjorken et al., Physical Review 185 (1969) 1975.

40. J. Friedman et al., Annual Review of Nuclear Science 22 (1972) 203.

41. D. Fox et al., Physical Review Letters 33 (1974) 1504;
Y. Watanabe et al., Physical Review Letters 35 (1975) 898;
C. Chang et al., Physical Review Letters 35 (1975) 901.

42. H. L. Anderson et al., Physical Review Letters 37 (1976) 4.

43. H. L. Anderson et al., Physical Review Letters 38 (1977) 1450.

44. E. M. Riordan et al., SLAC-PUB-1634, 1975;
W. E. Atwood, SLAC-PUB-185, 1975.

45. A. J. Buras et al., Nuclear Physics B132 (1978) 249.

46. R. Ball, Ph.D. Thesis, Michigan State University, 1979.

47. J. P. Boymond et al., Physical Review Letters 33 (1974) 112;
J. A. Appel et al., Physical Review Letters 33 (1974) 722;
L. B. Leipuner et al., Physical Review Letters 34 (1975) 103;
D. Bintinger et al., Physical Review Letters 35 (1975) 72.

48. S. J. Brodsky et al., Physical Review 145 (1966) 1018.

49. H. Deden et al., Physics Letters 58B (1975) 361;
J. Blietschau et al., Physics Letters 60B (1976) 207.

50. C. Chang, Ph.D. Thesis, Michigan State University, 1975.

51. L. Jones et al., Physical Review D17 (1978) 759, 2332;
J. Babcock et al., Physical Review D18 (1978) 162;
M. Shifman et al., Nuclear Physics B136 (1978) 157;
H. Fritzsch et al., Physics Letters 72B (1978) 385;
M. Gluck et al., Physics Letters 79B (1978) 453;
J. Leveille et al., Nuclear Physics B147 (1979) 147.

52. M. Atac, editor, Proceedings of the Calorimeter Workshop, Fermilab publication, Batavia, Illinois, 1975.

Chapter II

1. Y. Watanabe, Ph.D. Thesis, Cornell University, 1975.
2. D. Bauer, Ph.D. Thesis, Michigan State University, 1979.
3. C. Richard-Serre, CERN report 71-18, Geneva, 1971.
4. S. Herb, Ph.D. Thesis, Cornell University, 1975.
5. E. McLaughlin et al., Nuclear Instruments and Methods 70 (1969) 343.
6. C. Chang, Ph.D. Thesis, Michigan State University, 1975.
7. R. Ball, Ph.D. Thesis, Michigan State University, 1979.

Chapter III

1. Fermilab Experiment 319 Proposal, 1974.
2. W. A. Loomis et al., Physical Review Letters 35 (1975) 1483.
3. L. Litt, FNAL Expt. 319 internal memo, Aug 1976.
4. D. Bauer, FNAL Expt. 319 internal memo, Sep 1978.
5. L. Litt, FNAL Expt. 319 internal memo, Oct 1976.
6. D. Bauer, Ph.D. Thesis, Michigan State University, 1979.
7. P. Schewe, Ph.D. Thesis, Michigan State University, 1978.
8. R. Ball, Ph.D. Thesis, Michigan State University, 1979.
9. L. Litt, FNAL Expt. 382 internal memo, Mar 1976.
10. C. Chang, Ph.D. Thesis, Michigan State University, 1975.
11. C. Richard-Serre, CERN 71-18, Geneva, 1971.

Chapter IV

1. D. Fox et al., Physical Review Letters 33 (1974) 1504;
Y. Watanabe et al., Physical Review Letters 35 (1975) 898;
C. Chang et al., Physical Review Letters 35 (1975) 901.

2. B. Ball et al., Michigan State University MSU-CSL-40, 1977.

3. C. Chang et al., Physical Review Letters 39 (1977) 519;
K. W. Chen et al., Physical Review Letters 40 (1978) 1417.

4. R. C. Ball et al., Physical Review Letters 42 (1979) 866.

5. A. J. Buras et al., Nuclear Physics B132 (1978) 249.

6. P. Bevington, Data Reduction and Error Analysis for the Physical Sciences, McGraw Hill, New York, 1969.

7. L. Yuan et al., Methods of Experimental Physics 5A, Academic Press, New York, 1961.

8. B. Rossi, High Energy Particles, Prentice-Hall Inc., Englewood Cliffs, N.J., 1965.

9. L. Yuan et al., Methods of Experimental Physics 5A, Academic Press, New York, 1961.

10. P. M. Joseph, Nuclear Instruments and Methods 75 (1969) 13.

11. Y.S. Tsai, Reviews of Modern Physics 46 (1974) 815.

12. C. Richard-Serre, CERN report 71-18, Geneva, 1971.

13. J. D. Jackson, Classical Electrodynamics, John Wiley and Sons, New York, 1975.

14. E. D. Cashwell et al., Monte Carlo Method for Random Walk Problems, Pergamon Press, New York, 1959.

15. J. P. Boymond et al., Physical Review Letters 33 (1974) 112;
J. A. Appel et al., Physical Review Letters 33 (1974) 722;
L. B. Leipuner et al., Physical Review Letters 34 (1975) 103;
D. Bintinger et al., Physical Review Letters 35 (1975) 72.

16. A. Van Ginneken, FNAL Report FN-272, 1975.

17. W. Loomis et al., Physical Review Letters 35 (1975) 1483.

18. A. Van Ginneken, private communication, 1978.

19. A. Van Ginneken et al., High Energy Particle Interactions in Large Targets, Fermi National Accelerator Lab, Batavia, Il, 1977.

20. R. Hagedorn, Suppl. Nuovo Cimento 3 (1965) 147;
R. Hagedorn et al., Suppl. Nuovo Cimento 6 (1968) 169.

21. H. Grote et al., Atlas of Particle Spectra, CERN publication, Geneva, 1970.

22. S. J. Brodsky et al., Physical Review 145 (1966) 1018.

23. M. Tannenbaum, Physical Review 167 (1968) 1308.

24. S. Stein et al., Physical Review D12 (1975) 1884.

25. Dan Bauer, Ph.D. Thesis, Michigan State University, 1979.

26. F. Bletzacker et al., Physical Review Letters 37 (1976) 1316;
F. Bletzacker et al., ITP-SB-77-44, Stony Brook, New York, 1977.

27. R. Hagedorn et al., Suppl. Nuovo Cimento 6 (1968) 168.

28. W. Bacino et al., Physical Review Letters 43 (1979) 1073.

29. I. Hinchliffe et al., Nuclear Physics B114 (1976) 45.

30. P. A. Piroue et al., Physical Review 148 (1966) 1315.

31. R. Taylor, Proceedings of the XIX International Conference on High Energy Physics, Tokyo, August 1978.

32. A. Kotlewski, FNAL experiment 26 internal memo, 1975.

33. P. Schewe, Ph.D. Thesis, Michigan State University, 1978.

34. L. Hand, Proceedings of the 1977 International Symposium on Lepton and Photon Interactions at High Energies, Hamburg, 1977.

35. V. Barger et al., University of Wisconsin preprint COO-881-83, 1979;
V. Barger et al., Physical Review D21 (1980) 299.

36. L. M. Jones et al., Physical Review D17 (1978) 759, 2332;
J. Babcock et al., Physical Review D18 (1978) 162;
M. A. Shifman et al., Nuclear Physics B136 (1978) 157.

Chapter V

1. D. Bauer, Ph.D. Thesis, Michigan State University, 1979.

2. D. Bauer et al., Physical Review Letters 43 (1979) 1551.

3. A. Van Ginneken, FNAL Report FN-272, 1975.

4. S. J. Brodsky et al., Physical Review 145 (1966) 1018.

5. V. Barger et al., University of Wisconsin preprint COO-881-83, 1979.

6. F. Bletzacker et al., Physical Review Letters 37 (1976) 1316.

7. L. Jones et al., Physical Review D17 (1978) 759, 2332;
J. Babcock et al., Physical Review D18 (1978) 162;
M. Shifman et al., Nuclear Physics B136 (1978) 157;
H. Fritzsch et al., Physics Letters 72B (1978) 385;
M. Gluck et al., Physics Letters 79B (1978) 453;
J. Leveille et al., Nuclear Physics B147 (1979) 147.

8. R. Odorico et al., Nuclear Physics B136 (1978) 333.

9. V. Barger et al., Physical Review D16 (1977) 746.

10. Fermilab Experiment 203 Proposal, 1973.

11. CERN Experiment NA2 and NA4 Proposals, 1976.